Approval Sheet

Title of Thesis: The Total Cross Section for $\nu_\mu e$ Elastic Scattering

Name of Candidate: Kenneth Alan Lefler
Doctor of Philosophy, 1981

Thesis and Abstract Approved by:

Dr. Andris Skuja
Associate Professor of Physics
Department of Physics and Astronomy

Date Approved: November 19, 1981

FERMILAB
LIBRARY

JAB2023

Vita

Name: Kenneth Alan Lefler

Permanent Address: 2817 Russell Dr.
Fairborn, Ohio 45324

Degree and Date to be Conferred: Doctor of Philosophy, 1981

Date of Birth: June 12, 1953

Place of Birth: Dayton, Ohio

College Institutions Attended	Date	Degree	Date of Degree
Ohio University	1971-1975	B.S.	June, 1975
University of Maryland	1975-1981	Ph.D.	Dec., 1981

Degree for which Thesis is Submitted: Ph.D.

Major: Physics

Minor: General Physics

Publications:

Measurement of the Cross Section for Neutrino Electron Elastic Scattering, Physical Review Letters 44, 629 10 March 1980.

Professional Positions Held:

Teaching Assistant, University of Maryland, Aug. 1975-June 1977
Research Assistant, University of Maryland, June 1977-July 1981
Staff Scientist, ENSCO, Inc., July 1981 -

The Total Cross-Section for $\nu_\mu e$ Elastic Scattering

by
Kenneth A. Lefler

Dissertation submitted to the Faculty of the Graduate School
of the University of Maryland in partial fulfillment
of the requirements for the degree of
Doctor of Philosophy
1981

The Total Cross-Section for $\nu_\mu e$ Elastic Scattering

by Ken Lefler

Abstract

An experiment was performed at Fermi National Accelerator Laboratory to measure the total cross section for $\nu_\mu e$ elastic scattering. A total of 0.7×10^{19} 350 GeV protons were incident on the neutrino area target. The secondaries were horn focussed to produce a wide-band neutrino beam. The neutrinos were incident on a modular electromagnetic shower detector with good angular and energy resolution. A total of 190,000 triggered events were collected. The data were reduced to a sample of 26,000 events by demanding that only a single electron shower be present. These remaining events were reconstructed by computer and scanned visually for a final event selection. Kinematic cuts were applied to isolate the $\nu_\mu e$ events. The background subtracted and efficiency corrected signal was 33.0 ± 11.3 events. This corresponds to a cross section of $1.6 \pm .5$ (statistical) $\pm .5$ (systematic) $\times 10^{-42}$ E_ν cm^2/Gev and a Weinberg angle given by $\sin^2\theta_W = .25 \pm .06$ (statistical) $\pm .06$ (systematic).

Acknowledgments

Today's high energy physics experiments require the collaboration and cooperation of a great many individuals. I never could have completed this thesis without the generous help of many friends and collaborators. In particular I would like to thank my thesis advisor, Dr. Andris Skuja, for giving me the opportunity to work on this experiment and his patient guidance towards its completion. His help and instruction in the techniques of experimental physics are greatly appreciated.

I am also indebted to Dr. Norman Booth for his gracious hospitality during my stay at the Nuclear Physics Laboratory, Oxford University. His help and encouragement at a crucial stage of the analysis were essential for the completion of this thesis.

At at time when the trend in experimental high energy physics is to ever larger collaborators, I had the good fortune to work closely with a small number of collaborators. I would like to thank Dr. Richard Heisterberg, Dr. Al Abashian, and in particular, Dr. Luke Mo for their contribution to the experiment and their contributions to my development as a physicist. The collaboration also involved three visiting physicists from the Institute for High Energy Physics, Peking, China, C. C. Chang, C. Li, and C. H. Wang. Their help during the data taking and analysis was essential to the completion of the experiment.

I would also like to thank Brenda Dunn and Mary Graminski for their careful typing of the thesis. I am also indebted to Joan Wright of the drafting department for her excellent drawing of the Figures.

In addition, I would like to thank Prof. George Snow and the other members of the Maryland high energy physics group for their generous financial support.

Table of Contents

Chapter	page
Acknowledgments	iii
List of Tables	vii
List of Figures	viii
I. Introduction	1
II. Theoretical Considerations	8
A. Kinematics	8
B. Phenomenological Lagrangian	13
C. Electroweak Model	19
III. Neutrino Production	27
IV. Apparatus	35
A. General Layout	35
B. Chamber Operation	39
C. Calorimetric Properties	50
D. Fast Electronics	61
E. Experimental Trigger	67
F. Online Program	71
Appendix IV.1. Determination of Chamber Constants	74
Appendix IV.2. Energy Calibration at the Experimental Site	79
Appendix IV.3. Electron Energy Resolution	82
V. Neutrino Flux	84
VI. Event Reduction	101
A. Data Taking	101
B. Event Reconstruction	107
C. Fitting Algorithm	115
D. Event Display	117
E. Computer Cuts	120
F. Scanning Cuts	133
G. Final Event Reduction	137
Appendix VI.1. Tap Hit Fiducial Cut	147
VII. Backgrounds	151
A. Quasielastic Background	151
B. Neutrino Nucleon Backgrounds	161

Page

Appendix VII.1. Muon Identification Probability 173

VIII. Results 176
A. Selection Efficiency 176
B. Results 177

IX. Conclusions 189

List of Tables

Table		Page
II.1	Definition of the phenomenological neutral current coupling parameters	18
II.2	Isospin and weak hypercharge assignments for the leptons and quarks	21
III.1	Neutrino producing decay modes	31
IV.1	Characteristics of Aluminum	38
IV.2	Energy calibration and resolution	63
V.1	Summary of $\bar{A}$·Maj running	87
V.2	Comparison of the ratio of deposited ionization energy to total incident energy for several calorimeters	92
V.3	Comparison of data and Monte Carlo results	98
VI.1	Summary of data taking	102
VI.2	Reconstruction pair status and edge redundancy	112
VI.3	Computer cuts and their efficiency	131
VI.4	Description of scan cuts	134
VII.1	Experimental measurements of the ratio of single π° production by the neutral and charged currents.	169
VIII.1	Details of background subtraction	179
VIII.2	Details of systematic errors	179

List of Figures

Figure		Page
II.1	Kinematic variables for $\nu_\mu e$ elastic scattering	9
II.2	Kinematics of $\nu_\mu e$ elastic scattering	11
II.3	Kinematics of $\nu_\mu N$ scattering	12
II.4	Feynman diagrams for neutrino-electron scattering	23
II.5	Total cross sections for $\overset{(-)}{\nu}_\mu$ elastic scattering as a function of $\sin^2\theta_W$	25
III.1	Schematic diagram of the Fermilab Accelerator	28
III.2	Schematic diagram of the detector	30
IV.1	Schematic diagram of the detector	36
IV.2	Schematic diagram of the detector electronics	40
IV.3	Details of the delay-line proportional chamber construction	42
IV.4a,b	Details of the chamber operation	44,45
IV.5	Examples of the chamber operation	48
IV.6	Edge Slewing between neighboring taps	49
IV.7	Spatial resolution for muons	51
IV.8	Spatial resolution for electromagnetic showers	52
IV.9	Schematic diagram of electron test run	55
IV.10	Energy deposition by a 10 GeV electromagnetic shower	56
IV.11	Longitudinal energy deposition by electromagnetic showers	57
IV.12	Integrals of the energy deposition curves	59
IV.13	Shower energy calibration in equivalent particles	60
IV.14	Shower energy resolution for 30 GeV shower	62
IV.15	Schematic diagram of hodoscope electronics	65

		Page
IV.16	Schematic diagram of chamber electronics	66
IV.17	Schematic diagram of scintillator electronics	68
IV.18	Schematic diagram of trigger electronics	69
AIV.1	Schematic diagram of velocity calibration run	75
AIV.2	Schematic diagram of pulse edge slewing	78
AIV.3	Examples of scintillator ADC calibration	81
V.1	Results of NUADA neutrino flux calculation	85
V.2	Hadronic shower containment curve	90
V.3	Calculated incident neutrino flux	94
V.4	Energy distribution with ± .40 m fiducial cut	95
V.5	Energy distribution with ± .30 m fiducial cut	96
V.6	Incident electron type neutrino flux	99
VI.1	Vertex distribution of the raw triggers	104
VI.2	Energy distribution of the raw triggers	105
VI.3	Angular distribution of the raw triggers	106
VI.4	Hit reconstruction example	110
VI.5	Details of chamber hit reconstruction	111
VI.6	Examples of matches and edge types	114
VI.7	Examples of class and redundancy types	116
VI.8	Example of a typical $\nu_\mu N$ interaction without π° production	118
VI.9	Example of a typical $\gamma_\mu N$ interaction with π° production	119
VI.10	Example of a $\nu_\mu e$ candidate	121
VI.11	Example of display class and redundancy codes	122
VI.12	Redundancy distribution for 10 GeV electrons	123
VI.13	Redundancy distribution from the neutrino data	124

		Page
VI.14	Nonshower hit distribution for 10 GeV electrons	126
VI.15	Nonshower hit distribution for the neutrino data	127
VI.16	Shower width distribution for 10 GeV electrons	128
VI.17	Shower width distribution for the neutrino data	129
VI.18	Example of the final event reconstruction and fit	139
VI.19	Angular distributions for the observed neutral and charged currents	141
VI.20	Energy distributions for the observed neutral and charged currents	142
VI.21	$E\theta^2$ distributions for the observed neutral and charged currents	143
VI.22	Vertex distribution of the observed neutral currents	144
VI.23	Vertex distributions of the observed charged currents	145
VI.24	Longitudinal vertex distributions for the observed neutral and charged currents	146
AVI.1	Example of a simulated tap hit for the scanning fiducial cut simulation	148
AVI.2	Calculated X and Y shower acceptance	150
VII.1	The total cross section for $\nu_\mu n \rightarrow \mu^- p$ quasielastic scattering	153
VII.2	The differential cross section for $\nu_\mu n \rightarrow \mu^- p$ quasielastic scattering	154
VII.3	The Pauli nuclear suppression factor $F(q^2)$	156
VII.4	The calculated energy distribution for quasielastic scattering	158
VII.5	The calculated angular distribution for quasielastic scattering	159
VII.6	The calculated $E\theta^2$ distribution for quasielastic scattering	160
VII.7	Ratio of neutral to charged current inclusive events as a function of Y	165

		Page
VII.8	Ratio of neutral to charged current inclusive events as a function of X	166
VII.9	The calculated muon identification probability	168
VII.10	The computed $\nu_\mu N$ neutral current background for R = .60 ± .15 and .42 ± .14	171
AVII.1	The average shower length as a function of energy	174
VIII.1	Angular distribution of the neutral current sample after background subtraction	178
VIII.2	The energy distribution of the selected events compared to the electroweak model	181
VIII.3	The experimentally allowed values for g_V and g_A	183
VIII.4	The allowed regions for g_V and g_A from several experiments	184
VIII.5	A comparison of the electroweak cross section with the experimental cross section	186

CHAPTER I

INTRODUCTION

The last decade has seen major advances in both our theoretical and experimental understanding of weak and strong interactions. At the beginning of the decade the V-A theory of the weak interaction offered a good description of the low energy weak phenomenology, but violated the unitarity limit at high energy. Many of the symmetries of the strong interaction were understood, but a fundamental theory of the dynamics was lacking. The completion of the new high energy accelerators early in the decade allowed a more detailed probing of strong interaction effects and the advent of high energy neutrino beams enabled physicists to study the weak interaction in new, untested regions. These important experimental results were accompanied by major theoretical advances as well. Throughout this period much theoretical work went into studying the application of nonabelian gauge theories and spontaneous symmetry breaking to the weak and strong interactions. By the end of the decade, serious models of both of these interactions had been developed. These new models represent a great unification of ideas and have considerable predictive power. This thesis deals with a fundamental test of the new electroweak model of weak interactions.

The foundations of the original V-A theory were laid in 1956 by the suggestion of Lee and Yang[1] that the weak interactions may be parity violating. This was later confirmed by Wu, et al.[2] in 1957. The V-A theory[3] of weak interactions proposed in 1958 can be thought

of as a low energy, first order approximation to the electroweak model. In this approximation the weak interaction is considered a current-current interaction. For example, in inverse beta decay, $\nu_e n \rightarrow e^- p$, the leptonic current ($\nu_e \rightarrow e$) interacts with the hadronic current ($n \rightarrow p$). The currents are charged currents since the initial and final leptons differ in electric charge. In 1973 neutral currents were first observed.[4] In the neutral current analog to inverse beta decay, $\nu_e n \rightarrow \nu_e n$, the lepton current ($\nu_e \rightarrow \nu_e$) interacts with the hadronic current ($n \rightarrow n$). The currents are neutral since the electric charge of the initial and final leptons is identical. The neutral current interaction was a new type of interaction anticipated by the theoretical work of Weinberg, Salam, and Glashow[5] in the development of the electroweak model.

This model was a major contribution to theoretical physics in general, as well as to weak interaction theory. It formally unified the weak and electromagnetic interactions and, more importantly, illustrated the use of nonabelian gauge theories and spontaneous symmetry breaking in the study of fundamental interactions. Gauge theories have since been developed for the strong interaction (QCD) and for unified theories of the strong, weak and electromagnetic interactions.

Since the theoretical ideas used in the electroweak model are gaining such wide use, it is essential that the model be given a rigorous experimental test. The purely leptonic interaction $\nu_\mu e \rightarrow \nu_\mu e$ is an excellent test of the model since the interaction is not predicted by the standard V-A theory and since the cross section can be calculated without the necessity of additional

assumptions regarding the target constituents. Neutrino interactions with nucleons are complicated by the fact that the quark content of the nucleons is not well known. Since the neutrino and electron are point particles, the theoretical calculation of the cross section is relatively simple. Unfortunately, the experiment is very difficult to perform since the cross section is so small. This is well illustrated by a comparison of the $\nu_\mu e$ cross section (10^{-42} E_ν cm^2/GeV) with the $\nu_\mu N$ cross section (10^{-38} E_ν cm^2/GeV) and the pp cross section (10^{-26} cm^2). It is further complicated by the fact that the $\nu_\mu N$ interactions are a major source of background which must be rejected.

The experiment to measure the $\nu_\mu e \rightarrow \nu_\mu e$ total cross section was performed at Fermi National Accelerator Laboratory with data taking beginning in November of 1978. The experiment was a collaboration of physicists from Virginia Polytechnic and State University, University of Maryland, Oxford University, National Science Foundation, and the Institute of High Energy Physics, Peking, China. A 12 ton target mass, modular detector was used to observe the $\nu_\mu e$ interactions. The detector was designed to trigger on the electromagnetic shower produced by the recoiling electron. Delay-line readout proportional chambers measured the position and angle of the shower and an aluminum-scintillator sandwich calorimeter measured the energy. A total of 250,000 triggers were written to tape during the six months of data taking.

The theoretical aspects of neutrino electron scattering are discussed in greater detail in chapter II. A phenomenological Lagrangian can be written for this interaction which requires two phenomenological coupling parameters g_V and g_A. Hung and Sakurai[6] have done a phenomenological study of all neutral current interactions and derived

a set of factorization relations between the phenomenological coupling parameters of different interactions. These relations can be used to set constraints on the allowed values for g_V and g_A based on the results of other neutral current experiments. The electroweak model is also described in the chapter and the phenomenological coupling parameters related to the one free parameter of the model, the Weinberg angle, θ_W.

The chapter also discusses the kinematics of neutrino electron scattering. The kinematics of neutrino elastic scattering from a small electron mass is very different from neutrino inelastic scattering from a nucleon mass. This fact is exploited to isolate the neutrino electron signal from the neutrino nucleon background.

The accelerator and neutrino area are described in Chapter III. The neutrinos are among the decay products of pion and kaon decay. A neutrino beam is produced by colliding high energy protons into a target to produce a beam of secondary pions and kaons and then allowing the secondaries to decay. The intensity of the beam is enhanced by focussing the secondaries while the hadronic and muonic backgrounds are decreased by shielding the detector from the non-neutrino decay products.

The detector is described in Chapter IV. The recoiling electron from the $\nu_\mu e$ interaction will form an electromagnetic shower as it passes through the detector. Since kinematic cuts are used to isolate the signal from the background, the detector must accurately measure the energy and angle of the electron shower. The construction and operation of the delay-line proportional chambers are described along with the calibration and resolution of the alumimum-scintillator calorimeter. Details of the trigger and data recording electronics are also given.

Chapter V discusses the determination of the incident neutrino flux. Calculations based on the spectra of secondaries from the target have been performed to determine the incident flux. These spectra are known to be incorrect below 50 GeV in neutrino energy. The low energy flux was calculated using a Monte Carlo program of the neutrino nucleon interactions and data from a special low energy threshold trigger. The neutrino flux input to the Monte Carlo program was adjusted until the predicted hadronic shower energy agreed with the observed energy distribution. Estimates are also made on the error in the flux and their effect on the event rate.

The offline data analysis is discussed in Chapter VI. A computer program was used to make loose cuts on the data to eliminate the obvious background. The program then generated pictures of the 20% of the raw sample which were accepted. A display of each of these events was scanned by a physicist implementing a tighter criteria to obtain the final event sample.

The principle backgrounds which survive the scan cuts are the quasielastic interactions $\nu_e n \rightarrow e^- p$ and $\bar{\nu}_e p \rightarrow e^+ n$ as well as single pion production by the neutral current $\nu_\mu N \rightarrow \nu_\mu N \pi^\circ$. A Monte Carlo calculation was used to obtain the contribution from the quasielastic channel. The neutral current single π° production background was obtained from the measurement of the charged current π° production. Chapter VII discusses the details of how the backgrounds were determined.

The results on the total cross section for $\nu_\mu e$ elastic scattering are presented in Chapter VIII. The various selection efficiencies are discussed and the coupling constants g_V and g_A are determined. The cross sections for $\bar{\nu}_\mu e$ and $\bar{\nu}_e e$ elastic scattering and the SLAC

interference experiment with factorization are used to remove all the ambiguity in the allowed values for g_V and g_A. The Weinberg angle is also determined.

An outline of the experiment, data analysis and results is presented in the concluding chapter.

REFERENCES FOR CHAPTER I

1. T. D. Lee and C. N. Yang, Physical Review, 104, 254 (1956).
2. C. S. Wu, et al., Physical Review, 105, 1413 (1957).
3. R. Feynman and M. Gell-Mann, Physical Review, 109, 193 (1958)
   E. Sudarshan and R. Marshak, Physical Review, 109, 1860 (1958)
   J. Sakurai, Nuovo Cimento, 7, 649 (1958).
4. F. J. Hasert, et al., Physics Letters, 46B, 138 (1973).
5. S. Weinberg, Physical Review Letters, 19, 1264 (1967)
   A. Salam, Elementary Particle Theory, ed. N. Svartholm, Stockholm, p. 367 (1968)
   S. Glashow, Nuclear Physics, 10, 107 (1959)
   S. Glashow, Nuclear Physics, 22, 579 (1961).
6. P. Hung and J. Sakurai, Physics Letter, 72B, 208 (1977).

CHAPTER II

THEORETICAL CONSIDERATIONS

Kinematics

A schematic diagram of neutrino electron scattering is shown in Figure II.1. The following variables can be defined:

$(E_{\nu i}, P_{\nu i})$ = Four momentum of the incident neutrino

$(E_{\nu o}, P_{\nu o})$ = Four momentum of the scattering neutrino

(E_e, P_e) = Four momentum of the recoiling electron

θ = Scattering angle of the recoiling electron relative to the incident neutrino direction (II-1)

q^2 = Four momentum squared transferred to the electron

ν = Energy transferred from the incident neutrino to the electron = $E_e - m_e$

y = Ratio of $\nu/E_{\nu i}$

x = $-q^2/(2m\nu)$

The Bjorken scaling variable, x, is often used in neutrino nucleon inclusive scattering with m equal to the proton mass, although in neutrino electron scattering, and all elastic scattering, x is kinematically constrained to be 1.0.

Using conservation of four momentum and the fact that $m_e/E_{\nu i} << 1$, several important formulas can be derived. The relationship between scattering electron energy E_e, scattering angle θ, and incident neutrino energy $E_{\nu i}$ is given by:

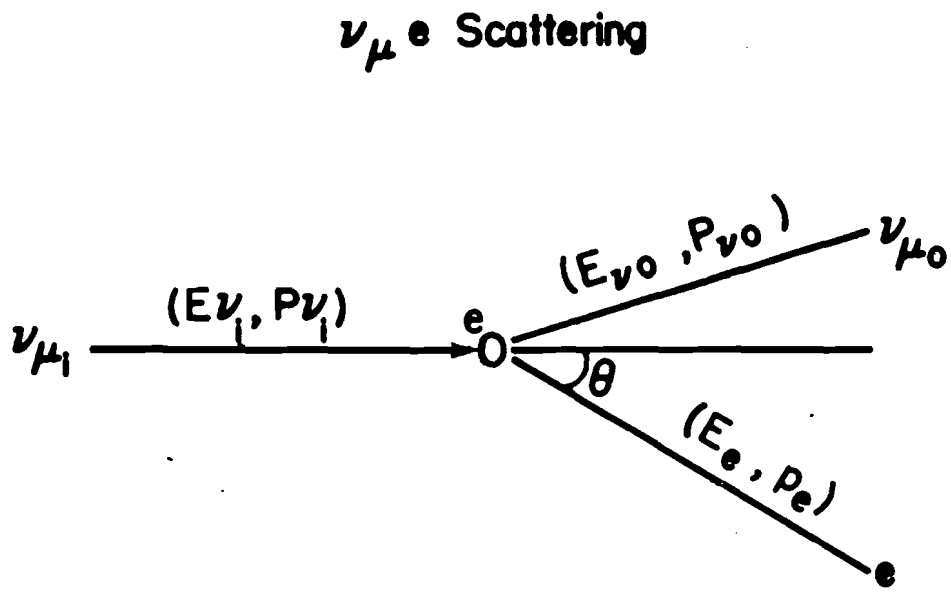

Fig. II.1. Kinematic variables for $\nu_\mu e$ elastic scattering

$$E_e = \frac{2E_{\nu i}^2 m_e \cos\theta}{E_{\nu i}^2 \sin^2\theta + 2\, E_{\nu i} m_e} \qquad \text{(II-2)}$$

or, in the small angle limit:

$$E_e \theta^2 = 2m_e (1 - y) \qquad \text{(II-3)}$$

This relationship between the electron energy and recoil angle from equation (II-2) is plotted in Figure II.2 for incident neutrino energies of 10, 20, 30, and 50 GeV. The neutrino flux peaks at about 10 GeV. With an electron energy cut at 4 GeV, all of the neutrino electron scattering signal should be confined below 16 milliradians, assuming perfect angular resolution. The neutrino nucleon background events are not subject to these tight kinematic constraints since the interaction in general is not elastic and the nucleon mass is much larger than the electron mass. The allowed kinematic region for $\nu_\mu N$ inclusive scattering is shown in Figure II.3. The angular distribution of the $\nu_\mu N$ background is not confined to small angles. Since the number of background events far exceeds the neutrino electron events, the kinematic constraint is crucial in isolating the signal from the large background.

Since, by conservation of energy, the value of y must be less than 1.0, the kinematic variable $E_e\theta^2$ is constrained to values less than $2m_e$ ~ 1 MeV. The neutrino electron signal should be evident at small values of $E_e\theta^2$ in the $E_e\theta^2$ distribution of the final event sample. In order for this relation to be useful it is essential that the apparatus have good angular resolution.

The $\nu_\mu e$ kinematic plot also illustrates the difficulty in obtaining accurate y distributions. In principle, since the interaction is

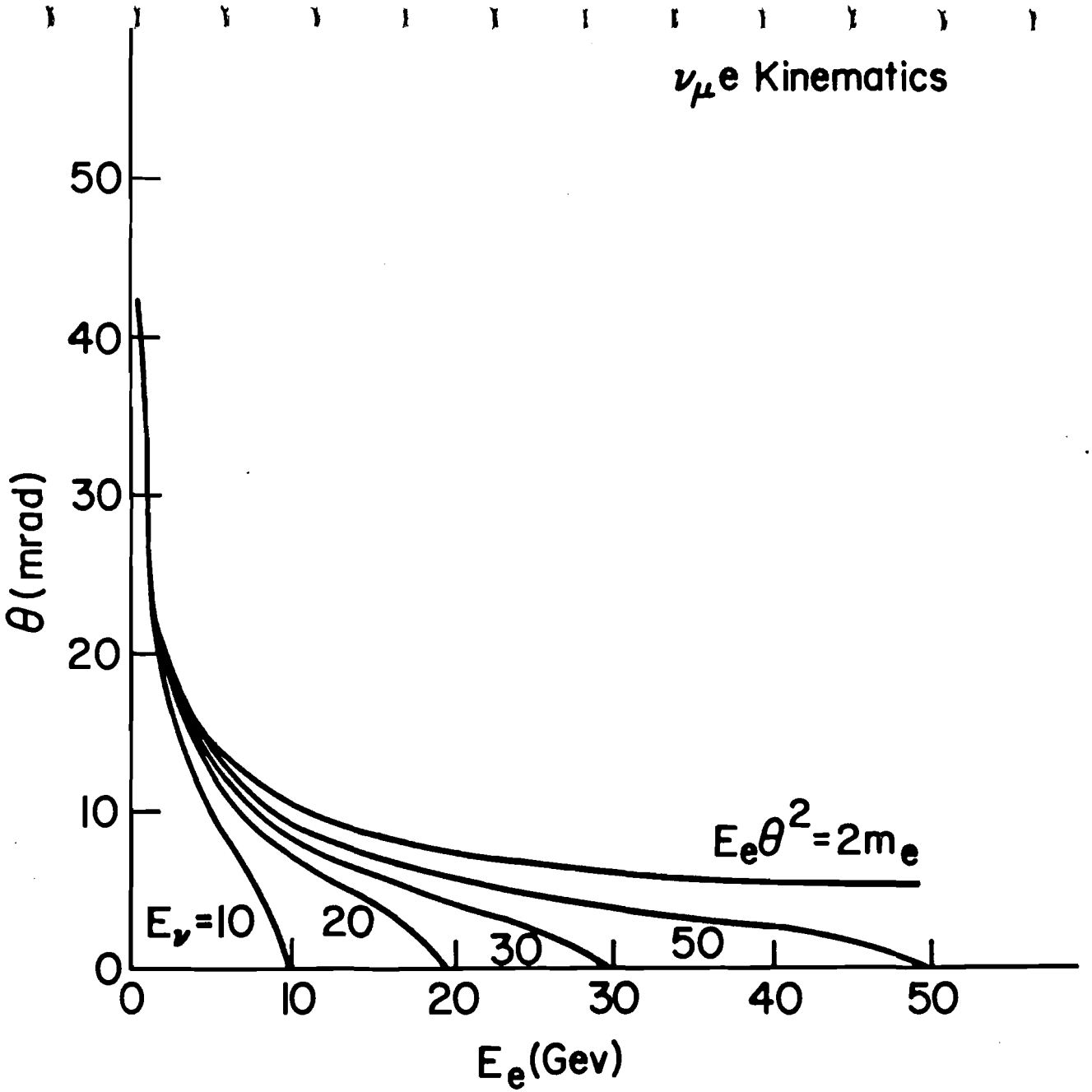

Fig. II.2. Kinematics of $\nu_\mu e$ elastic scattering

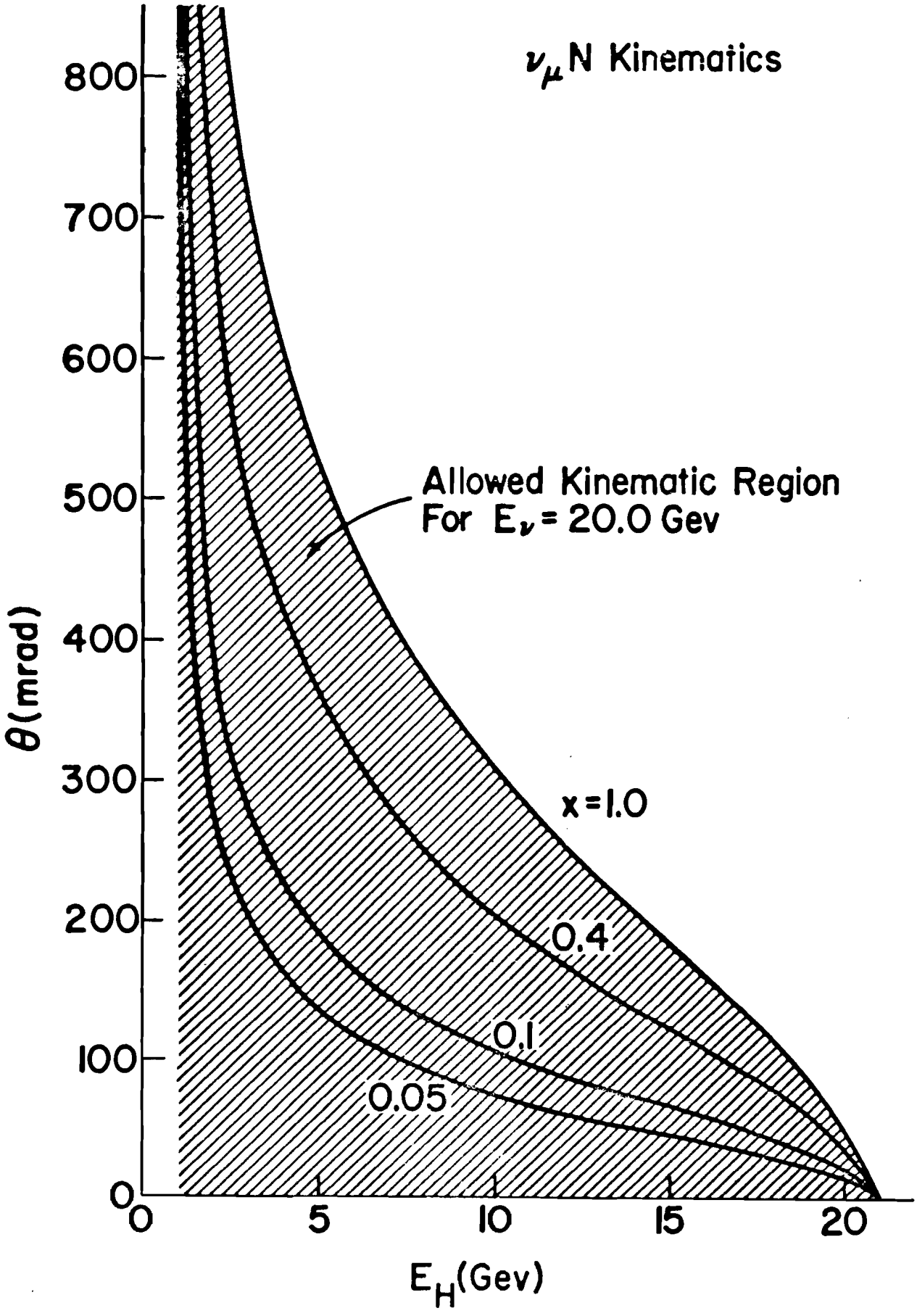

Fig. II.3. Kinematics of $\nu_\mu N$ Scattering

elastic scattering, the incident neutrino energy could be calculated from the recoiling electron energy and angle, and the resulting y distribution computed. The error in this computation is very sensitive to the angular resolution. For example, assuming an angular resolution of 10 milliradians, a 10 GeV electron shower at an angle of 5 milliradians will have a value for y of 0.75 ± 1.00.

PHENOMENOLOGICAL LAGRANGIAN

A phenomenological neutral current Lagrangian can be written for the interaction $\nu_\mu e \rightarrow \nu_\mu e$ based on experimental constraints and guided by general theoretical principles. The neutrinos incident on the detector are the decay products from pion and kaon decays upstream. Experiments have shown these neutrinos to be left-handed.[1] The most general local Lorentz invariant Lagrangian with nonderivative couplings assuming left-handed incident neutrinos and unpolarized target electrons is:

$$L = \frac{G}{\sqrt{2}} [\bar{\nu}_\mu \gamma_\alpha (1 - \gamma_5) \nu_\mu \bar{e} \gamma^\alpha (g_V - g_A \gamma_5) e + \bar{\nu}_\mu (1 - \gamma_5) \nu_\mu \bar{e} (g_S - g_P \gamma_5) e + g_T \bar{\nu}_\mu \sigma_{\alpha\beta} (1 - \gamma_5) \nu_\mu \bar{e} \sigma^{\alpha\beta} e] \qquad \text{(II-4)}$$

The parameters g_i, $i = (S,P,V,A,T)$ are the scalar, psuedoscalar, vector, axial vector, and tensor coupling constants respectively. Hermiticity implies that the constants g_V and g_A are real. Time reversal invariance would imply that the other constants g_S, g_P and g_T are also real, although this has not been assumed in the following discussion.

The differential cross section resulting from this Lagrangian is:

$$\frac{d\sigma}{dy} (\nu_\mu e \rightarrow \nu_\mu e) = \frac{G^2 E_\nu m_e}{4\pi} [2 (g_V + g_A)^2 + 2(g_V - g_A)^2 (1 - y^2) + (|g_s|^2 + |g_p|^2) y^2 + 32 |g_T|^2 (1 - y/2)^2 - 8\mathrm{Re}[g_T (g_S^* + g_P^*)] y (1 - y/2)] \qquad \text{(II-5)}$$

Terms of order m/E have been neglected.

The values of the coupling constants g_i are related to the Lorentz structure of the neutral current. The values of these parameters are unknown, however some assumptions can be made based on the results from related experiments.

The Lorentz structure of the charged current interaction has been extensively studied in nuclear and elementary particle decay (e.g. $\pi^+ \to \mu^+\nu_\mu$). The study of these interactions lead to the V-A theory of weak interactions.[3] This theory describes the point interactions of weak currents J^μ consisting of leptonic and hadronic parts $J^\mu = J^\mu_\ell + J^\mu_h$. The Lagrangian is of the form:

$$L = \frac{G}{\sqrt{2}} (J^\mu_\ell + J^\mu_h) ((J_\ell)_\mu + (J_h)_\mu)^\dagger \qquad \text{(II-6)}$$

The Fermi constant G has a value of $10^{-5}\ m_p^{-2}$.

Experimentally, the explicit form of the leptonic current was found to be consistent with

$$J^\mu_\ell = \bar{\nu}_e \gamma^\mu (1 - \gamma_5) e + \bar{\nu}_\mu \gamma^\mu (1 - \gamma_5) \mu \qquad \text{(II-7)}$$

Since the operator $(1 - \gamma_5)/2$ is a left-handed helicity projection operator for mass zero states, only left-handed neutrinos participate in the charged current interactions. This is consistent with the two component neutrino hypothesis which states that the neutrino is always left-handed and the antineutrino always right-handed.

Since the hadrons are not point particles, no explicit form of the hadronic current could be written. It has been established through a long series of experiments that the current is an isovector and contains vector and axial vector parts $J^\mu_h = V^\mu_h - A^\mu_h$.[4]

By analogy with the charged current it is natural to assume that the neutral current also contains nonzero vector and axial vector terms.

The presence of these terms in the neutral current Lagrangian was confirmed by the SLAC interference experiment.[5] In this experiment polarized electrons were scattered from a deuterium target.

$$e(\text{polarized}) + D \rightarrow e + X \tag{II-8}$$

The experiment measures the scattering asymmetry:

$$A = \frac{\sigma_R - \sigma_L}{\sigma_R + \sigma_L} \tag{II-9}$$

The parameter σ_L is the cross section for the scattering of left-handed electrons and σ_R is the cross section for the scattering of right-handed electrons. The presence of this asymmetry is due to the interference of the parity violating portion of the weak neutral current with the electromagnetic current. This asymmetry can be parameterized by:[6]

$$\frac{A}{q^2} = a_1 + a_2 \left[\frac{1 - (1 - y)^2}{1 + (1 - y)^2}\right] \tag{II-10}$$

The parameter a_1 measures the strength of the $A_{lepton}V_{quark}$ interference term and the parameter a_2 measures the strength of the $V_{lepton}A_{quark}$ term in the Lagrangian. The experimental observation of both of these terms indicates that the weak neutral current has both nonzero vector and axial vector parts.

As is evident from equations (11-4) and (II-5), the different Lorentz terms in the Lagrangian give contributions of different functional form to the differential cross section $d\sigma/dy$. In particular, the scalar and pseudoscalar terms contribute a cross section rising with y, while the contributions from the other terms are either flat or falling. The observation of a rising differential cross section would indicate the presence of scalar and/or pseudoscalar terms in the Lagrangian. This measurement has not been done for the purely leptonic

interaction $\nu_\mu e \rightarrow \nu_\mu e$, but measurements have been made for the neutral current interaction $\nu_\mu N \rightarrow \nu_\mu + X$. The phenomenological Lagrangian for this interaction is identical to equation (II-4) if one replaces the field e with the quark fields and integrates over the quark distributions in the nucleon. The resulting y distribution has the same form as equation (II-5). By studying the y distributions measured in neutrino nucleon inclusive scattering, several experiments have put limits on the values of g_A and g_V. A CERN experiment has observed falling y distributions which lead to the constraint:[7]

$$\frac{(|g_S|^2 + |g_P|^2)}{(g_V+g_A)^2 + (g_V-g_A)^2} = 0.04 \pm 0.14 \qquad \text{(II-11)}$$

This limit can only be set by assuming CP invariance and that $g_T=0$. This is a consequence of the confusion theorem[8] which states that the differential cross section produced by any mixture of vector and axial vector couplings can also be produced by an appropriate combination of scalar, pseudoscalar and tensor terms. Without the above assumptions the g_S and g_P contributions cannot be separated from the g_V and g_A contributions and no limit set. As a corollary to this theorem, the observation of a differential cross section which can be reproduced by a Lagrangian with only vector and axial vector terms is not sufficient evidence to conclude that the Lagrangian is solely vector and axial vector.

The scalar, pseudoscalar, and tensor terms are helicity flipping terms. An incident left-handed neutrino will flip its helicity to become an outgoing right-handed neutrino. The presence of these terms would violate the two component neutrino hypothesis. This hypothesis

has not been tested in neutral current interactions. It is possible that only charge current interactions obey the hypothesis.

Based on all the indirect evidence stated above, it is usually assumed that the leptonic neutral current is composed of only vector and axial vector parts. The Lagrangian then has the simple form:

$$L = \frac{G}{\sqrt{2}} \bar{\nu}_\mu \gamma_\alpha (1 - \gamma_5) \nu_\mu \bar{e} \gamma^\alpha (g_V - g_A \gamma_5) e \qquad \text{(II-12)}$$

The differential cross section and total cross section are:

$$\frac{d\sigma}{dy} = \frac{G^2 E_\nu m_e}{2\pi} \left[(g_V + g_A)^2 + (g_V - g_A)^2 (1 - y)^2 \right] \qquad \text{(II-13)}$$

and:

$$\sigma = \frac{G^2 E_\nu m_e}{2\pi} \left[(g_V + g_A)^2 + \frac{(g_V - g_A)^2}{3} \right] \qquad \text{(II-14)}$$

Hung and Sakurai have done a phenomenological analysis of the weak neutral current interactions.[9] They consider neutrino-electron, neutrino-nucleon, electron-nucleon, and electron-muon scattering. The Lorentz structure of the neutral current is assumed to be vector and axial vector and the hadronic neutral current is allowed to have isoscalar and isovector parts. There are 13 coupling constants required to describe all of these interactions. See Table II.1 for a definition of the constants.

If one assumes that the weak current is mediated by the exchange of a single boson, then six factorization relations can be derived. An important relation is the following:

$$\frac{g_V}{g_A} = \frac{(\alpha + \gamma/3)(\tilde{\beta} + \tilde{\delta}/3)}{(\tilde{\alpha} + \tilde{\gamma}/3)(\beta + \delta/3)} \qquad \text{(II-15)}$$

The parameters $\tilde{\alpha}, \tilde{\beta}, \tilde{\gamma}$, and $\tilde{\delta}$ are involved in the SLAC interference and atomic parity violation experiments and α, β, γ, and δ are involved in

$\overset{(-)}{\nu}_\mu N \to \overset{(-)}{\nu}_\mu + X$

$$L = \frac{-G}{\sqrt{2}} \; \nu_\mu \gamma^\lambda (1 + \gamma_5) \; \nu_\mu \{ 1/2 (\bar{u} \gamma_\lambda (\alpha + \beta \gamma_5) u - \bar{d} \gamma_\lambda (\alpha + \beta \gamma_5) d)$$

$$+ 1/2 \; (\bar{u} \gamma_\lambda (\gamma + \delta \gamma_5) u + \bar{d} \gamma_\lambda (\gamma + \delta \gamma_5) d) \}$$

$\overset{(-)}{\nu}_\mu e \to \overset{(-)}{\gamma}_\mu e$

$$L = \frac{-G}{\sqrt{2}} \; (\bar{\nu}_\mu \gamma^\lambda (1 + \gamma_5) \; \nu_\mu)(\bar{e} \; \gamma_\lambda (g_V + g_A \gamma_5) e)$$

$e^+ e^- \to \mu^+ \mu^-$

$$L = \frac{-G}{\sqrt{2}} \; (h_{vv} (\bar{e} \gamma_\lambda e + \bar{\mu} \gamma_\lambda \mu) \; (\bar{e} \gamma^\lambda e \; + \bar{\mu} \gamma^\lambda \mu)$$

$$+ \; 2h_{va} \; (\bar{e} \gamma_\lambda e + \bar{\mu} \gamma_\lambda \mu)(\bar{e} \gamma^\lambda \gamma_5 e + \bar{\mu} \gamma^\lambda \gamma_5)$$

$$+ \; h_{AA} (\bar{e} \gamma_\lambda \gamma_5 e + \bar{\mu} \gamma_\lambda \gamma_5 \mu)(\bar{e} \gamma^\lambda \gamma_5 e + \bar{\mu} \gamma^\lambda \gamma_5 \mu))$$

Atomic Parity violation, γ-Z° Interference

$$L = \frac{-G}{\sqrt{2}} \{ \bar{e} \gamma_\lambda \gamma_5 e \; (\frac{\tilde{\alpha}}{2} (\bar{\mu} \gamma^\lambda \mu - \bar{d} \gamma^\lambda d) + \frac{\tilde{\gamma}}{2} (\bar{\mu} \gamma^\lambda \mu + \bar{d} \gamma^\lambda d))$$

$$+ \; \bar{e} \gamma_\lambda e \; (\frac{\tilde{\beta}}{2} (\bar{\mu} \gamma^\lambda \gamma_5 \mu - \bar{d} \gamma^\lambda \gamma_5 d) + \frac{\tilde{\gamma}}{2} (\bar{\mu} \gamma^\lambda \gamma_5 \mu + \bar{d} \gamma^\lambda \gamma_5 d)) \}$$

Table II.1 Definition of phenomenological neutral current coupling parameters

neutrino nucleon current scattering. The measurement of g_V and g_A and the results from the other neutral current experiments can test this factorization relation and indirectly the single boson hypothesis. Conversely, assuming the validity of the factorization relations, the SLAC interference and neutrino nucleon inclusive scattering experiments can be used to set constraints on the allowed values of g_V and g_A.

ELECTROWEAK MODEL

A major advance in our understanding of weak interactions occurred with the publication of the electroweak model by Weinberg and Salam in 1967.[10] The model formally unified weak and electromagnetic interactions by combining the ideas of gauge theories with spontaneous symmetry breaking. A model first published by Glashow[11] in 1958 contained the idea of unification and in 1970 was extended by Glashow, Maiani, and Iliopoulos[12] to include hadrons as well as leptons. The theoretical ideas began to gain wide acceptance in 1971 when t'Hooft showed that the theory was renormalizable.[13]

The electroweak model is a gauge theory in which the symmetry of the theory plays a fundamental role in determing the form of the Lagrangian. The gauge symmetry of quantum electrodynamics is a U(1) symmetry corresponding to changing the phase of the charged fields. The symmetry is local in that the change in phase can be a function of space-time. The invariance of electromagnetism with respect to this transformation implies the existence of a massless gauge boson, in this case the photon. The electroweak model postulates that in addition to a U(1) symmetry there is a SU(2) gauge symmetry corresponding to the local transformation of the weak isospin of the fields.

The fermions of the theory, the leptons and quarks, transform according to the transformations of the SU(2) group in special ways. The left-handed neutrino and the left-handed state of the charged lepton are assigned to a doublet. The right-handed state of the charge lepton is assigned to a singlet. The left-handed quark states are also assigned to doublets and the right-handed states to singlets. The weak isospin (I) assignments for the leptons and quarks are shown in Table II.2. The quantum number for the group U(1) is the weak hypercharge (Y) and is also shown in the Table. The electric charge of the particle is given by $q = I_3 + Y/2$, in analogy to the Gell-Mann-Nishijima formula.

The basic assumption of the model is that the fundamental interactions between the particles described by the Lagrangian are invariant with respect to the transformations of the groups U(1) and SU(2). By demanding that the Lagrangian be invariant with respect to these transformations four gauge boson fields are required. A gauge boson is assigned to each generator of the group. The field B° is associated with the generator of U(1) and the fields W^+, W^- and W° are assigned to the three generators of the group SU(2). The resulting leptonic Lagrangian is:

$$L = i\bar{L}\gamma^\lambda(\partial_\lambda - \frac{1}{2} ig\vec{\tau}\cdot\vec{W}_\lambda + \frac{1}{2} ig'B^\circ_\lambda)L +$$

$$i\bar{e}_R\gamma^\lambda(\partial_i + ig'B^\circ_\lambda)e_R + (e \leftrightarrow \mu) \qquad \text{(II-16)}$$

$$L = \binom{\nu_e}{e_L}$$

The fields e_R and L are the right and left-handed fermion fields respectively, g' is the coupling constant between B° and the fermions,

Isodoublets

		Y					
		-1	-1	-1	1/3	1/3	1/3
I_3	1/2	ν_e	ν_μ	ν_τ	u_L	c_L	t_L
	-1/2	e_L	μ_L	τ_L	d_L	s_L	b_L

Isosinglets

		Y								
		-2	-2	-2	4/3	-2/3	4/3	-2/3	4/3	-2/3
I_3	o	e_R	μ_R	τ_R	u_R	d_R	c_R	s_R	t_R	b_R

Table II.2 Isospin and weak hypercharge assignments for the leptons and quarks.

and g is the coupling constants between the W and the fermions. The vector $\vec{\tau}$ represents the Pauli spin matrices, the generators of the group SU(2). The full Lagrangian contains additional terms representing the kinetic energy of the fermions and bosons.

A linear combination of the neutral fields B° and W° with a mixing angle θ_W forms the photon and the orthogonal combination forms the Z°, the mediator of the weak neutral current. The model predicts a neutral current weak interaction as well as the charged current interaction. The Feynman diagrams for some of the weak leptonic interactions are shown in Figure II.4. Demanding that the photon couple to an electron with a charge e gives a relation between the coupling constants g and g':

$$\tan\theta_W = g'/g \quad e = gg' \; (g^2 + g'^2)^{-1/2} \qquad \text{(II-17)}$$

The parameter θ_W is the only free parameter required to determine all the dynamical interactions of the particles.

So far the gauge bosons are massless. Explicit mass terms destroy the gauge invariance of the Lagrangian. The major contribution of Weinberg and Salam was to merge the idea of Yang-Mills gauge theory discussed so far with the Higgs mechanism[14] to generate masses. A doublet of scalar particles ϕ is added to the Lagrangian. These interact with the bosons in a SU(2) x U(1) invariant way and with the fermions by a Yukawa coupling. The resulting Lagrangian is still gauge and Lorentz invariant. Masses are generated by spontaneous symmetry breaking. It is assumed that the vacuum expectation value of the scalar fields is nonzero and not gauge invariant. Rewriting the Lagrangian in terms of the observable fields $\phi - \langle\phi\rangle$ generates mass terms for the charged fermions and W^+, W^-, and Z°. The photon and neutrino remain massless.

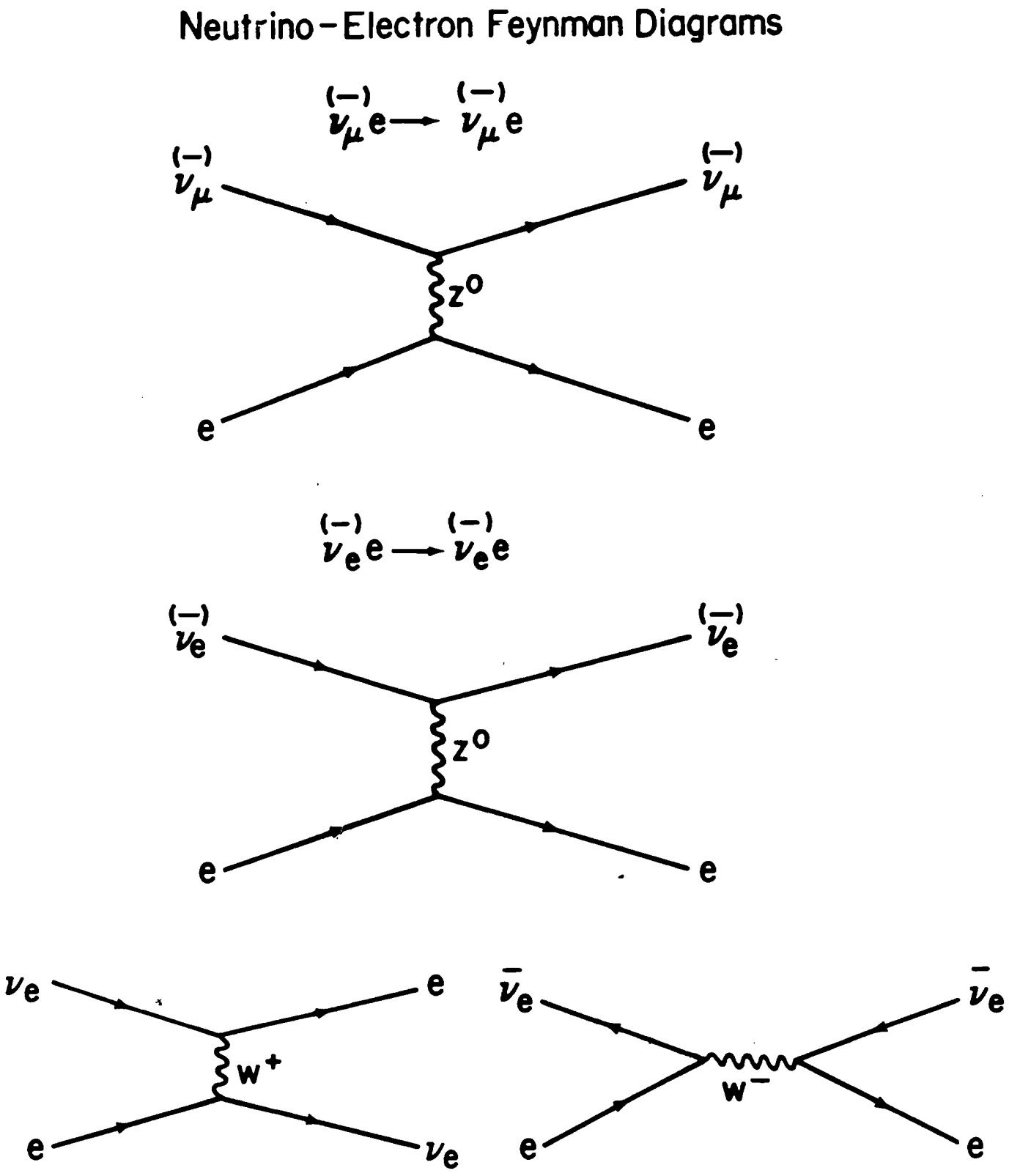

Fig. II.4. Feynman diagrams for neutrino-electron scattering

The first order effective Lagrangian in the electroweak model is of the form of equation (II-12) with $g_A = -1/2$ and $g_V = -1/2 + 2\sin^2\theta_w$ with θ_w the Weinberg mixing angle. Experimentally, the momentum transfers involved are so small compared to the exchanged boson mass squared that propagator effects can be ignored. A typical q^2 at the experimentally available energies is 10^{-2} GeV^2, while the Z° mass squared is thought to be of the order of 10^4 GeV^2. The differential cross section in the zero q^2 limit is given by:[15]

$$\frac{d\sigma}{dy} = \frac{G^2 E_\nu m_e}{2\pi} \left[(1 - 2\sin^2\theta_w)^2 + 4\sin^4\theta_w (1 - y)^2\right] \qquad \text{(II-18)}$$

and the total cross section by:

$$\sigma = \frac{G^2 E_\nu m_e}{2\pi} \left[(1 - 2\sin^2\theta_w)^2 + 4\,\frac{\sin^4\theta_w}{3}\right] \qquad \text{(II-19)}$$

Figure II.5 shows the total cross section as a function of $\sin^2\theta_w$.

The electroweak model has been very successful in describing the experimental data. The data from the study of the νN interactions agrees well with the model. Indeed, the model has been used as a basis for studying the structure of the nucleon. The SLAC interference and parity violation in atomic physics experiments also agree with the model. All of these experiments give a consistent value for $\sin^2\theta_w$ near 0.23. The neutrino electron interaction represents a good test of the theory since, in contrast to the above mentioned interactions, no additional assumptions must be made about the quark content of the nucleon. In principle, the cross section can be calculated exactly.

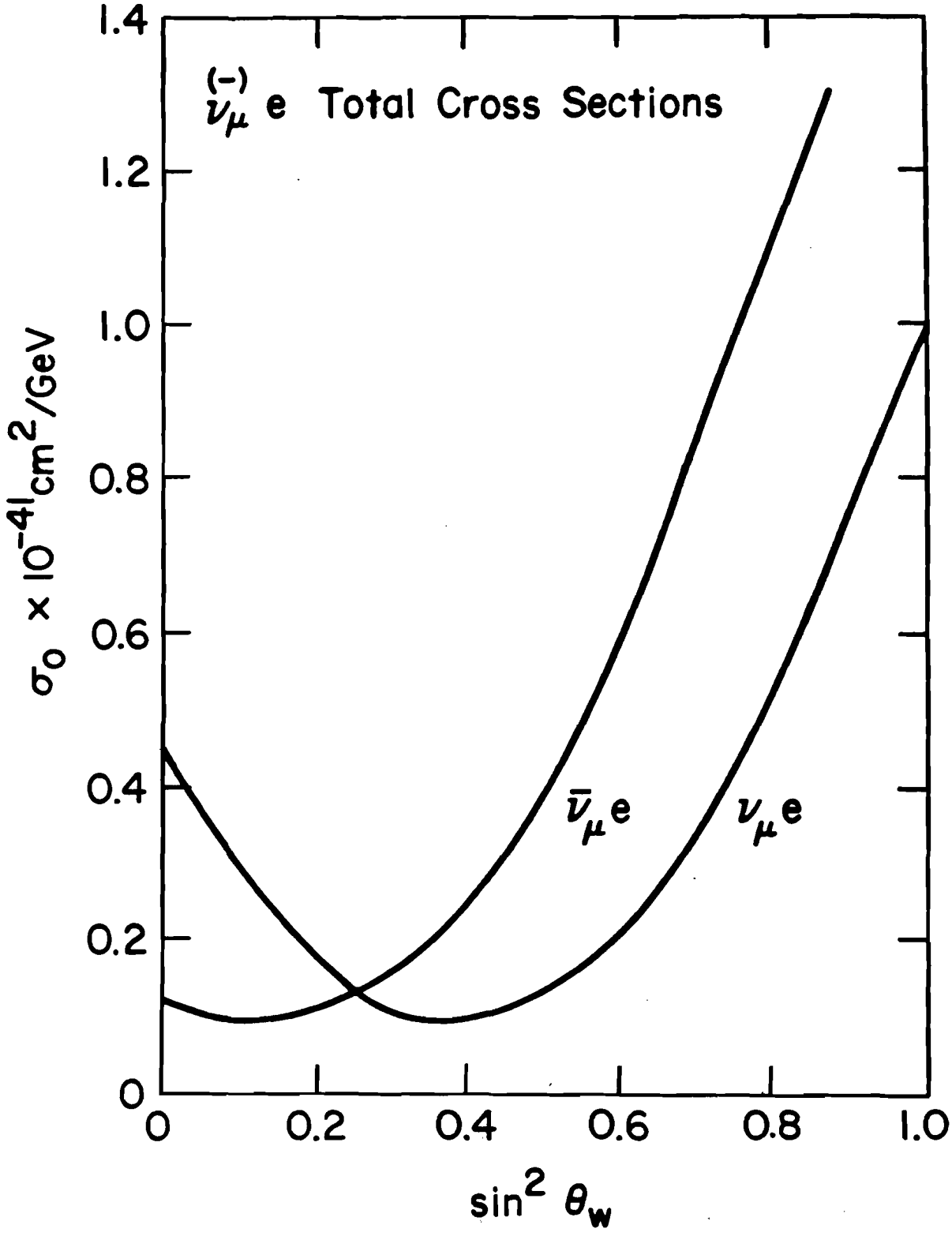

Fig. II.5. Total cross sections for $\overset{(-)}{\nu}_\mu$e elastic scattering as a function of $\sin^2\theta_W$

REFERENCES FOR CHAPTER II

1. R. Garwin, L. Lederman, and M. Weinrich, Physical Review, 105, 1415 (1957)
   J. Friedman and V. Telegdi, Physical Review, 105, 1681 (1957).
2. R. Kingsley, F. Wilczek, and A. Zee, Physical Review D, 10, 2216 (1974).
3. R. Feynman and M. Gell-Mann, Physical Review, 109, 193 (1958)
   E. Sudershan and R. Marshak, Physical Review, 109, 1860 (1958)
   J. Sakurai, Nuovo Cimento, 7, 649 (1958).
4. R. Marshak, Riazuddin, and C. Ryan, Theory of Weak Interactions in Particle Physics, Wiley-Interscience, New York (1969).
5. C. Prescott, et al., Physics Letters, 77B, 347 (1978).
6. R. Cahn and F. Gilman, Physical Review D, 17, 1313 (1978).
7. M. Holder, et al., Physics Letters, 72B, 254 (1977).
8. B. Kayser, et al., Physics Letters 52B, 385 (1974).
9. P. Hung and J. Sakurai, Physics Letters, 72B, 208 (1977).
10. S. Weinberg, Physical Review Letters, 19, 1264 (1967)
    A. Salam, Elementary Particle Theory, ed. N. Svartholm, Stockholm, p. 367 (1968).
11. S. Glashow, Nuclear Physics, 10, 107 (1959).
12. S. Glashow, J. Iliopoulos, and L. Maiani, Physical Review D, 2 1285 (1970).
13. G. t'Hooft, Nuclear Physics, B33, 173 (1971).
14. P. Higgs, Physical Review, 145, 1156 (1966).
15. G. t'Hooft, Nuclear Physics, B37, 195 (1971).

CHAPTER III

NEUTRINO PRODUCTION

Neutrinos are among the principal decay products of pion and kaon decay. To produce a high energy and high intensity neutrino beam, one must first produce a high energy and well collimated beam of pions and kaons. The major features of the neutrino production system are a proton synchnotron to accelerate protons to 350 GeV, a neutrino area target in which the protons interact to produce pions and kaons, a focussing system to collimate the beam of secondaries, and a decay and shielding region where the secondaries decay and the non-neutrino decay products are filtered from the neutrino beam.

A schematic diagram of the Fermilab accelerator is shown in Figure III.1.[1] Protons from the Cockroft-Walton preinjector are first accelerated in the proton linac to 200 MeV and then injected into the booster. In the synchnotron booster the protons are rebunched and accelerated to 8 GeV and then transferred to the main proton synchnotron. In the main ring the protons are bunched into RF "buckets" corresponding to stable phase regions of the 52 megahertz RF field. The spacing between RF "buckets" is 18 nanoseconds. The particles are accelerated to 350 GeV and then extracted into the neutrino area beamline. The extraction occurs over a 1.5 millisecond period with typically 10^{13} protons per spill extracted. Secondary emission monitors (SEM) and beam torroids (TOR) monitor the proton beam intensity to the neutrino production area.

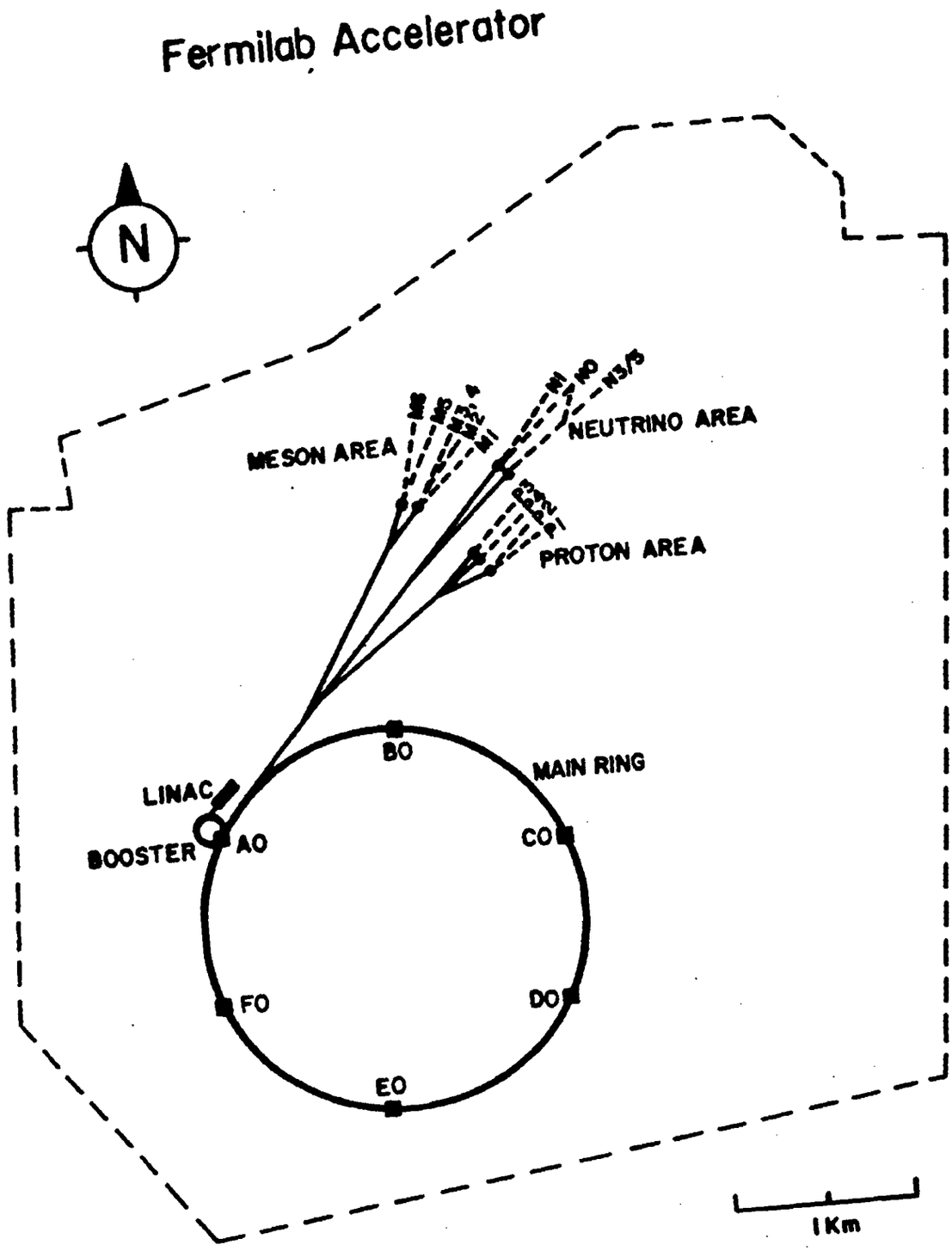

Fig. III.1. Schematic diagram of the Fermilab Accelerator

The main features of the neutrino area beamline are shown in Figure III.2. The 350 GeV protons are extracted from the main ring and are incident on the neutrino area target. The target consists of one interaction length of berylium oxide imbedded in a water cooled aluminum block. The noninteracting protons are stopped by a beam dump further downstream.

The charged particles resulting from the proton interactions in the target, mostly pions and kaons, are focussed by the horn.[2] The horn is a conical shaped aluminum conducting sheet which produces a torroidal magnetic field. Eighty kiloamps of current are pulsed into the horn during the fast spill to produce the magnetic field. This field causes a radial inward average transverse momentum kick of .15 GeV/c to the positive particles focussing them parallel to the beam direction. The negative particles, correspondingly, tend to be kicked away from the beam direction. The horn serves the dual purpose of a lens to focus the positive charges and a filter to eliminate the unwanted negative charges.

The secondaries passing through the horn enter a 1000 foot decay region. The decay particles will be neutrinos, muons, and other particles. The relevant decay modes are shown in Table III.1. Muon neutrinos result from the decay of π^+ and K^+, while muon antineutrinos result from the decay of π^- and K^-. Electron type neutrinos result from K^+ and K° decay. Even though the negative particles are dispersed rather than focussed by the horn, some negative particles will decay in the beam pipe to create a contamination of antineutrinos. The resulting neutrino beam is composed of muon and electron type neutrinos in roughly the ratio $\nu_\mu:\bar{\nu}_\mu:\nu_e:\bar{\nu}_e$ = 400:50:2:1. Two torroids at the end

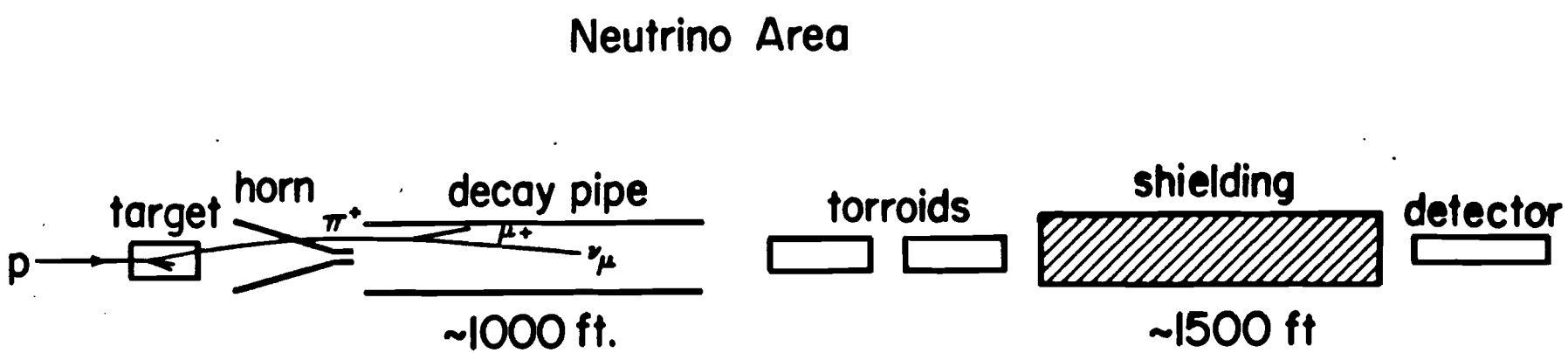

Fig. III.2. Schematic diagram of the neutrino area beam line

ν_μ producing decays	branching ratio
$\pi^+ \to \mu^+ \nu_\mu$	$\sim$100%
$K^+ \to \mu^+ \nu_\mu$	63%
$K^+ \to \pi^o \mu^+ \nu_\mu$	3%
$K_L{}^o \to \pi^- \mu^+ \nu_\mu$	27%
$\mu^- \to e^- \bar{\nu}_e \nu_\mu$	100%
$\bar{\nu}_\mu$ producing decays	
$\pi^- \to \mu^- \bar{\nu}_\mu$	100%
$K^- \to \mu^- \bar{\nu}_\mu$	63%
$K^- \to \pi^o \mu^- \bar{\nu}_\mu$	3%
$K_L{}^o \to \pi^+ \mu^- \bar{\nu}_\mu$	27%
$\mu^+ \to e^+ \nu_e \bar{\nu}_\mu$	100%
ν_e producing decays	
$K_L{}^o \to e^+ \pi^- \nu_e$	39%
$K^+ \to e^+ \pi^o \nu_e$	5%
$\mu^- \to e^+ \bar{\nu}_\mu \nu_e$	100%
$\bar{\nu}_e$ producing decays	
$K_L^o \to e^- \pi^+ \bar{\nu}_e$	39%
$K^- \to e^- \pi^o \bar{\nu}_e$	5%
$\mu^- \to \nu_\mu \bar{\nu}_e$	100%

Table III.1 Neutrino producing decay modes

of the decay pipe deflect a portion of the positive muons out of the beam-line. The remaining particles enter a region of 1500 feet of shielding consisting of steel, concrete, and earth. The strongly interacting particles range out by interacting in the shielding while the muons undergo an ionization loss. Muons of energy up to 250 GeV range out in the shielding. The neutrinos pass through the shielding essentially unimpeded and are incident on the detector.

The experimental areas begin after the 1500 feet of shielding. The detector for this experiment (E-253) and a detector for a charmed particle lifetime measurement (E-531) are housed in the Wonder building. The bubble chamber is 1500 feet further downstream. All of these experiments were running simultaneously. The neutrino beam to these experiments consisted of ν_μ with a background of other neutrinos and muons. The muons were not a significant problem for the bubble chamber since it is shielded by an additional 1500 feet of earth, but they were a problem at the Wonder building.

A high flux of muons will increase the trigger and veto dead times and interfere with the clean operation of the detector. The decision to run the accelerator at 350 GeV rather than the usual 400 GeV was made to decrease this muon background flux at the Wonder building. In addition, the torroids were added to further reduce the muon flux. The torroids have the unfortunate side effect of interfering with the operation of the external muon identifier (EMI) of the bubble chamber. Muons deflected by the torroids multiple scatter from the edge of the earth shielding into the EMI. For this reason the torroids were not used when the bubble chamber was in operation. About half of the data was taken with the torroids on. The torroids reduce the muon flux

through the detector by a factor of 8.

In order to determine the total cross section for $\nu_\mu e$ elastic scattering, one must know the magnitude and energy distribution of the incident neutrinos. Over the years a Monte Carlo program has been developed (NUADA) to model the neutrino production process and predict the neutrino flux. The results of this program have been found to be correct for neutrino energies above 50 GeV, but it underestimates the lower energy flux.

The low energy results of the program were supplemented using data from a low energy threshold neutrino trigger for our detector and a Monte Carlo program which models the energy deposition of the $\nu_\mu N$ events in the calorimeter. The low energy flux which is input to the Monte Carlo is adjusted so that the predicted energy distribution agrees with the observed distribution.

The details of the NUADA program and the low energy flux determination procedure are given in Chapter V.

REFERENCES FOR CHAPTER III

1. 200 BeV Accelerator Design Study, University of California at Berkeley Publication UCRL 1600, (1965).

2. S. Mori, Wide-Band Single Horn System, Fermilab Technical Memo, TM-663, (1977).

CHAPTER IV

APPARATUS

GENERAL LAYOUT

Most of the neutrinos incident on the detector pass through without interacting. Of those that do interact, the vast majority are neutrino nucleon interactions and only rarely does a neutrino electron interaction occur. Since such a rare interaction is under study, great care must be taken in designing a detector which can discriminate the $\nu_\mu e$ events from the $\nu_\mu N$ events. The trigger must be designed to accept a large fraction of the $\nu_\mu e$ events while, at the same time, rejecting as many $\nu_\mu N$ events as possible. Since kinematic cuts are used to isolate the signal from the large background, the detector must have excellent angular and energy resolution. In order to satisfy all of these requirements with the additional constraints of reliability and low cost, a modular detector was designed using delay-line readout proportional chambers to measure the angle of the electron shower and an aluminum-scintillator sandwich calorimeter to measure the shower energy.

A schematic diagram of the apparatus is shown in Figure IV.I. The detector consists of a front veto hodoscope (A) composed of 36 scintillation counters of overall dimensions of 1.5mx4.0m. Since the shielding is incapable of stopping the high energy muons, the hodoscope is essential in preventing incident background muons from triggering the apparatus.

After the front veto wall are 49 detector modules. Each module consists of 1.1 radiation lengths of aluminum, a delay-line proportional

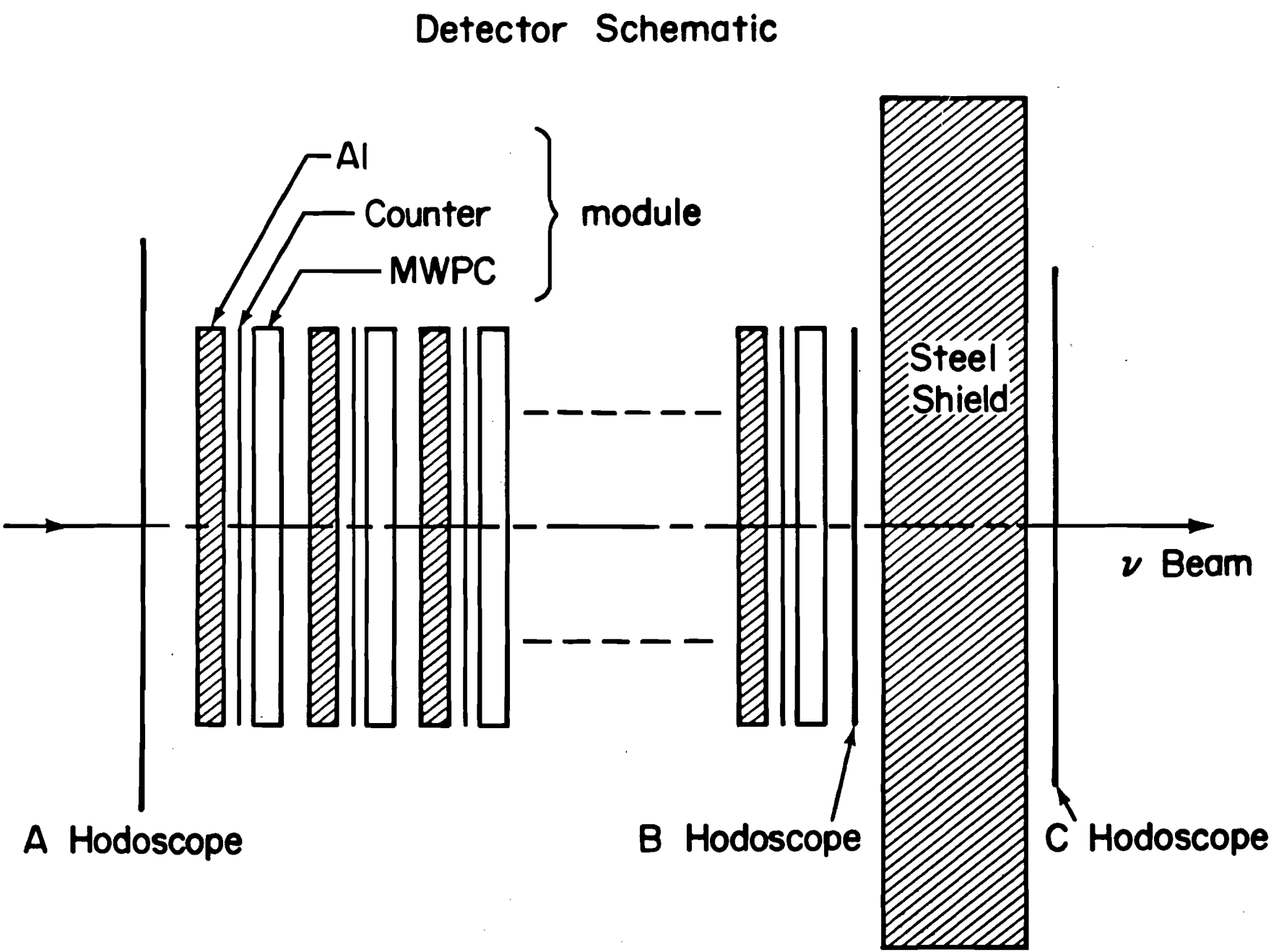

Fig. IV 1. Schematic diagram of the detector

chamber, and a layer of 1/2 inch thick plastic scintillator. The transverse size of the module is 1m x 1m with the modules spaced longitudinally one foot apart. The total mass of the detector is 12 tons with a fiducial mass of 8 tons.

Table IV.1 summarizes some of the relevant characteristics of aluminum. The aluminum is the principle source of the target mass. Among cheap and common materials it has a large number of electrons per radiation length and a high ratio of electrons to nucleons. The incident neutrino will interact with an electron in the aluminum and the high energy recoiling electron will initiate an electromagnetic shower which propagates through the detector. In addition to being the source of target mass, the aluminum also serves as the radiator for the electromagnetic shower.

Pulses on the cathode plane of the delay-line proportional chamber induced by the passage of the electrons in the shower through the chamber are used to determine the x and y position of the shower. The energy of the shower is determined from the scintillator pulse height. The chamber anode pulse and scintillator pulse heights are both used in the energy deposition trigger for the detector.

After the last module is a tagging hodoscope (B) which detects the leakage of particles out of the end of the calorimeter. This hodoscope consists of 21 scintillators and measures 1.6m x 1.6m.

In front of the final muon identifying hodoscope (C) is a 4'x10'x10' steel hadron absorber. The final hodoscope measures 3.0mx3.0m and is composed of 27 scintillators. The steel is 70 radiation lengths and 7 absorption lengths in thickness. All of the electrons in the electromagnetic shower will

Atomic number	z	13	
Atomic weight	A	27	
density	ρ	2.7 gm/cm^3	
collision length	L_{coll}	68.9 gm/cm^2	25.5 cm
absorption length	λ	37.2 cm	
radiation length	x_o	24.01 gm/cm^2	9.0 cm
critical energy	ε_c	34 MeV	

Table IV.1. Characteristics of Aluminum.

range out in the aluminum or steel absorber with only the muons and a few hadron punch throughs penetrating into the back hodoscope. The back hodoscope is useful in identifying and rejecting the hadronic events.

The electronics is summarized in Figure IV.2. Each hodoscope counter is latched and the front hodoscope used as a muon veto in the trigger. The pulse on the anode plane of the proportional chamber is digitized by an analog to digital converter (ADC). The anode pulses are also input to the chamber trigger logic. A trigger (labeled CH) is issued if the total energy deposited in six consecutive chambers is above threshold. The pulses on the cathode plane are input to a time to digital converter (TDC). The positions of the showers in the chamber can be determined from the digitized arrival times.

The energy of the shower is determined from the scintillator pulse heights. The scintillator phototube signal is digitized by two sets of ADC's. One set digitizes the direct phototube pulses. These digitized values are used to compute the shower energy. Another set of ADC's digitizes an amplified phototube signal. This amplified set extends the dynamic range of the pulse height measurement to below minimum ionizing. These amplified pulse height measurements are used to identify muons by their energy deposition. In addition, a trigger (labelled SC) is issued if the phototube pulse height in each of four consecutive scintillators is above threshold. The master trigger is a coincidence between the chamber trigger (CH) and the scintillator trigger (SC) in anticoincidence with the muon veto hodoscope, ($\bar{A}\cdot CH\cdot SC$).

CHAMBER OPERATION

The Delay-line proportional wire chambers consist of an anode plane of wires and two cathode planes.[1] The anode wires are gold plated

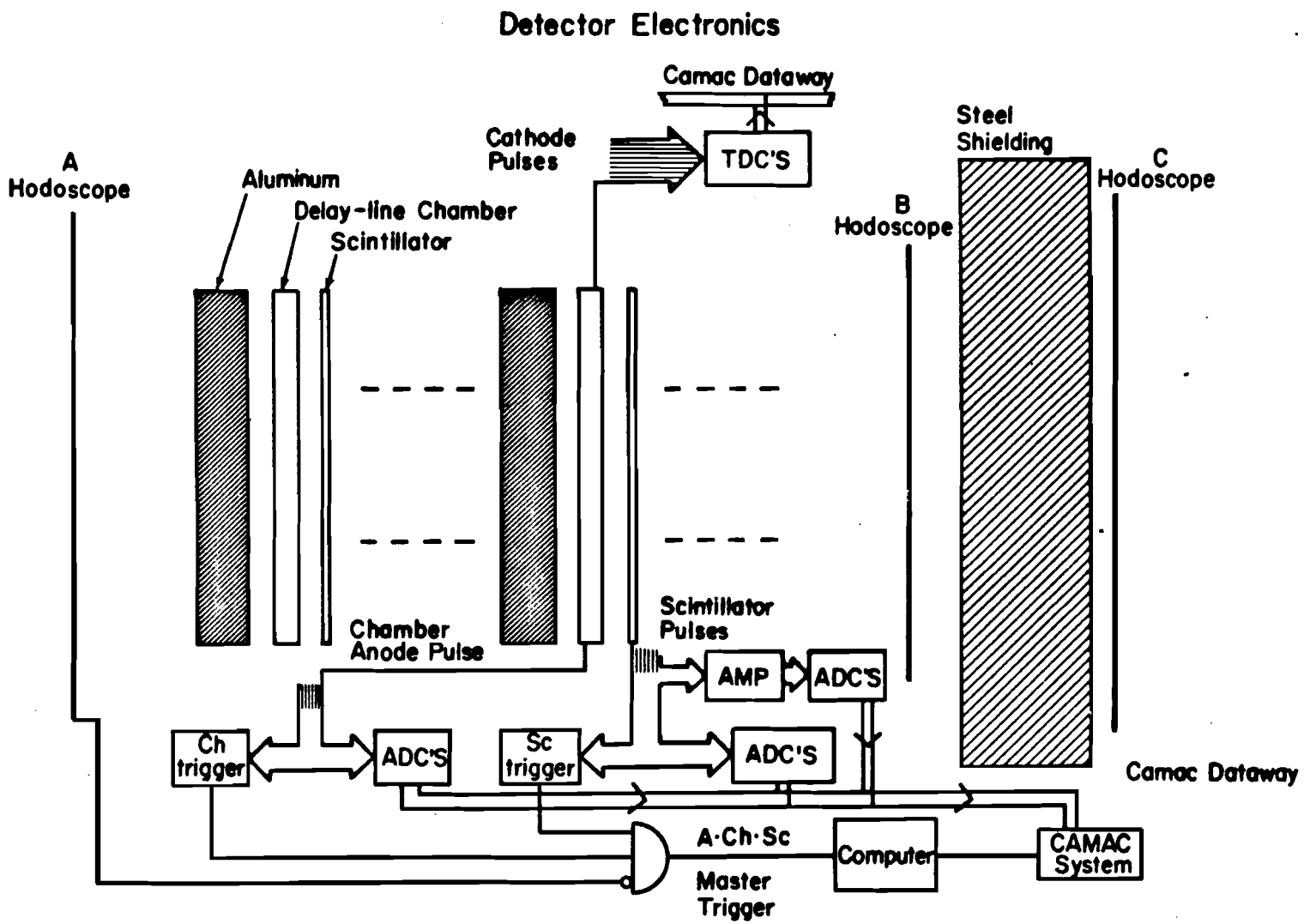

Fig. IV.2. Schematic diagram of the detector electronics

tungsten of 20 micron diameter spaced 3 mm apart. The anode wires are 'or'ed together to form one output anode pulse. One quarter inch on either side of the anode plane are the cathode planes at ground potential. Each cathode plane is a sandwich of G-10 plastic and copper. The back face of the G-10 is epoxied to a sheet of aluminum for support and to provide the ground plane for the delay-line. The copper face is milled into a zig-zag conducting delay-line (see Fig. IV.3). The spacing between neighboring paths is 1/16". The pulse traveling on the delay-line is sensed at 5 tap points spaced 10" apart. The chamber is filled with a gas mixture of 80% CO_2, 19.7% Ar, and 0.3% Freon-13-B1.

The passage of the charged particles in the shower through the chamber will create ion pairs in the chamber gas. The high mobility electrons will migrate to the nearest anode wires and in the process create an avalanche of more ion pairs. The motion of the electrons toward the anode wires and the motion of the positive ions away from the anode induce pulses on both the anode and cathode delay-line. The anode pulse is capacitively coupled to an anode amplifier which outputs an amplified signal to an analog to digital converter (ADC). The cathode pulse will begin on that portion of the delay-line nearest the anode wires where the avalanche is occurring and propagate in both directions to the rest of the delay line.

Consider a tap point on the delay-line which is displaced laterally 10 inches from the point where the shower passed through the chamber.

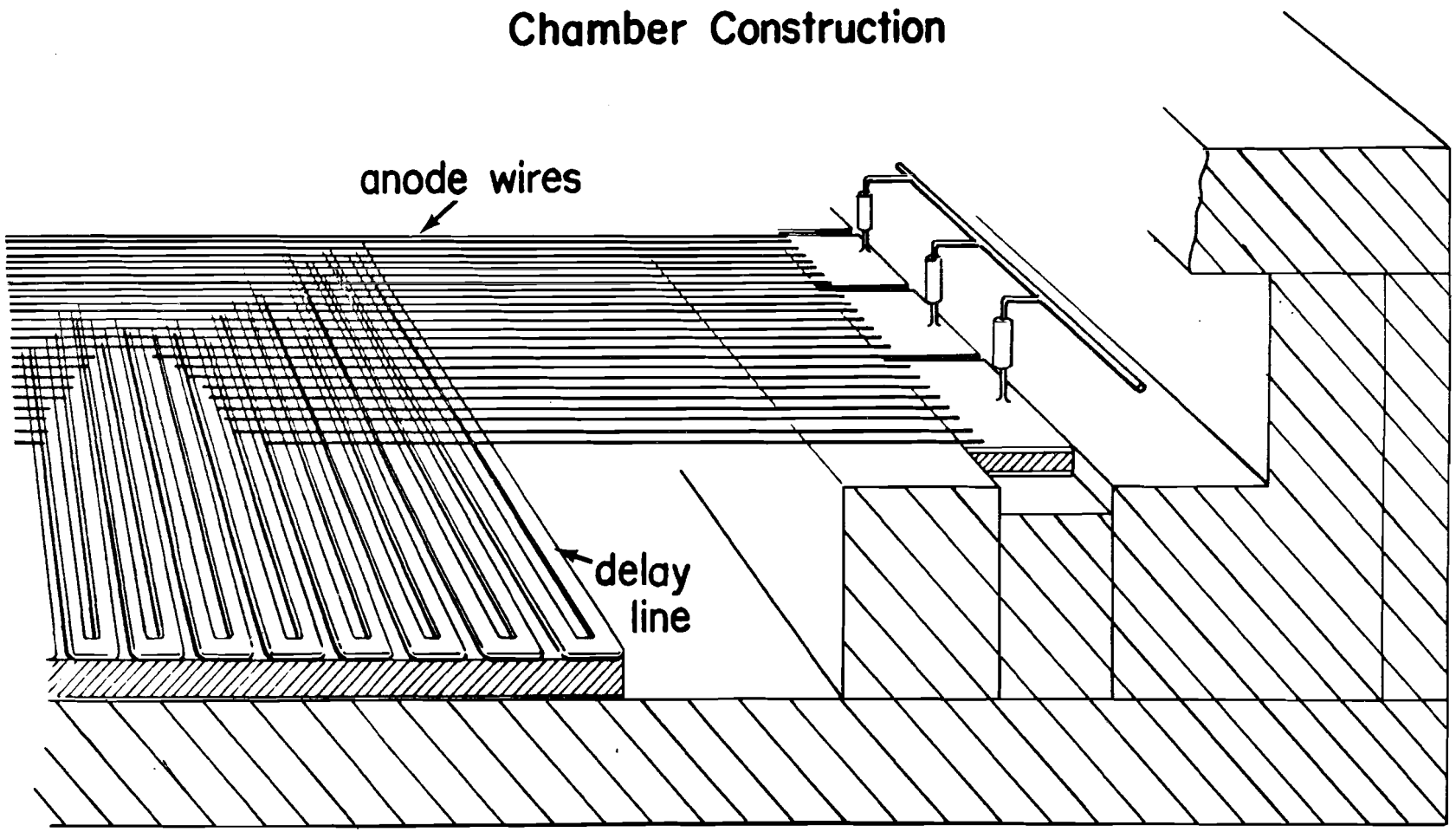

Fig. IV.3. Details of the delay-line proportional chamber construction.

As the positive ions drift toward the cathode a positive pulse is induced on the delay-line and a negative pulse on the collecting anode wire. In addition the positive ions drifting away from the avalanche wire will induce a positive pulse on the neighboring anode wires. This pulse forms a negative image pulse on the delay-line. The total induced pulse on the delay-line is a directly induced positive pulse superimposed on a broader negative pulse. The total pulse propagate to the tap points. The magnitude of the negative delay-line pulse will depend on the capacitance between the anode and delay-line.

A pulse traveling on the delay-line is sensed by cathode amplifiers at each tap point (see Figure IV.4a,b). The difference amplifier differentiates and discriminates the delay-line pulse to form an output logic pulse. The logic pulse begins when the differentiated delay-line pulse first exceeds the preset threshold. The logic pulse then returns to zero when the trailing edge of the differentiated delay line pulse falls below threshold. The width of the logic pulse gives a crude measure of the width of the shower or track inducing the pulse. The thresholds of all the cathode amplifiers were set identically using a standard square wave into the test input of the amplifier and then increasing the threshold level from below until a logic pulse is triggered.

Figure IV.4 also shows the difference in pulse formation between the X and Y delay-lines. The initial negative pulse on the Y-delay-line is larger than the comparable pulse on the X delay-line since the anode-cathode capacitance is different. The zig-zag of the X delay-line

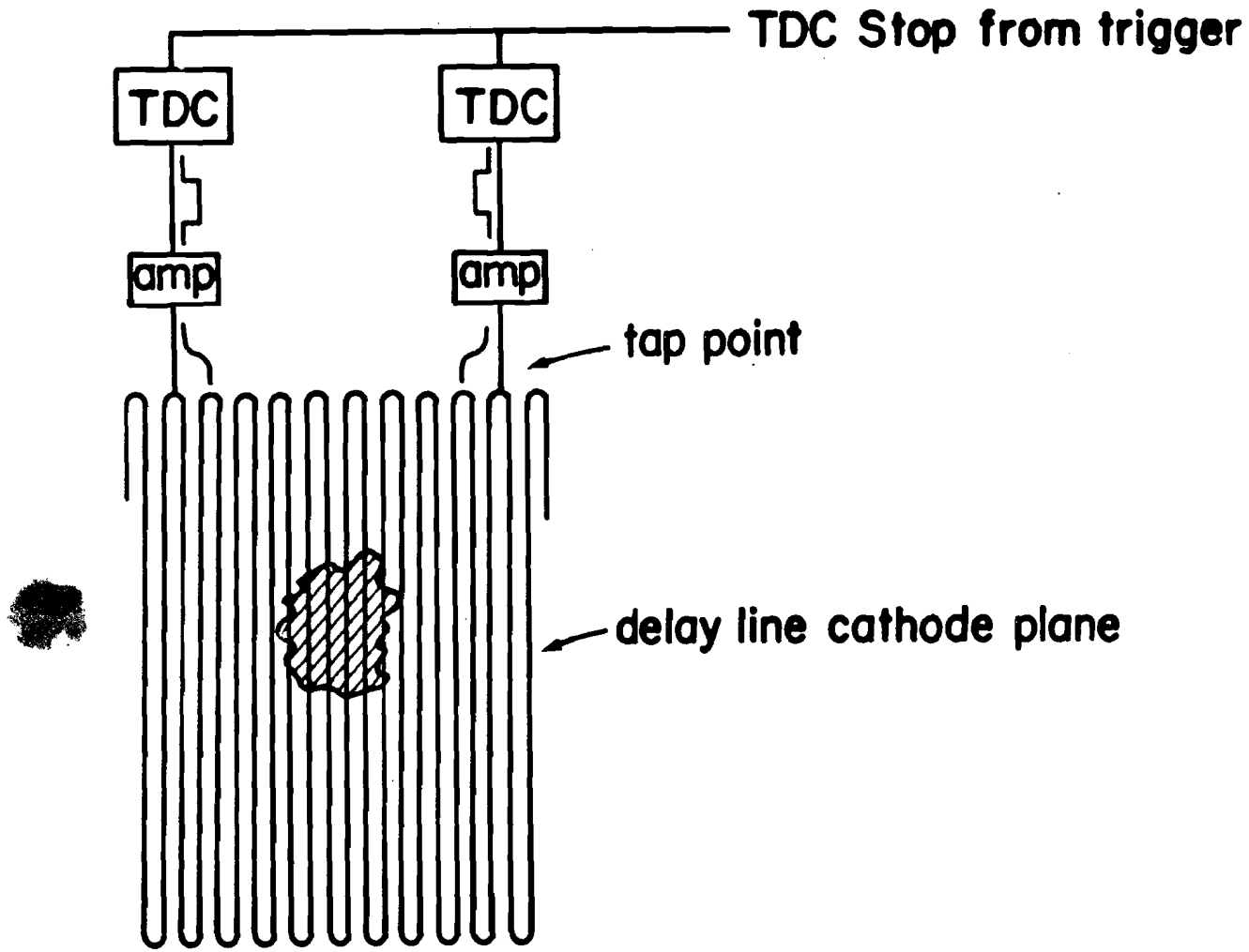

Fig. IV.4a. Details of the chamber operation

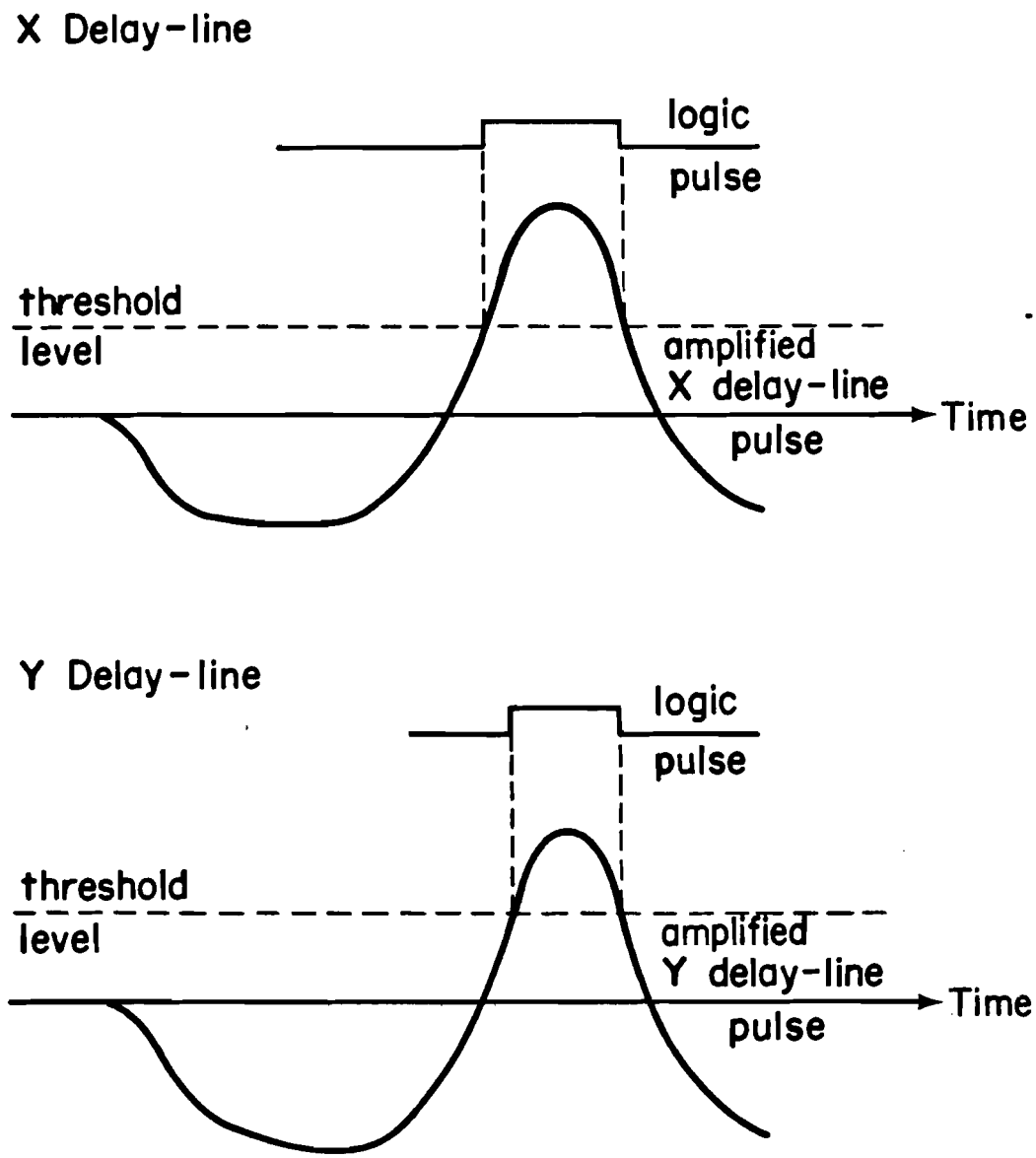

Fig. IV.4b. Details of the chamber operation

is perpendicular to the anode wires. While the zig-zag of the Y delay line is parallel to the anode wires, causing the difference in the capacitance. This causes the Y delay-line to be slightly less efficient on isolated charged particles since the absolute magnitude of the delay-line pulse is smaller.

The logic pulse resulting from the passage of a shower or charged particle through the chamber then goes to a TDC which digitizes the time between the arrival of the cathode logic pulse and the TDC stop pulse. The TDC stop pulse arrives a fix time after the event occurs in the detector. The farther away the shower is from the tap point, the longer will be the propagation time on the delay-line and the shorter will be the digitized time. The TDC also digitizes the width of the cathode pulse which is related to the width of the shower.

The position of the leading edge and width of the electron shower is given by:

$$X = X_{TAP} \pm \beta\ (TOF - t_D) \qquad \omega = \beta\omega_D \qquad \text{(IV-1)}$$

X_{TAP} = Position of Tap

β = Delay-line Pulse Velocity

TOF = Time of Flight Constant

t_D = Digitized Time

ω_D = Digitized Width

A right-left ambiguity is introduced due to the fact that the pulse sensed at the tap could be traveling from either direction on the delay-line. See Appendix IV.1 for a description of how the constants TOF and β are determined.

The shower position is reconstructed as in Figure IV.5. Assume the shower passes through the cathode plane between taps 3 and 4. Taps 2 and 3 will sense the left edge of the shower and taps 4 and 5 will sense the right edge. All of these taps will also sense the approximate width of the shower. Tap 1 is too far away from the shower to give any information. The right-left ambiguity of taps 2, 3, and 4 is shown in the figure. Typically the width of the shower as measured by the TDC is overestimated by 50 per cent. This cathode information is reconstructed into a shower between taps 3 and 4 with the left edge defined by the average of the left edges seen by taps 2 and 3 and the shower right edge defined by the average of the right edges from taps 4 and 5. The centroid of the shower is the midpoint between the two shower edges.

One of the limits to the spatial resolution attainable with this detector is due to the attenuation and dispersion on the delay-line. The pulse attenuation is about a factor of two between tap points. This will cause a shift in the measured position of the edges relative to the true shower position. Figure IV.6 shows the difference in a shower edge position as seen from two neighboring taps. The average shift is about 8 mm per 10 cm traveled on the delay-line. A first order correction to the measured positions was added to compensate for this dispersion effect (See Appendix IV.1). In addition, slewing of the TDC stop pulse relative to the time the event occurred will also degrade the detector resolution. This effect was minimized by using the fast rise time of the scintillator pulse to set the trigger and TDC stop timing.

A more fundamental limit to the resolution results from fluctuations in the shower shape itself. The shower consists of a central core of high energy particles at small relative angles and a

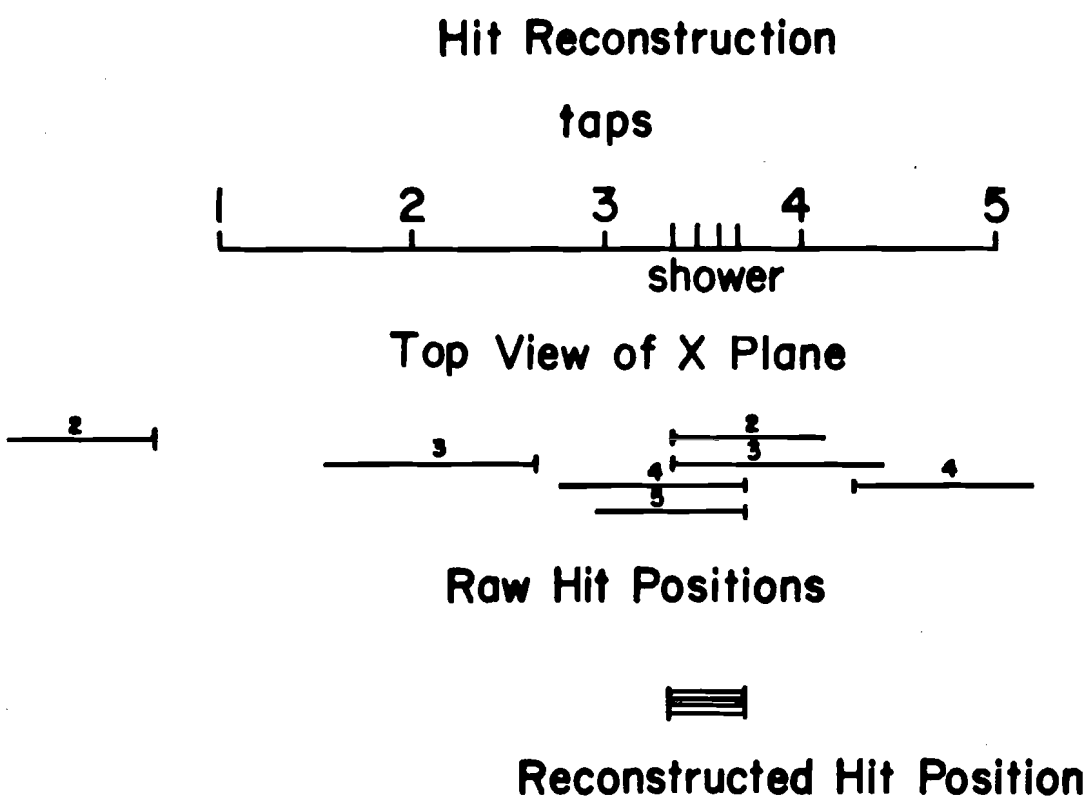

Fig. IV.5. Example of the chamber hit reconstruction

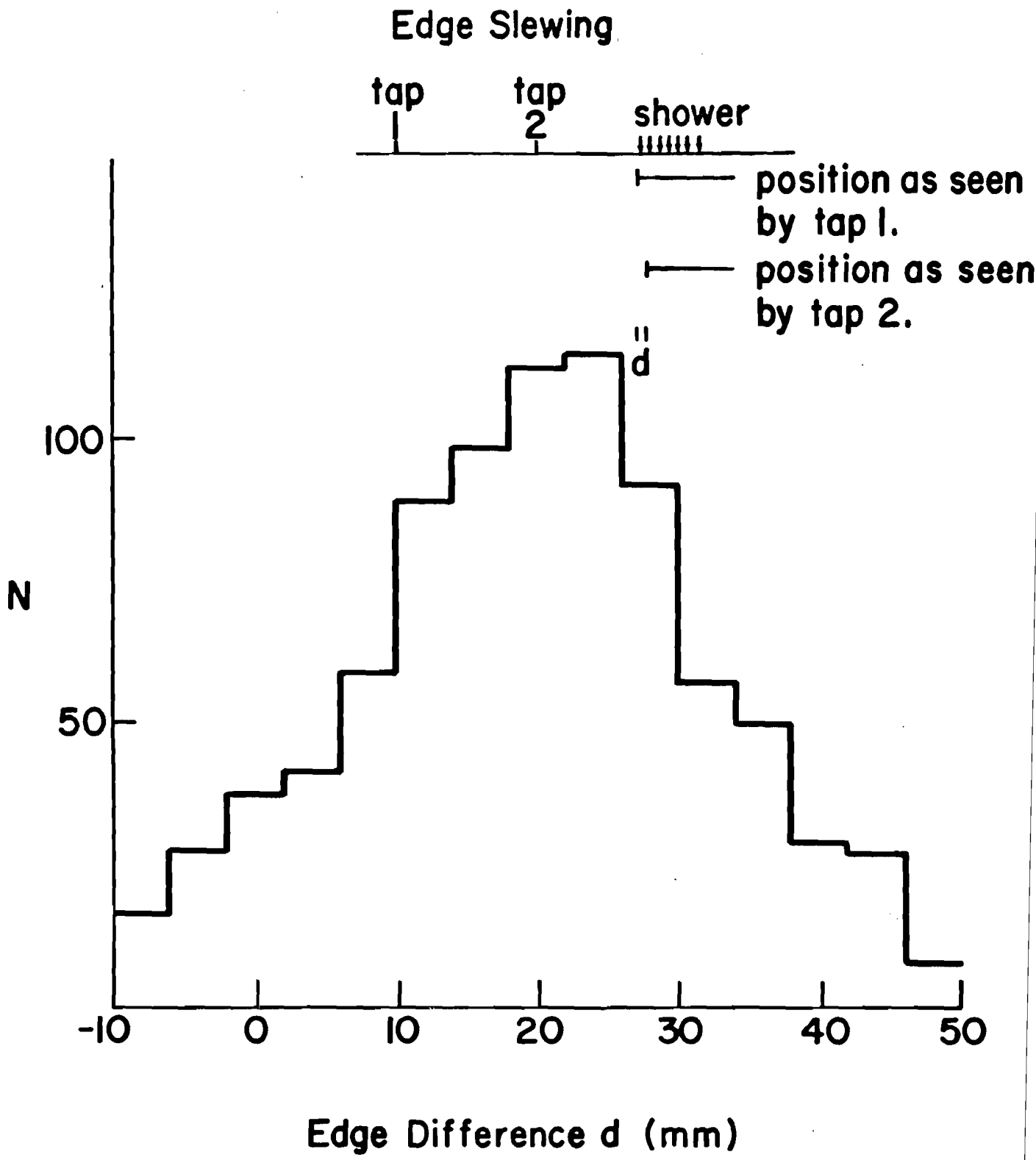

Fig. IV.6. Edge Slewing between neighboring taps

lower energy cloud of particles that may be at larger angles. Due to fluctuations in the shower process, the centroid of the lower energy cloud may not coincide with the centroid of the high energy core. The chambers are sensitive to the low energy particles and therefore measure the low energy centroid. This cloud of low energy particles will range out in the aluminum of the next module with a new cloud being generated by the high energy core. Because of this effect one would expect the spatial resolution of the electron shower to be worse than the resolution for muons. The resolution for muons is shown in Figure IV.7. Figure IV.8 shows the spatial resolution for showers as a function of module number. The resolution in the first chamber of the shower is the same as the muon resolution. The resolution then increases logarithmically with the logitudinal development. This spatial resolution leads to a calculated angular resolution of 10 milliradians for electromagnetic showers.

CALORIMETRIC PROPERTIES

The high energy recoiling electron resulting from the interaction with the incident neutrino will subsequently interact with the dense material through which it passes to form an electron shower. The purpose of the calorimeter is to measure the energy of the shower.

The electron looses energy by collisions with the atomic electrons or by radiating a photon. At high energies the predominant energy loss mechanism is by radiation. The radiated photon can loose energy by pair production or by Compton scattering. The energy of the initial electron becomes shared among the secondary electrons and photons. These processes repeat until the average particle energy is low enough to stop the multiplication process. The number of shower particles then

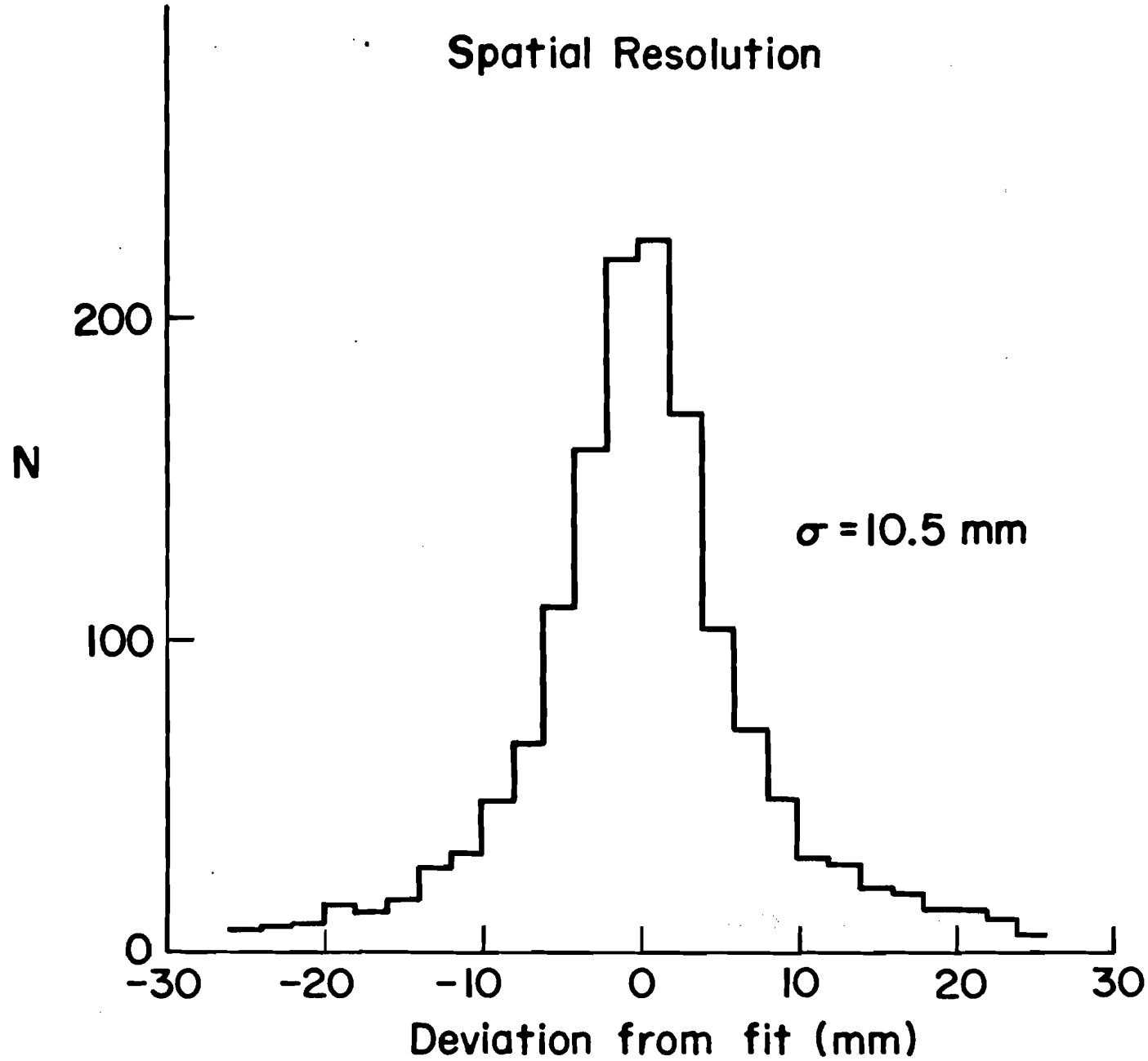

Fig. IV.7. Spatial resolution for muons

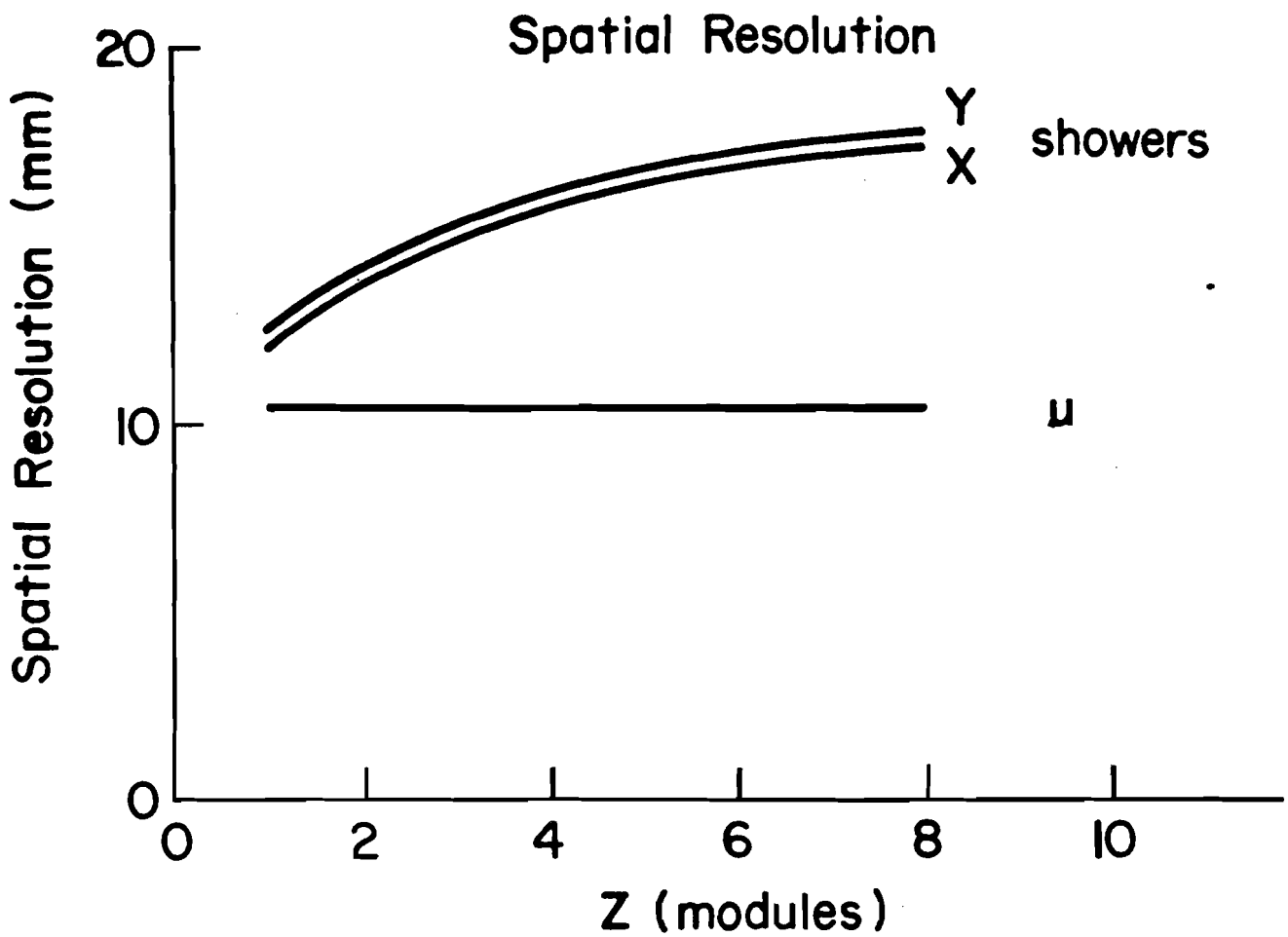

Fig. IV.8. Spatial resolution for electromagnetic showers

decreases with the dominant mode of energy loss being due to atomic collisons and compton scattering. There are two parameters which describe how the electron shower developes in a material. The radiation length is defined as the distance necessary for the initial electron energy to fall to 1/e of the original value because of radiation loss. The critial energy is that energy at which the probable ionization loss is equal to the probable radiation loss. The radiation length is a good measure of the scale of the longitudinal development of the shower and the critical energy determines the number of particles at shower maximum.

A detailed mathematical analysis of the shower development process is extremely complicated.[2] After making various simplifying approximations, analytic expressions can be obtained. Some of the important formulas are summarized here. The position of the shower maximum is given by:

$$T_{max} \sim \ln(E/_{\varepsilon}) - 1. \qquad \text{(IV-2)}$$

T_{max} is measured in radiation lengths, E is the incident electron energy and ε is the critical energy. Note that the length of the shower development varies only logarithmically with energy.

The rms width of the shower is given by:

$$R_m = (21 \text{ MeV}) \times X_{o/\varepsilon}$$

X_o is the radiation length and ε the critical energy. The width is essentially independent of energy.

It is very useful to know the longitudinal development of the number of charged particles in the shower. The formula presented here is a generalized version of a simple expression derived by Heisenberg.[3]

$$\Pi(E, \varepsilon, t) = Ce^{(-\alpha t + 2AB)} \qquad \text{(IV-4)}$$

$\Pi(E, \varepsilon, t)$ = The number of charged particles from an incident electron

of energy E with energy above the critical energy ε as a function of the radiation length t transversed

$$A = (\mu - \beta)^{1/2} \qquad C = A/(Bt^{1/2})$$

$$B = (t - \alpha)^{1/2} \qquad D = \kappa/(1.014 - 1)$$

$$\mu = \ln (E/\varepsilon) \qquad \alpha = 1.0028$$

$$\beta = 0.56 \qquad \kappa = 1.025$$

These constants were determined in an electron test beam (Figure IV.9). An electron of energy E was incident on an aluminum radiator of thickness t measured in radiation lengths. The light output of the scintillator furnished a direct measure of the number of charged particles in the shower. The multichannel analyser formed a histogram of the scintillator pulse height for electron showers from electrons of incident energy E passing through t radiation lengths of aluminum. From this distribution (Figure IV.10) the mean energy deposition was computed. Data was collected for incident electron energies of 5, 10, 20, and 30 GeV for radiation thickness from 1 to 10 radiation lengths. Data was also recorded for incident muons on 1 radiation length of aluminum. The mean pulse height from the muon traversing 1 radiation length of aluminum was defined as the equivalent particle pulse height. The resulting shower development curves indicating the mean pulse heights measured in units of equivalent particles as a function of radiation length is shown in Figure IV.11.

The modified Heisenberg formula was fit to the data for $t > 1.5$ radiation legths. For $t < 1.5$ the following was used to insure the proper small t behavior:

$$\Pi(E, \varepsilon, t) = 1 + C_1 t + C_2 t^2 \qquad \text{(IV-5)}$$

C_1 and C_2 are determined by demanding continuity in Π and $d\Pi/dt$ at $t=1.5$.

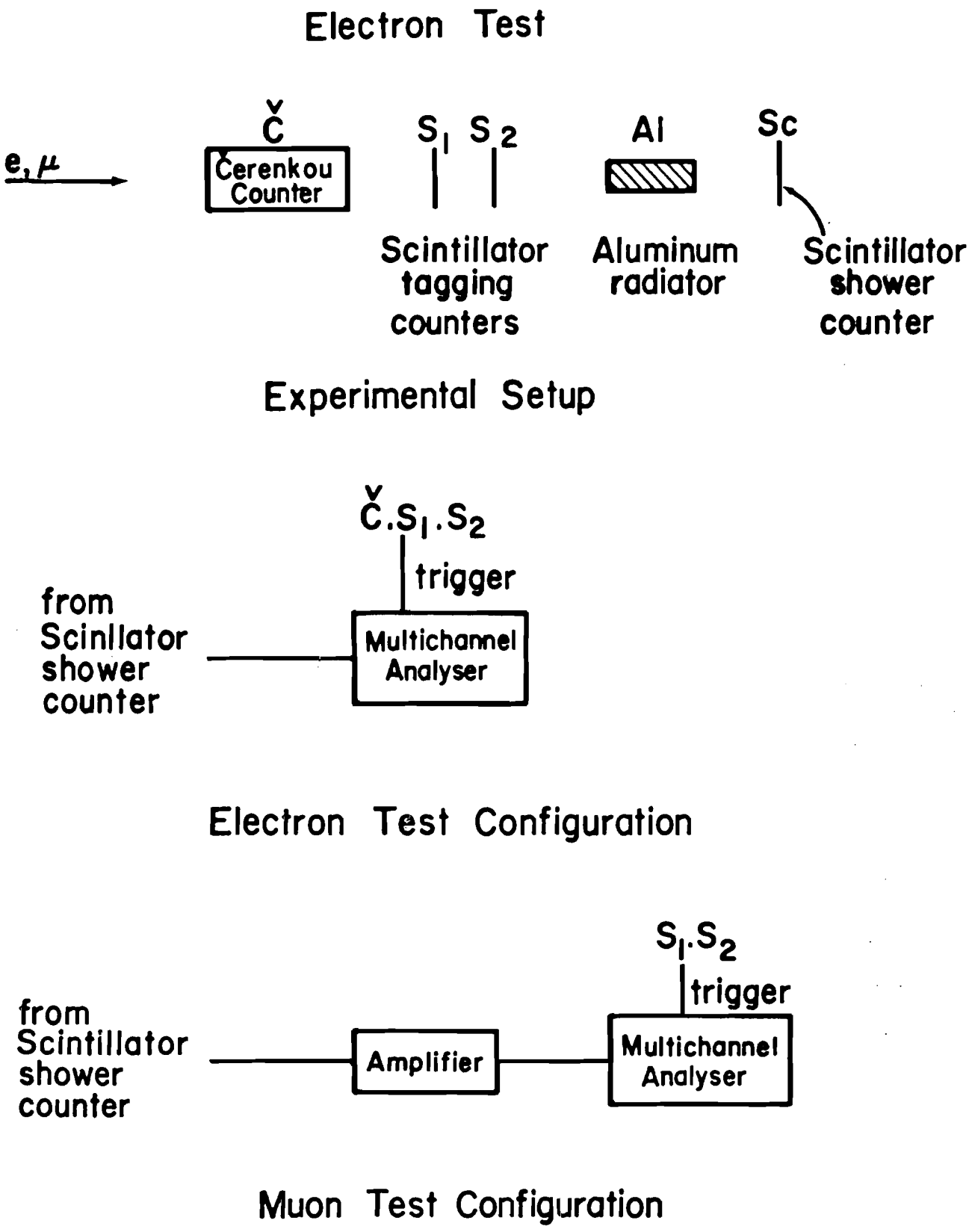

Fig. IV.9. Schematic diagram of electron test run

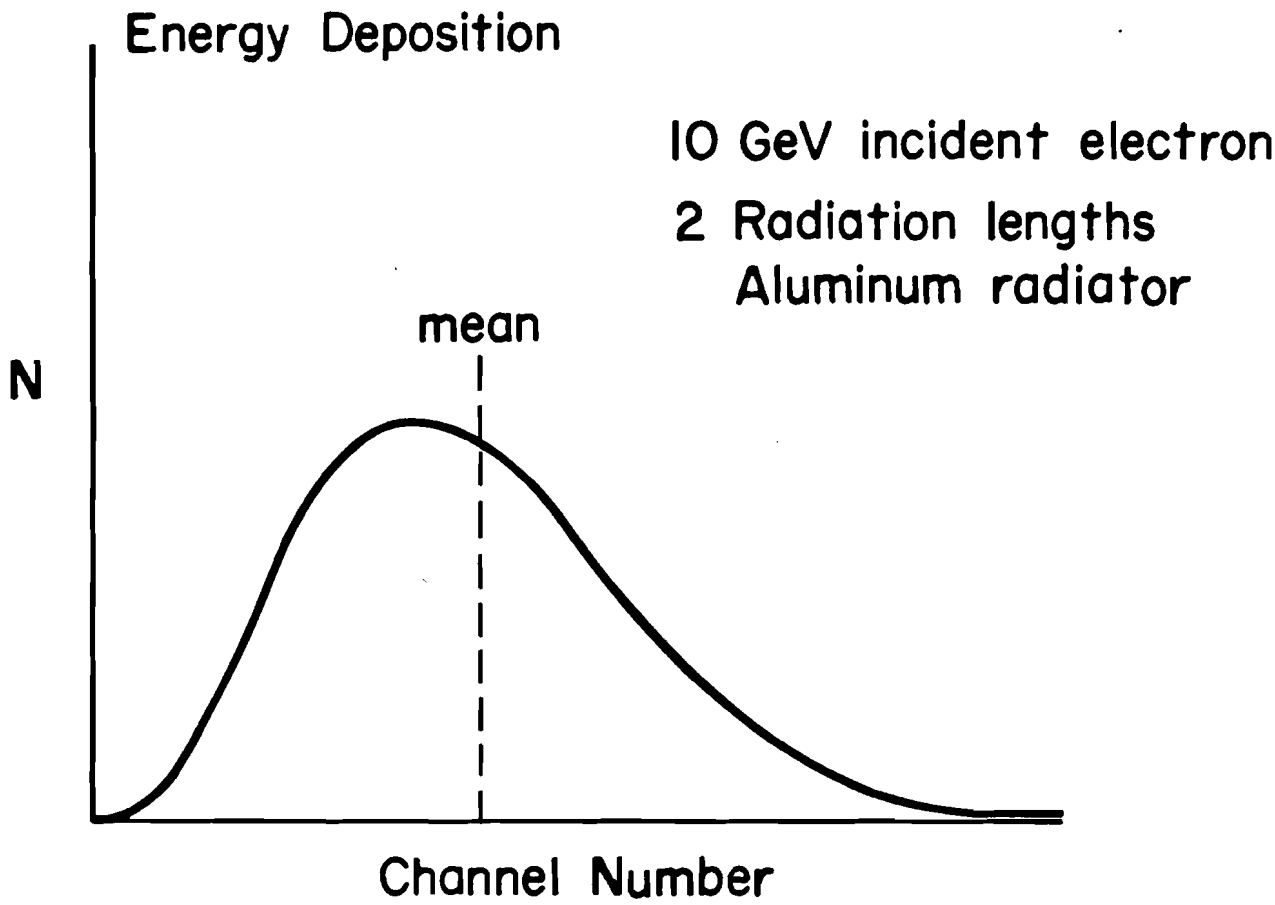

Fig. IV.10. Energy deposition by a 10 GeV electromagnet showers

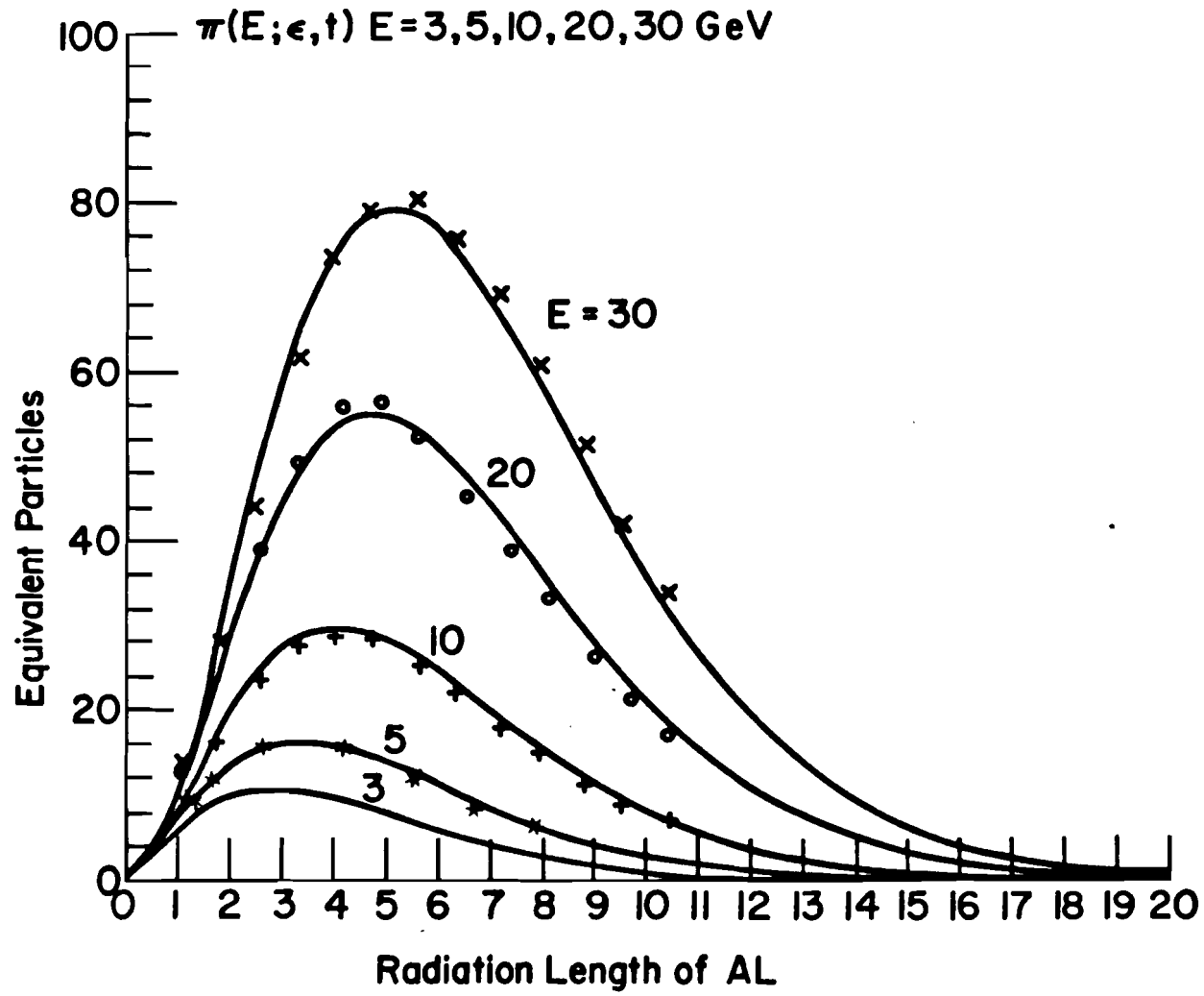

Fig. IV.11. Longitudinal energy deposition by electromagnetic showers

The resulting fitted curves are also shown in Figure IV.11.

Since the scintillators are sensitive to the ionization produced by the particles traveling through it, this shower development curve is actually measuring the ionization loss as a function of radiation length. Since ultimately all of the energy of the incident electron ends up in the form of ionization, the energy of the incident electron will be proportional to the integral of this shower development curve. The integral of the shower development curves are shown in Figure IV.12 and the relationship between the integral and the incident electron energy in Figure IV.13. Figure IV.13 gives the calibration between the summed pulse heights measured in units of equivalent particles and the incident electron energy.

In order for this calibration to be useful, one must be able to express the scintillater pulse heights in units of equivalent particles. The muon pulse height is used as the standard unit since it could be used at both the test site and at the detector in the neutrino area. Using data from the muon trigger and knowing the relative gains of the direct and amplified ADC's, the direct ADC channel numbers are calibrated in equivalent particles (see Appendix IV.2 for details). For each event the energy deposited in each module is computed using the above calibration curve (Figure IV.13) and the total energy computed from the sum over modules.

The scintillator is sampling only a small fraction of the total ionization which occurs in the detector. The bulk of the ionization occurs in the aluminum. Fluctuations in the distribution of this ionization will lead to fluctuations in the measured energy. Since the measured energy is proportional to the total number of ion pairs observed, one would expect the resolution to have the functional form:

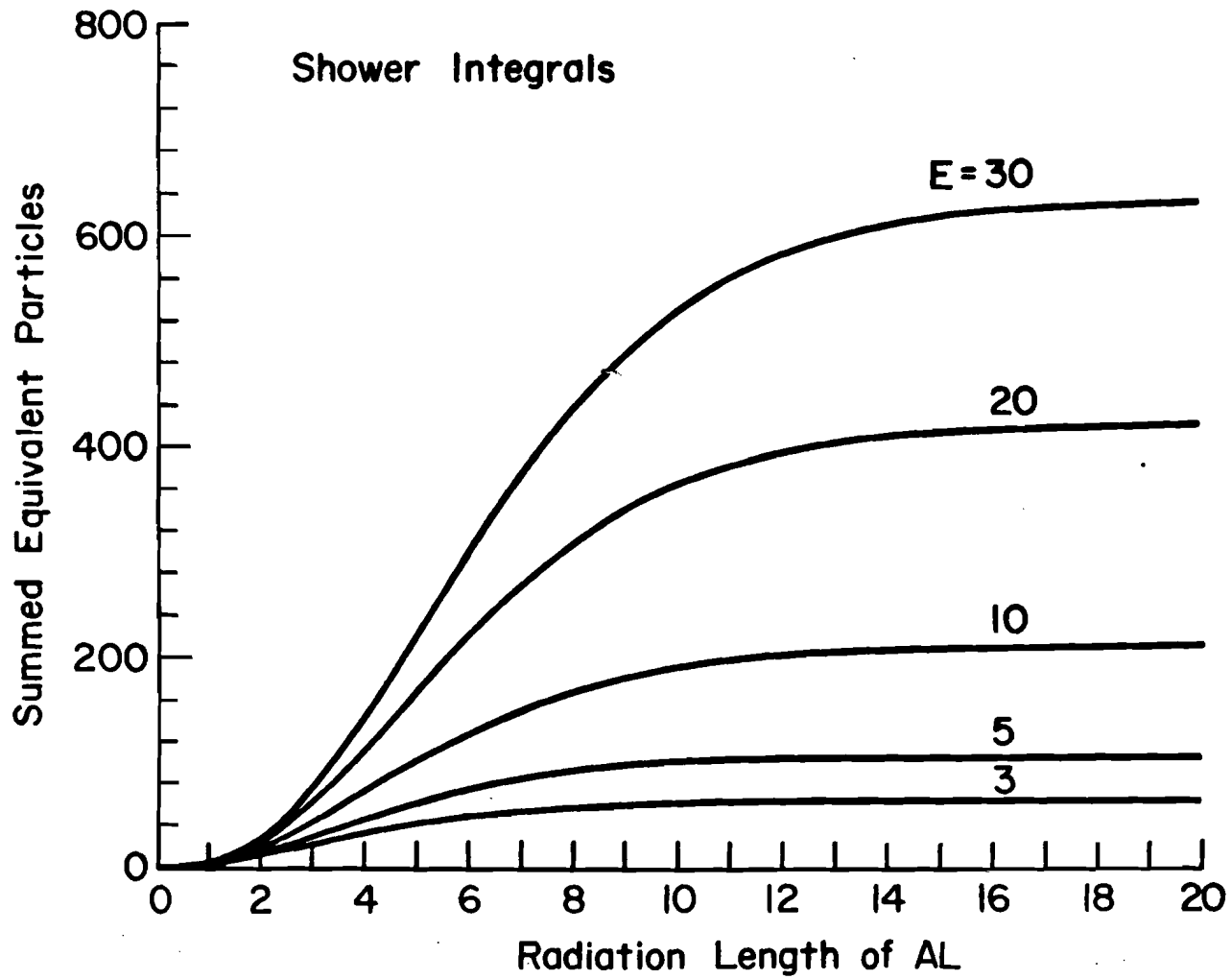

Fig. IV.12. Integrals of the energy deposition curves

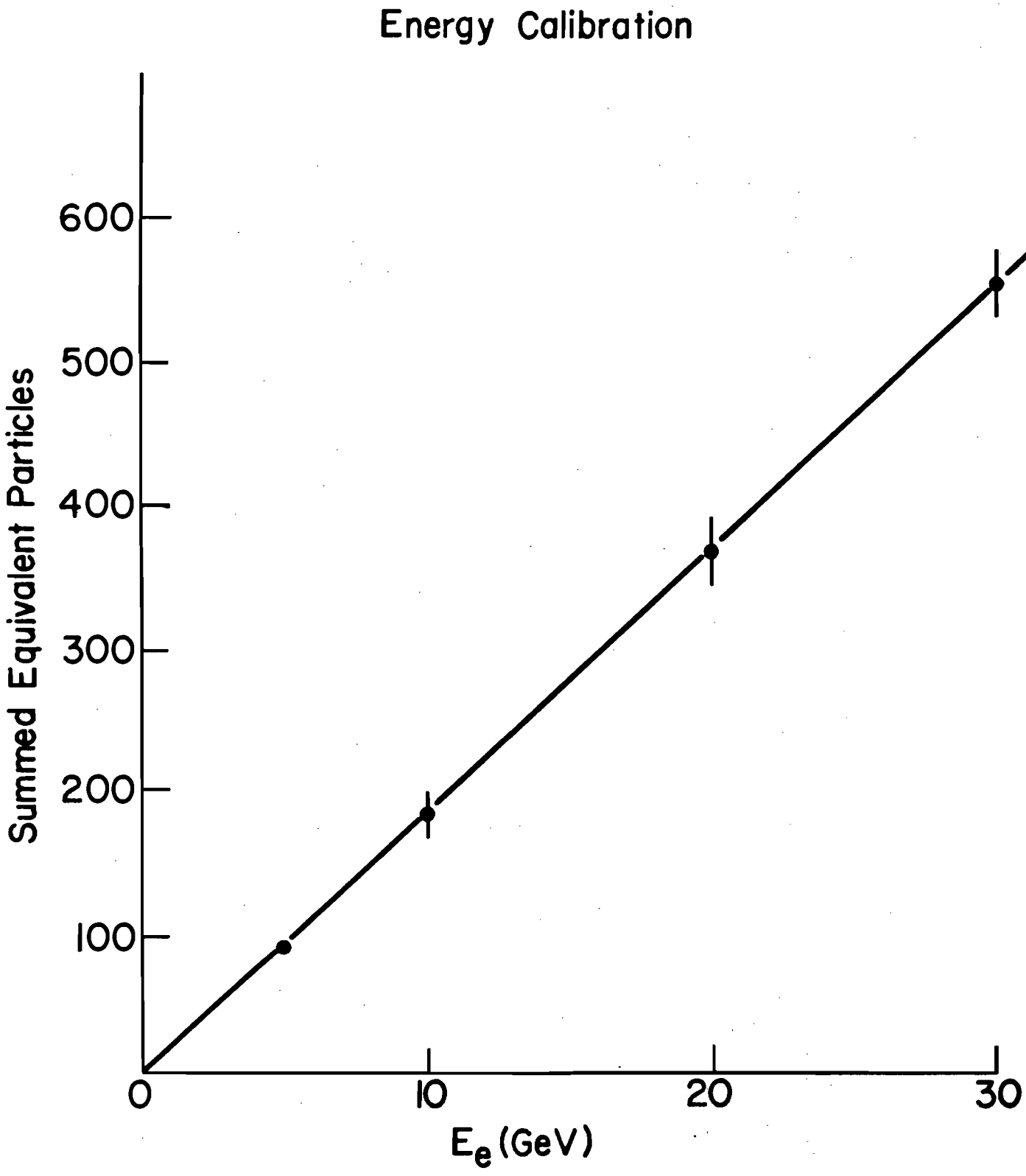

Fig. IV.13. Shower energy calibration in equivalent particles

$$\frac{\sigma_E}{E} \propto \frac{\sigma_N}{N} \propto \frac{\sqrt{N}}{N} \propto \frac{1}{\sqrt{E}} \qquad \text{(IV-6)}$$

A second more sophisticated calibration test was done to test the response of the detector to electrons. This test detector consisted of 10 fully instrumented modules and an electron tagging system. For each incident electron the test recorded the scintillator pulse height in the 10 modules. The pulse height from each module was normalized to insure that each module had the same phototube gain (see Appendix IV.3 for details). The energy of the incident electron was then found from the summed pulse height. A histogram of the summed pulse heights is shown in Figure IV.14. The low energy tail is due to events with an appreciable leakage out the end of the detector. The energy resolution is estimated from the half widths of the distributions. Table IV.2 summarizes the energy resolution for 10, 20, 30 GeV electrons. The energy resolution is described well by the formula:

$$\frac{\sigma_E}{E} = \frac{.29}{\sqrt{E}} \qquad \text{(IV-7)}$$

FAST ELECTRONICS

The detector electronics serves two important purposes, to trigger the data taking operations on those events with a high probability of being useful and to record the large amount of data measured by the apparatus in an easily accesible from for later analysis. The electronics can be divided into two parts, one part which is basically computer independent that is primarily concerned with triggering, and the camac system which serves as an interface between the detector system and records it onto magnetic tape. The various parts of the electronics are shown

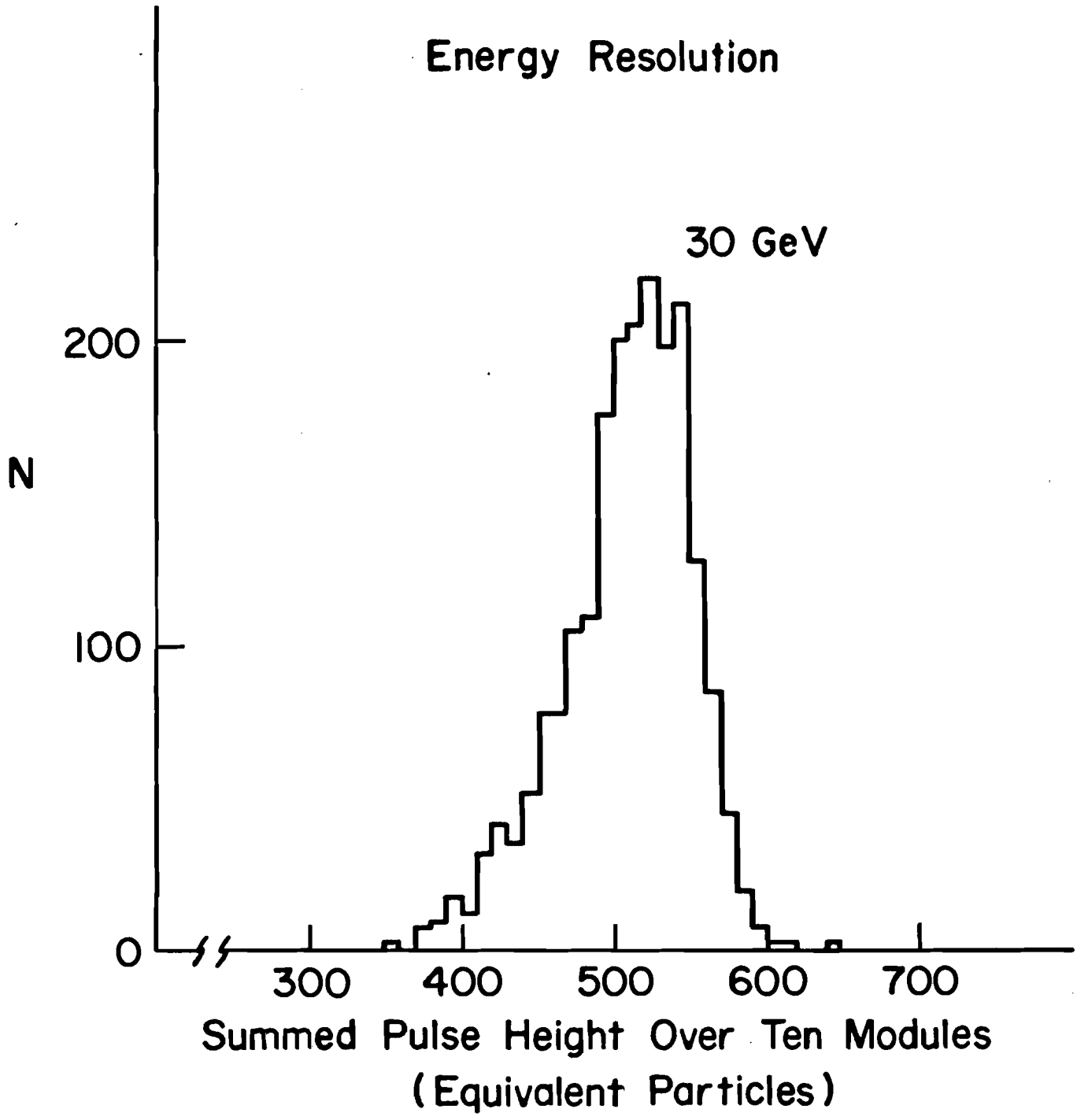

Fig. IV.14. Shower energy resolution for 30 GeV shower

E	$\int \pi(\varepsilon,t)dt$	σ_E	σ_E/E	a
10	184	17	0.092	.292
20	369	27	0.074	.330
30	555	26	0.046	.252

$$\frac{\sigma_E}{E} = \frac{a}{\sqrt{E}} \qquad \bar{a} = 0.29$$

Table IV.2. Energy calibration and resolution.

in Figures IV.15 to IV.18.

The pulse form each hodoscope counter is discriminated and latched (see Figure IV.15). The discriminated logic pulses from the counters within each bank are 'or'ed together to form logic pulses A, B, and C signifying a hit in hodoscopes A, B, and C, respectively. The logic pulses A, B, C, and other logic pulses are combined in various logical combinations to form trigger pulses such as $A \cdot B \cdot C$, $\overline{A} \cdot CH \cdot SC$, and $\overline{A} \cdot Maj$.

The chambers furnish information on the X and Y position of the electron shower and as an energy deposition measurement used in triggering (see Figure IV.16).

The output of the cathode amplifiers are logic pulses whose leading edge is time correlated with the position of the shower in the chamber and whose width is correlated with the width of the shower. A time to digital converter (TDC) digitizes the time between the arrival of this cathode logic pulse and a TDC stop pulse issued 680 nanoseconds after the trigger. The TDC also digitizes the width of the cathode logic pulse. The TDC has a range of 1000 nanoseconds and an accuracy of 1 nanosecond. If the TDC stop pulse does not occur within 1.2 microseconds after the arrival of the cathode pulse then the TDC resets itself and is ready to handle another cathode pulse. The TDC is capable of storing the results of only one digitization.

The anode pulses from the anode amplifiers are digitized by an analog to digital converter so that the pulse heights can be read out through the camac system. The amplified anode pulses from all the chambers are also input to a chamber trigger box. The chamber trigger box forms the analog sum of the anode pulse heights of all possible groups of six consecutive chambers. If one of these summed pulse heights is above the

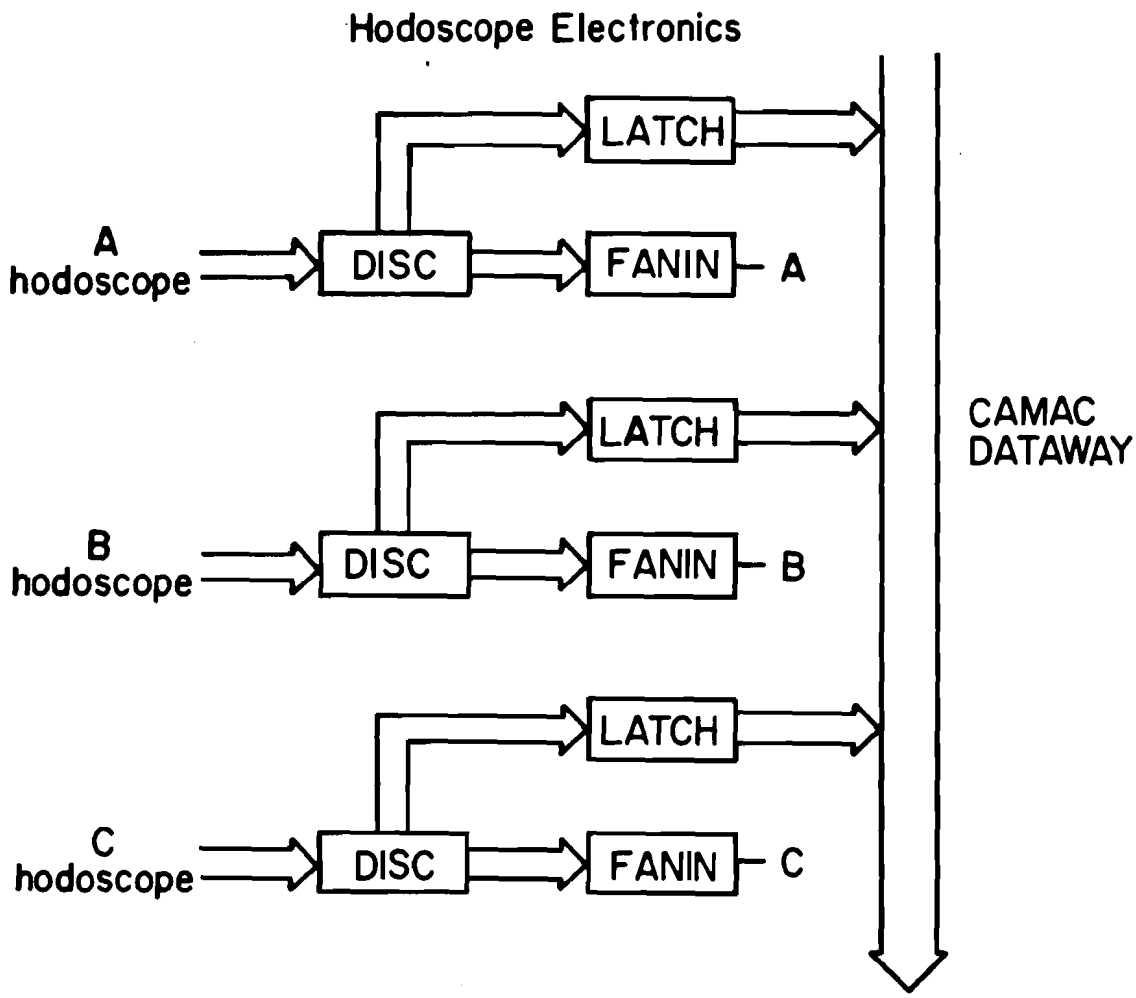

Fig. IV.15. Schematic diagram of hodoscope electronics

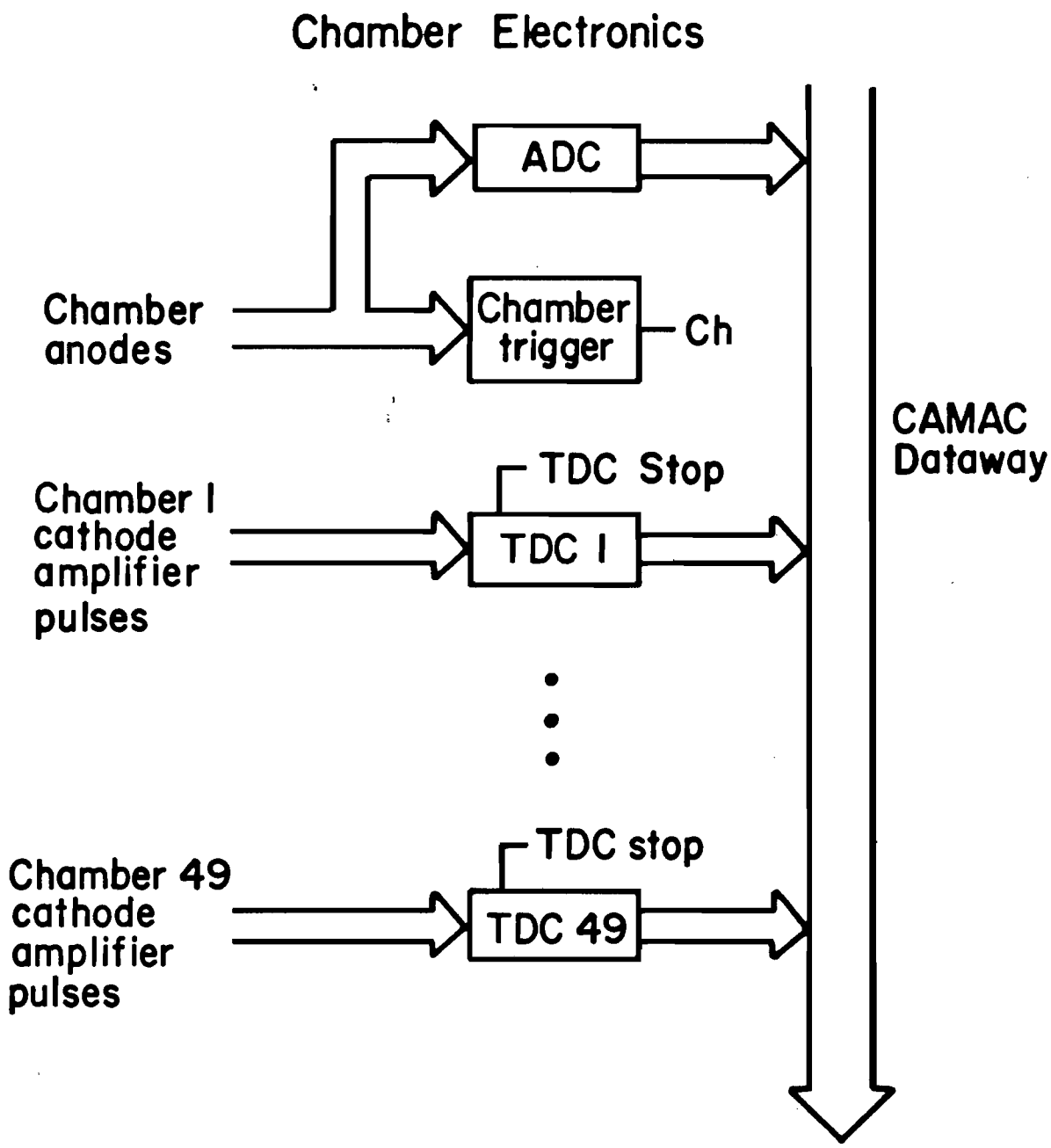

Fig. IV.16. Schematic diagram of chamber electronics

trigger level then a chamber trigger (CH) is issued.

Each module contains two scintillators of dimensions 21.5" x 43" mounted side by side (see Figure IV.17). The outputs of the two phototubes are added and then split at the mixer/splitter. One of the summed outputs goes to a x10 amplifier and then to an ADC. This ADC is sensitive to pulse heights near minimum ionizing. Another discriminated output of the amplifier goes to a majority trigger system. This trigger is determined by an integer M. If the number of modules sensing at least a minimum ionizing particle is greater than or equal to M then the majority trigger is issued.

The other output of the mixer/splitter goes directly to an ADC and a scintillator trigger box. This trigger box examines all groups of four consecutive scintillators. If each scintillator in the group has a pulse height above threshold, then a scintillator trigger results.

EXPERIMENTAL TRIGGER

Since the radiation length of aluminum is a factor of three smaller than the interaction length, electromagnetic showers will deposit their energy over a much shorter distance than will hadronic showers. An energy deposition trigger which requires a large amount energy per unit length will be more efficient on electromagnetic showers than hadronic showers. The main trigger used during the data taking runs required a coincidence between the chamber and scintillator trigger in anticoincidence with the front veto wall ($\bar{A}\cdot Ch\cdot Sc$) (See Figure IV.18). The chamber trigger discriminates on the sum of the pulse height of six consecutive chambers and the scintillater trigger requires four consecutive scintillators to have a pulse height above threshold. Low energy hadronic showers without an electromagnetic shower from π^0 decay have a low

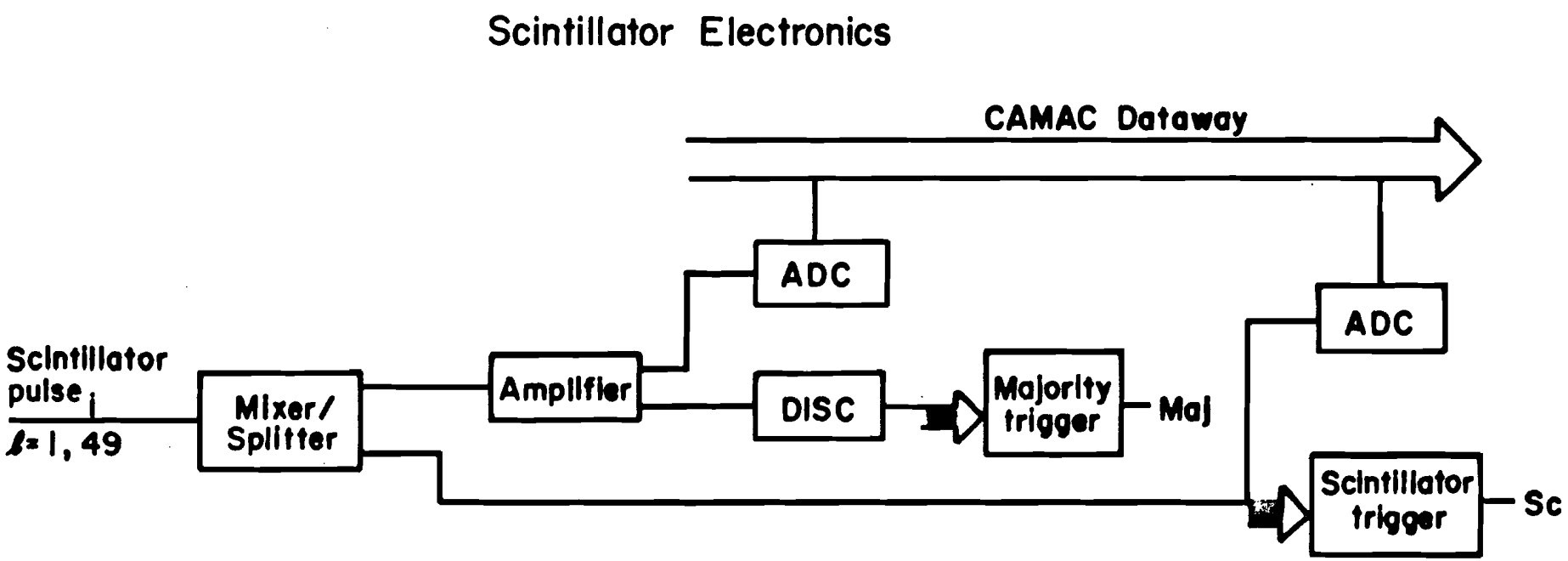

Fig. IV.17. Schematic diagram of scintillator electronics

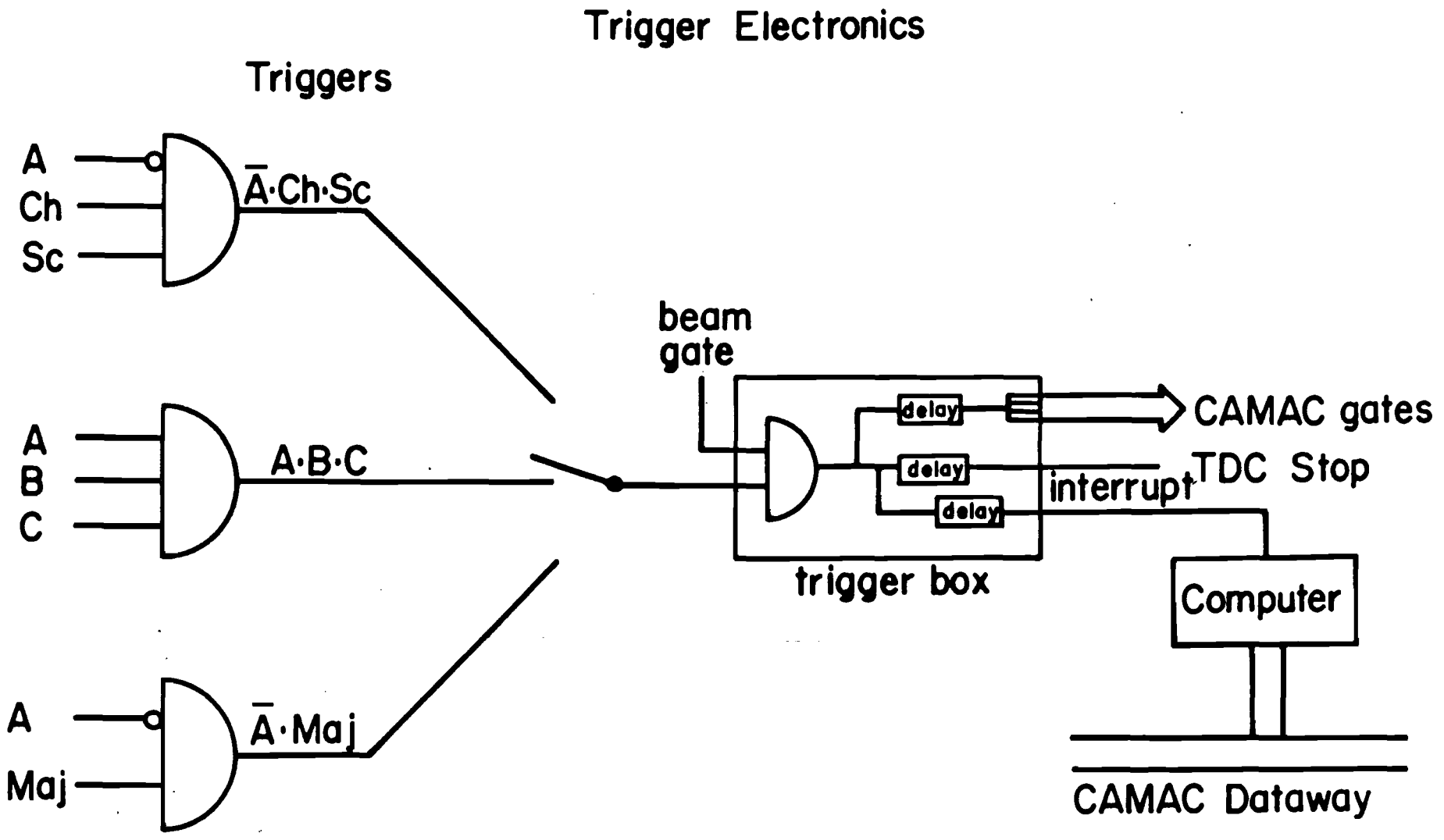

Fig. IV.18. Schematic diagram of trigger electronics

probablity of satisfying this trigger.

Other useful triggers are the coincidence of A, B, and C ($A \cdot B \cdot C$) as a trigger on incoming muons and the anticoincidence of A and Majority ($\overline{A} \cdot MAJ$) which is useful as a low energy neutrino trigger. The muon trigger was used to determine the lateral alignment of the chambers and as a pulse height standard used to calibrate the calorimeter. The low energy threshold neutrino trigger was used to determine the incident neutrino flux below 50 GeV.

If the preselected trigger is coincident with the beam gate signifying that a beam spill has occurred then the data recording process is initiated. The master trigger box issues camac gates to the ADC's, scalars, and latches. The TDC stop pulse is issued 680 nanoseconds after the trigger. A computer interupt is also issued notifying the computer to prepare to read the camac modules. At the end of the beam spill the computer reads the camac modules, formats the data and writes the data to magnetic tape.

The energy level of the $\overline{A} \cdot Ch \cdot Sc$ trigger is solely determined by the scintillator threshold level. The chamber threshold is much lower as is evident from the fact that the chamber trigger rate is a factor of 100 greater than the scintillator rate. By simultaneously inputing a test pulse to both the scintillator trigger box and the direct ADC while increasing the pulse amplitude from below until a trigger was obtained, the scintillator trigger level was found to correspond to channel 20 in the direct ADC. From the calibration discussed in Appendix IV.3 channel 20 corresponds to 4 equivalent particles. As an examination of Figure IV.11 will show, a two or three GeV electron shower energy will trigger at this threshold. In the data analysis an energy cut of four GeV was used in order to insure a high efficiency.

ONLINE PROGRAM

Due to the large amount of data and the high rate at which it becomes available, it is essential that the detector be computer controlled. The computer performs three functions, to read and record the data from the detector onto magnetic tape, to monitor the operation of the detector and notify the operator of equipment failures, and to graphically display the events.

The main purpose of the computer is to read and store the data from the detector. At the end of each beam spill the camac scalars are read and cleared. If no trigger occurs during that spill then only a scalar record is written to tape. If a trigger did occur, then the ADC's latches, and TDC's are also read and cleared and a complete data record written to tape.

In addition to the full data records and scalar records, the computer also writes a monitor record to tape. After every fiftieth spill and before the next splill a test pulse is sent to the TDC's and camac gates to the ADC's. The ADC contents consist of just the ADC pedestals since no inputs occur during this time. The TDC results can be used to monitor the TDC calibration during the run. The computer also monitors the status of the detector by checking the camac system status after every read operation. If a camac error occurs then a message to that effect is displayed on the system console so that the operator can correct the problem.

The computer also monitors the performance of the detector by keeping a running histogram of the digitized phototube pulse heights. At the end of each run the histograms are printed out and checked. If the gain of a phototube changes then the histogram distribution will change. The

phototube gains were constantly monitored and manually kept stable throughout the data taking period.

If the program is in the display mode, then after a trigger, the data is decoded and displayed graphically. The TDC information is partially reconstructed and the X and Y positions of the chamber hits displayed. Also displayed graphically are the direct and amplified scintillator ADC pulse heights. The display is a useful way to monitor the running conditions and performance of the detector.

REFERENCES FOR CHAPTER IV

1. T. Nunamaker, R. Heisterberg, and L. Mo, Nuclear Instruments and methods, 175, 331 (1980).

2. B. Rossi, High Energy Particles, Prentice Hall, Inc., New Jersey, P 214-299 (1952).

3. W. Heisenberg, Cosmic Radiation, Dover Publications, New York, P 11 (1946).

APPENDIX IV.1

DETERMINATION OF CHAMBER CONSTANTS

Velocity $\underline{\beta}$

Consider first the determination of the delay-line pulse velocity β. Each cathode amplifier has a test point which is coupled directly to the tap point on the delay-line. The test point can be used to examine delay-line pulses entering the amplifier and to insert test pulses onto the delay-line. See Figure AIV.1 for a schematic diagram of the test procedure used to measure the pulse velocity. A test pulse is input at the test point of amplifier A. This pulse will travel on the delay-line to amplifier B. It will also immediately trigger amplifier A. Amplifier A will send a logic pulse to the TDC through cable A which starts the TDC. When the pulse traveling on the delay-line reaches amplifier B, a logic pulse will be sent on cable B to stop the TDC. Since the lengths of cable A and B are identical, the time digitized by the TDC is the transit time of the delay-line pulse between tap points. The pulse velocity is defined by:

$$\beta = \frac{d}{t_d} \qquad \text{(AIV-1)}$$

The parameter d is the lateral distance between tap points (25.3 CM) and t_d is the digitized time. The actual conducting path distance is much greater than d due to the zig-zag nature of the delay-line.

This procedure gives a pulse velocity between every pair of tap points, so that a velocity can be assigned to every tap point. The

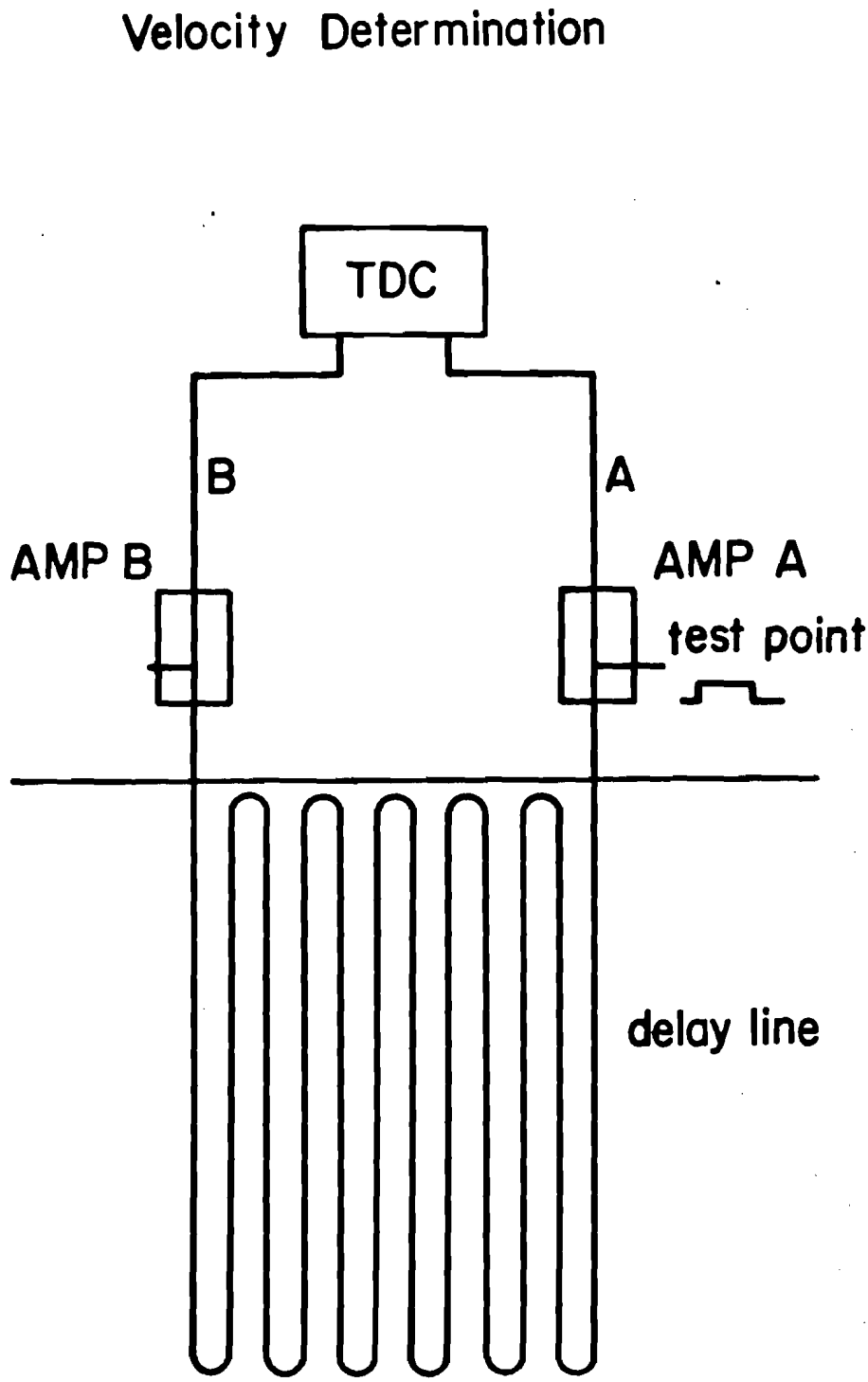

Fig. AIV.1. Schematic diagram of velocity calibration run

velocity assigned to the middle taps is the average of the velocity of a pulse approaching from the left and from the right. The typical pulse velocity along the delay-line zig-zag is 0.9c. This corresponds to a transit time between tap points of 480 nanoseconds.

TOF

Through the process of trial and error a nominal set of TOF constants were determined which gave good reconstruction efficiency on muon tracks. These constants were refined using shower data where the electron shower overlaps a tap point. If a shower overlaps a tap point, then the propagation time of the delay-line pulse to that tap point will be zero. Since the pulse propagation time is equal to (TOF-t_d), the TOF constant will equal the digitized time.

As a further refinement, the TOF constant can be made a function of the rise time of the delay-line pulse. The rise-time will be related to the width of the pulse. The TOF constants were fit to the formula:

$$TOF = a_o - b_o e^{c_o|w_d|} \qquad \text{(AIV-2)}$$

The parameters a_o, b_o, and c_o are constants and w_d is the digitized pulse width. A TOF constant is defined for each tap point by letting the parameter a_o vary between tap points. The constants b_o and c_o are independent of the tap point. Typical values for a_o are 980 nanoseconds while b_o and c_o were determined to be 50 nanoseconds and -7.5×10^{-3} nanoseconds^{-1}.

α

As discussed in Chapter IV, pulse attenuation and dispersion will cause a shift in the measured edge position relative to the true edge

position. The magnitude of this shift was determined by examining pulses which travel past two tap points. Suppose a shower occurs to the right of tap 3 (see Figure IV.2A). The left edge of this shower will be sensed by both tap 3 and tap 2. Pulse attenuation and dispersion will cause the edge positions as determined by these two taps to be slightly different. The difference in the edge position is shown in Figure IV.6. This shift can be corrected by assuming that the amount of shift is proportional to the travel time on the delay-line. The true travel time will then be:

$$t_t = t_m + \alpha\, t_m \qquad \text{(AIV-3)}$$

t_t = true travel time

t_m = measured travel time

α = constant

The parameter α was determined to be .06.

Combining all of these expressions into one formula gives a modified formula for computing the edge position from the digitized time and width.

$$x = x_{tap} \pm \beta[a_o - b_o e^{c_o|w_d|} - t_d]\,[1 + \alpha] \qquad \text{(AIV-4)}$$

The modifications in this formula over the expression given in Chapter IV give a correction to the shower centroid of typically a few millimeters.

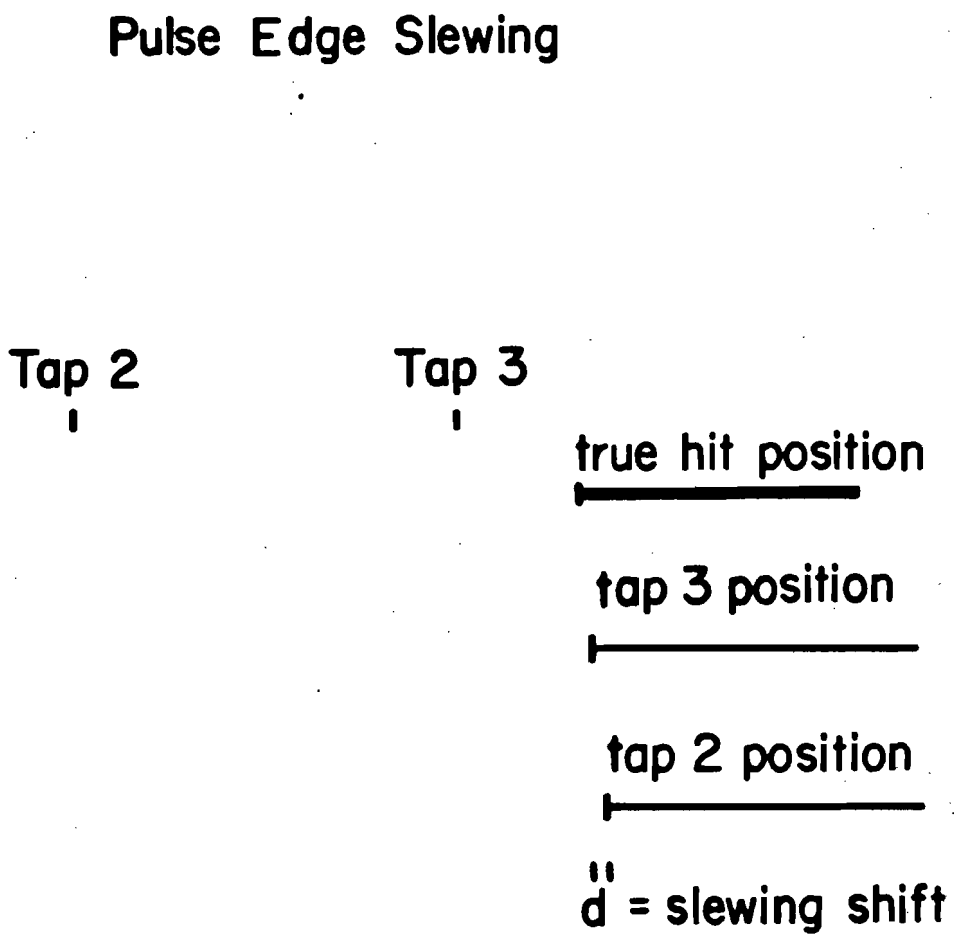

Fig. AIV.2. Schematic diagram of pulse edge slewing

APPENDIX IV.2

ENERGY CALIBRATION AT THE EXPERIMENTAL SITE

The calibration in the electron test beam furnished the relationship between the summed equivalent particles in the shower and total incident energy (see Figure IV.13). In order for this calibration to be useful, the direct scintillator ADC's for the complete detector at the experimental site must be calibrated in terms of equivalent particles.

An equivalent particle is defined as the scintillation pulse height recorded in the direct ADC's as a minimum ionizing particle passes through the detector. A calibration run was performed triggering on muons with the A.B.C trigger. Previous to this run the scintillator phototube gains were set approximately equal by demanding that the detector trigger uniformly on cosmic rays using the SC trigger. The calibration run gave the average muon pulse height in the amplified ADC's for each module. The direct scintillator ADC's do not have the dynamic range to respond to a single minimum ionizing particle. The corresponding pulse height in the direct ADC's can be found if the relative gain of the direct and amplified ADC's is known.

The relative gains were determined using a test pulse and a variable attenuator. The test pulses of variable amplitude were input to the direct and amplified ADC's to obtain a calibration relating the input amplitude to recorded channel number.

$$ch_d = r_d(ph) \qquad ch_a = r_a(ph) \tag{AIV.2-1}$$

ch_d = channel number in the direct ADC's

r_d = relationship between the input pulse height and direct ADC channel number

ch_a = channel number in the amplified ADC's

r_a = relationship between the input pulse height and amplified ADC channel number

ph = input pulse height

Typical calibration curves are shown in Figure AIV.3

If the average channel number for a minimum ionizing pulse height is ch_a in the amplified ADC's, then the input signal pulse height is $r_a^{-1}(ch_a)$ = ph. The corresponding channel number in the direct ADC's will be $ch_d = r_d(r_a^{-1}(ch_a))$. This constant gives the conversion from direct ADC channel number to equivalent particle pulse height.

The deposited energy is then determined from Figure IV.13.

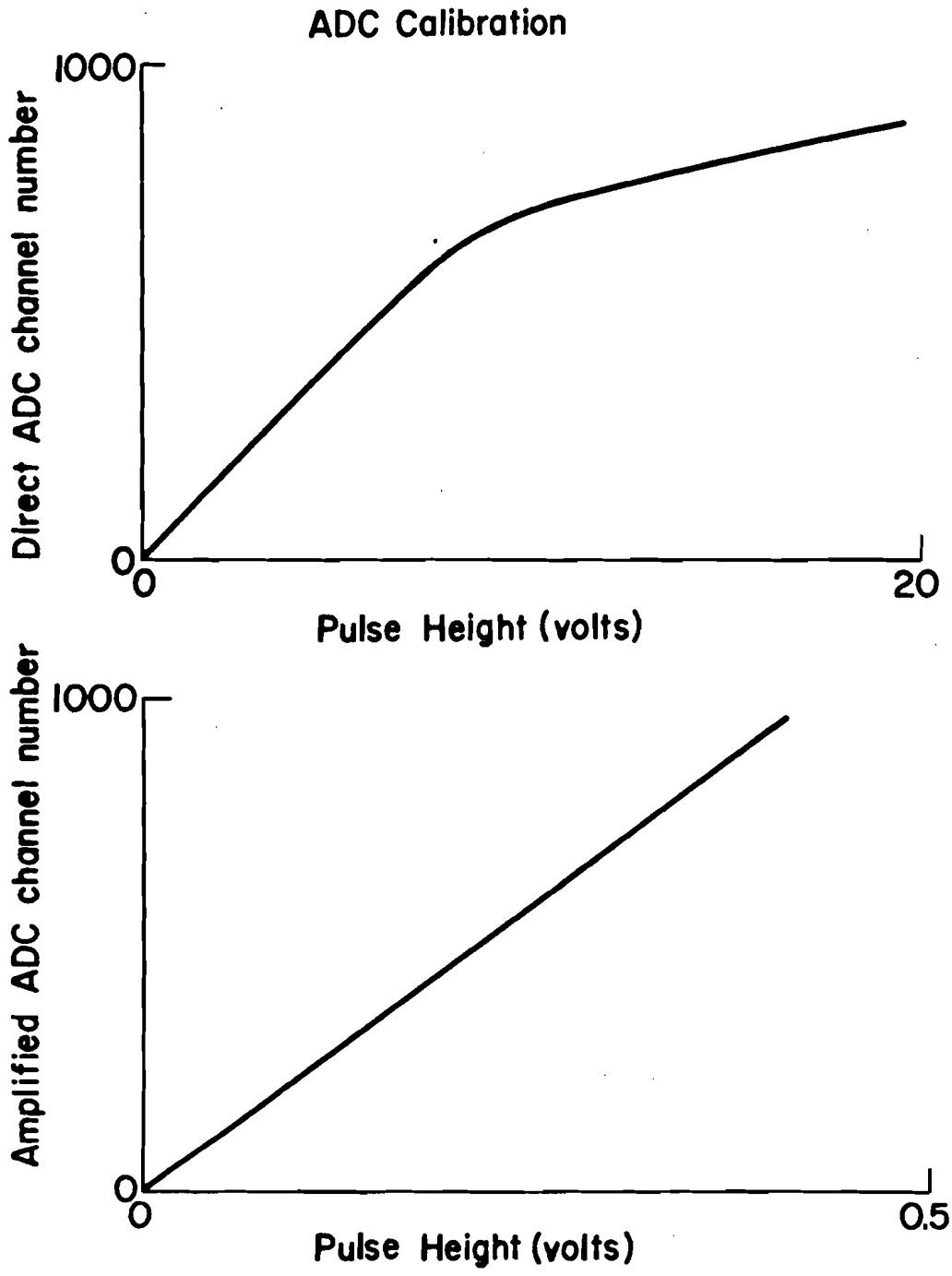

Fig. AIV.3. Examples of scintillator ADC calibration

APPENDIX IV.3

ELECTRON ENERGY RESOLUTION

A second electron beam test was used to determine the calorimeter energy resolution. Electrons of energy 10, 20 and 30 GeV were incident on 10 fully instrumented modules. The gains of the scintillator phototubes were set approximately equal using the minimum ionizing energy deposited by the incident muons. Before the event energy and calorimeter resolution could be determined, the exact relative phototube gains must be known.

The electron shower development curves were determined in a previous electron test. This test gave the mean number of equivalent particles in the shower at a depth of t radiation lengths resulting from an incident electron energy E. Let ep_j^ε be the mean equivalent particle pulse height in a shower of energy ε in the jth module. Let ch_{ij}^ε be the measured ADC pulse height in channel numbers from an incident electron energy ε for the ith event in the jth module. The relative gain factor α_j^ε is defined by:

$$ep_j^\varepsilon = \left(\frac{1}{N}\sum_i ch_{ij}^\varepsilon\right)\alpha_j^\varepsilon \qquad \text{(AIV.3-1)}$$

N is the number of events.

The energy of event i is given by:

$$E_i = \sum_j ch_{ij}\alpha_j \qquad \text{(AIV.3-2)}$$

Figure IV.14 is a histogram of the computed energy for events from an incident 30 GeV electron. The low energy tail results from the leakage

of energy out the back of the detector. The standard deviation of the distribuiton in the limit of full containment was determined by measuring the half width at half maximum on the high energy side of the observed distribution. For Gaussian distributions the half width is related to the standard deviation by the factor .588. The computed standard deviations are summarized in Table IV.2.

CHAPTER V

NEUTRINO FLUX

The spectra of the secondaries resulting from the proton interactions with the neutrino area target have been measured by Stefanski and White and fit to the following formula[1]:

$$\frac{d^2N}{dpd(\cos\theta)} = ABC^2p^2T/(10.E) \qquad A,B,C_o \text{ are constants}$$

$$C = C_o - 1.43e^{x-2x^2/3} \qquad T = e^{-Bx - c(p\sin\theta)}$$

θ = production angle $\qquad$ p = secondary energy

x = p/E $\qquad$ E = incident energy

Values of A, B, and C_o were determined for π^+, π^-, K^+, and K^- independently. These spectra are then input to the program NUADA[2] which traces the path of the secondary particles through the horn and into the decay region where they are allowed to decay. The energy distribution of the neutrinos resulting from these decays is then calculated. Figure V.1 shows the computed energy distribution of the muon neutrinos and antineutrinos incident on the detector. Previous experiments have shown that this calculation underestimates the flux of neutrinos below 50 GeV. A modified version of NUADA modeling the narrow band focussing system rather than the horn, when compared to the narrow band data, shows that the program correctly predicts the neutrino flux above 50 GeV and underestimates the flux below 50 GeV.[3] The results of the NUADA calculation are, therefore, not completely useful as a determination of the incident neutrino flux. It does serve two useful purposes however. It gives an accurate determination of the neutrino flux

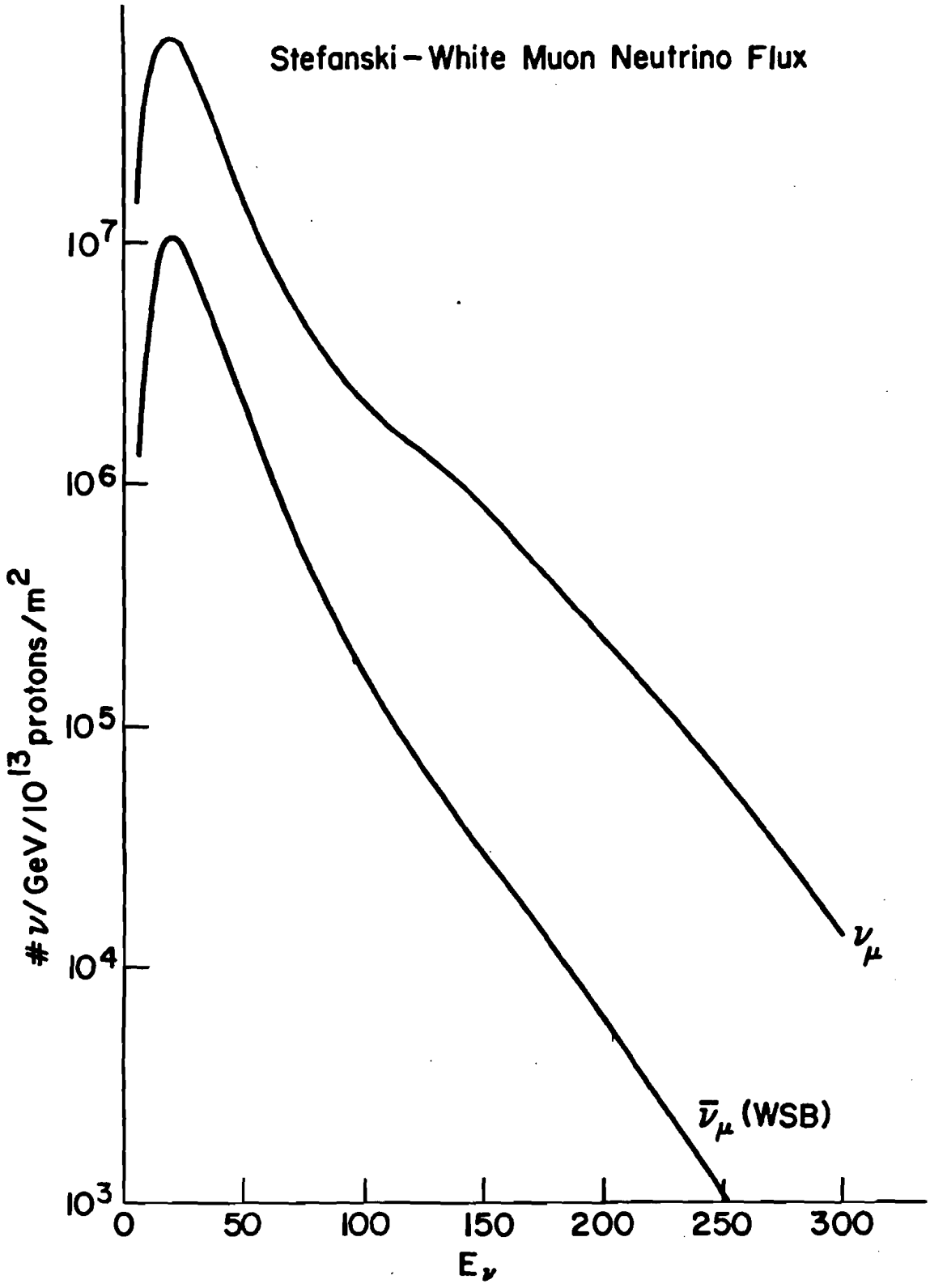

Fig. V.1. Results of NUADA neutrino flux calculation

above a neutrino energy of 50 GeV and, in our experimental determination of the low energy flux, we assumed that NUADA correctly predicts the ratio of the neutrino to antineutrino flux at all energies.

In order to determine the neutrino flux below 50 GeV, data was taken with a low energy threshold trigger. The trigger was $\overline{A}\cdot$MAJ (See Chapter IV for details of the trigger and apparatus). This trigger consisted of a veto from the front wall hodoscope and a Majority trigger requiring 12 out of the first 32 modules to have a pulse height greater than or equal to minimum ionizing. The vertex was required to be in the first 20 modules to minimize the number of muon triggers from background muons passing through the rear of the detector and thus improve the trigger dead time. See Table V.1 for a summary of the flux determination runs.

The analysis of these events was relatively straightforward. An offline analysis program displayed the X and Y hit positions and the longitudinal energy deposition of the trigger on an interactive graphics terminal. For details of the event reconstruction and an example of the event display see Chapter VI. A physicist scanned each event display rejecting the muon induced and cosmic ray triggers. The X and Y positions of the vertex for each neutrino event was marked using an interactive cursor. Both neutral and charged current events were accepted. The result of this analysis was the contained energy distribution of the neutrino nucleon events for fiducial cuts of $|x| < .4$m, $|y| < .4$m and $|x| < .3$m, $|y| < .3$m.

The neutrino flux was determined through the use of a Monte Carlo calculation. Given an input neutrino flux, the Monte Carlo modeled the neutrino interactions and predicted the observed hadronic shower energy. The flux was adjusted until the predicted shower energy distribution

Ā·Maj Running

total triggers	7127
total sem	1.37×10^{17} protons
dead time	61%
# ν Events	1829

Table V.1. Summary of Ā·Maj running

agreed with the measured distribution.

The Monte Carlo program first randomly selects the incident neutrino energy from the input neutrino flux. The energy of the hadron shower is determined from the $d\sigma/dy$ cross section:

$$\frac{d\sigma}{dy} = \frac{G^2 M E_\nu}{2\pi} [C_L + C_R (1 - y)^2] \qquad \text{(V-2)}$$

The constants C_L and C_R are measured experimentally by a CERN collaboration to be 0.85 and 0.15 respectively[4]. Once the energy is determined the angle of the shower for that event is set by the $d\sigma/dx$ distribution with $x = -q^2/2m\nu$. The experimentally observed distribution is[5]:

$$\frac{d\sigma}{dx} = \propto x^{1/2} (1 - x)^3 + .27(1 - x)^{8.5} \qquad \text{(V-3)}$$

The variable x is determined by first finding the kinematically allowed region for x given the neutrino energy and hadron shower energy already determined and then randomly selecting x from (V-3) subject to the kinematic constraints. The results of the Monte Carlo are insensitive to changes of ±1 in the x distribution exponents.

The vertex is assumed to be uniformly distributed in the volume defined by $|x| < .50$m, $|y| < .50$m, and z in modules 2 to 20. The individual hadrons in the shower are generated using Feynman-Field fragmentation functions[6] with a $p_T \propto e^{(-6m_T)}$. The event will trigger the detector if at least one charged particle from the vertex, either the muon, if the event is a charged current, or a particle in the hadron shower, traverses 12 modules.

Once the Monte Carlo event has passed the fiducial cuts and the trigger cut then the observed energy is computed. Several corrections to the kinematic hadron energy must be made to account for leakage out of

the detector, for hadronic calorimeter effects and for the energy resolution. The Harvard, Pennsylvania, Wisconsin, and Fermilab group has published leakage curves for hadronic showers.[7] These results also agree with a measurement by the Caltech-Fermilab group[8]. Given a shower of energy E and a detector of length z this curve gives the average fraction of the total energy contained in the calorimeter. This curve (see Figure V.2) was used to correct for leakage of the hadronic shower out the rear or sides of the detector.

The calorimetric response to this energy deposition will depend on how much of the energy ends up in ionization and on the spatial distribution of the ionization. The calorimeter was calibrated using electron showers. In electromagnetic showers essentially all of the incident energy ends up in the form of ionization. Since the light output of the scintillator depends directly on the ionization, the total energy will be proportional to the summed scintillator pulse heights (neglecting possible saturation effects). In hadronic showers only a fraction of the total energy is lost to ionization. Some of the incident energy is lost in nuclear binding energy, in the rest mass of stable particles, or in energy carried off by neutrinos or muons resulting from unstable particle decays. On average the ionization energy will be some fraction less than the incident hadronic shower energy. This fraction was determined by demanding that the number of Monte Carlo events with observed energy greater than 50 GeV agree with the measured number. Since the Stefanski-White flux is known to be correct above 50 GeV, the uncertainties in the neutrino flux do not effect this determination. The correction factor was determined to be 0.68 using this method. This compares favorably with the measured values for other calorimeters

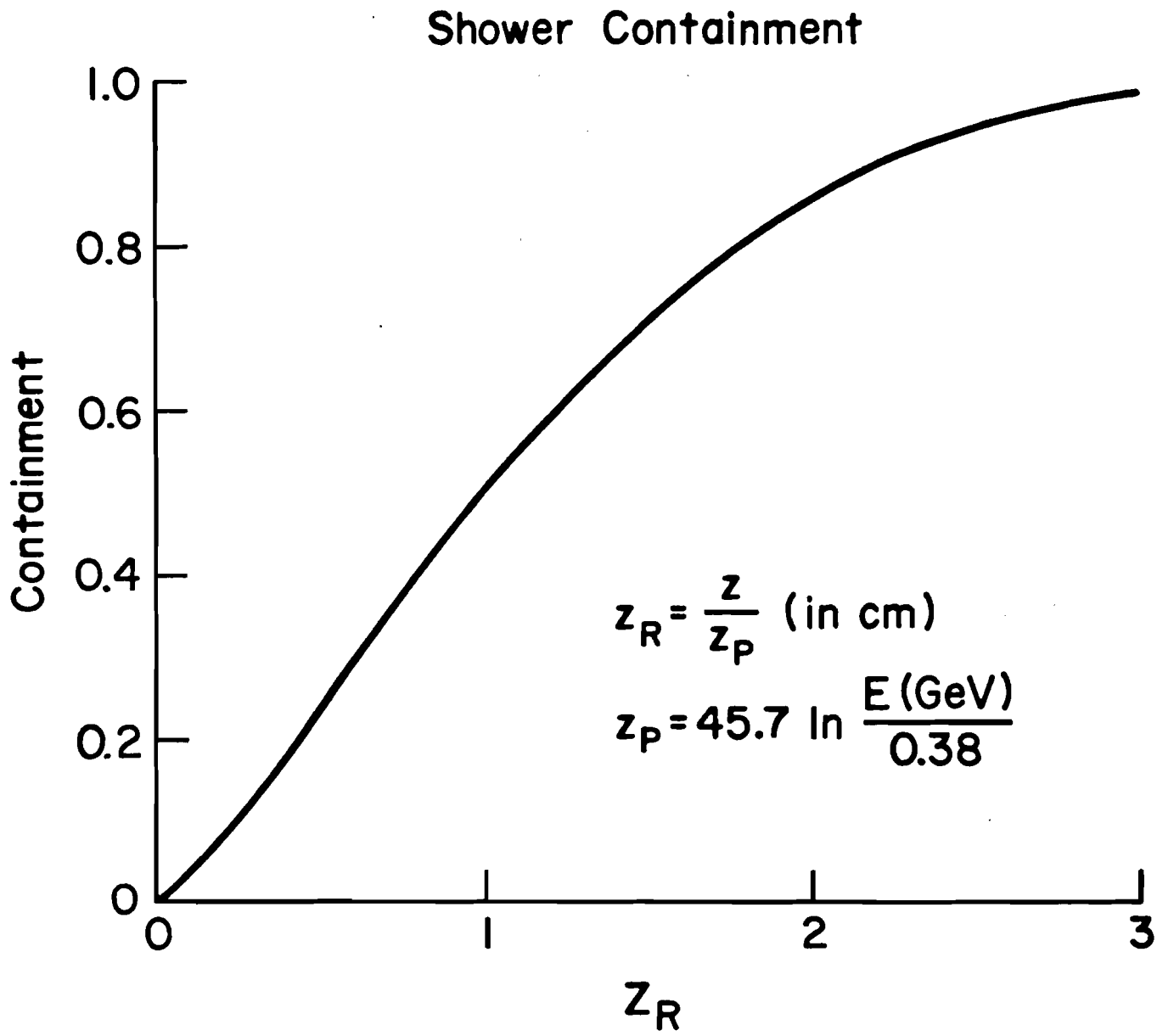

Fig. V.2. Hadronic shower containment curve

(see Table V.2). The contained energy is multiplied by this correction factor to obtain the deposited ionization energy.

In addition to this hadronic calibration factor one must take into account the energy resolution of the detector for hadronic showers. Since the calorimeter samples only a fraction of the total ionization, fluctuations in the energy deposition will lead to fluctuations in the measured energy. Hadronic showers can have additional fluctuations in the amount of the incident energy deposited as ionization. Typically the hadronic shower energy resolution is a factor of 2 worse than the electromagnetic shower energy resolution.[9] The hadronic energy resolution was assumed to be given by:

$$\frac{\sigma_E}{E} = \frac{.60}{\sqrt{E}} \qquad \text{(V-4)}$$

To summarize, the observed energy is computed by first correcting the kinematic hadron energy for possible leakage out the back or sides of the detector. The contained energy is then multiplied by the hadronic energy correction factor to obtain the deposited ionization energy. The program then randomly selects the predicted observed energy from the ionization energy taking into account the energy resolution of the detector. If the event is a charged current then the energy deposited by the muon (0.05 GeV/module) is also included in the total observed energy.

The Monte Carlo models both charged and neutral current contributions as well as neutrino and antineutrino contributions. In the data it is not possible to determine the identity of the incoming neutrino (neutrino or antineutrino) which initiates the hadron shower. One, therefore, cannot determine seperately the neutrino and antineutrino incident flux

Calorimeter	Reference	Ionization Energy/ Total Energy
liquid Scintillator	Benvenuti[7]	0.8
Fe-plastic scin.	Sciulli[8]	0.7
Fe-liquid scin.	Baum[9]	0.7

Table V.2. Comparison of the ratio of deposited ionization energy to total incident energy for several calorimeters.

and is forced to make assumptions as to the relative amount of anti-neutrinos in the neutrino beam. If was assumed that the Stefanski-White flux correctly predicts the bin by bin ratio of the antineutrino to neutrino flux as a function of neutrino energy. This assumption was checked using the results from experiment 531 located immediately downstream from our detector.[10] They measured the ratio of the number of μ^+ to μ^- from their emulsion target and found:

$$R = N(\mu^+)/N(\mu^-) = 0.08 \quad E_\mu > 8 \text{ GeV}$$

$$= 0.08 \quad E_\mu > 12 \text{ GeV}$$

The Monte Carlo using the above assumption predicts the values of R to be .08 for $E_\mu > 8$ GeV and .09 for $E_\mu > 12$ GeV, in agreement with the E531 result.

Two fiducial cuts were applied to the data and Monte Carlo, one demanding that $|x| < .4$m $|y| < .4$m and the other $|x| < .3$m $|y| < .3$m. Both cuts also required the vertex to be in modules 2 to 20 inclusive. The magnitude of the neutrino flux for neutrino energies below 50 GeV was then adjusted until the predicted hadronic energy distribution matched the measured distributions. The final corrected flux is labeled N in Figure V.3. The Monte Carlo prediction and the data with .40m fiducial cut are shown in Figure V.4. The Monte Carlo prediction for the fiducial cut of .30m is shown in Figure V.5. The Monte Carlo prediction follows the data fairly well for both fiducial cuts. The H and L flux in Figure V.3 represent high and low estimates of the incident flux. Flux H was found by adjusting the Monte Carlo prediction to the points one standard deviation above the data with the .40 fiducial cut. The L flux was found by fitting one standard deviation below the

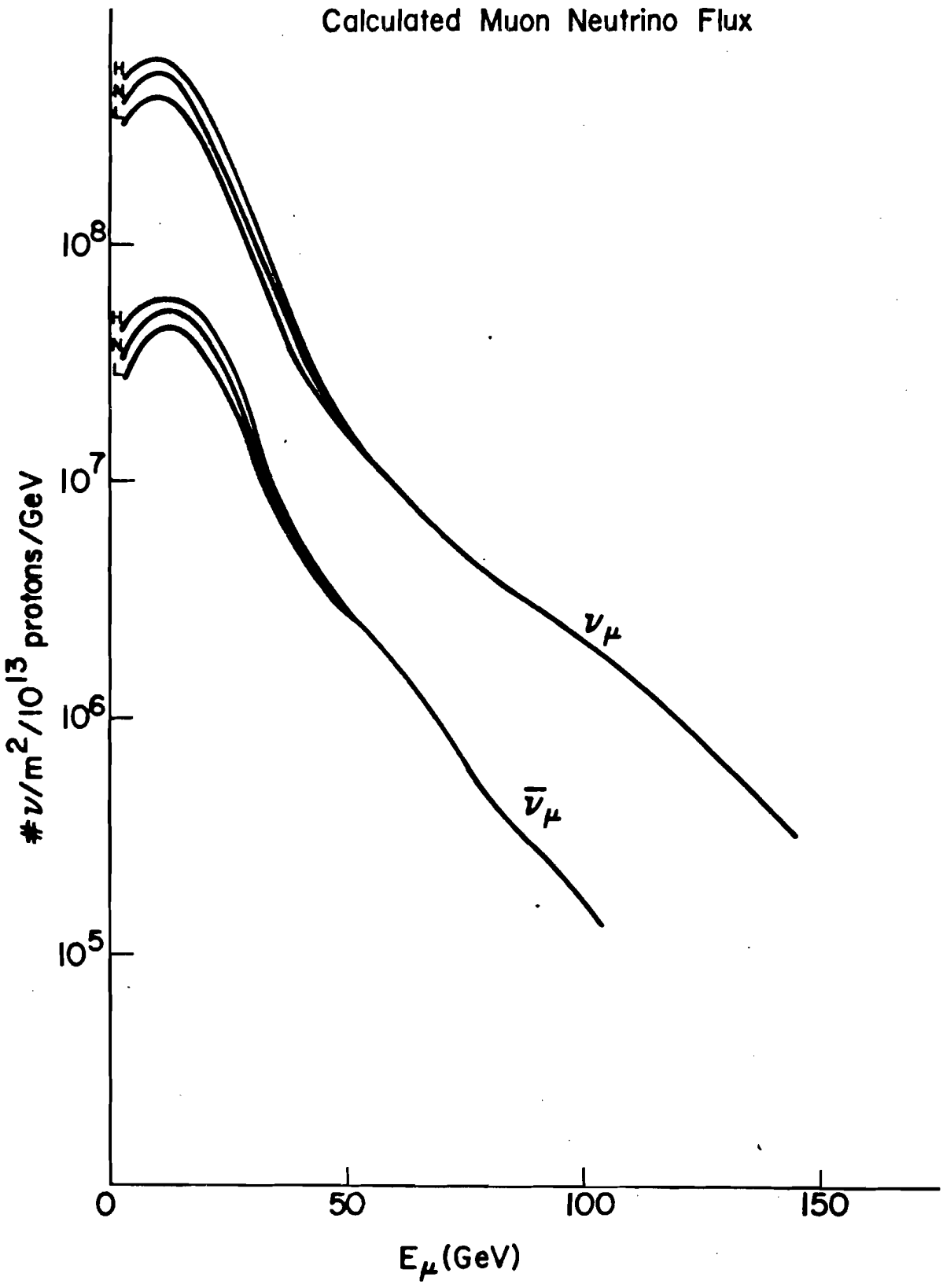

Fig. V.3. Calculated incident neutrino flux

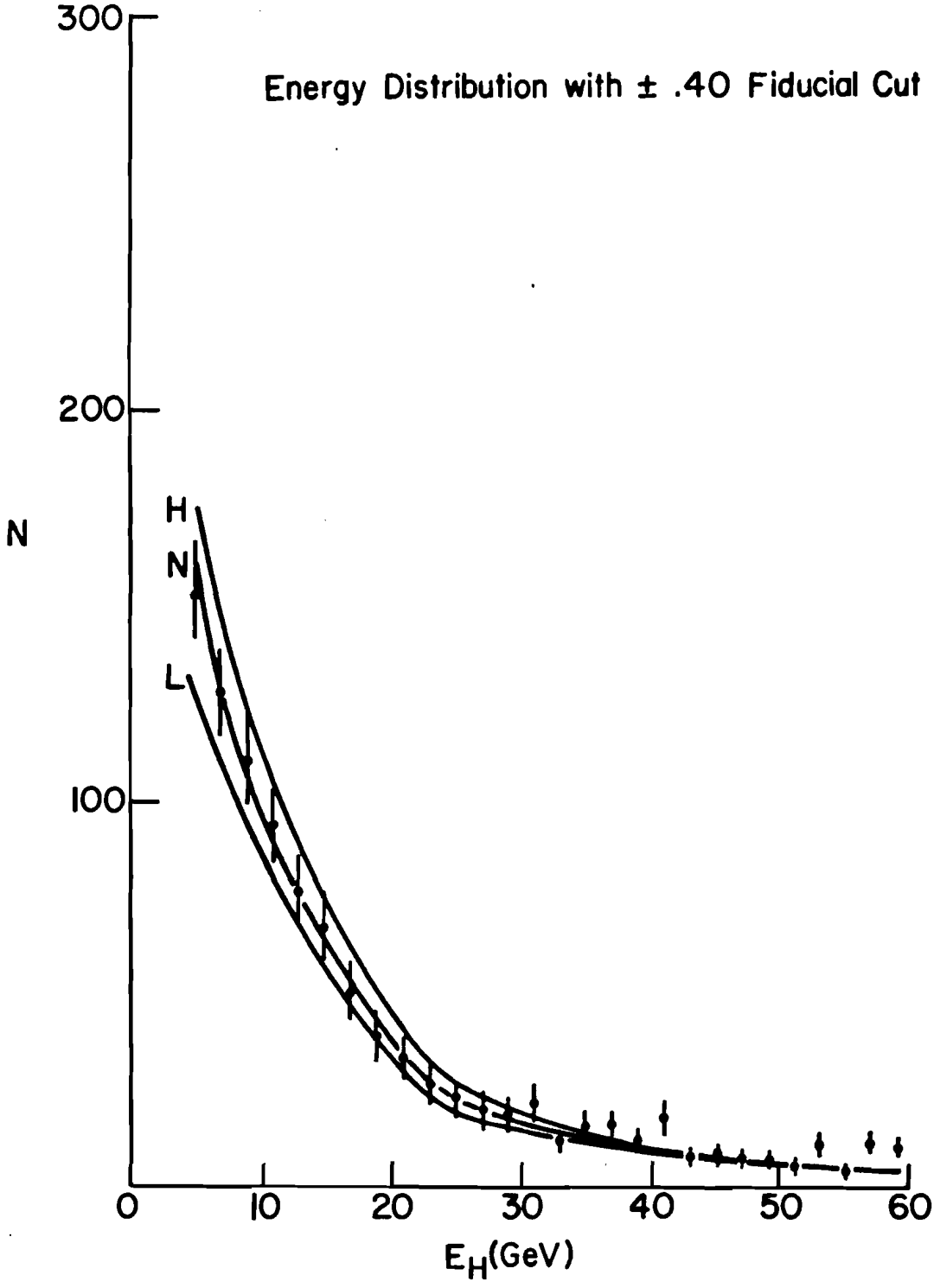

Fig. V.4. Energy distribution with ± .40 m fiducial cut

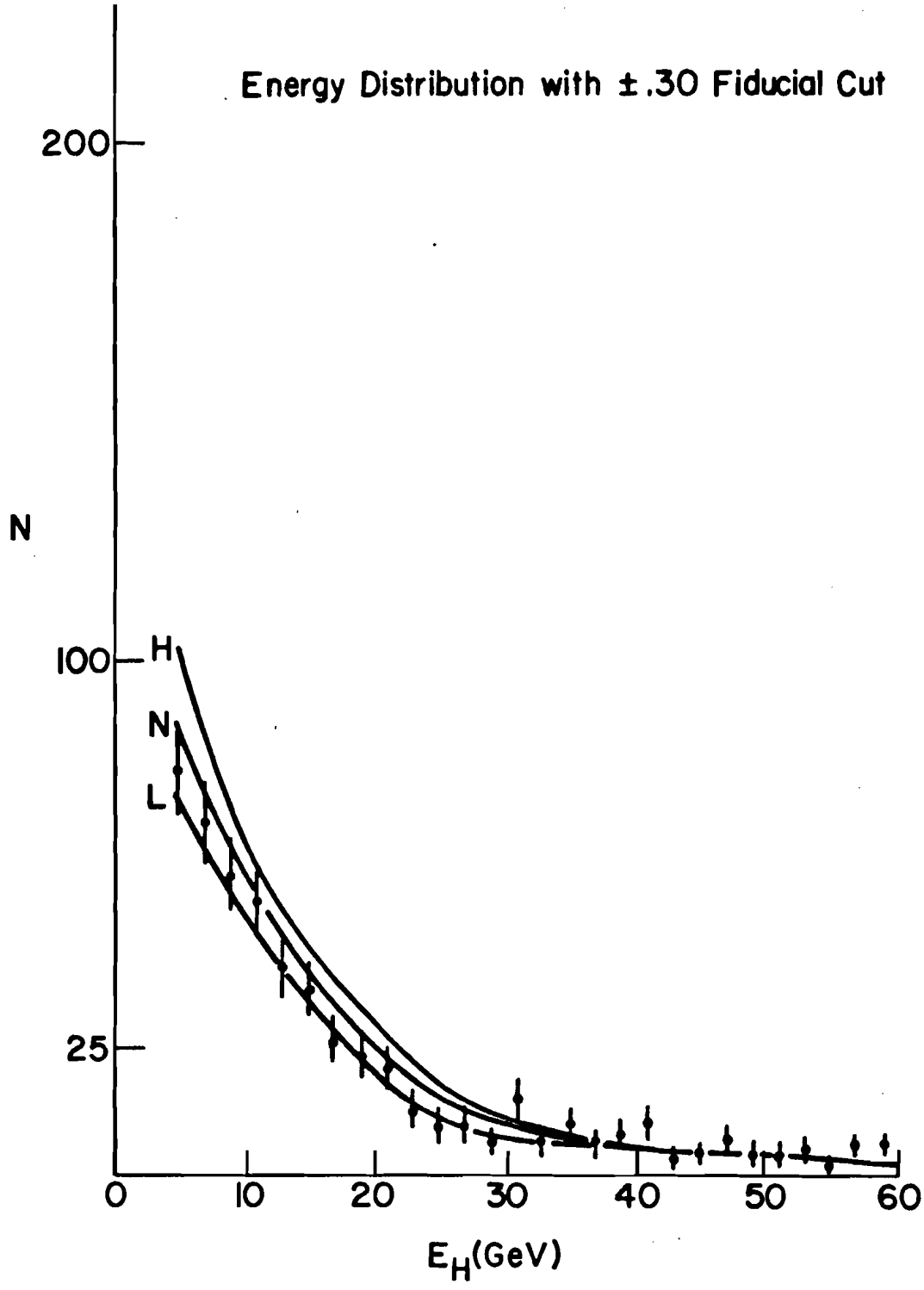

Fig. V.5. Energy distribution with ± .30 m fiducial cut

.30 fiducial cut data. The H and L flux represent a +10% and -14% error in the neutrino event rate (see Table V.3).

In order to estimate the systematic error in the corrected flux. The Monte Carlo prediction and the data were also compared with a fiducial cut at $|x| < .20$m and $|y| < .20$m. At this fiducial cut the uncertainties in the energy containment and triggering probability are minimized. The Monte Carlo predicted 276 events with hadron shower energy above 4 GeV compared with 290 ± 17 from the data. At an energy cut of 50 GeV the Monte Carlo predicted 25 compared to 32 ± 6 from the data. The Monte Carlo prediction and the data agree to within one standard deviation which represents a 6% error in event rate above 4 GeV and 20% error above 50 GeV. These errors can be compared to the H and L flux errors of 10% and 14% respectively. Both the H and L flux obviously disagree with the data below 40 GeV. The fact that the error with the 4 GeV cut is much smaller than the error with the 50 GeV cut may indicate an error in the flux shape as well as an error in the magnitude.

The error in the event rate due to uncertainties in the neutrino flux is estimated to be 15%. This nearly corresponds to the error using the H flux which is clearly too high. Since most of the events will be from neutrinos of an energy below 40 GeV, the fact that Monte Carlo was 20% too low above 50 GeV is not too important.

Figure V.6 shows the results of a Monte Carlo calculation done by the Fermilab Neutrino Department on the electron type neutrino flux. This flux is less than 1% of the muon neutrino flux.[11]

Fiducial Cut

	.40 m				.30 m				.20 m	
	data	N	L	H	data	N	L	H	data	N
E > 4	1068	1043	900	1151	581	618	538	692	290	276
> 40	147	140	140	140	86	83	83	83	50	37
> 50	100	99	99	99	58	62	62	62	32	25

Table V.3. Comparison of data and Monte Carlo results.

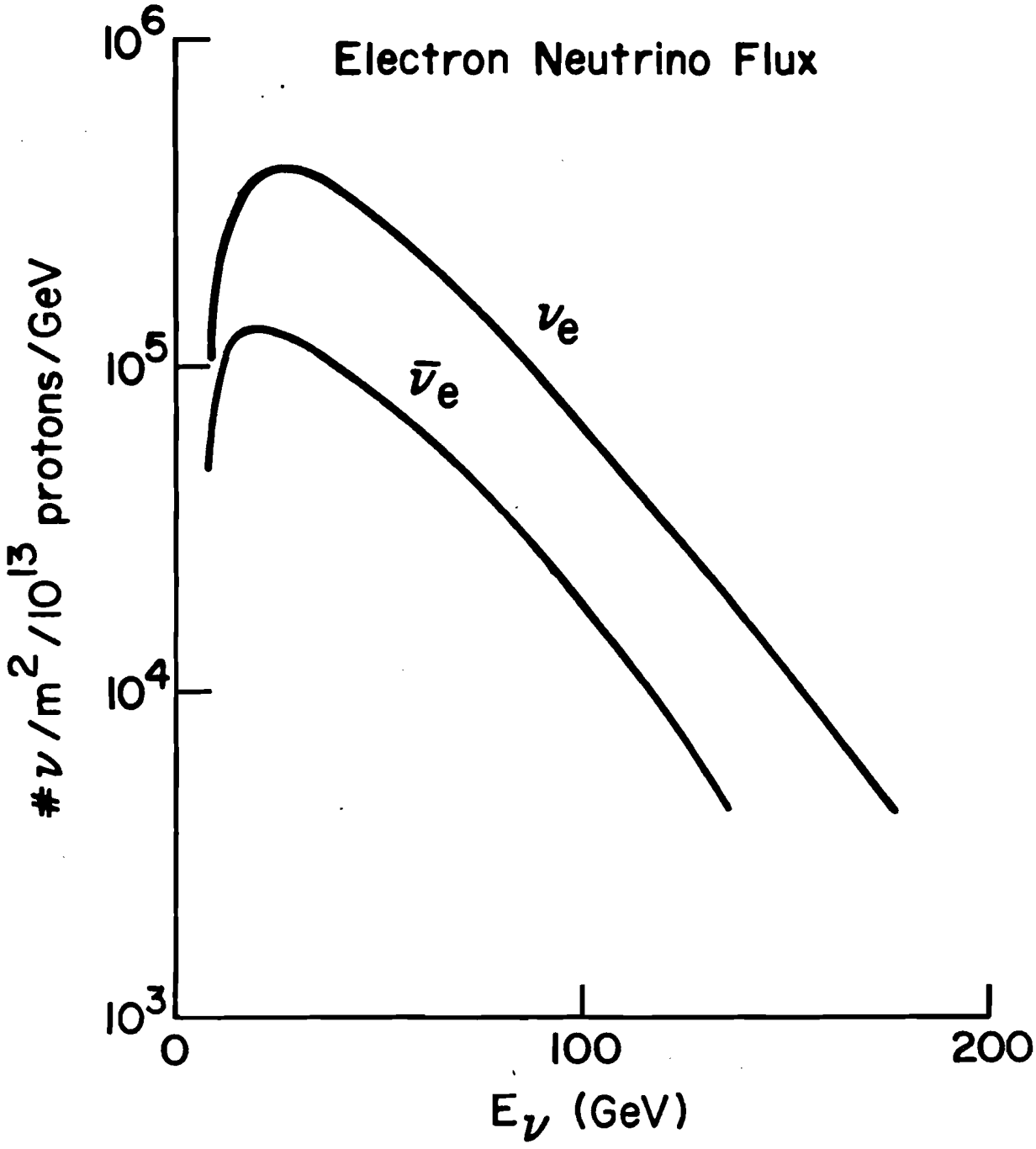

Fig. V.6. Incident electron type neutrino flux

REFERENCES FOR CHAPTER V

1. R. Stefanski and H. White, Neutrino Flux Distributions, FERMILAB Note FN-292, (1976).
2. D. Carey and V. White, Nuada, The FERMILAB Neutrino Flux Program, FNAL Computer Library, (1975).
3. R. Stefanski, FERMILAB Neutrino Department, private communication.
4. J. DeGroot, et al., Zeitschrift fur Physik C1, 143 (1979).
5. H. Wahl, Proceedings of the Neutrino 1979 Conference, Bergen, p. 335 (1979).
6. R. Feynman and R. Field, Nuclear Physics B136, 1 (1978).
7. A. Benvenuti, et al., Nuclear Instruments and Methods, 125, 447 (1975).
8. F. Sciulli, Proceedings of the Calorimetry Workshop, M. Atac, ed., FERMILAB, p. 79, (1975).
9. L. Baum, Proceedings of the Calorimetry Workshop, M. Atac, ed., FERMILAB, p. 295 (1975).
10. R. Sidwell, E-531, Private Communication.
11. S. Mori, Private Communication.

CHAPTER VI

EVENT REDUCTION

Since the cross section for neutrino electron elastic scattering is so much smaller than the cross section for the neutrino nucleon background processes, the overwhelming majority of the triggers are background and must be eliminated during the data analysis. Great care must be taken to insure that the cuts used to reject the background do not also reject the signal as well.

This chapter describes how the chamber cathode TDC information is used to reconstruct the position and angle of the shower. The distinguishing features of hadron showers and electron showers are used to develop a set of cuts which will eliminate much of the hadronic background. A conservative set of cuts if first implemented by the computer program to preselect a first pass sample. Displays of the preselected events are then scanned by a physicist implementing a tighter criteria to obtain the final data sample.

DATA TAKING

Data was taken at FERMILAB from November 1978 to March 1979. A total of $.95 \times 10^{19}$ 350 GeV protons were incident on the neutrino area target. This resulted in about 250,000 triggers.

About 190,000 of these events were analysed, corresponding to $.7 \times 10^{19}$ protons on target. See Table VI.1 for a summary of the data taking. The first part of the data was taken with the torroids off resulting in a much higher muon background flux. This represents about

	Torroids off running	Torroids on running	all running
number of runs	84	87	171
number of events	86K	103K	189K
total SEM	3.8×10^{18}	3.9×10^{18}	7.7×10^{18}
average deadtime	.39	.33	.36
average A.B.C. rate per 10^{13} protons	.22	.04	.13

Table VI.1. Summary of data taking.

45% of the data. The second part of the data was taken with the torroids on with the muon rates much lower. The total data sample analysed represents 171 runs with each run containing about 1200 events. The trigger dead times were calculated run by run with an average of about 40%. Almost all of the triggers represent neutrino induced events with less than 1% due to incident muons or cosmic rays. About a third are easily identifiable as charged currents because of the presence of a muon track.

Figures VI.I-3 show several event distributions from the raw triggers. The $\bar{A}\cdot Ch\cdot Sc$ trigger required a vertex before chamber 41. The resulting z distribution is flat from chambers 2 to 40. Chamber 1 has only 1 cathode plane causing the vertex finding algorithm to be inefficient at this chamber.

The energy distribution is shown in Figure VI.2. The dominate contribution to these distributions is from neutrino nucleon interactions. A Monte Carlo calculation of the energy distribution expected from this interaction is also shown in the figure. This calculation predicts the absolute number of events in a fiducial volume defined by $|X| < .5$m, $|Y| < .5$m, and $Z <$ module 41 without regard to any trigger requirements. The $\bar{A}\cdot Ch\cdot Sc$ trigger is efficient at rejecting these events below 12 GeV shower energy. Above 12 GeV the particle multiplicity is sufficiently high that at least one π° is probably produced directly or in subsequent hadronic shower interactions. The detector will trigger on the electromagnetic shower resulting from the π° decay . The trigger rejects about 60% of the $\nu_\mu N$ interactions.

Figure VI.3 shows the angular distribution of the raw triggers. The neutrino electron events are expected to be below 20 milliradians. Out

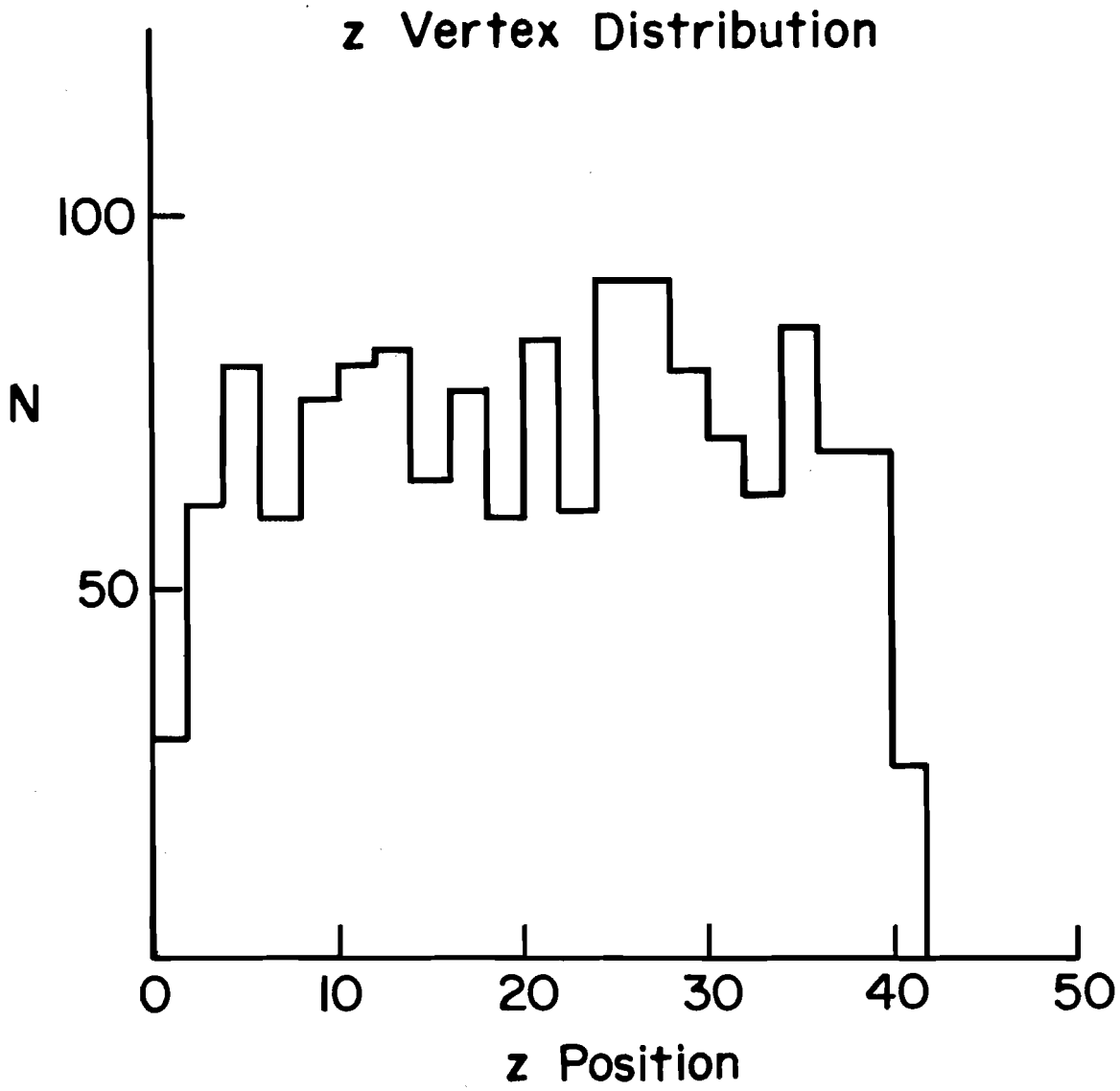

Fig. VI.1. Vertex distribution of the raw triggers

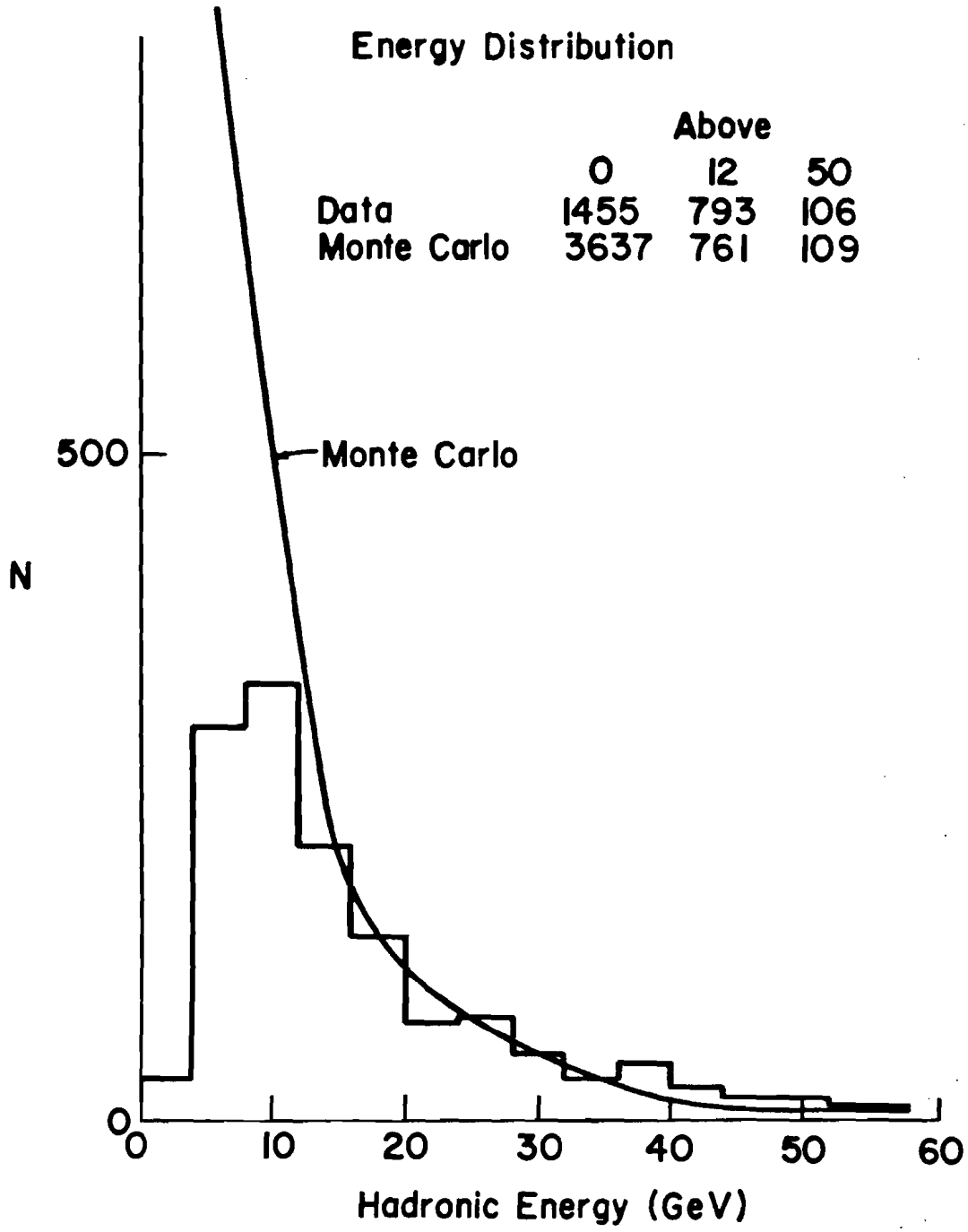

Fig. VI.2. Energy distribution of the raw triggers

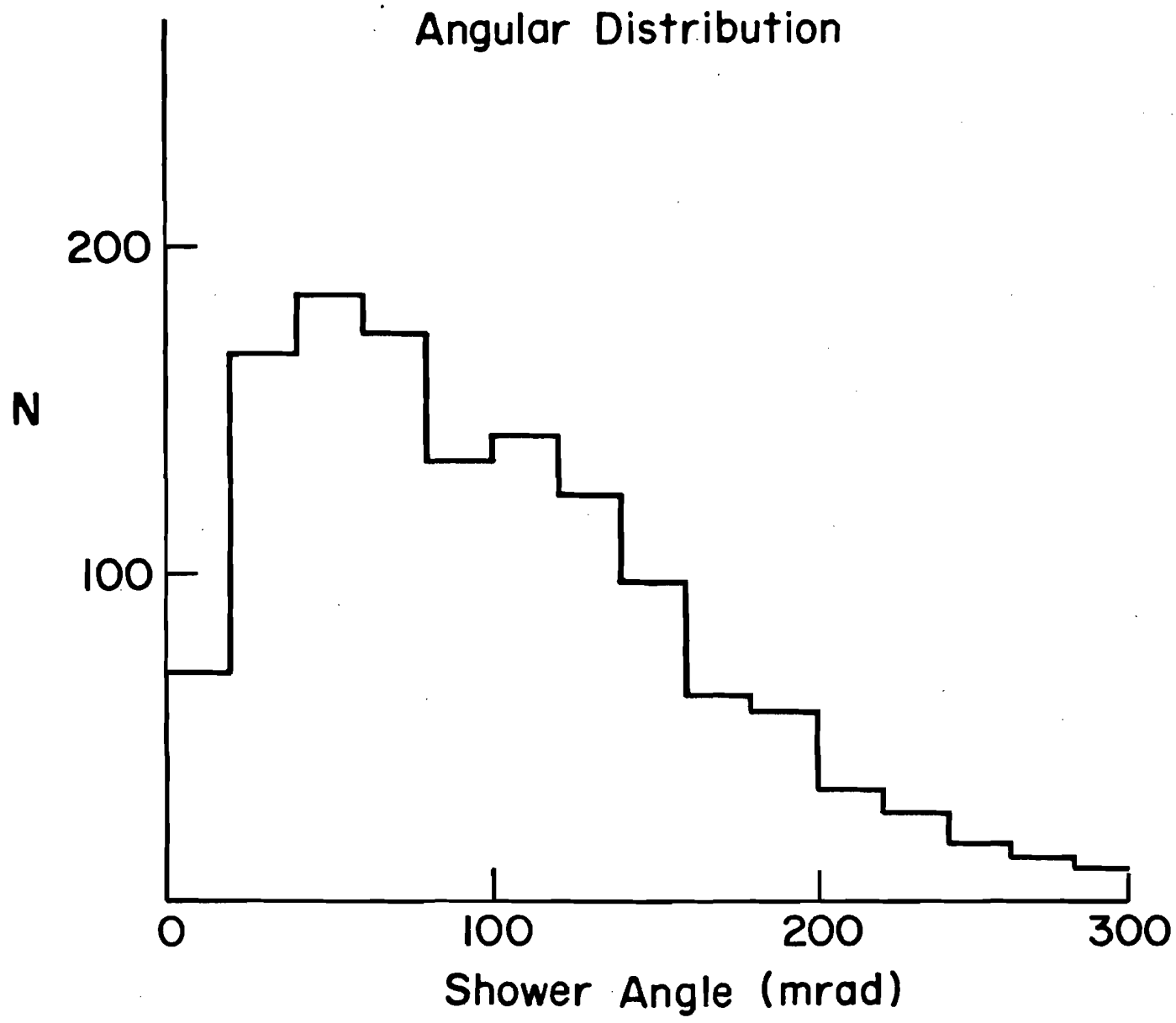

Fig. VI.3. Angular distribution of the raw triggers

of the 1400 events in the histogram less than one $\nu_\mu e$ event is expected. The average shower angle is about 100 Mrads for the $\nu_\mu N$ events.

EVENT RECONSTRUCTION

The first step of the event reconstruction is to determine the X, Y and Z position of all the chamber hits. A hit is defined as a region in the chamber where a shower or charged particle has passed through. Since the middle three taps on the delay-line have a right-left ambiguity, some of the computed hit positions are merely reflections and not real. These unresolved hit positions are characterized by the position of an edge of a shower or track and an estimate of the width of the hit. The unresolved hits are reconstructed into resolved hits which are characterized by both a left and right edge position and a shower centroid defined as the midpoint between the edges.

The Z position of the chamber hits is determined by the known Z position of the chamber. The Z position of the shower vertex is found by examining the energy deposition measured by the scintillator ADC's. The fitting algorithm then fits the shower centroids in the first eight chambers of the shower to a straight line to determine the shower angle.

The reconstruction and fit of electron showers is straightforward since each chamber sees only one hit. Hadronic events are often more complicated since, in addition to an electromagnetic shower, they usually contain accompanying and distinct charged particle tracks which can interfere with the event reconstruction. These accompanying tracks form the basis of many of the cuts which are used to reject these events.

The Z position of the shower vertex is found by checking the direct scintillator ADC's for the maximum pulse height and then searching the amplified scintillator ADC's preceding shower maximum until the pulse height drops below minimum ionizing. This procedure isolates the module which first contains the shower. The end of the shower is found by stepping through the shower until the pulse height drops below minimum ionizing. The energy deposited in each module is computed from the direct scintillator pulse height according to the method outlined in Appendix IV.3. The total energy is the sum of the module energies from the start of the shower to the end of the shower.

The X and Y chamber hit positions are obtained by reconstruction of the TDC information. The TDC information is first checked to insure that no CAMAC errors have occurred. The digitized time and width is then flagged according to the following codes:

0	Good information		(VI-1)
1	Taphit	ABS $(t_t) < 50$ Nanoseconds	
2	Out of Time Hit	$t_t < -50$ Nanoseconds	
3	Width Cutoff by TDC Stop	ABS $(t_d - w_d) < 5$ Nanoseconds	

t_d = Digitized time Between the Arrival of the Cathode Logic Pulse and the TDC Stop Pulse

w_d = Digitized Width

t_t = Transit Time of Pulse to Tap t_t = TOF - t_t

Code 1 implies that the shower overlaped the tap so that the measured edge was not the true edge of the shower. Since the transit time to the tap must be greater than zero, a negative number indicates that the hit was out of time and not event associated. These code 2 hits are

discarded. If the TDC stop pulse arrives before the cathode logic pulse has fallen back to zero then the digitization of the width will be terminated early resulting in an inaccurate value. The leading edge information for these type of hits is still accurate however.

Formula (IV-1) and the TDC information are used to compute the possible positions of the hit edge and hit width. Due to the right-left ambiguity of the three center taps, there are two possible hit positions for these taps which furnish identical TDC information.

The reconstruction algorithm can best be described by the use of an example (See Figure VI.4). Suppose a hadronic event occurs upstream forming an electromagnetic shower and a large angle charged particle which pass through the chamber (Figure VI.5A). All the TDC information is flagged and the possible hit positions are computed (Figure VI.5B). The positions computed for tap 3 are flagged as tap hits. The number of possible left edges is three and the number of possible right edges is three. Tap hit edges are not real and are not used. The object of the reconstruction algorithm is to match the left edges to the proper right edges and to remove the reflections.

All possible combinations of left-right pairings are tried and then classified as unambiguous, ambiguous, or no match (see Table VI.2A). Matches are unambiguous if the overlap of the widths is greater than half the distance between the left and right edge and if the reflections of the pairing used in the match are not used in another match. A match is ambiguous if the width overlap is greater than zero and not classified as unambiguous, or if the distance between edges is less than 100 millimeters and there is no overlap. See Figure VI.6A for

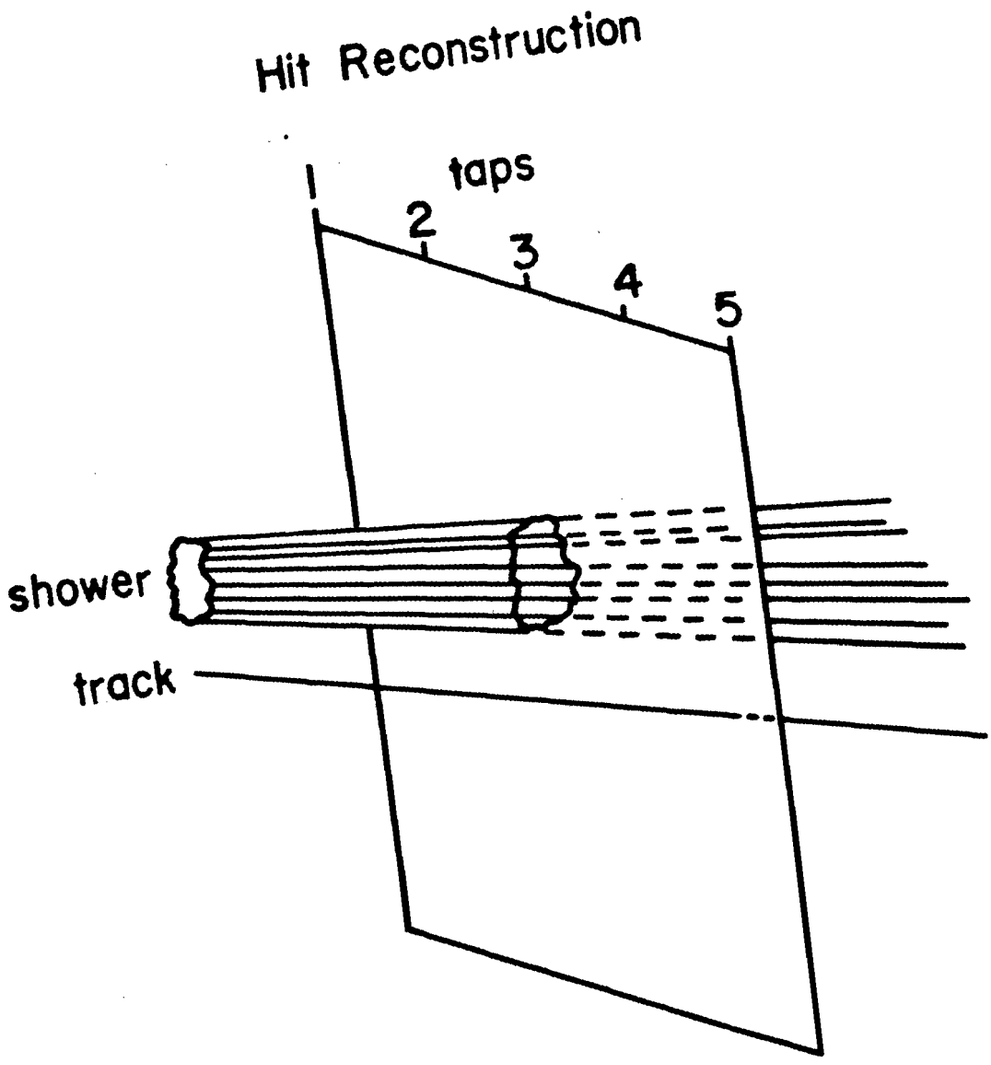

Fig. VI.4. Hit reconstruction example

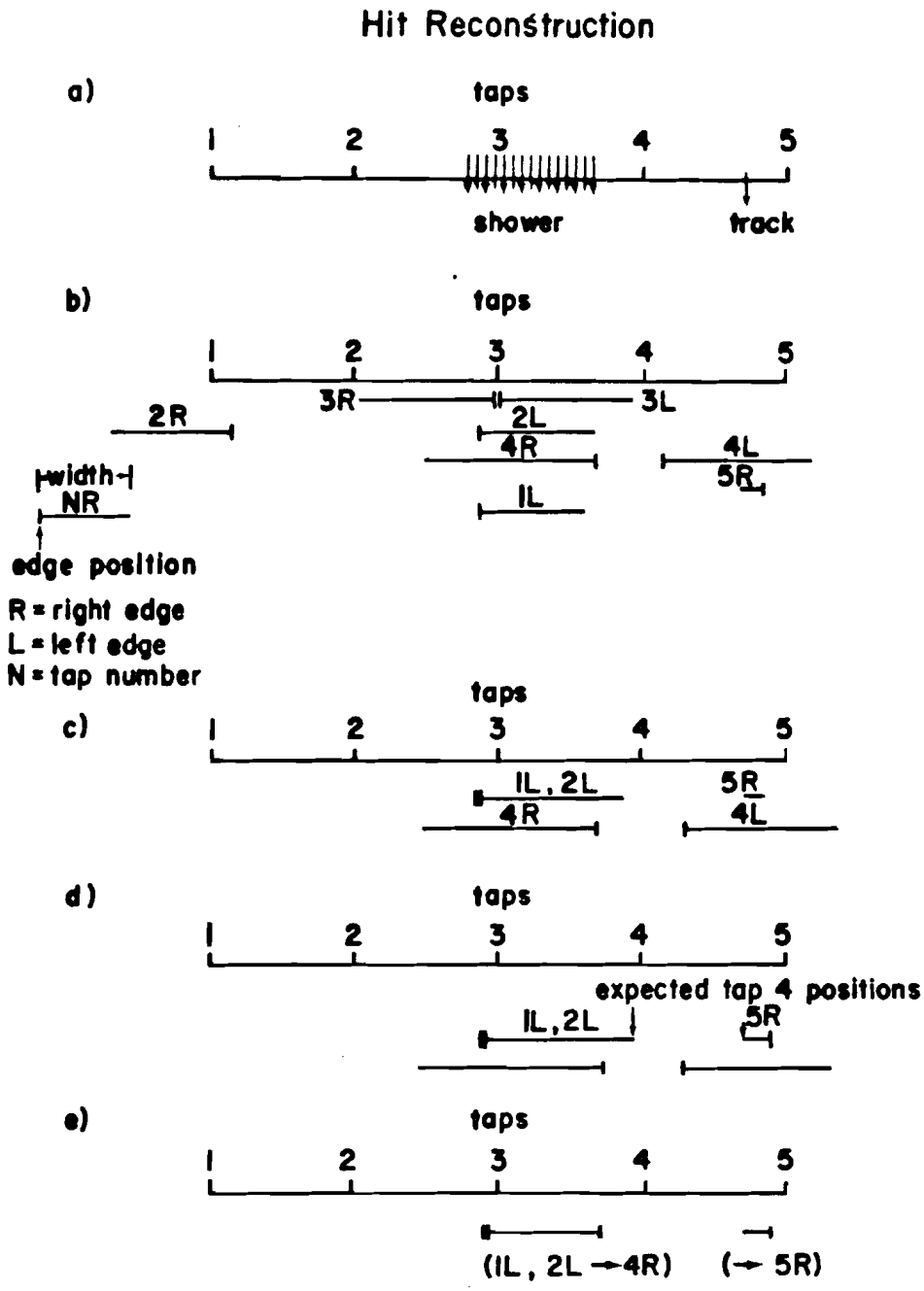

Fig. VI.5. Details of chamber hit reconstruction

Pair	Status	Comments
1L-2R	no match	no overlap
1L-3R	no match	tap 3 is tap hit
1L-4R	ambiguous	good overlap but 4L-5R also match
1L-5R	no match	no overlap
2L-3R	no match	tap 3 is tap hit
2L-4R	ambiguous	good overlap but 4L-5R also match
2L-5R	no match	no overlap
3L-4R	no match	tap 3 is tap hit
3L-5R	no match	tap 3 is tap hit
4L-5R	ambiguous	good overlap but 4R matches with 1L, 2L

A. Match Status

Edges	Redundancy	Comments
1L-2L	good	edge positions within 50mm cut
1L-3L	no	tap hit at tap 3
1L-4L	no	edges outside cut
2L-3L	no	tap hit at tap 3
2L-4L	no	edges outside cut
3L-4L	no	tap hit at tap 3
2R-3R	no	tap hit at tap 3.
2R-4R	no	edges outside cut
2R-5R	no	edges outside cut
3R-4R	no	tap hit at tap 3
3R-5R	no	tap hit at tap 3
4R-5R	no	edges outside cut

B. Edge redundancy

Table VI.2. Reconstruction pair status and edge redundancy

examples. In the example in Figure VI.5B, all the matches are ambiguous. Comparisons are then made among left edges and then among right edges to check for same side edge redundancy (See Figure VI.6B and Table VI.2B). If two left-left or right-right edge positions are within 50 mm, then a pairing is found and the corresponding reflections eliminated (see Figure VI.5C).

This process has resolved the tap information for all taps except tap 4 in the example. Position 4R matches with 1L and 2L, and position 4L matches with 5R. Only one of these matches can be correct. There is no rule which will give the correct pairing 100 per cent of the time in this situation. One should note that in neutrino electron scattering this situation will not occur since the shower will rarely produce a large angle isolated charged particle. The complete set of rules used to resolve this ambiguity is rather tedious to describe in detail. The general aim is to try to predict where the possible tap 4 positions should be based on the other tap information. Since the TDC widths of positions 1L and 2L are wide, one would expect the matching edge to be near tap 4. The TDC width of 5R is small so that the expected matching edge is far from tap 4. The TDC will digitize the pulse which arrives at the tap first (see Figure VI.5D). Consequently, the most probable match is 1L and 2L with 4R (See Figure VI.5E). The tap information for this chamber projection has been resolved into a shower in the middle of the chamber and an isolated hit at the side.

Reconstructed hits are assigned a redundancy and class codes. The redundancy is the number of edges used to reconstruct that hit. The class refers to the validity of the computed centroid of the shower. Class 1 (2) are partially reconstructed hits for which only left (right)

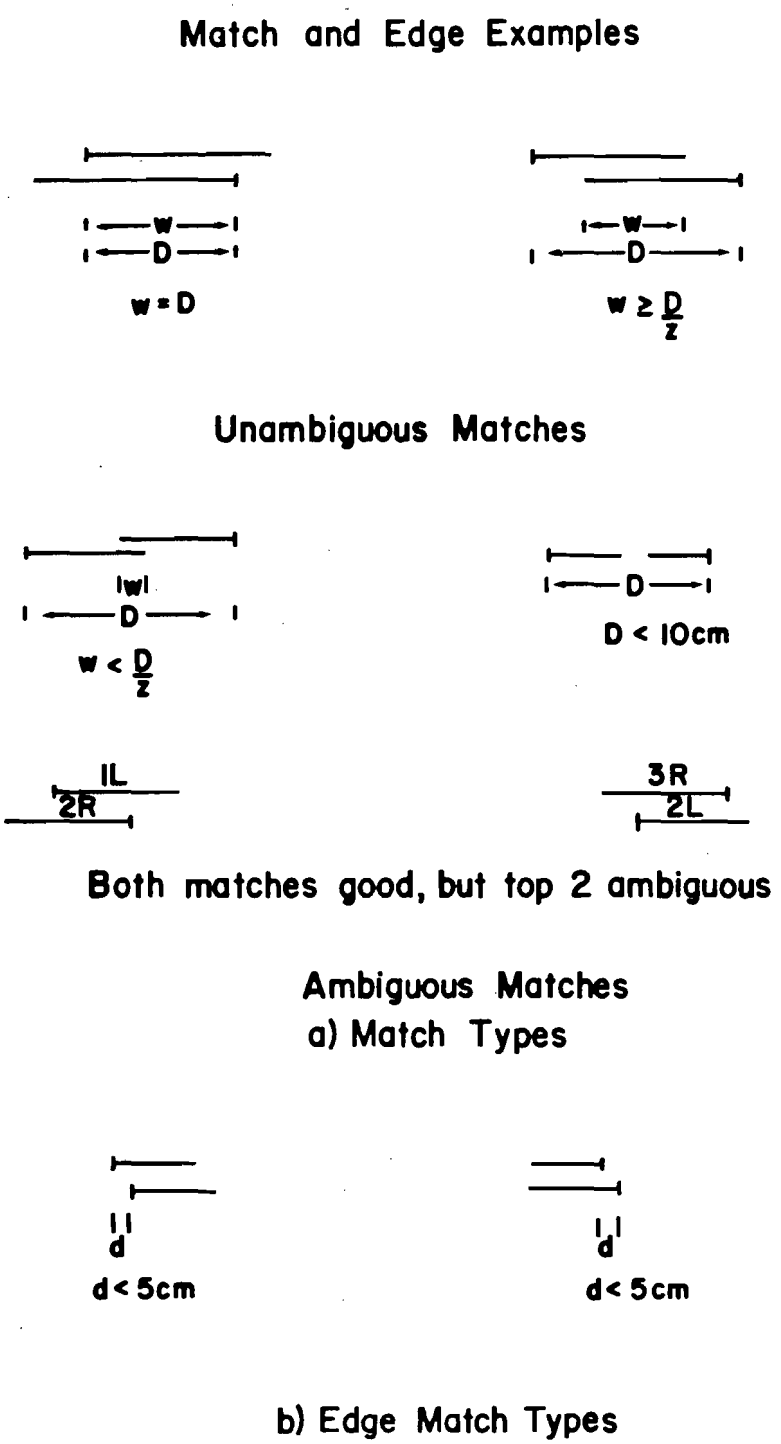

Fig. VI.6. Examples of matches and edge types

edges were found. The centroid of these showers are assumed to be 50 mm from the edge. Class 3 hits are fully reconstructed with both a left and a right edge with the centroid defined as the midpoint between the edges. See Figure VI.7. In the example in Figure VI.5E the shower hit is a class 3 hit with a redundancy of three and the track hit is a class 2 hit with a redundancy of one.

FITTING ALGORITHM

Two fitting cuts are used to select the useful events, the projected angle must be less than 50 milliradians and the chi-squared per degree of freedom must be less than 2.5. (The selection criteria are described in greater detail in a later section.) The fitting algorithm is conservatively designed to insure that no fitting errors are made which might reject a possibly good event. Bad fits can sometimes result because of extraneous hits left from muon tracks which are accidentally coincident with the trigger. These extra hits can interfere with the reconstruction algorithm to give erroneous chamber centroids.

The first 8 chambers sensing the shower are used in the fit. The starter fit assumes that the shower is at zero angle. The class 3 reconstructed chamber hits are fit to the formula $X(Z)=A_0$ (A constant). At least three class 3 hits must be found or the fitting is aborted and the event rejected. At the next pass all class three positions witin ±15 cm of the starter fit are fit to the formula $X(Z)=A_0+A_1*Z$. This process is repeated with the deviation cut of the centroids from the previous fit being reduced from 15 to 10 and finally to 5 cm. The final fit must contain at least 3 points. If three points are not found then the whole

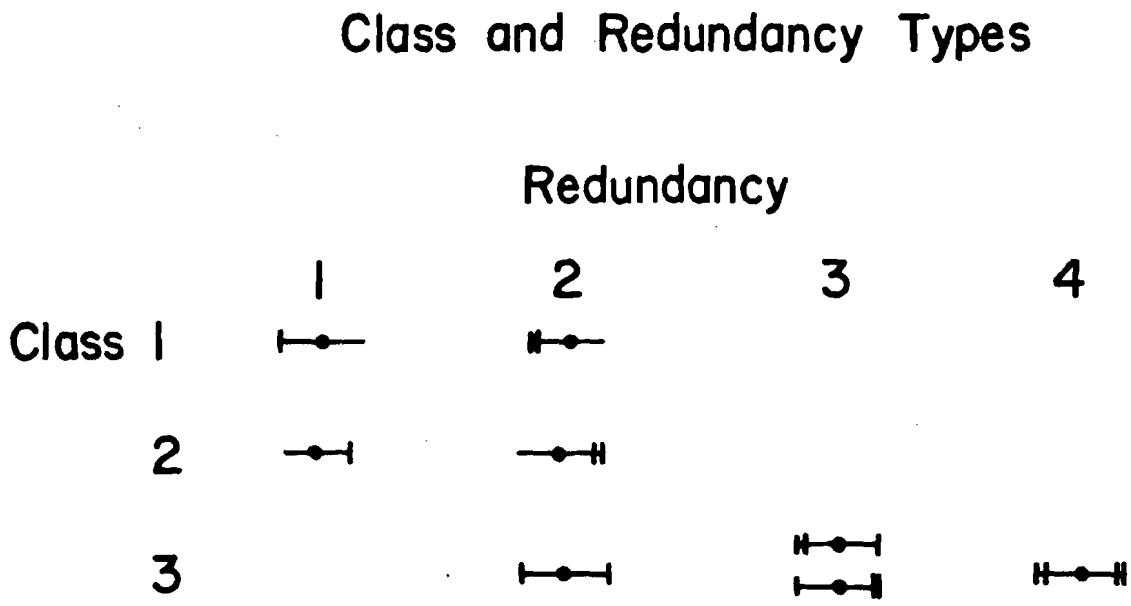

Fig. VI.7. Examples of class and redundancy types

process is repeated from the starter fit but accepting class 1 and 2 hits with a redundancy greater than 1. The fit resulting from this algorithm gives an unbiased estimate of the angle of the shower relative to the incident neutrino direction. This angle represents the direction of the energy flow in the shower.

In order to assure that the good events are not lost due to bad fits, this unbiased fit is checked if the angle is greater than 50 mrad and the number of points greater than 3. The fit is checked by removing one point out of the N points used in the unbiased fit and refitting the remaining N-1 points. This is done for each of the N points in the fit. The fit corresponding to the smallest angle is assumed to be the best fit to the shower. This represents a fit biased to angles below 50 mrad in keeping with the conservative approach at this stage of the event reduction.

A cut is also made on the chi-squared per degree of freedom at 2.5. If the chi-squared per degree of freedom is found to be greater than this value then the fit is checked in a similar manner as above to find a fit that satisfies the cut. Single points are removed and the remainder refit to find the fit with the minimum chi-squared per degree of freedom.

As is obvious from this description, the fitting algorithm is constructed in a manner which biases the analysis to insure that single electron events pass the cuts.

EVENT DISPLAY

The result of the reconstruction and fitting routines can be displayed on a graphics terminal. Figure VI.8 and VI.9 are the displays

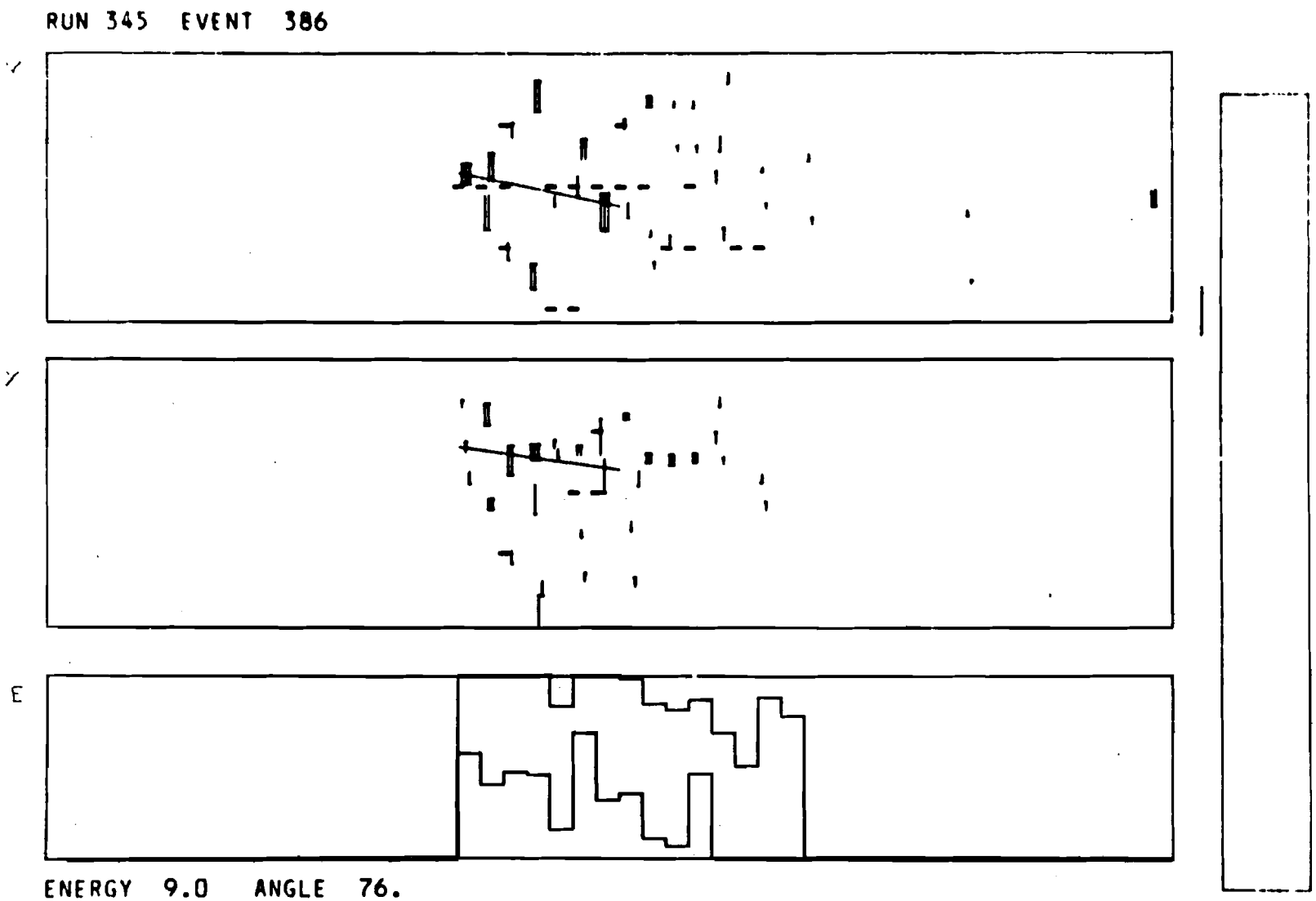

Fig. VI.8. Example of a typical $\nu_\mu n$ interaction with π° production

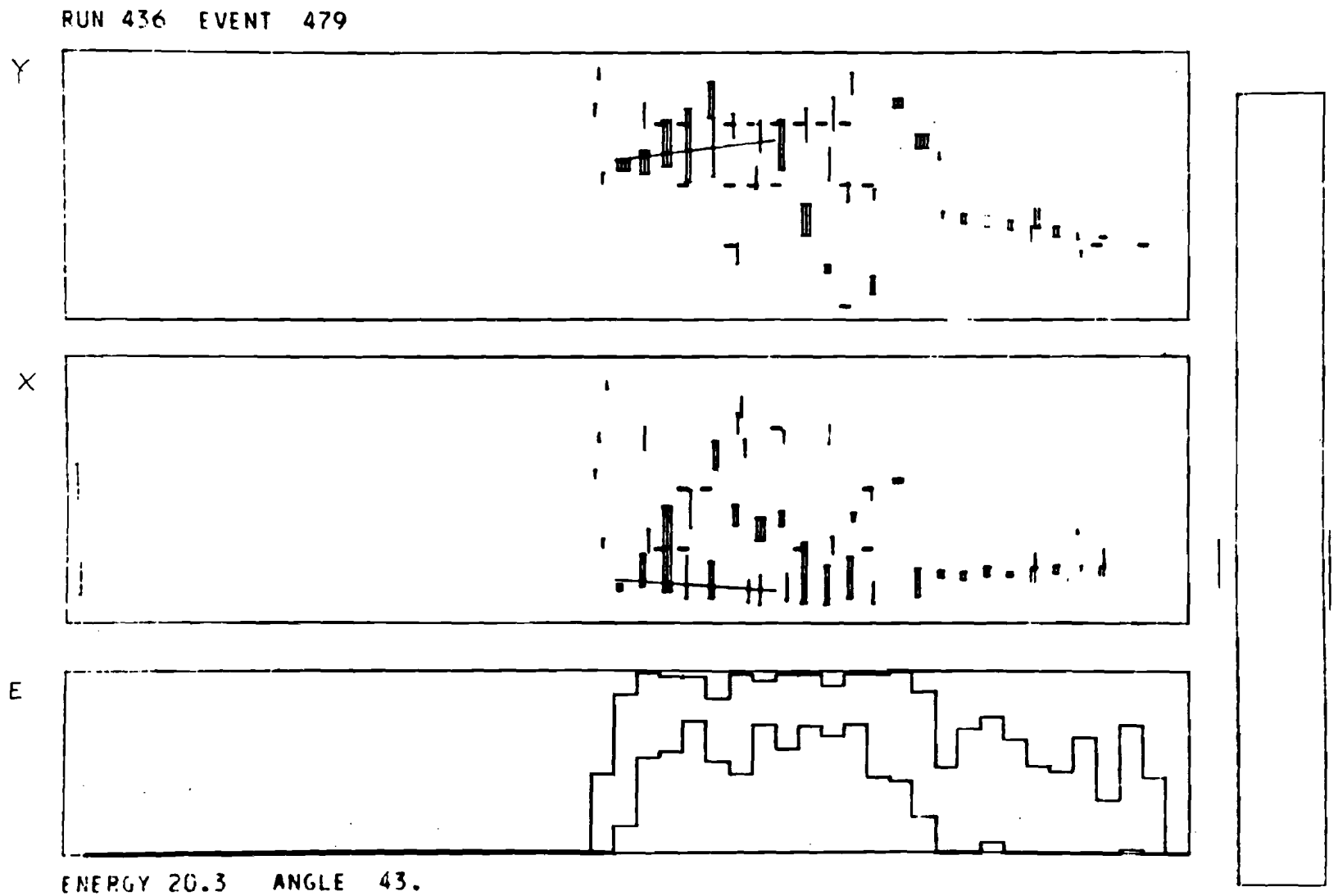

Fig. VI.9. Example of a typical $\nu_\mu N$ interaction with π production

of typical neutrino nucleon triggers, while figure VI.10 is a neutrino electron candidate.

The display shows the Y position of the chamber hits in the top box below the event header, the X positions in the middle box, and the energy deposition in the bottom box. The neutrinos are incident from the left. The chamber boxes are of a lateral dimension of 1 meter and a longitudinal dimension of 50 feet (15.2 meter). Both the direct and amplified scintillator ADC's are shown on a logarithmic scale. The box at the right represents the steel hadron absorber. The X position of any counter hits in hodoscopes B and C are also shown. The redundancy and class of the chamber hits are displayed according to the examples in Figure VI.11. The energy and angle are printed at the bottom of the display.

COMPUTER CUTS

The characteristics of electron showers were studied in an electron test beam using ten fully instrumented chambers. This study indicated several distinguishing characteristics of electron showers which can be used to isolate $\nu_\mu e$ events from the hadronic background.

Figure VI.12 shows the average hit redundancy for chamber hits in the first eight chambers of a 10 GeV electron shower. The redundancy is the number of tap points sensing the hit. Figure VI.13 shows the average redundancy from the neutrino data sample. Electron showers have a high average redundancy since the showers are not associated with long isolated charged particle tracks. Any large angle electron scatter will also be at a very low energy and will usually be stopped at the next layer of aluminum, hadronic showers have a low redundancy because of the

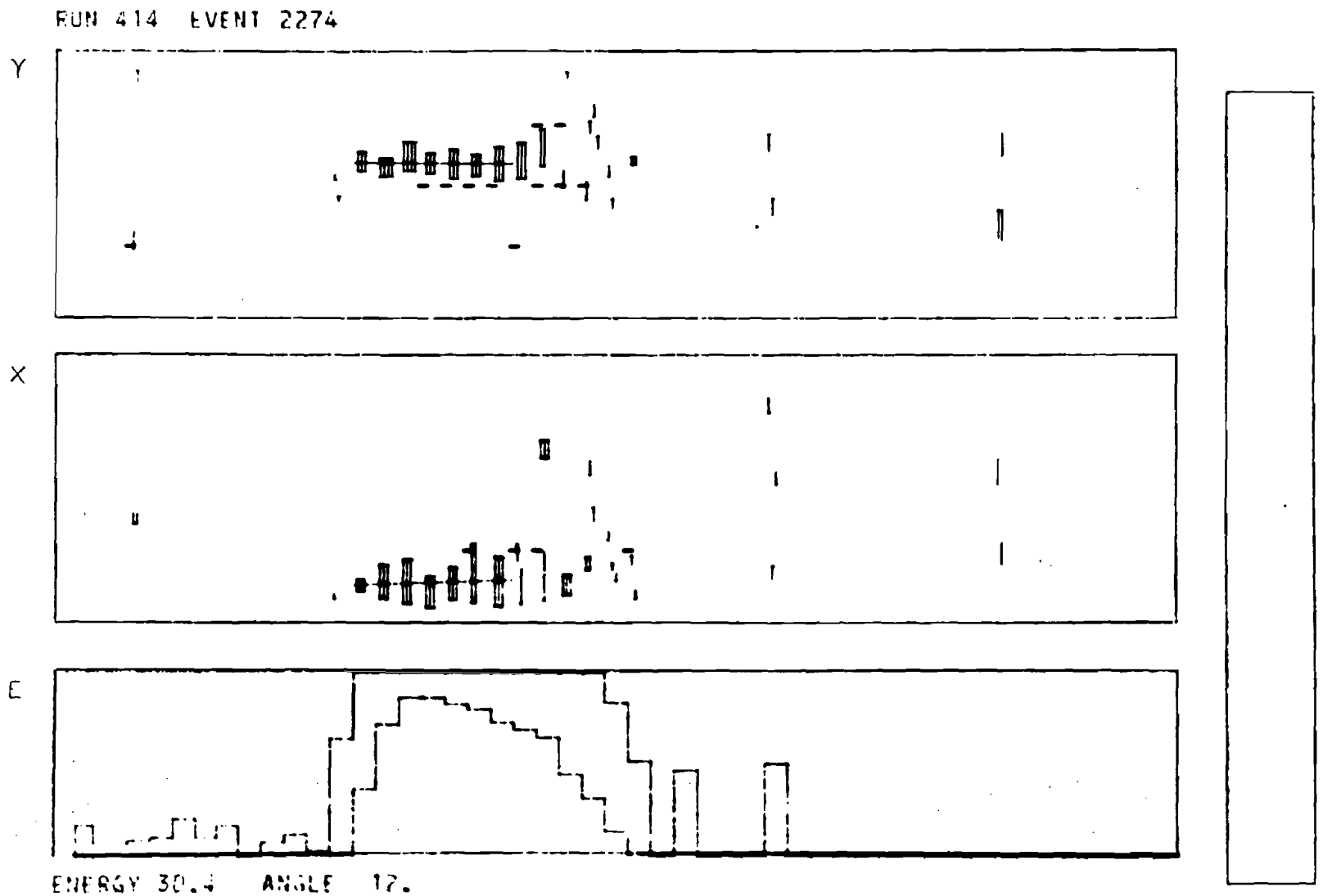

Fig. VI.10. Example of a $\nu_\mu e$ candidate

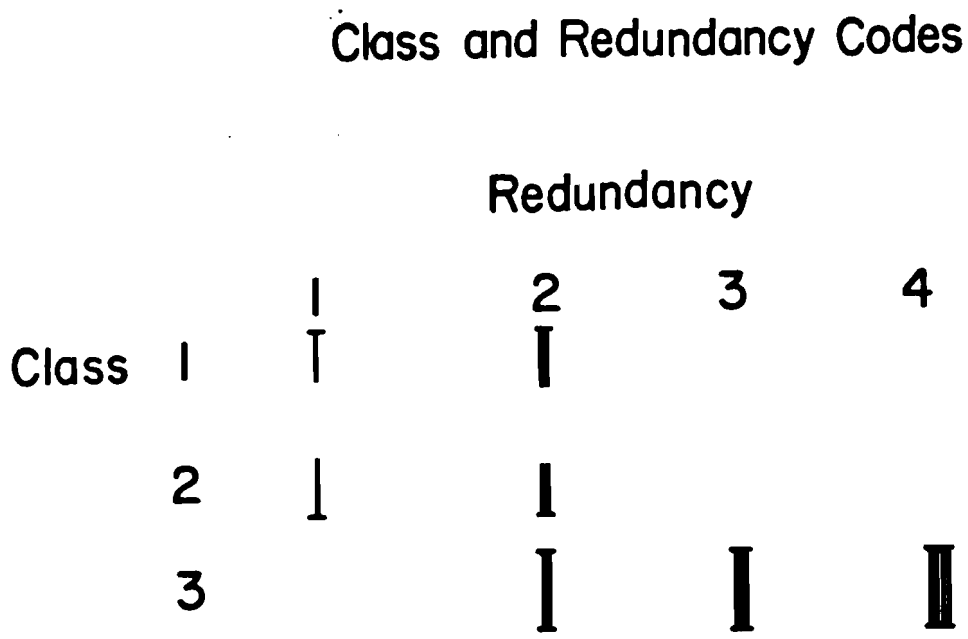

Fig. IV.11. Example of display class and redundancy codes

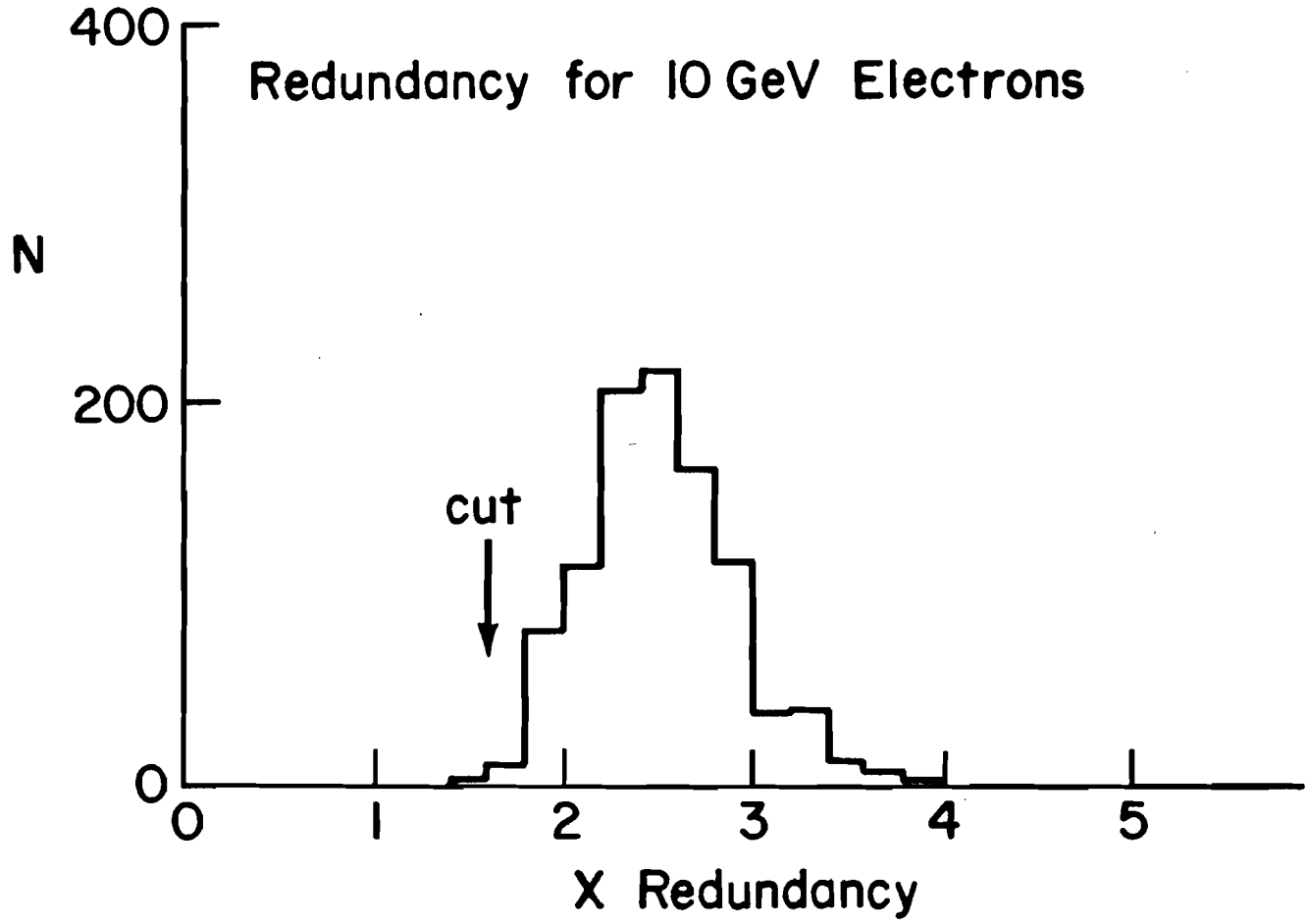

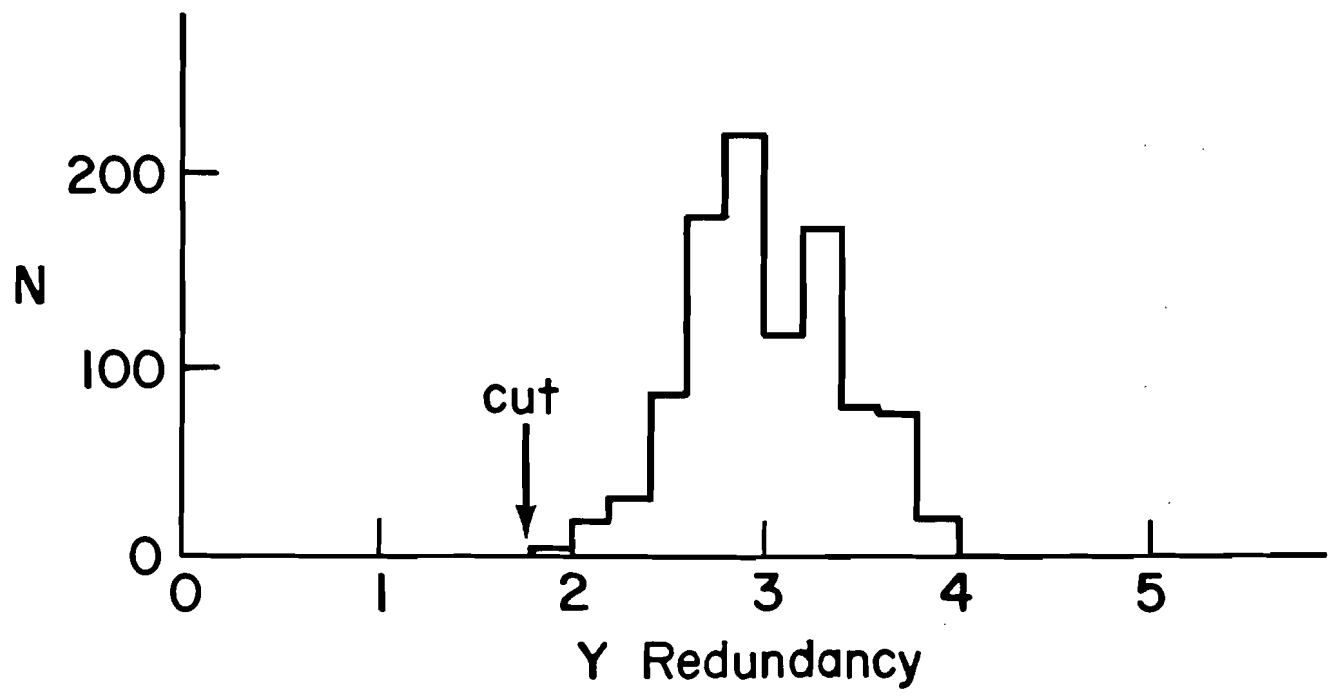

Fig. IV.12. Redundancy distribution for 10 GeV electrons

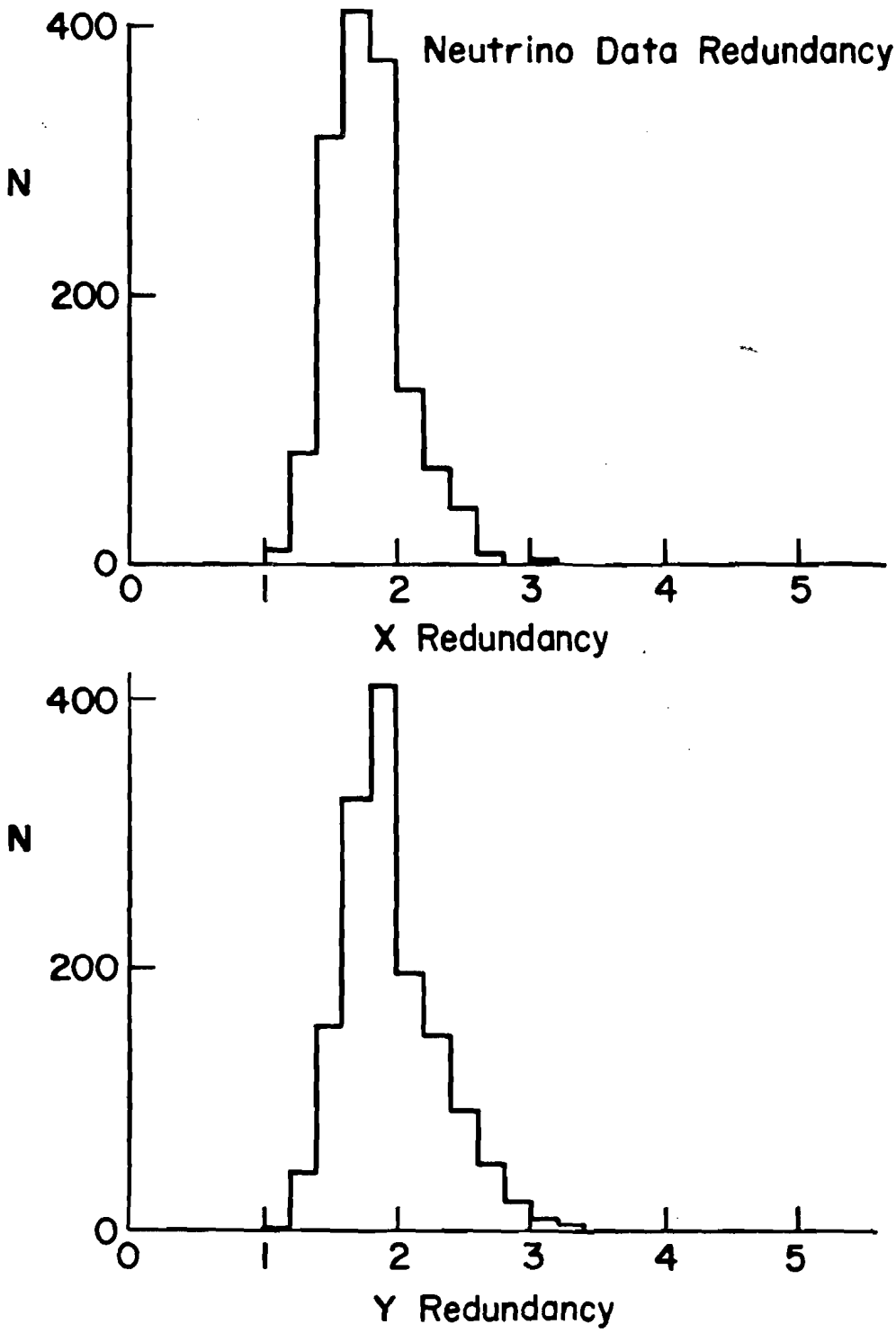

Fig. VI.13. Redundancy distribution from the neutrino data

the likely presence of several isolated charged particle tracks. The more isolated hits in the chamber, the lower will be the average redundancy. The X redundancy is slightly lower than the Y redundancy since the X delay-line is more efficient at sensing isolated tracks. Redundancy cuts of 1.6 for X and 1.75 for Y are applied to the data. If the vertex is within 5 cm of a tap point so that tap hits are likely for that tap point, then the X and Y cuts are lowered to 1.4 and 1.5 respectively.

Cuts on the number of nonshower hits associated with the event are also efficient at isolating electron showers. Shower hits are defined as those hits with a centroid within 10 cm of the shower fit. Nonshower hits have centroids outside this cut and are caused by particles isolated from the electromagnetic shower. Electron showers will have few nonshower hits in the first eight chambers of the shower. Figure VI.14 shows the number of nonshower hits for a 10 GeV electron shower and Figure VI.15 shows the distribution from the neutrino data. An event passes the cut if less than 7 nonshower hits are found in the X view and less than 5 found in the Y view.

Hadronic showers will be composed mostly of pions and a few kaons. Any π° in the shower will quickly decay into two gamma rays. Although the opening angle between the gamma rays can be 20 mrad or larger, two separate showers are not seen because of their close proximity. The two showers will merge into one wide shower. Hadronic showers with multiple π° production will also produce wide showers. Figure VI.16 shows the average shower width for 10 GeV electron showers while Figure VI.17 shows the average width of showers from the neutrino data sample. Cuts

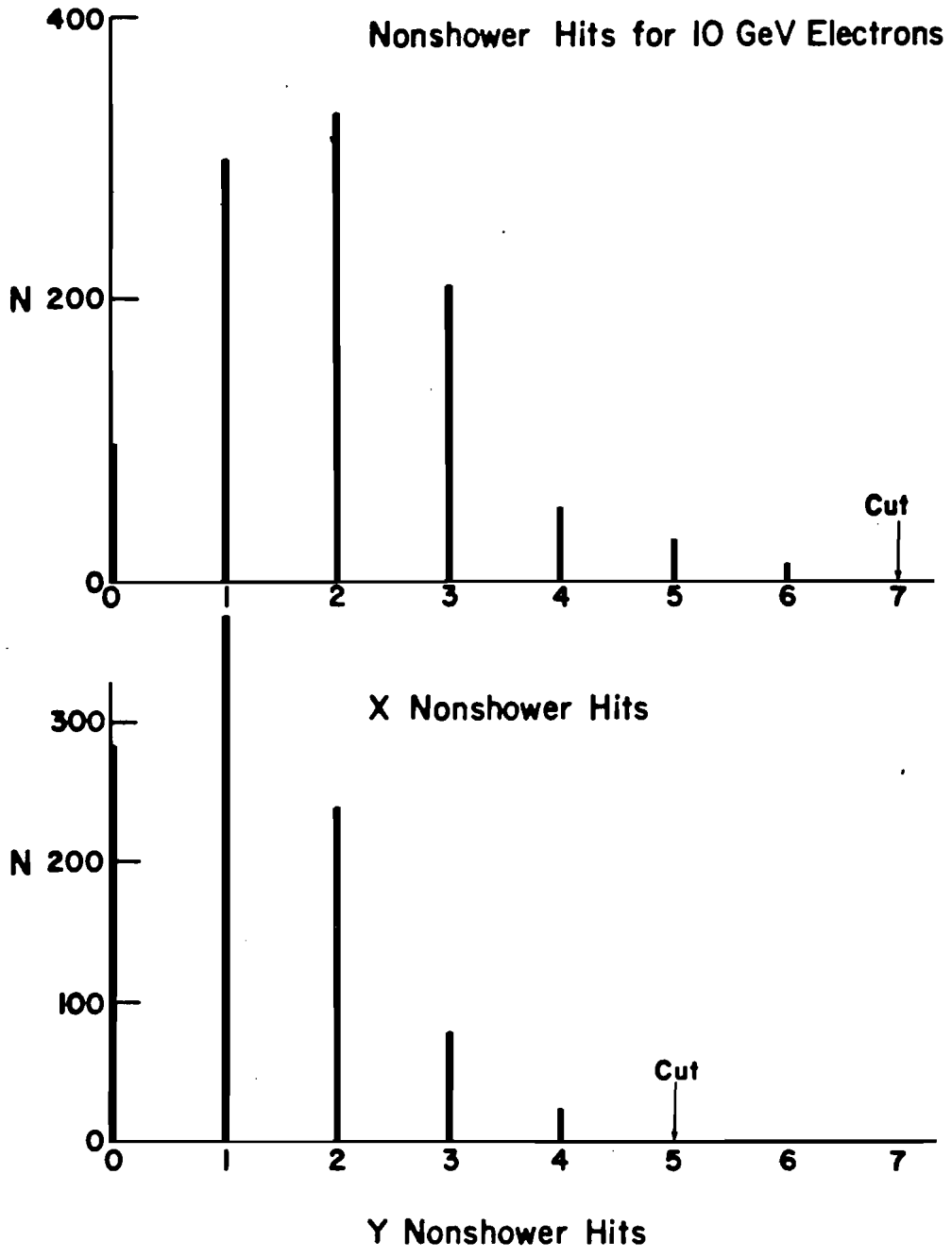

Fig. VI.14. Nonshower hit distribution for 10 GeV electrons

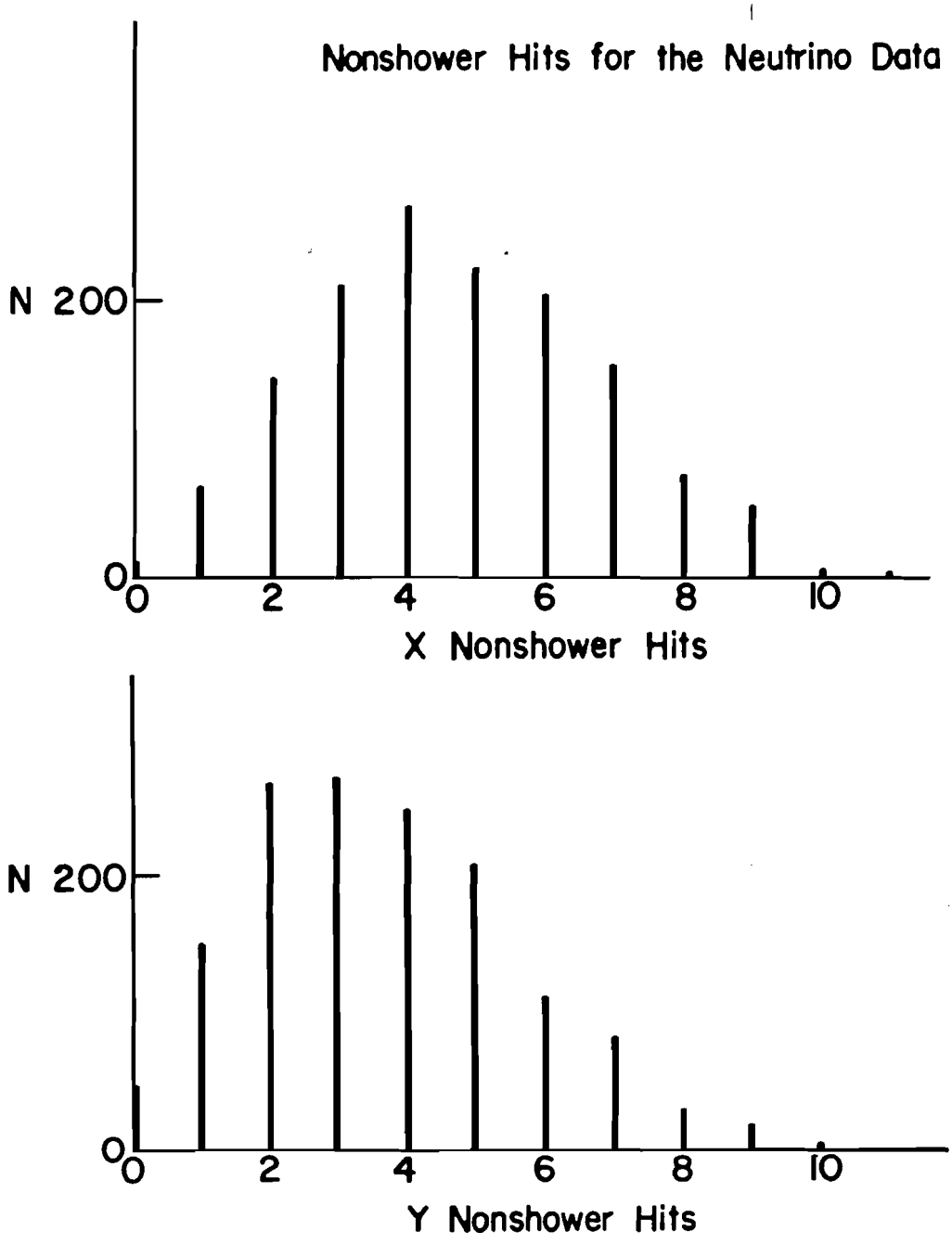

Fig. VI.15. Nonshower hit distribution for the neutrino data

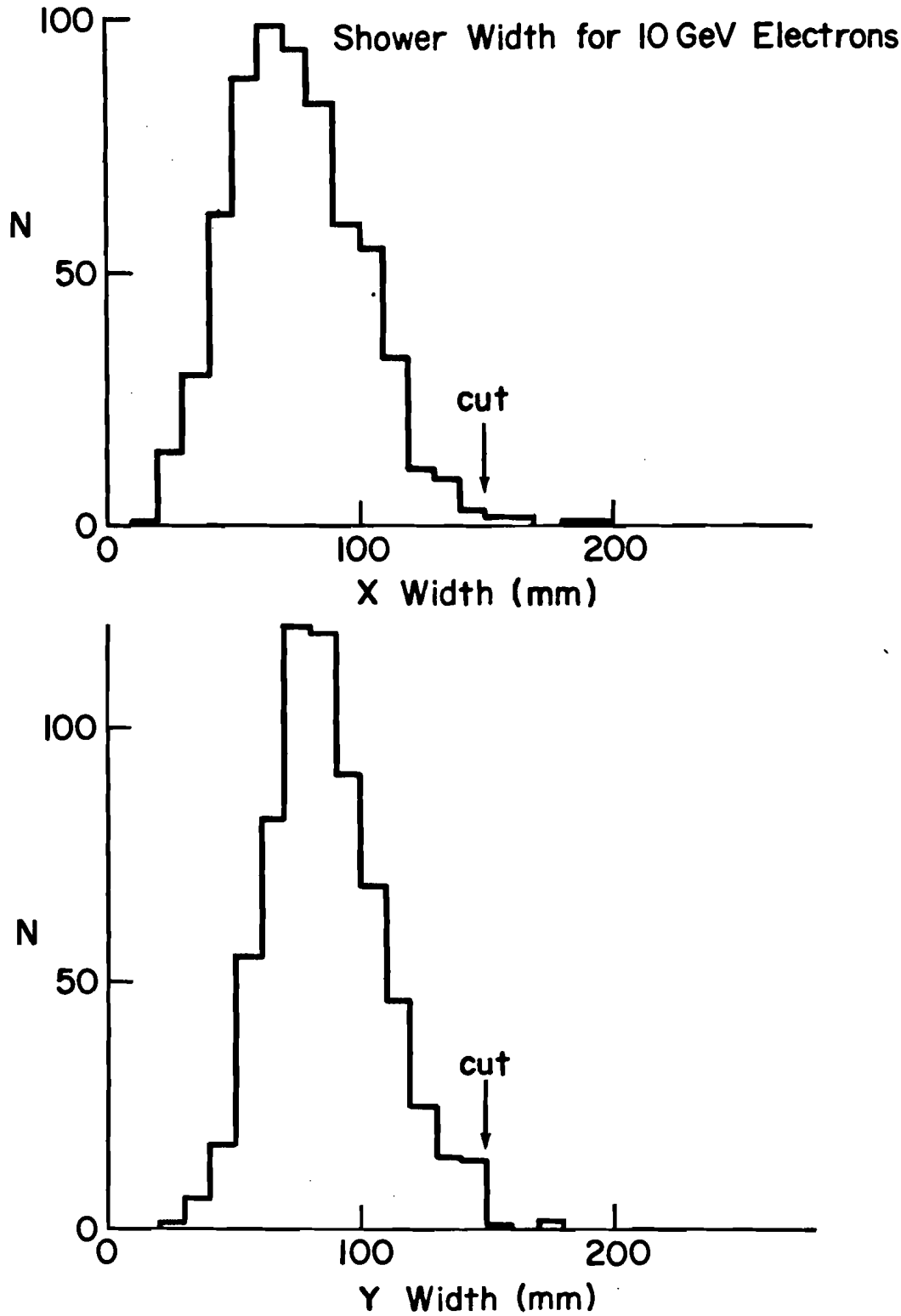

Fig. VI.16. Shower width distribution for 10 GeV electrons

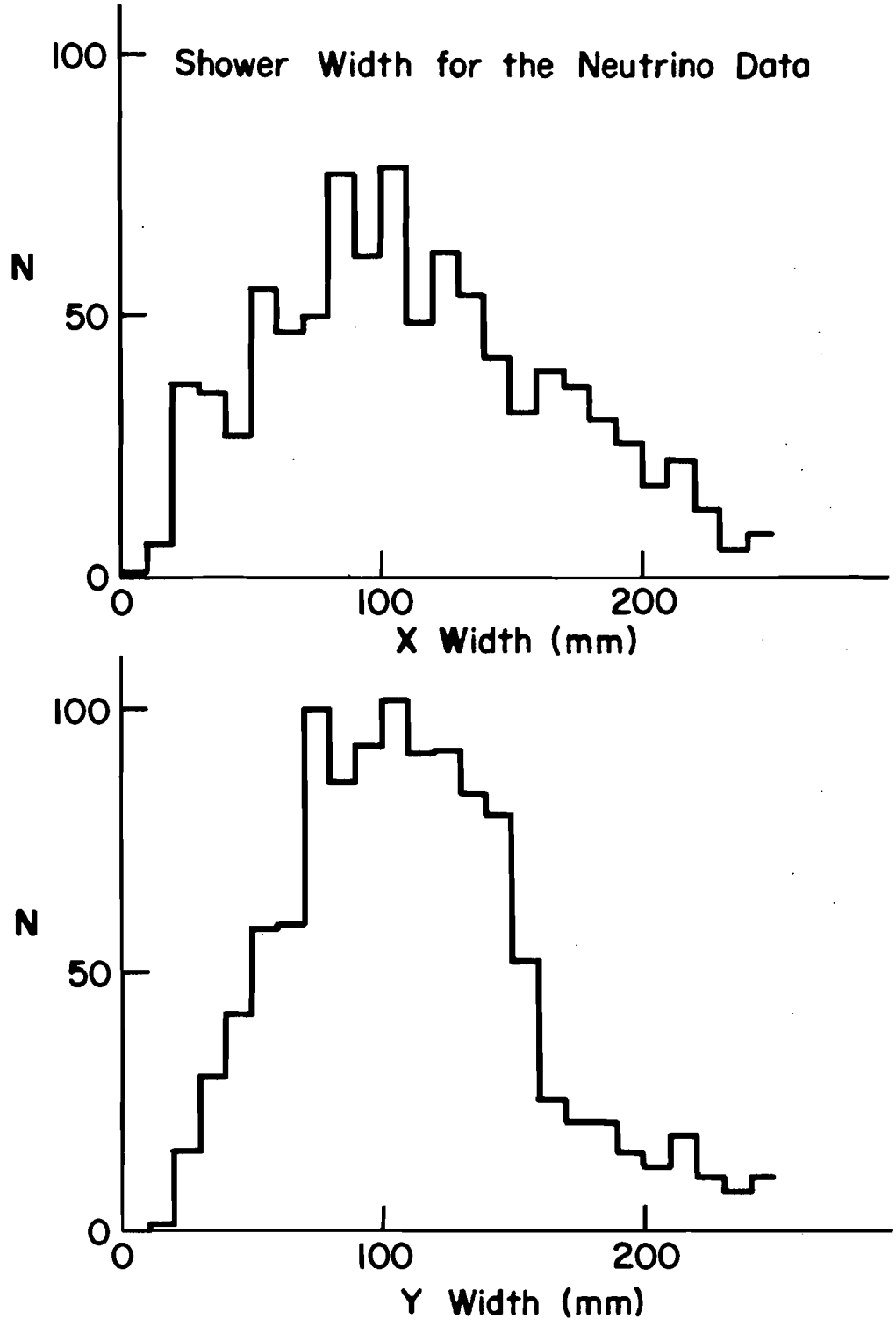

Fig. VI.17. Shower width distribution for the neutrino data

at 150 mm were used to isolate electron showers.

In addition to the cuts discussed so far which cut on the event topology, kinematic cuts are also applied to the data. The most distinguishing feature of the $\nu_\mu e$ events is their small angle relative to the incident neutrino direction. A cut on the shower angle is very efficient at rejecting hadronic events.

An event is immediately rejected if the fitting algorithm fails to fit the event. The fitting algorithm requires at least three class 3 chamber hits out of the first 8 chambers of the shower. High multiplicity hadronic events without an electromagnetic shower sometimes fail to pass the fitting routine. A cut at 50 mrad on the projected angle is made to reject the large angle hadronic events. A cut is also made on the chi-squared per degree of freedom of the fit at 2.5. The electromagnetic component of the hadronic shower is a superposition of showers from at least two gamma rays and possibly more if multiple π^0's are produced. Since the electromagnetic component has several independent sources, the chi-squared per degree of freedom is often larger than for single showers from $\nu_\mu e$ scattering. To insure that good events are not lost due to the presence of accidental muon hits, the fitting algorithm was biased toward satisfying these fit cuts.

Table VI.3 lists all of the cuts used and their efficiencies for 10 GeV electrons. The basic aim behind these cuts is to throw away only those events which are clearly not neutrino electron events and to leave the tighter cuts for the later phase of the analysis where a physicist's judgement could be used. These cuts are conservative with redundancy built into the selection process to insure that little signal is lost.

	Computer Cuts	Efficiency
1.	Number of points in fit ≥ 3	100%

2.	If vertex > 5 cm from top, then
	x redundancy > 1.6
	y redundancy > 1.75
	
	If vertex $\leq$ 5 cm from top, then
	x redundancy > 1.4
	y redundancy > 1.5
		99%

3.	Number of nonshower hits in x view ≤ 6 y view ≤ 4	100%
4.	$E\theta^2 < 20$ MeV	100%
5.	$\theta_x < 50$ Mrad	100%
6.	X view χ^2/degree of freedom < 2.5	94%
7.	X view average shower width < 150 mm	96%
8.	$\theta_y < 50$ Mrad	100%
9.	y view χ^2/degree of freedom < 2.5	98%
10.	y view average shower width < 150 mm	97%
11.	dirty event flag, more than four out of time hits before or after shower	——
12.	Alternate redundancy cut x redundancy > 1.7 y redundancy > 1.7	96%

Table VI.3. Computer cuts and their efficiency

A trigger is rejected if it fails the fit, redundancy, or nonshower hit cuts. The remaining cuts are divided into a X view and a Y view set. Each set consists of the 50 milliradian angle cut, the chi-squared per degree of freedom cut, and the shower width cut for that view. If any event passes the first three cuts and either one of the X view or Y view cuts the event is accepted. The event passes if the following logical expression is true:

$$c_1 \cdot c_2 \cdot c_3 \cdot (c_4 \cdot c_5 \cdot c_6 + c_7 \cdot c_8 \cdot c_9) \qquad \text{(VI-2)}$$

where c_i is the truth value of cut i. This represents a loose electron cut since an event can be accepted even when cuts in one of the views fail. A good $\nu_\mu e$ candidate should pass all of these cuts.

Three additional cuts were used to provide an alternate selection criteria. Especially during the early half of the running when the muon background flux was high, it is possible that an accidentally coincident muon could leave extraneous hits which can interfere with the reconstruction of the event causing an acceptable candidate to be lost. This alternate criteria was designed to pick up these events.

An event is flagged as containing a possible accidentally coincident muon by examing the ten chambers before and after the shower region. The CAMAC gates to the scintillator ADC's are 100 nanoseconds long while the active input time to the TDC's is 1000 nanoseconds. These accidental muons will usually leave chamber hits, but no apparent energy deposition since the scintillator pulses will miss the CAMAC gate. These chambers will not be identified as part of the shower region since no measured energy deposition occurred. If four chamber hits are found in the ten chambers in front of or behind the shower region, then the event is flagged as containing an accidentally

coincident muon.

If no accidental muon is found, then an event can be accepted by the alternate criteria if the $E\theta^2$ for the event is less than 20 MeV and the X and Y redundancy are greater than 1.7. If the event is flagged as containing the muon, then the redundancy requirement is waived. The following logical expression must be true for an event to be accepted by the alternate criteria:

$$C_{10} \cdot (C_{11} + C_{12}) \qquad \text{(VI-3)}$$

an event is accepted if it satisfies either the original or alternate selection criteria.

About 1/7 of the raw triggers are preselected by the computer program for scanning. Once an event is preselected, the computer generates a picture of the event on a graphics terminal (see Figure VI.8). A microfiche camera photographs the picture and the event displays are then scanned from the microfiche.

SCANNING CUTS

The first pass event reduction reduced the raw data sample of 190,000 to about 26,000 events. These events were each scanned by a physicist implementing a tighter set of cuts to further reduce the data sample. Several scanning passes were performed with each pass reducing the data by a factor of 1/4 until the final sample was obtained. The scanning criteria were applied to both neutral and charged current events. The final sample of charged current events was used to estimate the neutrino nucleon background in the neutral current sample.

A list of the cuts used is in Table VI.4. In implementing these cuts care was taken to distinguish event related chamber hits from stray

Scan Cuts

Event rejected if:

1) track - 4 hits pointing to vertex or main body of shower, not identifiable as a muon
2) more than 3 event related nonshower hits but within ± 20 cm of shower
3) shower width > 150 mm in either view
4) penetrating component in shower
5) energy deposition not like a single electromagnetic shower
6) total angle > 50 mrad
7) backscatter - first chamber of shower has hit > 20 mm from fit
8) vertex outside fiducial volume defined by $3 \leq z \leq 40$ modules, $|x| \leq .45$ m, $|y| \leq .45$m

Charge current if

1) 5 chambers of minimum ionizing pulse height after shower
2) B·C hodoscope coincidence
3) hit in c hodoscope and 2 chamber hits consistent with μ from vertex

Table VI.4. Description of scan cuts

hits due to out of time muons. These out of time muons can leave tracks in the chambers but no recorded pulse height since the phototube signal will miss the CAMAC gate. By examining the chamber hits before and after the shower region one can visually determine whether chamber hits in the shower region are event related or due to out of time muons. These stray hits were generally not a problem during the later part of the running when the muon background flux was low, but occasionally were a problem during the first part of the running when the torroids were off.

The principle background are neutrino nucleon events where much of the energy is carried by π^{o}'s which form electromagnetic showers. These events will usually be accompanied by charged particles. The cuts are principally designed to check for the presence of the charged particles and on this basis reject the event.

A track is defined as four chamber hits outside the main body of the shower which form a straight line pointing back to the shower. The charged particle leaving this track may originate at either the vertex or from a secondary hadronic interaction in the shower. All showers accompanied by a track are rejected unless the track also satisfies the muon criteria in which case the event is kept.

Low energy tracks may range out before passing through 4 modules or chamber inefficiencies may cause the chambers to record less than 4 chamber hits. An event can also be rejected if there is a total of more than 3 chamber hits outside the main body of the shower but within $\pm$ 20 centimeters of the shower fit. The cut is not made any tighter since occasionally an electron or photon in the electromagnetic shower will undergo a large angle scatter out of the main body of the shower. It is

unlikely however that this large angle scatter will pass through 3 radiation lengths since the large angle scatters are usually low energy.

Sometimes the extra charged particles will be buried in the electromagnetic showers. Since the interaction length is much greater than the radiation length, the hadrons will tend to travel farther than the shower. Events of this type can be rejected if there is an abnormally long penetrating component to the shower not identifiable as a muon.

The secondary interactions of the hadrons in the shower can sometimes also produce π°'s forming another electromagnetic shower. Events of this type can produce abnormal energy deposition curves that are not consistent with being a single electromagnetic shower.

An event is also rejected by the fiducial cut if the shower is close to the edge of the detector. If any of the first five taps of the shower has a tap hit at a tap at the edge of one of the chambers, then the event is rejected. This cut preferentially rejects hadronic events since these events are more likely to have large angle charged particles which will cause the tap hit. See Appendix VI.1 for a discussion of the efficiency of this cut. A cut is also made on the Z position of the shower vertex. If the vertex is in chambers 1 or 2, or past chamber 40, then the event is not accepted.

If the interaction does not produce several charged particles then the energy will probably be shared among several π°'s. The electromagnetic shower resulting from the decay of these pions will often be much wider than a single electron shower due to the opening angles of the pions. This cut is strengthened over the computer cut by demanding that the width be less than 15 cm. in both views.

If the total angle of the shower is greater than 50 mrad then the event is rejected. If the first hit of the shower is more than 20 millimeters from the fit then the event is classified as containing a backscatter and rejected.

Events passing the above criteria are classified as neutral or charged currents based on a set of muon identification cuts. A muon is present if the 5 modules after the shower has died away show a minimum ionizing pulse height or if hits in hodoscopes B and C are consistent with a muon from the vertex. A muon can also be identified by a hit in hodoscope C and 2 chamber hits which line up with the vertex.

These scanning criteria were applied to the 26,000 events selected by the computer and resulted in a sample of 149 neutral current and 104 charged current events being selected.

Ten GeV electron showers from the test run were scanned to determine the selection efficiency of the scan cuts. The scanning efficiency independent of the fiducial cut is 80%. Of the 20% which fail, over half fail because of the cut on the number of nonshower hits. About a third fail because of an apparent backscatter in the first chamber. The fiducial tap hit cut efficiency is 83%, giving an overall efficiency of 66%.

FINAL EVENT REDUCTION

The sample of events resulting from the scanning are all characterized by a shower consistent with the shape and shower development of a single electromagnetic shower without accompanying hadrons. The fits to the large angle events are still biased to smaller angles due to the design of the fitting algorithm.

The reconstruction and fit for each of these events is reanalyzed by displaying the raw positions graphically, a physicist then reconstructs the event and picks the centroids to be used in the fit. Care must be taken to insure that this is done in an unbiased way. Before the event is displayed the coordinate system is rotated so that the computer fit is at a zero angle in the new coordinate system. Since the computer fit is usually close to the shower direction, all the events will appear at zero angle to the physicist reanalyzing the event. Since the physicist has no knowledge of the true direction of the shower, the reanalyzed fit will be unbiased in angle.

All of the unresolved shower edges and possible centroids are displayed. A starter fit is chosen by positioning the fitted line to maximize the number of centroids within $\pm$ 20 cm of the line. Each centroid selected is associated with a right edge and a left edge. The right (left) edge for the resolved shower position is defined as the average of the right (left) edges associated with the centroids selected in the starter fit. The resolved centroid position is the midpoint between the resolved edges. The shower centroids found in the first 8 chambers of the shower are then fit to a straight line to determine the projected angle of the event. See Figure VI.18 for an example of the method.

After all the events have been reanalyzed an additional fiducial cut is added by demanding that the X and Y vertex position be within $\pm$ 45 cm from the center of the chamber. Since the chamber is 40 inches square, this cut rejects events with a vertex within about 5 cm of the edge of the detector. In addition, the corners of the chambers defined by $X^2 + Y^2 > (530)^2$ are also eliminated from the fiducial volume.

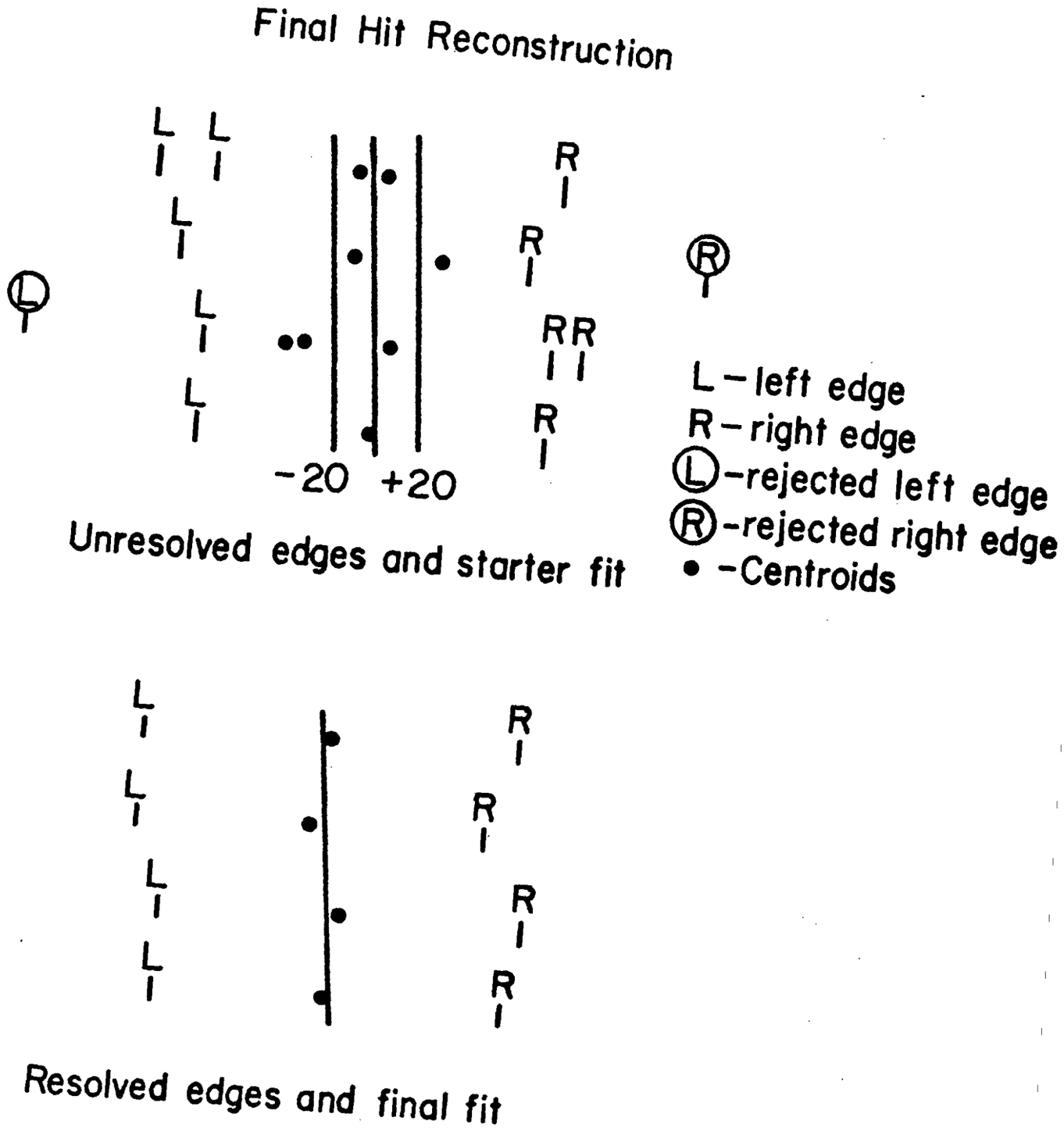

Fig. VI.18. Example of final event reconstruction and fit

The angular, energy, and $E\theta^2$ distributions are shown in Figure VI.19-21 for both the neutral and charged current samples. A clear signal is seen in the neutral current samples at small angles and small $E\theta^2$. These distributions will be discussed in greater detail in later chapters.

The vertex distributions are shown in Figures VI.22-24. Both distributions show an excess of events near the edge of the chambers. This is due to systematic effects of the cuts used to reduce the data sample. Showers with associated large angle hadrons are more likely to be rejected if the vertex is in the center of the detector than if it is near the side. The large angle hadrons can escape detection if the event is near the side by escaping out the side of the detector. This same event if near the middle of the detector would be rejected since the hadrons could then be seen. The Z vertex distributions are also shown with both the neutral and charge current distributions consistent with uniform distribution.

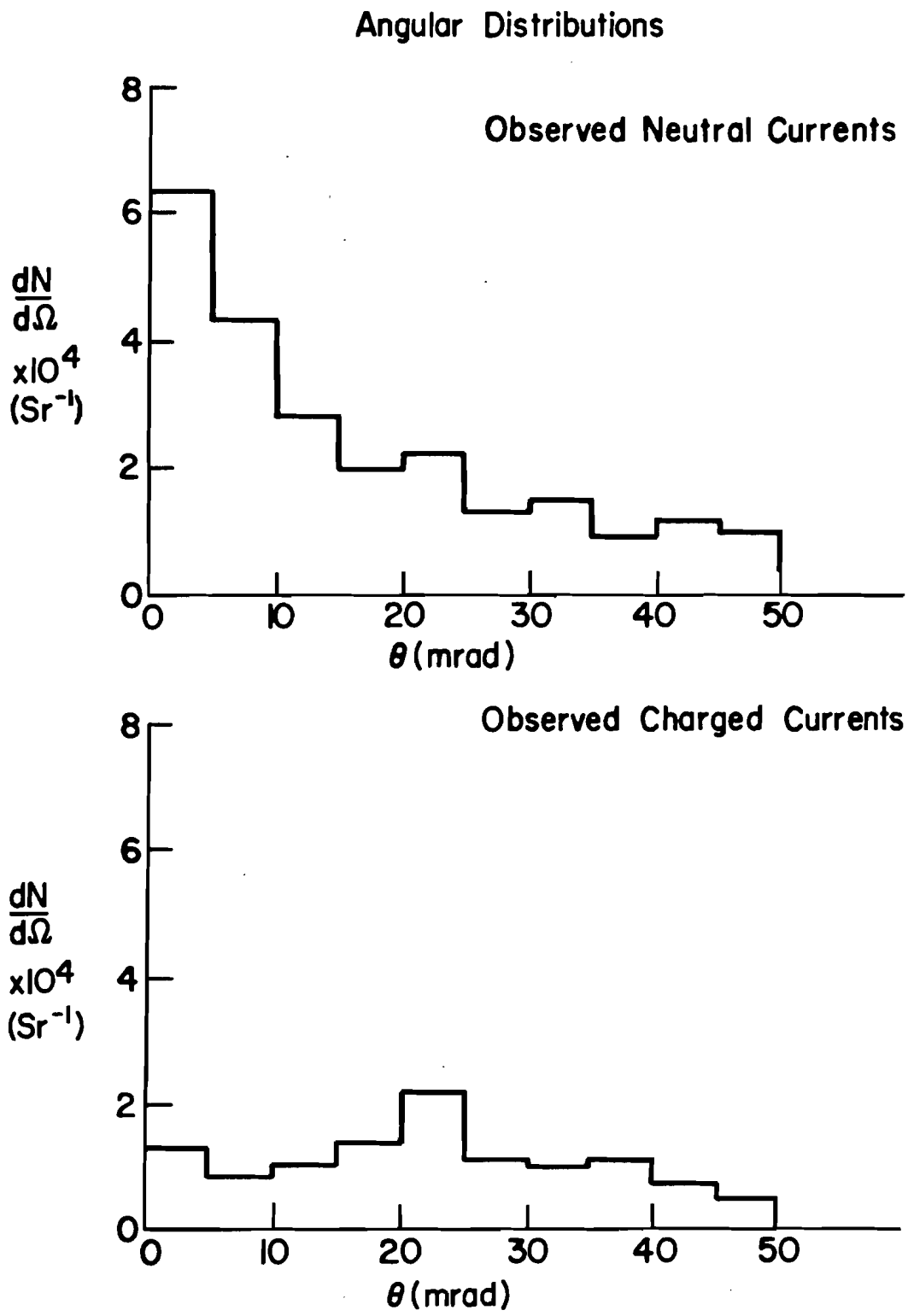

Fig. VI.19. Angular distributions for the observed neutral and charged currents

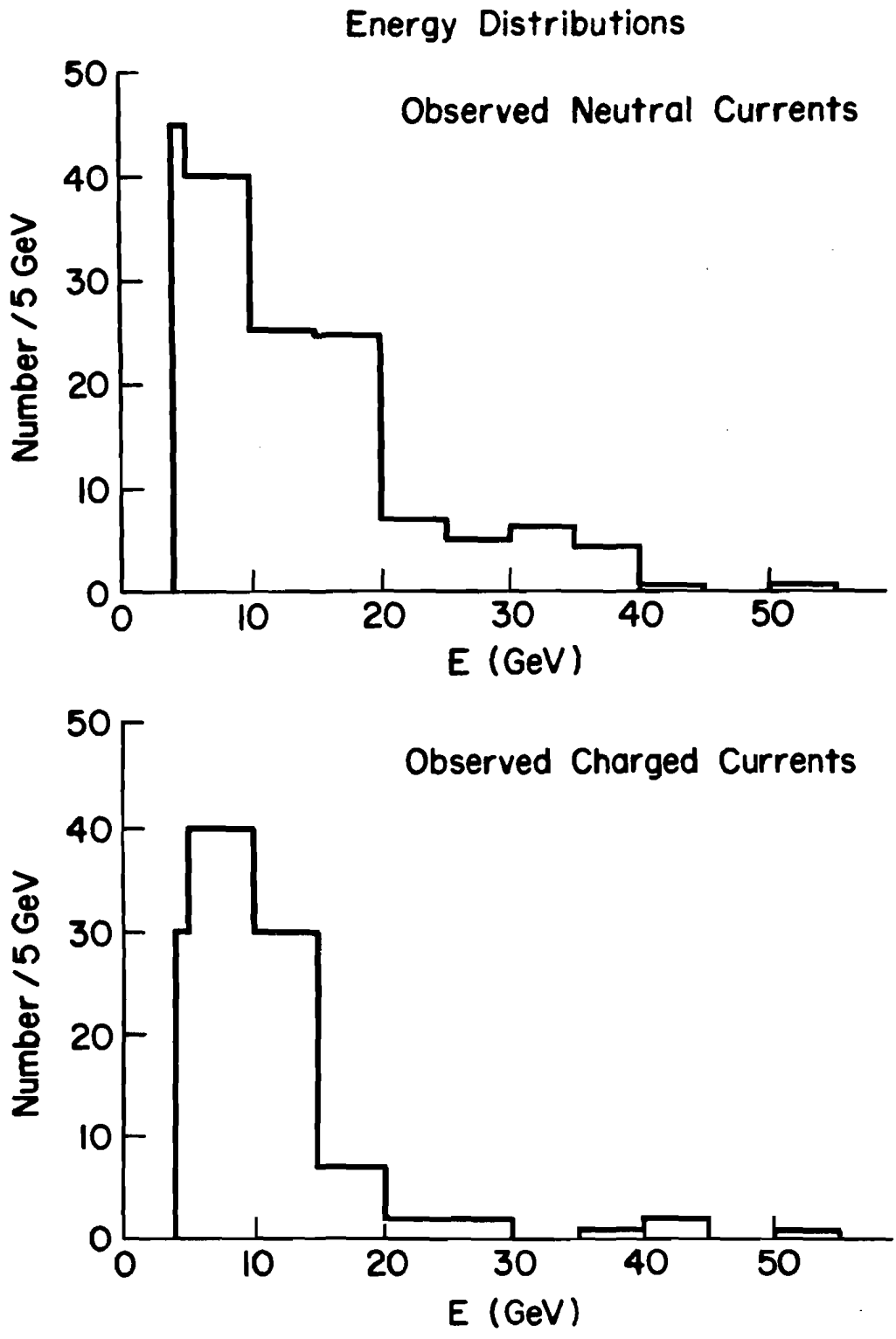

Fig. VI.20. Energy distributions for the observed neutral and charged currents

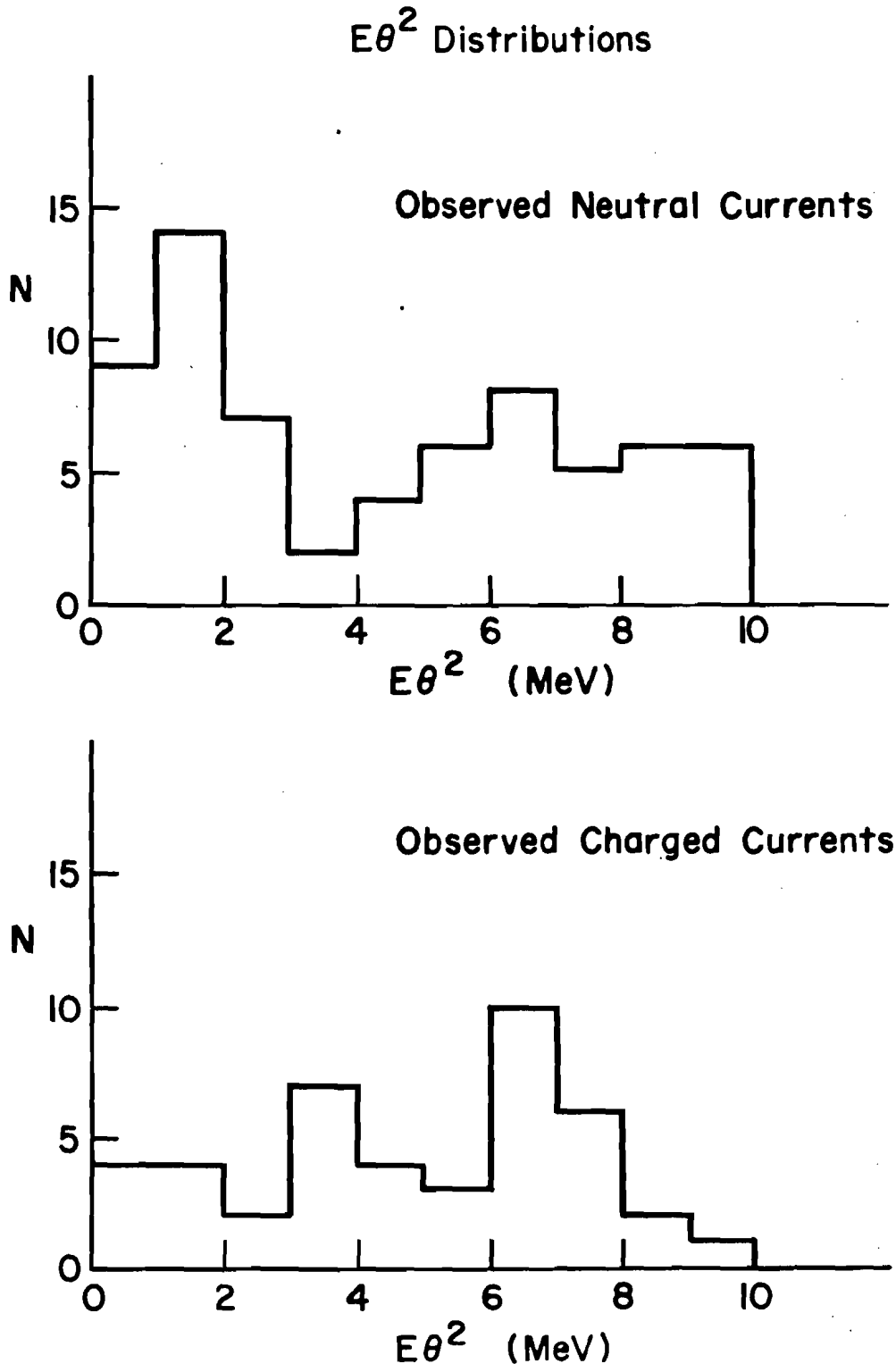

Fig. VI.21. $E\theta^2$ distributions for the observed neutral and charged currents

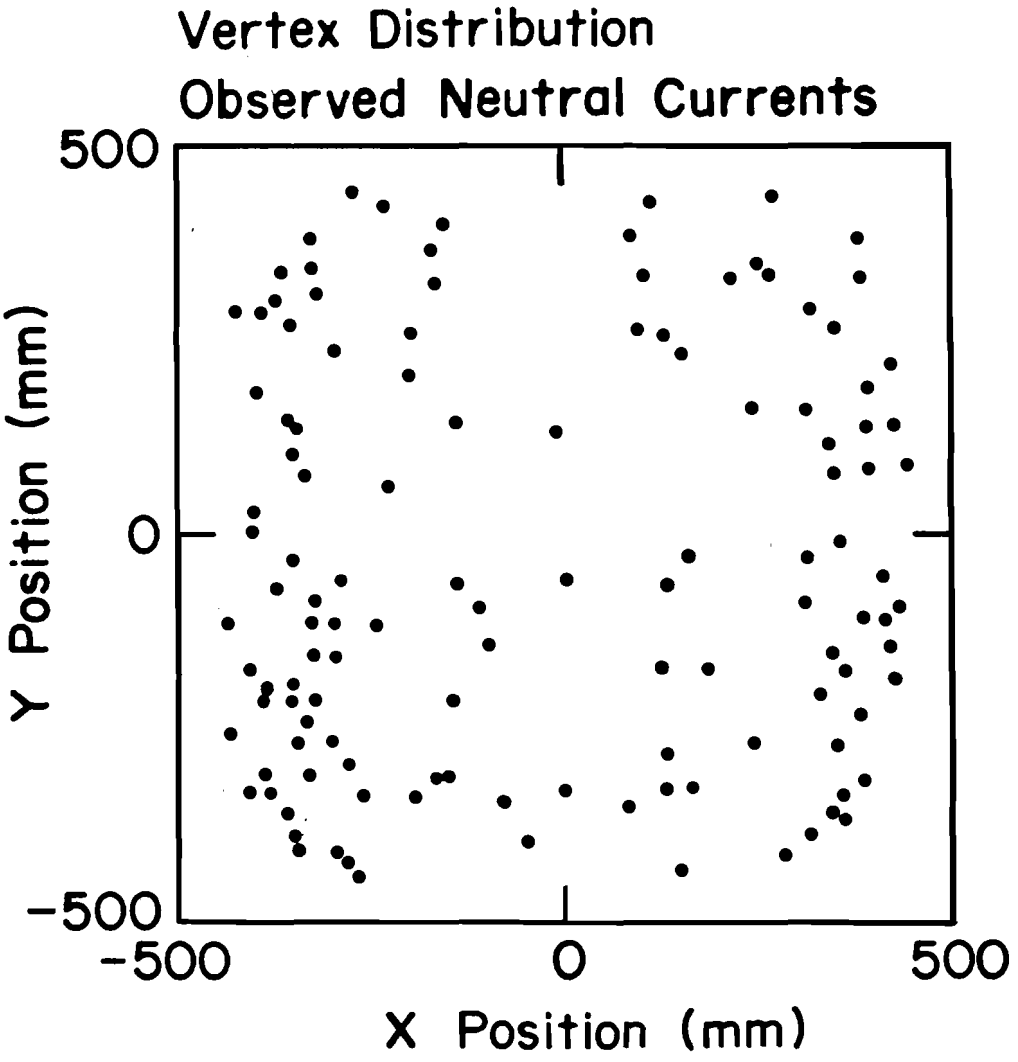

Fig. VI.22. Vertex distribution of the observed neutral currents

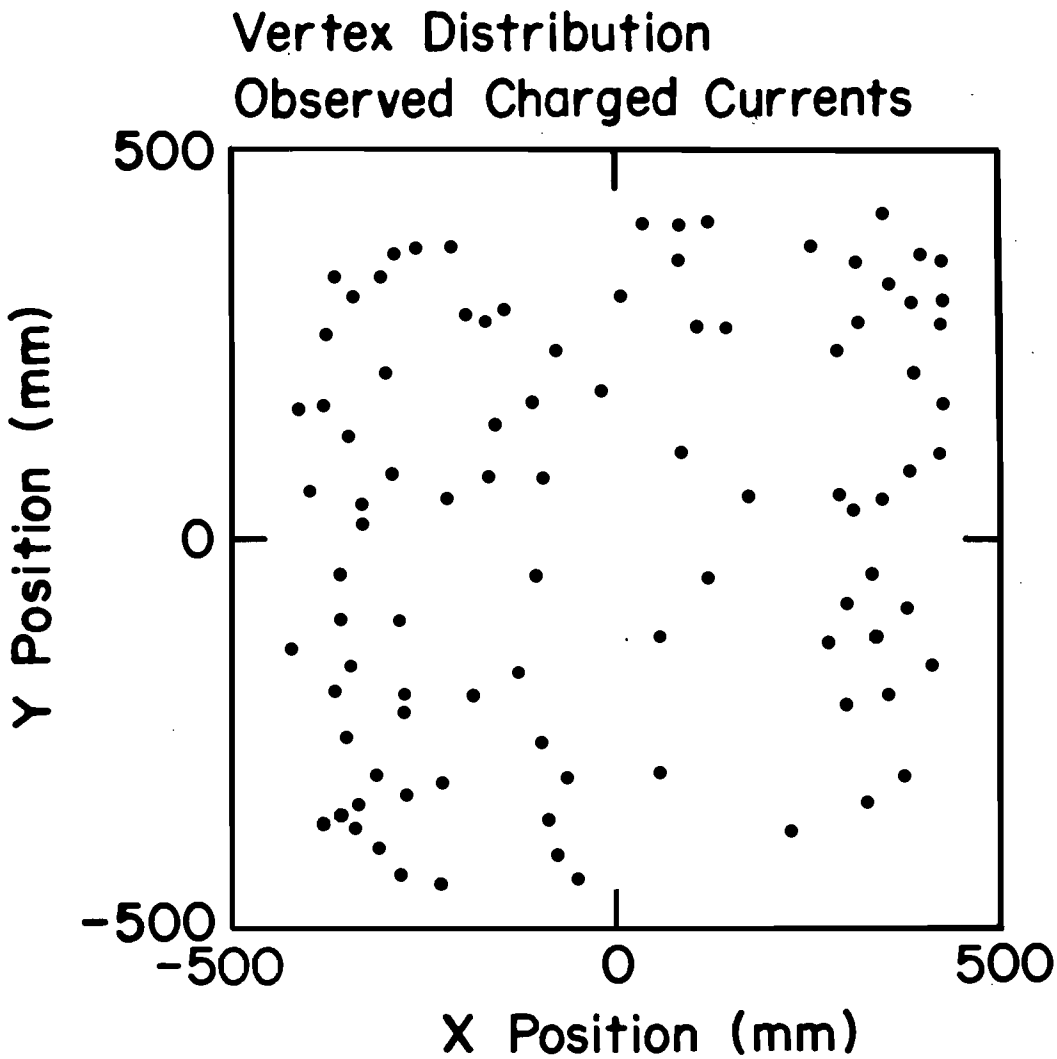

Fig. VI.23. Vertex distribution of the observed charged currents

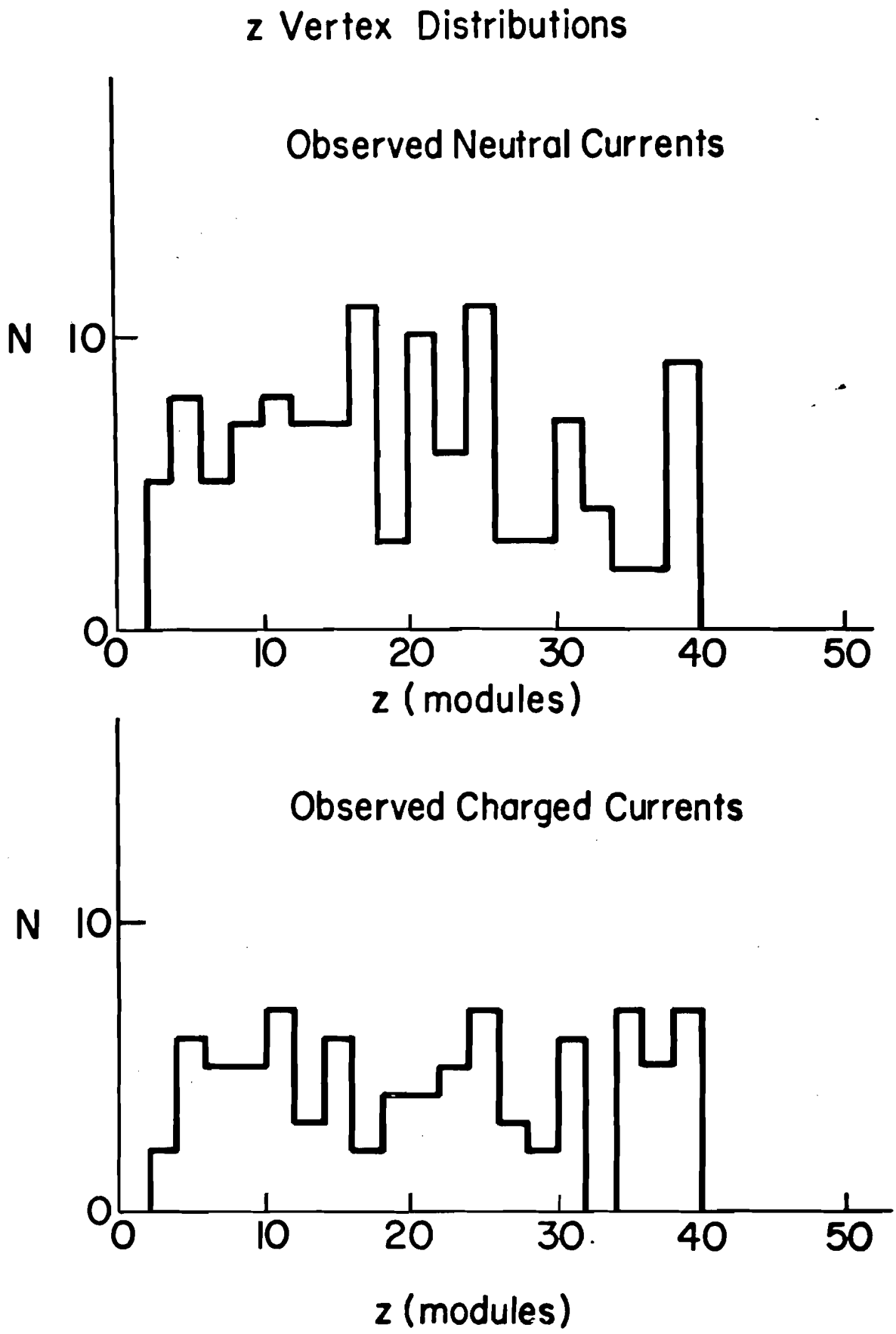

Fig. VI.24. Longitudinal vertex distributions for the observed neutral and charged currents

APPENDIX VI.1

TAP HIT FIDUCIAL CUT

A scanning fiducial cut is applied to the preselected events by demanding that no tap hits occur at an edge tap in the first five chambers containing the shower. This cut is in addition to the fiducial volume cut which requires the shower vertex to be at least 5 cm from the chamber edge. Since hadronic showers are much more likely to contain large angle particles which could cause a tap hit, this cut is less efficient on hadronic showers than on electron showers. The efficiency of the cut on accepting electron showers was determined by using 10 GeV electron test data.

In the electron test 10 GeV electrons were incident on ten fully instrumented modules. The electron beam was centered on the middle of the chambers. The fiducial cut was simulated by constructing an imaginary edge plane a distance 'd' from the vertex of the shower and parallel to the edge of the chamber. If a hit in one of the first five chambers of the shower intersects the imaginary edge plane than an edge tap hit would have occurred. For each event the distance of the imaginary plane from the shower vertex was varied and the possible tap hits noted.

Statistics were kept which furnished the probability that an electron shower with a vertex a distance 'd' from the edge of the chamber will induce a tap hit in one of the first 5 chambers of the shower. See Figure AVI.1. The statistics were kept for both the X and Y views

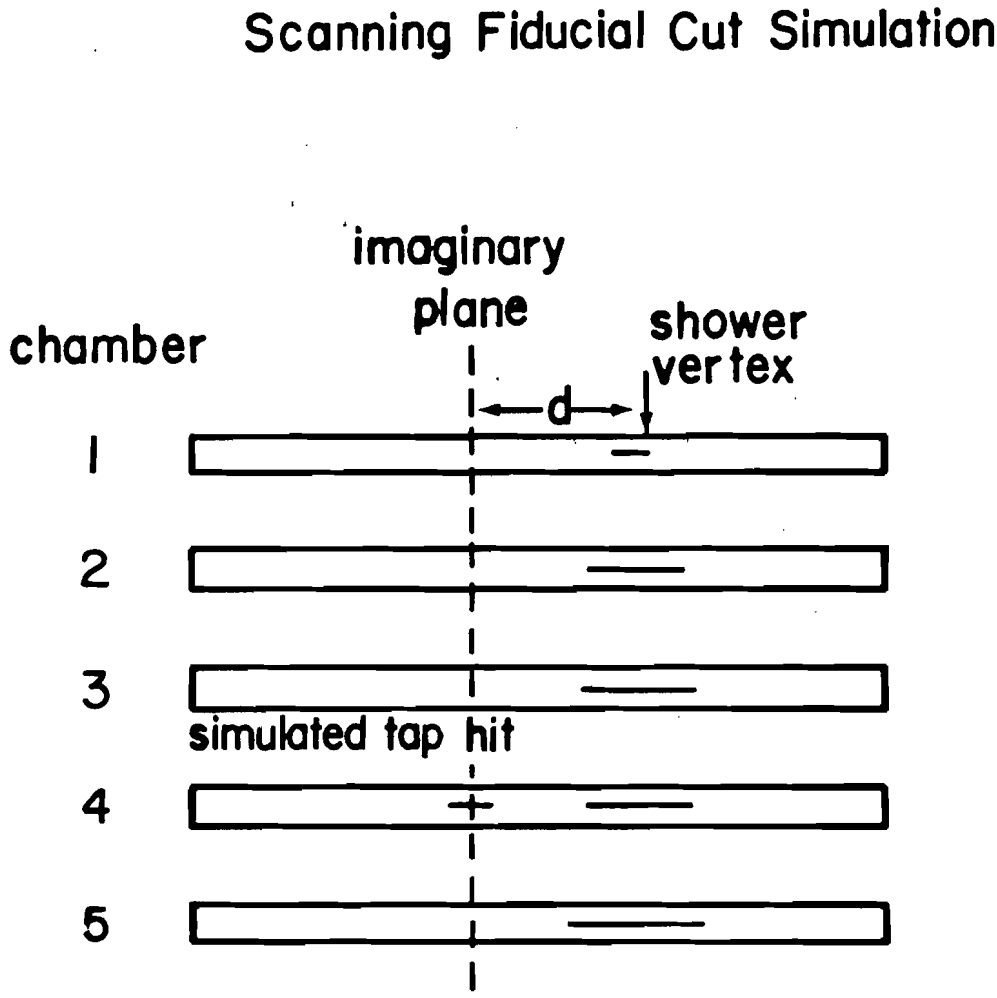

Fig. AVI.1. Example of a simulated tap hit for the scanning fiducial cut simulation

independently. The x and y acceptance is shown in Figure AVI.2. The overall acceptance of the cut determined from this probability distribution for events in the fiducial volume is 83%.

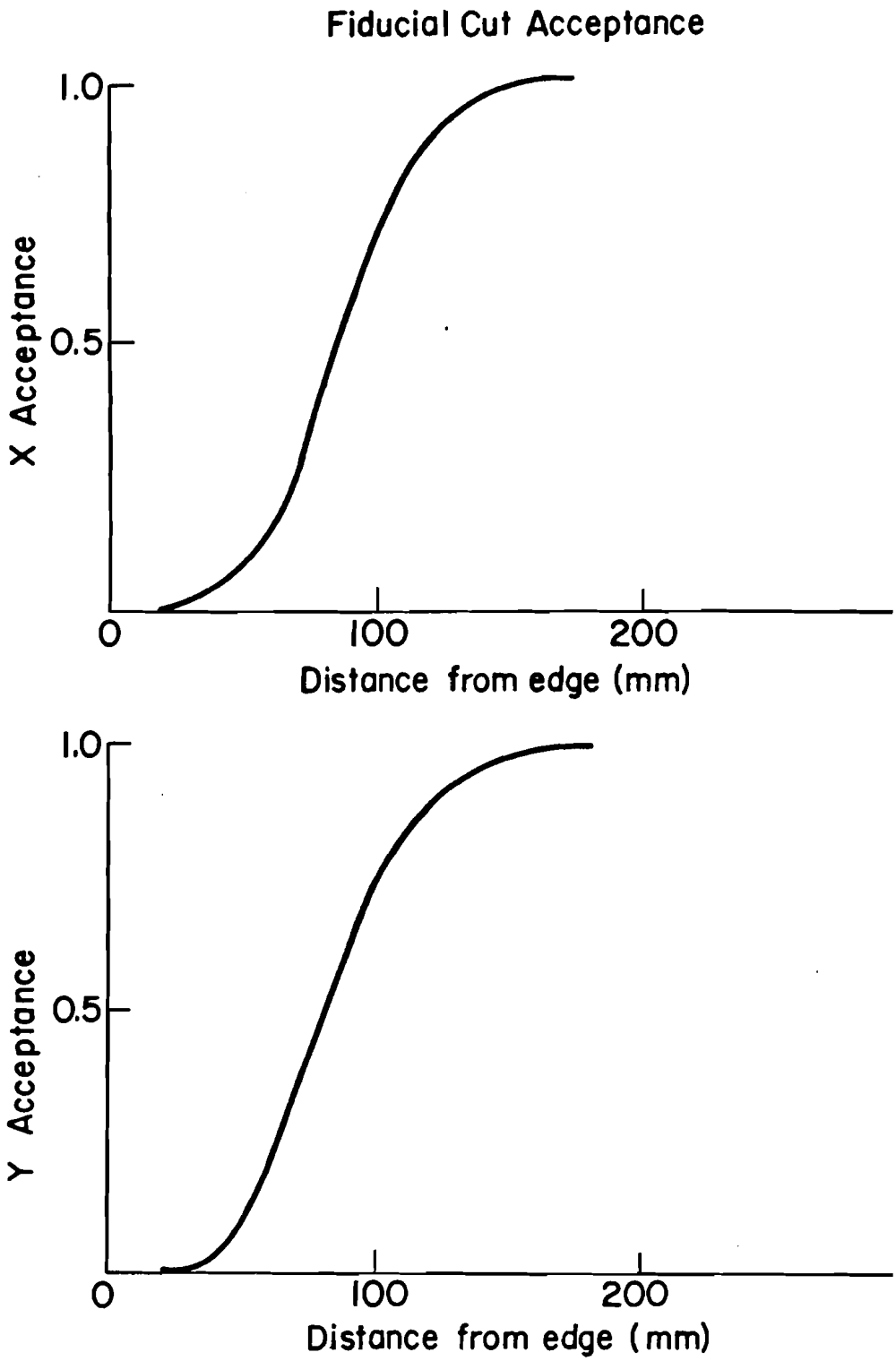

Fig. AVI.2. Calculated X and Y shower acceptance

CHAPTER VII

BACKGROUNDS

The scanning cuts are designed to accept only those triggers consisting of a single electromagnetic shower. If the shower is accompanied by any tracks from charged hadrons, then the event will be rejected. These cuts are designed to separate the neutrino electron interactions from raw data. In addition to the $\nu_\mu e$ signal, there are two types of backgrounds which will also be accepted by the selection criteria. Single electromagnetic showers can result from the quasielastic interactions $\nu_e n \rightarrow e^- p$ and $\bar{\nu}_e p \rightarrow e^+ n$, and from single pion production as in $\nu_\mu N \rightarrow \nu_\mu N\pi^\circ$ and $\nu_\mu N \rightarrow \mu^- N\pi^\circ$ with the muon unidentified. A monte carlo calculation was done to compute the quasielastic background contribution. The neutral current single pion background was calculated using the observed charged current π° production.

QUASIELASTIC BACKGROUNDS

The incident electron neutrino flux is about a factor of 400 smaller than the muon neutrino flux. The background is still significant since the total cross section is on the order of 10^{-38} cm^2 compared to the $\nu_\mu e$ cross section on the order of 10^{-42} E_ν cm^2/GeV. Although quasielastic interactions with electron type neutrinos have been observed using nuclear reactors as the neutrino source,[1] no data exists at accelerator energies. Much more data exists on the quasielastic interaction with muon type neutrinos. Using electron

muon universality and the fact that mass effects can be ignored since $E_\nu >> m_\mu$, the quasielastic data from muon type neutrinos can be used to calculate the quasielastic background from electron neutrinos.

The total and differential cross section has been measured using the CERN-PS neutrino beam and the Gargamelle Bubble Chamber.[2] The total and differential cross sections are shown in Figures VII.1 and VII.2 respectively. The differential cross section is strongly peaked at low q^2. The incident neutrino will transfer little energy to the target nucleon with most of the energy being carried by the electron shower. This is in contrast to neutrino electron scattering in which the scattered electron typically receives less than half the incident neutrino energy.

Assuming time-reversal invariance and the presence of first class currents only, then the differential cross section is given by:[3]

$$\frac{d\sigma}{dq^2} = \frac{G^2}{4\pi}\left\{\frac{(g_A - g_V)q^2}{2\,E_\nu^{\,2}} + (g_A \pm g_V)^2 + (g_A \mp g_V)^2\left(1 - \frac{q^2}{2mE_\nu}\right) + \left[2 - \frac{q^2(m + 2E_\nu)}{2mE_\nu^{\,2}}\right]\left[(4m^2 + q^2)f_v^{\,2} - 4mf_v g_v\right]\right\} \qquad \text{(VII-1)}$$

The upper (lower) sign refers to neutrino (antineutrino) scattering. The form factors g_V, g_A, and f_v are real. The conserved vector current hypothesis[4] can be used to relate the weak vector form factors g_V and f_v to the form factors observed in electron nucleon scattering:[5]

$$g_V = \left(1 - \frac{q^2}{2M^2}\right)\left(G_E^v\,(q^2) - \frac{q^2}{4M^2}\,G_M^v\,(q^2)\right)$$
$$f_V = \left(1 - \frac{q^2}{2M^2}\right)\left(\frac{1}{2M}\right)\left(G_M^v(q^2) - G_E^V(q^2)\right) \qquad \text{(VII-2)}$$

The dipole form factors G_E^V and G_M^V have been measured to be:[6]

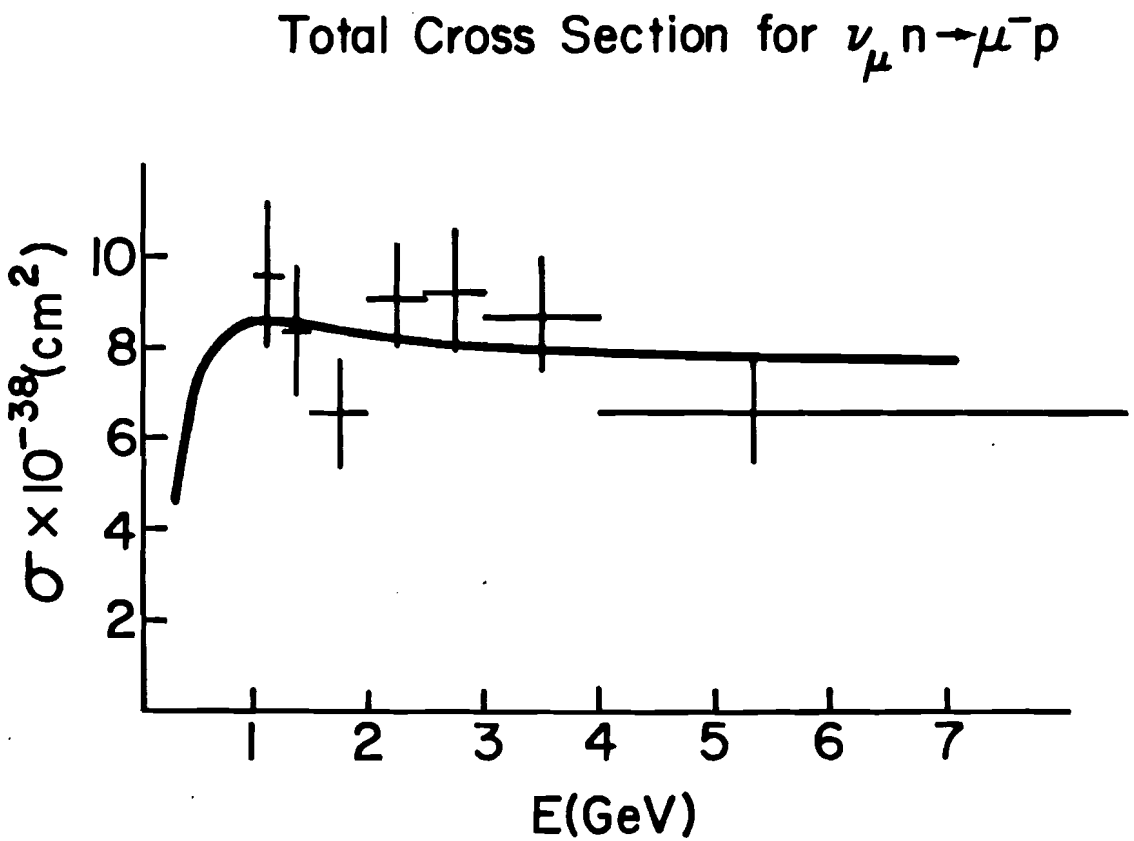

Fig. VII.1. The total cross section for $\nu_\mu n \to \mu^- p$ quasielastic scattering (See Ref. VII.2).

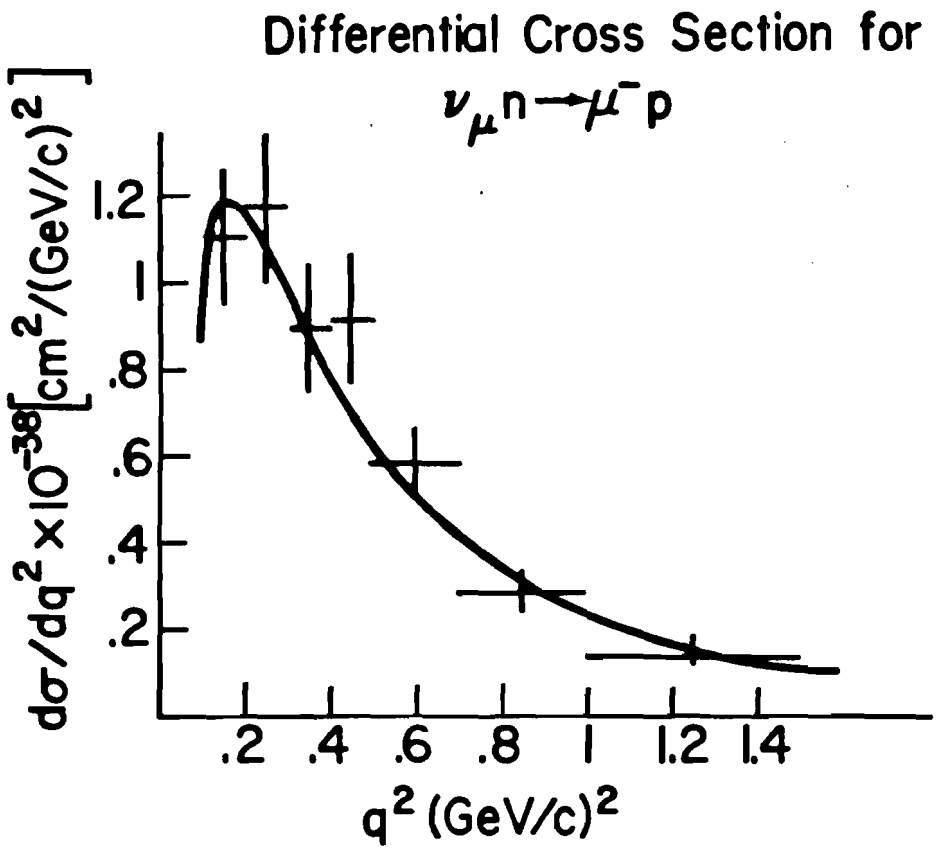

Fig. VII.2. The differential cross section for $\nu_\mu n \rightarrow \mu^- p$ quasielastic scattering (See Ref. VII.2)

$$G_E^V(q^2) = (q^2) = \frac{1}{\left(1 - \frac{q^2}{(.71)^2}\right)} \quad G_M^V = \frac{4.71}{\left(1 - \frac{q^2}{(.71)^2}\right)} \tag{VII-3}$$

The form factor g_A is also assumed to have the dipole form. The form factor determined in $\nu_\mu n \rightarrow \mu^- p$ is:[7]

$$g_A = \frac{1.23}{\left(1 - \frac{q^2}{(.88)^2}\right)^2} \tag{VII-4}$$

The differential cross section shown in equation VII-1 assumes the incident neutrino is scattered from a single isolated nucleon. Since the target nucleons are confined in an aluminum nucleus, the cross section must be modified to correct for nuclear structure effects.

Goulard and Primakoff have studied the effect of the Fermi motion and Pauli exclusion principle on the quasielastic differential cross section.[8] The correction is largest at low momentum transfers since the recoiling nucleon must recoil into an unoccupied momentum state. If the momentum transfer is greater than twice the Fermi level momentum then the recoiling nucleon is assured to be above the Fermi level and the correction factor is unity. The observed cross section will be given by:

$$\frac{d\sigma^{obs}}{dq^2} = \left(\frac{d\sigma}{dq^2}\right) F(q^2) \tag{VII-5}$$

The cross section correction factor $F(q^2)$ for aluminum is shown in Figure VII.3.

Given the incident neutrino flux and effective differential cross section, the Monte Carlo program calculates the energy and angular

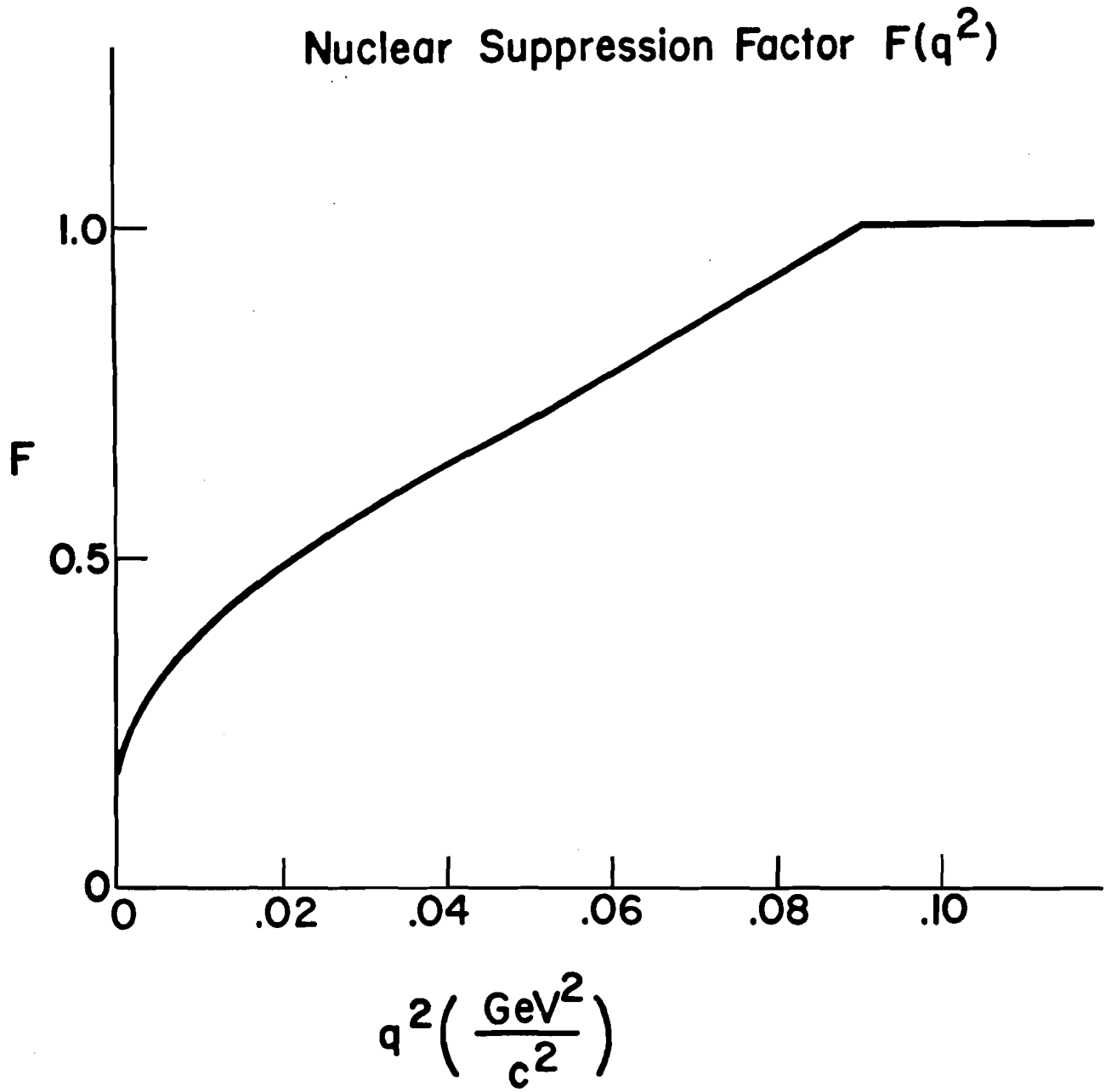

Fig. VII.3. The Pauli nuclear suppression factor $F(q^2)$

distributions for the quasielastic interactions. The program first randomly selects the interacting neutrino energy form the incident neutrino energy distribution and, from the differential cross section given by equation VII-1, determines the q^2 for that interaction. The energy and angle of the electron shower can be computed from the incident neutrino energy and q^2. The resolved shower angle and energy are determined from the kinematic values taking into account the detector angular and energy resolution. Histograms of the energy, angle, and $E\theta^2$ are accumulated using an energy cut of 4 GeV and weighing the events with the weight factor F defined in equation VII-5.

The calculated energy, angular and $E\theta^2$ distributions are shown in Figures VII.4 to VII.6 respectively. The angular distribution is weakly peaked at small angle due to the peaking of the differential cross section at low q^2. The most distinguishing feature of these events is their high average energy and correspondingly broad $E\theta^2$ distributions the average shower energy is about 50 GeV. The total number of events with energy above 4 GeV and angle less than 50 milliradians is 14.9 from the interaction $\nu_e n \rightarrow e^- p$ and 4.2 from $\bar{\nu}_e p \rightarrow e^+ n$.

The errors in the quasielastic background calculation are due to the uncertainties in the incident electron neutrino flux and uncertainty in the cross section. As is evident from an examination of Figure VII.1, the experimental uncertainty in the total cross section is about 20%. A much greater uncertainty exists in the incident electron neutrino flux. The magnitude of the incident flux is based on a calculation starting from an estimate of the secondary production from the neutrino area target. The accuracy of this estimate is unknown. In the case of the incident muon neutrino flux, a low energy threshold trigger was used to

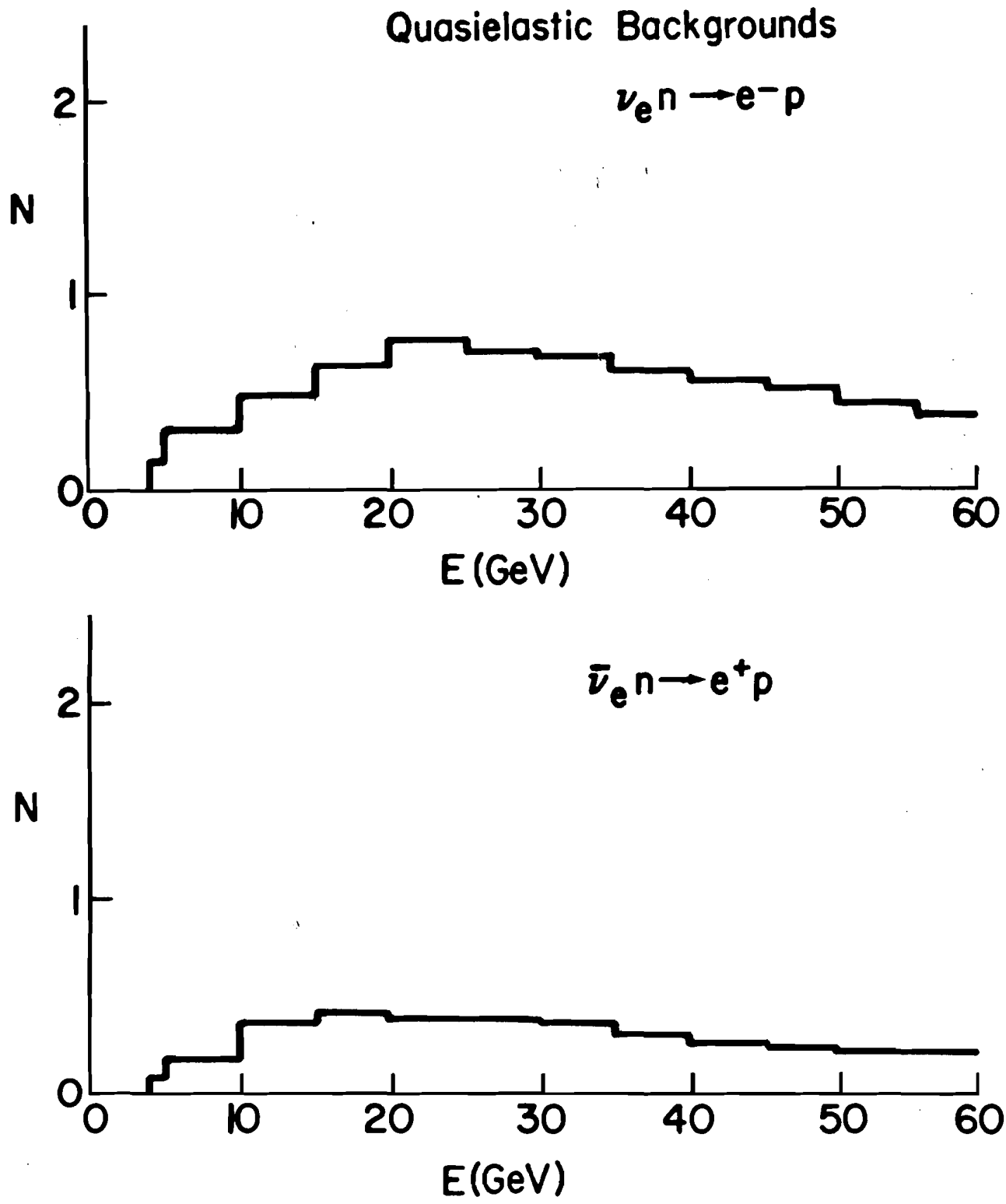

Fig. VII.4. The calculated energy distribution for quasielastic scattering

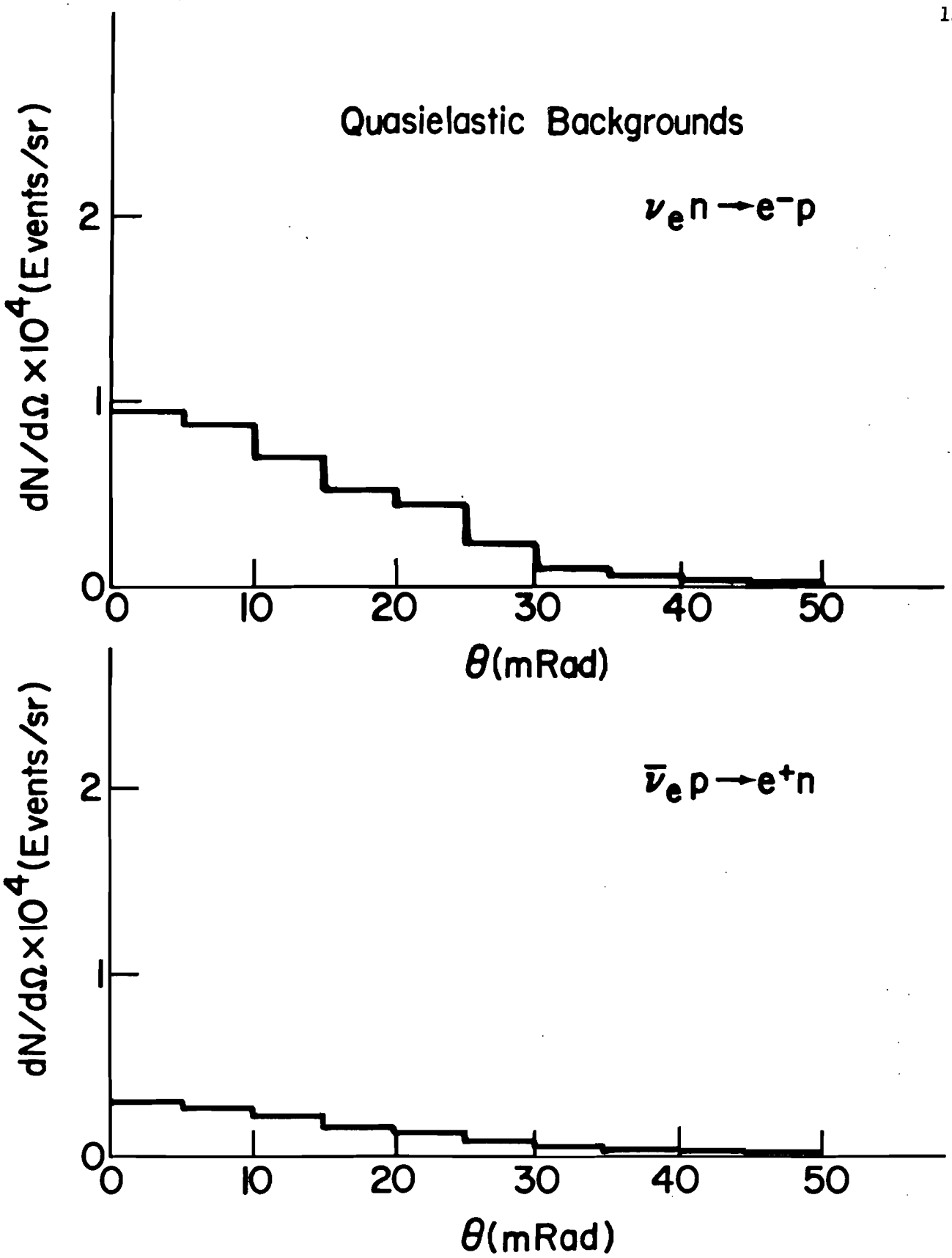

Fig. VII.5. The calculated angular distribution for quasielastic scattering

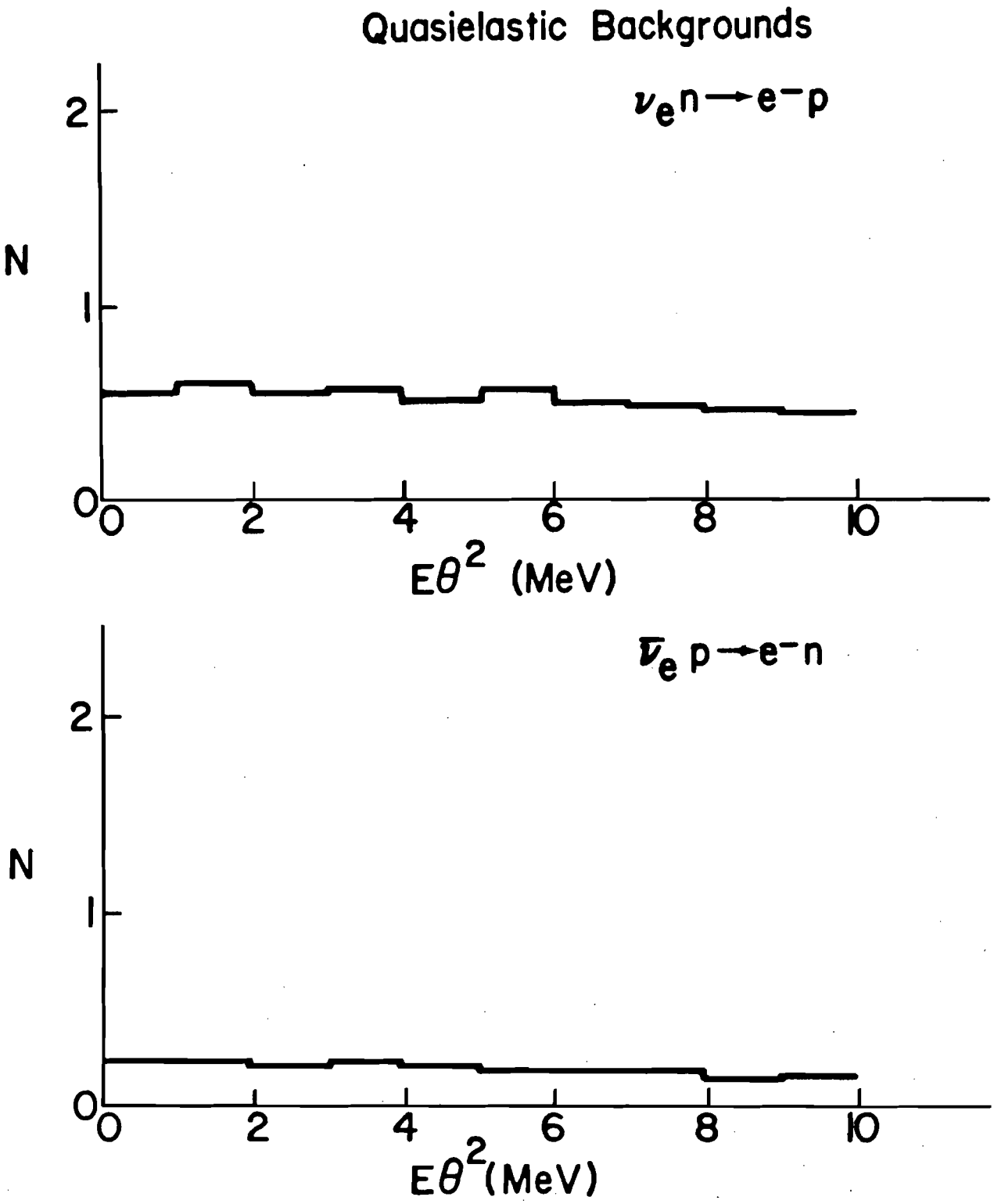

Fig. VII.6. The calculated $E\theta^2$ distribution for quasielastic scattering

determine the incident muon flux from the data. This is impossible to do for electron type neutrinos since they represent such a small portion of the incident flux and since they cannot be distinguished from the ν_μ events. The expected event rate from the corrected muon neutrino flux was a factor of 2 greater than the event rate calculated from the Stefanski-White flux. The Stefanski-White flux is also based on a calculation of the secondary production from the neutrino area target. The same errors in the Stefanski-White Flux may also be in the calculation of the electron neutrino flux. It is conservatively assumed that the error in the event rate from the quasielastic interactions due to the uncertainty in the electron neutrino flux is 100%. The total number of events from the quasielastic background is then 19.1 ± 19.1.

NEUTRINO NUCLEON BACKGROUND

Background from the $\nu_\mu N$ single pion production is more difficult to calculate since a precise theoretical understanding of these events is lacking. In addition, any $\nu_\mu N$ event with a large electromagnetic component in the shower and in which any accompanying charged hadrons are not seen can survive the cuts. Since no universally accepted model exists for these hadronic neutral current backgrounds, the observed charged current production was used to determine the neutral current background.

Throughout the data reduction process the neutral and charged current interactions have been subject to the same selection criteria. The preselection criteria by computer included a loose cut on the number of nonshower hits in the first 8 modules. It is possible, though unlikely, that the muon could leave enough nonshower hits to be rejected. The chamber efficiency for sensing a minimum ionizing

particle depends on the number of charged particles passing through the chamber. If only a single minimum ionizing particle passes through the chamber then the efficiency is above 80%, but if a shower is also passing through, then the efficiency at sensing an isolated minimum ionizing particle is below 10%. Therefore, one would expect most of the single pion events produced by the charged current to pass the pre-selection cuts. During the scanning the selection criteria were strengthened, but the presence of any muon track was ignored so that the selection or rejection of the event was based solely on shower characteristics.

The basic assumption in the calculation of the $\nu_\mu N$ background in the neutral current sample is that the physical processes involved in producing the shower do not depend on whether the exchanged boson is a Z° or W^+. This implies that the angle and energy distribution of the single pion is the same for both neutral and charged current events. The observed charged current distributions can be used to calculate the background in the neutral current sample.

The physics of the neutrino interaction which produces the π° can be considered in three stages. First the neutrino emits a virtual boson at the leptonic vertex. If a neutral current interaction occurs then a Z° is exchanged. If a charged current interaction occurs then a W^+ is exchanged. The exchanged boson will then interact with one of the quark constituents of the nucleon. Finally, during the fragmentation process, the struck quark, spectator quarks, and quarks generated from the sea rearrange themselves into the observed hadrons.

Since the incident neutrino energy is much greater than the muon mass, to a good approximation the muon mass can be neglected. The

kinematics at the leptonic vertex will be identical for both the neutral and charged current interactions so that the distribution in q^2 carried by the exchange bosons will be nearly identical. The q^2 is still small enough that propagator effects due to the difference in boson masses can be ignored. The difference in mass between the Z° and W^+ will only affect the overall interaction rate and not the shape of the differential cross section.

The principle quark constituents of the nucleon are the u and d quarks and a smaller s quark contribution. Since the target aluminum nucleus has nearly as many protons (13) as neutrons (14), to a good approximation the target is isoscalar. Therefore, the momentum distribution of the u quark in the target will be the same as the momentum distribution of the d quark. If $u(x)$ is the probability of finding a u quark in the target with fractional momentum x and $d(x)$ is the probability of finding a d quark with fractional momentum x, then $u(x) = d(x)$. An exchanged Z° will couple to all the quarks in the nucleon while an exchanged W^+ will couple only to the d and s quarks. The coupling of the bosons to the s quarks can be ignored since they comprise a small fraction of the nucleon and since it is unlikely that the s quark will fragment to produce a π°. Since the target is nearly isoscalar, the momemtum distribution of a scattered d quark from the exchanged W^+ will be the same as the distribution of the u and d quarks scattered by a Z°.

Finally, the scattered quark will fragment to produce a π°. Let $D_q^h(z)$ be the probability that a quark q will fragment into a hadron h with fractional momentum z, the u and d quarks have an equal probability of fragmenting to produce a π°, $D_u^{\pi^\circ}(z) = D_d^{\pi^\circ}(z)$.

Since at each stage of the interaction, from the emission of the exchanged boson at the leptonic vertex to the rearrangement of the final state quarks into the observed hadrons, the kinematics of the neutral current interaction are identical to the charged current interaction, the angular and energy distributions of the final state π° produced by the neutral current will be the same as the π° distributions produced by the charged currents. Since the Z°-quark and W^+-quark coupling strengths are different, the angle and energy distribution of the π° for the neutral current interaction are proportional and not identical to the charged current distributions.

This prediction has not been tested in the case of single pion production. Sufficient data does exist on the inclusive interactions $\nu_\mu N \rightarrow \nu_\mu + X$ and $\nu_\mu N \rightarrow \mu^- + X$. In inclusive scattering, the identity of the hadrons is not determined. It is assumed that the shower energy and direction represent the energy and angle of the recoiling quark. By the same argument as above, one would expect the shower energy and angle in neutral current events to be proportional to the distributions in the charged current events. The CHARM collaboration at CERN have tested this prediction.[10] Figure VII.7 shows the ratio of the number of neutral current to charged current events as a function of y. If the energy distributions are proportional then this ratio should be flat as a function of the variable y. Figure VII.8 shows the ratio of the number of neutral to charged current events as a function of the kinematic variable x. Although the statistics are limited, this ratio is also flat. This implies that the angular distributions are also proportional. Both of these figures are consistent with the assumption that:

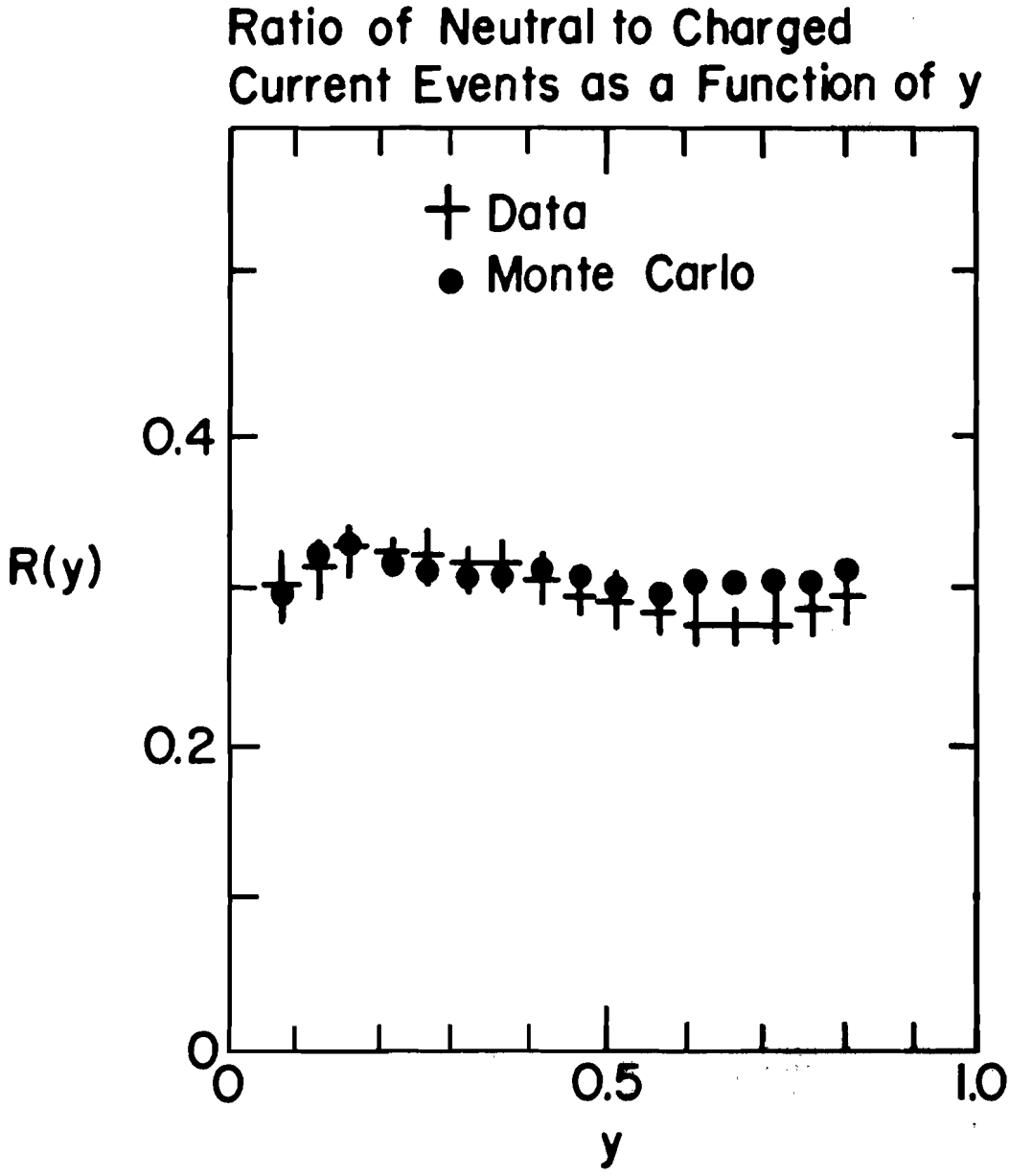

Fig. VII.7. Ratio of neutral to charged current inclusive events as a function of Y (See Ref. VII.10)

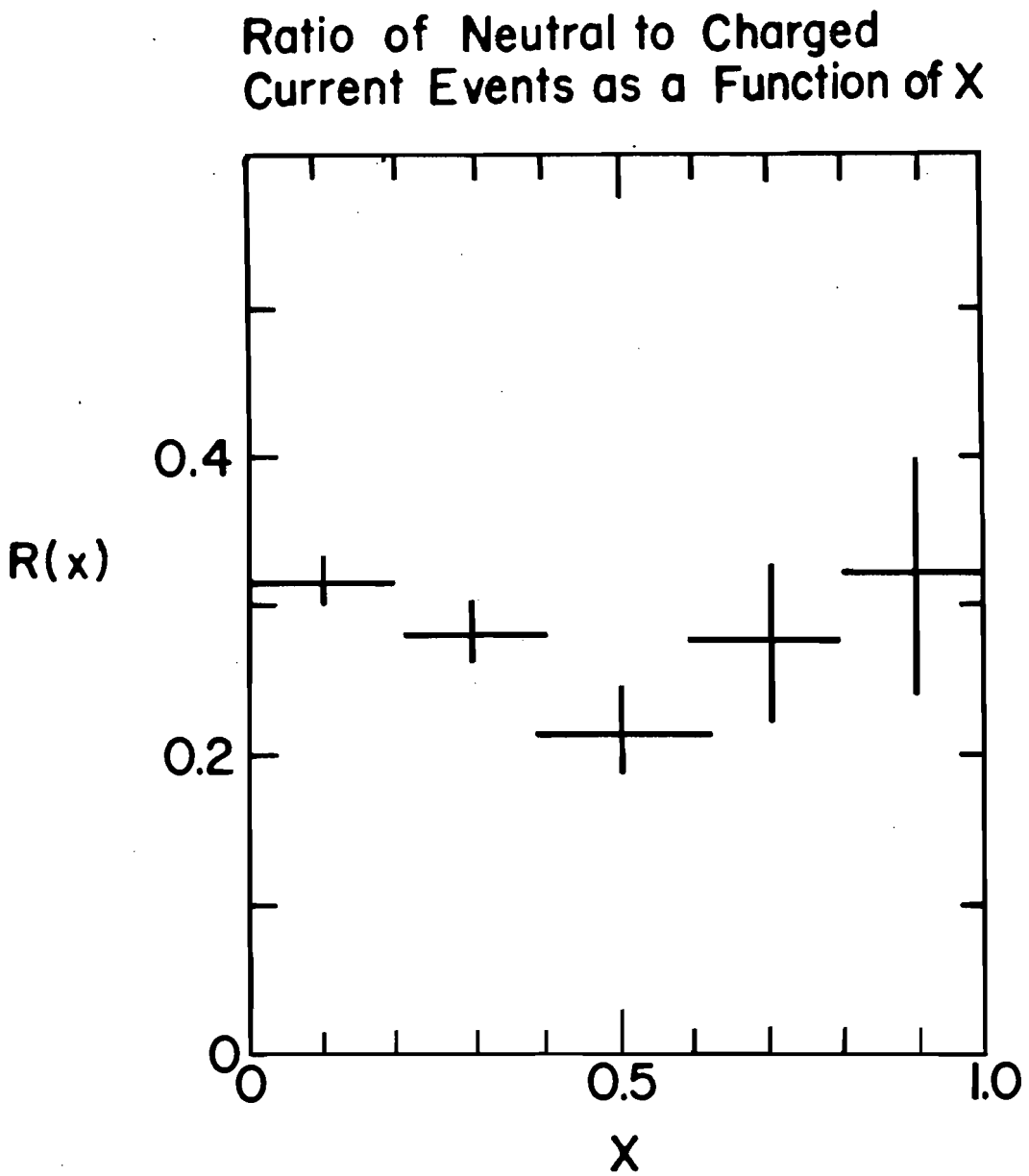

Fig. VII.8. Ratio of neutral to charged current inclusive events as a function of X (See Ref. VII.10)

$$\left.\frac{d^2N}{d\theta dE}\right|_{\nu_\mu N(NC)} = R \left.\frac{d^2N}{d\theta dE}\right|_{\nu_\mu N(CC)} \qquad \text{(VII-6)}$$

The constant of proportionality R is independent of energy and angle.

Not all of the charged current events will be identified as charged currents since the muon will sometimes escape undetected. Let $\alpha(\theta)$ be the probability that a charged current event with shower angle θ is classified as a charged current. The observed charged current distribution will be:

$$\left.\frac{dN}{d\theta}\right|^{obs}_{\nu_\mu N(CC)} = \alpha(\theta) \left.\frac{dN}{d\theta}\right|_{\nu_\mu N(CC)} \qquad \text{(VII-7)}$$

The misidentified charged currents will be classified as neutral currents. The observed neutral current distribution will be:

$$\left.\frac{dN}{d\theta}\right|^{obs}_{\nu_\mu N(NC)} = \left.\frac{dN}{d\theta}\right|_{\nu_\mu N(NC)} + (1 - \alpha(\theta)) \left.\frac{dN}{d\theta}\right|_{\nu_\mu N(CC)} \qquad \text{(VII-8)}$$

Combining equations VII-6 to VII-8 gives:

$$\left.\frac{dN}{d\theta}\right|^{obs}_{\nu_\mu N(NC)} = \frac{R + 1 - \alpha(\theta)}{\alpha(\theta)} \left.\frac{dN}{d\theta}\right|^{obs}_{\nu_\mu N(CC)} \qquad \text{(VII-9)}$$

The background from single π° production in the observed neutral current sample can be calculated from the observed production by the charged current if the parameters $\alpha(\theta)$ and R are known.

The muon identification probability $\alpha(\theta)$ was determined using a Monte Carlo calculation which modeled the muon identification criteria. See Appendix VII.1 for the details of the calculation. Figure VII.9 shows the muon identification probability as a function of θ.

Several experimental determinations of the ratio of the neutral current to charged current rates have been done and are summarized in Table VII.1. The values range from .30 $\pm$ .02 in neutrino inclusive

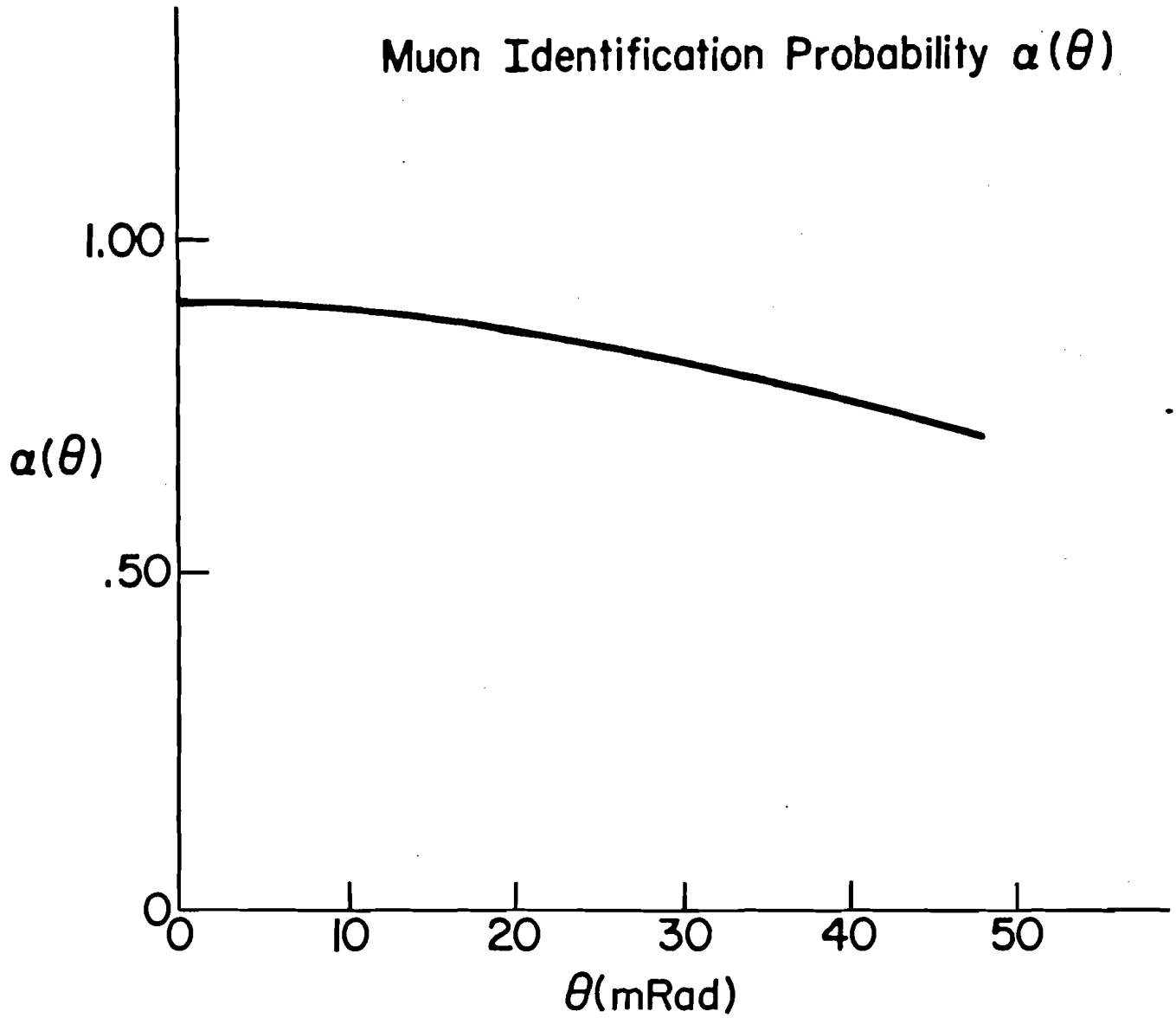

Fig. VII.9. The calculated muon identification probability

Reference	Target	R
Lee, et al.[11]	Aluminum	$.34 \pm .08$
Hansl, et al.[12]	Aluminum	$.80 \pm .12$
Hasert, et al.[13]	Freon	$.20 < R < .40$
	Weighted Average	$.42 \pm .14$
Krenz, et al.[14]	Propane	$.45 \pm .16$
Winter, et al.[15]	Marble	$.30 \pm .02$

$$R = \frac{\nu_\mu A \to \nu_\mu A' \pi^\circ}{\nu_\mu A \to \mu^- A' \pi^\circ} \qquad A = \text{Atomic nucleus}$$

Table VII.1. Experimental measurements of the ratio of single π° production by the neutral and charged currents.

scattering to .90 ± .16 in single pion production on a propane target. The value of .42 ± .14 from single pion production on complex nuclei is a weighted average from three experiments. This measurement represents the value most relevant to single pion production on aluminum.

The value for R can also be computed from the data. The $\nu_\mu e$ signal in the observed neutral current sample will be confined below 20 milliradians. Above 20 milliradians the sample will be composed of quasielastic and $\nu_\mu N$ background events. The value of R can be computed by fitting the angular distributions above 20 milliradians using the formula:

$$\left.\frac{dN}{d\theta}\right|^{obs}_{\substack{NC \\ \theta>20}} = \varepsilon_R \left.\frac{dN}{d\theta}\right|^{(-)}_{\substack{\nu_e \\ \theta>20}} + \frac{R + 1 - \alpha(\theta)}{\alpha(\theta)} \left.\frac{dN}{d\theta}\right|^{obs}_{\substack{\nu_\mu N(cc) \\ \theta>20}} \qquad \text{(VII-10)}$$

The constant ε_R is the efficiency for accepting electrons and will be described in greater detail in the next chapter. The value for R computed by this method is .60 ± .15. This is somewhat higher than the experimental value for R measured in other experiments with complex nuclei. The discrepancy may be due to an inefficiency for preselecting charged currents events as compared to neutral current events by the computer prior to scanning. This value probably gives the most accurate determination of the single pion production background since it correctly fits the data in the large angle region.

The angular distribution of the $\nu_\mu N$ background in the observed neutral current sample using the values for the ratio R of .60 ± .15 and .42 ± .14 are shown in Figure VII.10. The distributions are relatively flat with the uncertainty in R giving about a 30% difference in the magnitude of $dN/d\Omega$. Chapter VIII discusses the error introduced by this uncertainty in greater detail.

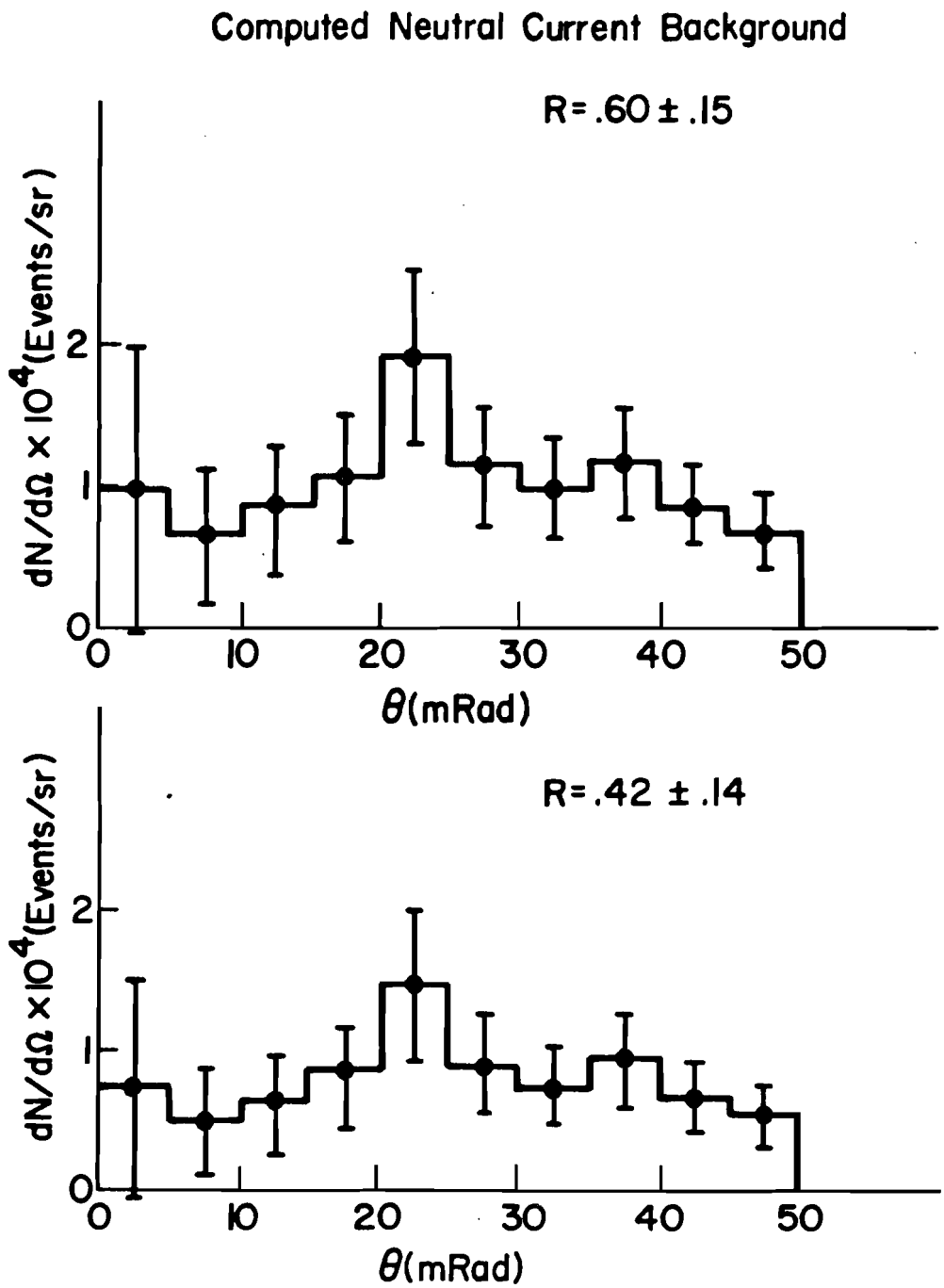

Fig. VII.10. The computed $\nu_\mu N$ neutral current background for $R = .60 \pm .15$ and $.42 \pm .14$

CHAPTER VII

REFERENCES

1. F. Reines and C. Cowan, Jr., Physical Review, 113, 273 (1959); F. Nezrick and F. Reines, Physical Review, 142, 852 (1965).
2. M. DeWitt, Proceedings of the Topical Conference on Neutrino Physica at Accelerators, Oxford, p. 75 (1978).
3. T. Lee and C. Yang, Physical Review, 126, 2239 (1962).
4. R. Feynmann and M. Gell-Mann, Physical Review, 109, 193 (1958).
5. C. Llewellyn Smith, Physics Reports, 3C, 261 (1972).
6. B. Bartoli, et al., Rivista Del Nuovo Cimento, 2, 241 (1972).
7. M. DeWitt, Proceedings of the topical Conference on Neutrino Physics at Accelerators, Oxford, p. 75 (1978).
8. B. Goulard and H. Primakoff, Physical Review, 135, 1139 (1964).
9. R. Field and R. Feynman, Nuclear Physics, B136, 1 (1978).
10. K. Winter, Proceedings of the 1979 International Symposium on Lepton and Photon Interactions at High Energies, Fermilab, p. 258 (1979).
11. W. Lee, et al., Physical Review Letters, 38, 202 (1978).
12. T. Hansel, et al., Proceedings of the International Neutrino Conference, Aachen, p. 278 (1976).
13. F. Hasert, et al., Physics Letters, 33, 485 (1975).
14. W. Krenz, et al., Nuclear Physics, B135, 45 (1978).
15. K. Winter, Proceedings of the 1979 International Symposium on Lepton and Photon Interactions at High Energies, Fermilab, p. 258 (1979).

APPENDIX VII.1

MUON IDENTIFICATION PROBABILITY

The calculation of the n neutral current background from the observed charged current events requires the knowledge of the muon identification probability. Not all charged current events will be classified as charged currents since the muon may escape the detector unseen. During the scanning process events are classified as charged currents if five consecutive chambers after the shower has dispersed show a minimum ionizing pulse height, or if there is a coincidence between hodoscopes B and C, or if a hit in hodoscope C, two chamber hits and the shower vertex are all consistent with a muon from the vertex. The muon identification probability was determined by simulating these criteria using a monte carlo program.

The monte carlo program first randomly selects the incident neutrino energy from the neutrino flux distribution. The angle of the resulting shower is randomly chosen between 0 and 50 milliradians while the shower energy is chosen between 0 and the incident neutrino energy. The four momentum of the final state muon is determined by conservation of energy and momentum. The shower vertex is randomly distributed in the fiducial volume.

The selected neutral current sample was used to determine the relationship between the shower energy and length (see Figure AVII.1). The dispersion was five radiation lengths. The program randomly selects the shower length given the energy and the above distribution. If the

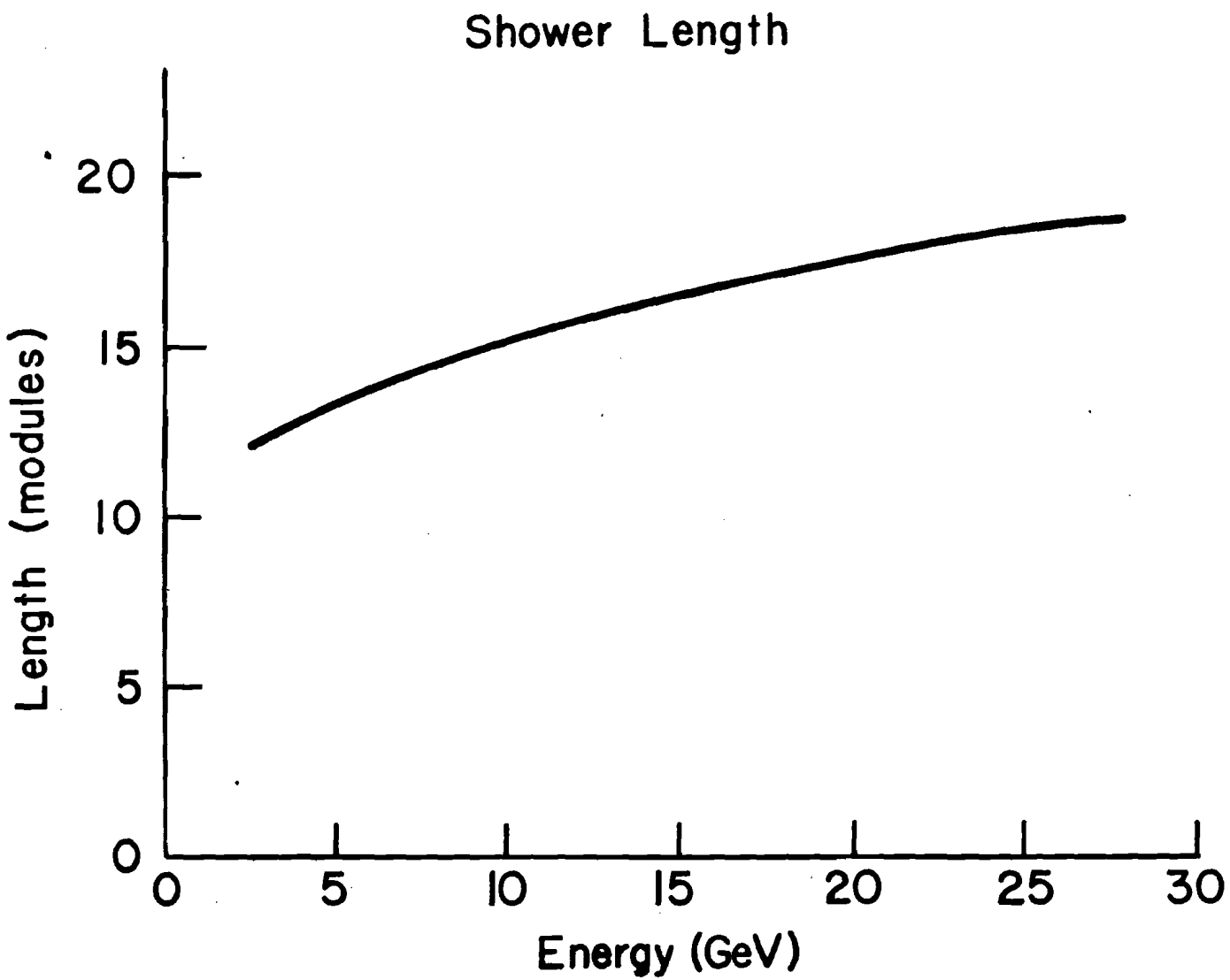

Fig. AVII.1 The average shower length as a function of energy

shower is exiting out the side of the detector, then the length is the smaller of the containment length or the randomly selected length.

The program will classify the event as a charged current if the muon containment length is more than four modules greater than the shower length, or if the muon passes through both the B and C hodoscopes or if the muon containment length is greater than 8 modules and passes through hodoscope C.

Statistics were kept which gave the probability that a charged current event with shower angle is classified as a charged current. The muon identification probability is shown in Figure VII.9.

CHAPTER VIII

RESULTS

The observed neutral current sample contains contributions from $\nu_\mu e$ events, $\overset{(-)}{\nu}_e$ quasielastic interactions, and events from single π° production in $\nu_\mu N$ scattering. The $\overset{(-)}{\nu}_e$ quasielastic and $\nu_\mu N$ backgrounds were calculated in the previous chapter. The angular distribution of the $\nu_\mu e$ signal can be determined from the equation:

$$\left.\frac{dN}{d\Omega}\right|_{\nu_\mu e} = \frac{1}{\varepsilon}\left[\left.\frac{dN}{d\Omega}\right|_{NC} - \left.\frac{dN}{d\Omega}\right|^{calc}_{\nu_\mu N(NC)}\right] - \left.\frac{dN}{d\Omega}\right|_{\overset{(-)}{\nu}_e} \qquad \text{(VIII-1)}$$

The parameter ε is the overall efficiency for selecting $\nu_\mu e$ events from the raw data sample. This efficiency will be a product of the efficiency of the computer preselection algorithm for selecting electromagnetic showers, the efficiency of the scanning criteria for selecting $\nu_\mu e$ events, and the efficiency of the scanner in implementing the scanning criteria consistently.

SELECTION EFFICIENCY

The overall efficiency is given by:

$$\varepsilon = \varepsilon_c \cdot \varepsilon_s \cdot \varepsilon_{SN} \qquad \text{(VIII-2)}$$

ε_c = computer selection efficiency

ε_s = scanning selection efficiency

ε_{SN} = scanner efficiency

As discussed in Chapter VI, the computer selection efficiency was found to be .97 ± .05 by applying the preselection algorithm to the 10

GeV test data. The scanning selection efficiency was determined to be .69 ± .06 by applying the scanning criteria to the test data sample and by calculating the scanning fiducial cut acceptance from the same sample.

The scanner efficiency measures the ability of the scanning physicist to apply the scanning cuts to the preselected data sample in a consistent manner. The scanning efficiency was determined by rescanning 20% of the preselected events. The rescanned sample consisted of 17 runs from the torroids off running and 17 runs from the torroids on running. The scanner efficiency is .81 ± .16. Applying equation VIII-2 gives the overall selection efficiency of .54 ± .12.

RESULTS

Using this selection efficiency and the calculated backgrounds in Chapter VII, the $\nu_\mu e$ signal can be determined from equation VIII-1. Figure VIII.1 shows the angular distribution for the neutral current sample after the backgrounds have been subtracted. The $\nu_\mu e$ signal is clearly seen. A Monte Carlo calculation of the expected distribution from the electroweak model with $\sin^2\theta_W$ of .25 and an angular resolution of 5 milliradians is also shown. Applying an angle cut at 20 milliradians gives a ν_μ signal of 35.9 ± 13.0.

A tighter cut can be made by using the kinematic constraint on $E\theta^2$. Neglecting resolution effects, the variable $E\theta^2$ is constrained to be below $2m_e \sim 1$ MeV. An examination of Figure VI-19 shows a peak in the $E\theta^2$ distribution for the observed neutral current sample below 3 MeV. Table VIII.1 shows the details of a background subtraction using cuts on the data and Monte Carlo results of $\theta < 20$ milliradians and $E\theta^2 < 3$ MeV.

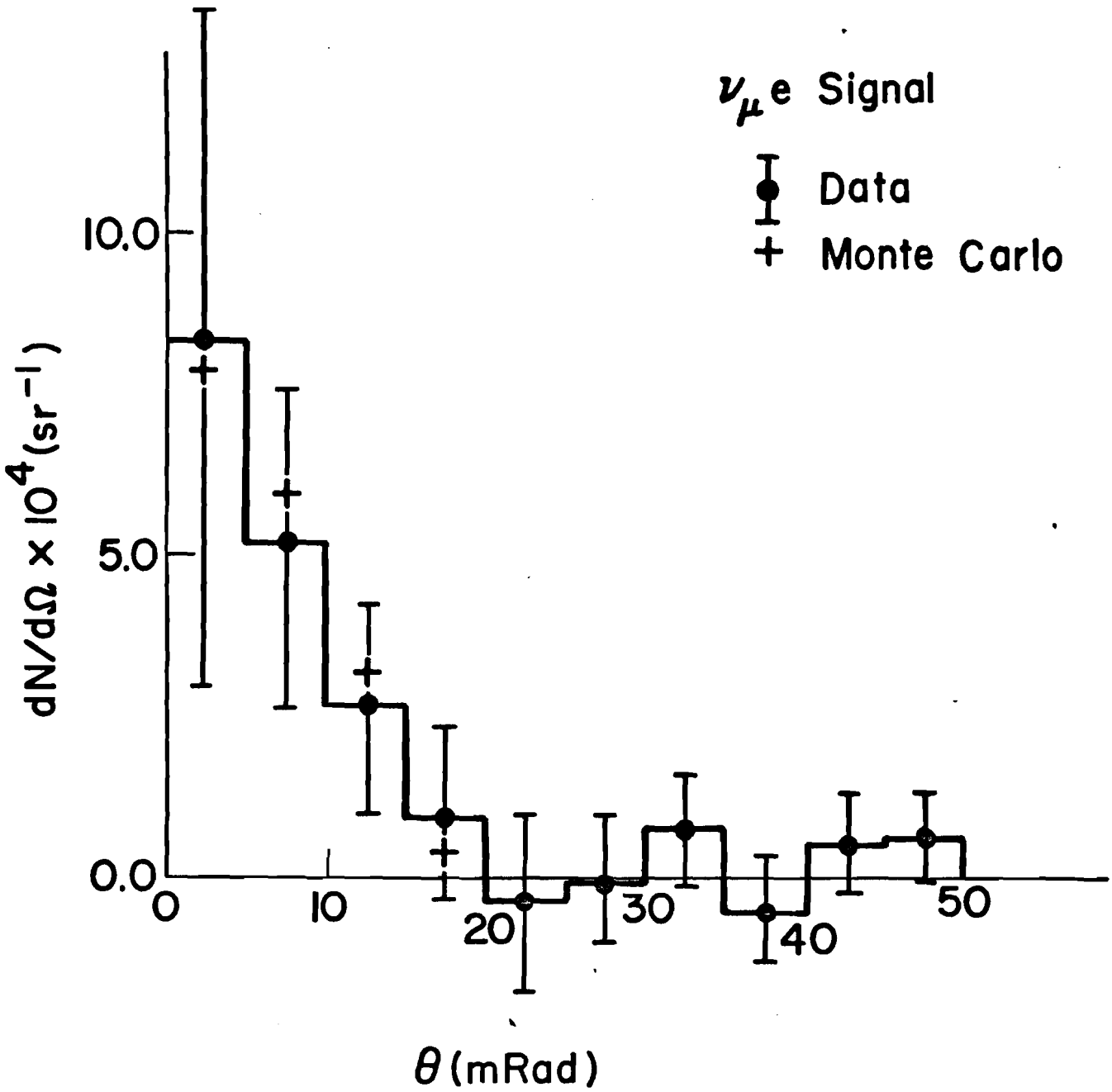

Fig. VIII.1 The angular distribution of the neutral current sample after background subtraction

	# with $\theta < 20$ mrad, $E\theta^2 < 3$ MeV
Observed Neutral Currents	28 ± 5.3
Observed Charged Currents	10 ± 3.2
Calculated $\nu_\mu N$ background	8.4 ± 3.2
Corrected for efficiency	36.0 ± 11.4
Calculated $\overset{(-)}{\nu}_e$ background	3.0
$\nu_\mu e$ signal	33.0 ± 11.3

Table VIII-1. Details of background subtraction.

Measured Signal	events 33.0 ± 11.3	% of signal
Error from $\overset{(-)}{\nu}_\mu$ flux	5.0	15%
Error from $\overset{(-)}{\nu}_e$ flux	3.0	10%
Error from uncertainty in R	2.0	7%
Error in selection efficiency	7.9	24%
Summed error	10.0	33%

Table VIII-2. Details of systematic errors.

The signal is given by:

$$N_{\nu_\mu e} = \frac{1}{\varepsilon}\left[N_{NC}\Big|_{E\theta^2<3}^{\theta<20} - \frac{R+1-\tilde{\alpha}}{\tilde{\alpha}} N_{cc}^{obs}\Big|_{E\theta^2<3}^{\theta<20}\right] - N_{\overset{(-)}{\nu}_e}\Big|_{E\theta^2<3}^{\theta<20} \qquad \text{(VIII-3)}$$

The parameter $\tilde{\alpha}$ is the average muon identification probability for charged current events satisfying the angle and $E\theta^2$ cuts. This calculation gives a ν_μ signal of 33.0 ± 11.3 which is consistent with the previous calculation.

As a consistency check one can compare the energy distribution of the events satisfying the angle and $E\theta^2$ cuts with the expected energy distribution using the electroweak model with $\sin^2\theta_W$ of .25. Figure VII.2 shows the energy distribution for the data compared to a Monte Carlo calculation using the electroweak model. There is an excess of events in the data since the quasielastic and single pion production background are not subtracted. Of the 28 events in the observed neutral current sample, 8 are background events due to $\nu_\mu N$ single π° production and one is due to $\overset{(-)}{\nu}$ quasielastic scattering. The shape of the Monte Carlo calculation is consistent with the data.

The measured signal of 33.0 ± 11.3 represents the number of $\nu_\mu e$ events and a smaller number of $\bar{\nu}_\mu e$ events occurring in the fiducial volume with a shower energy above 4 GeV. Since the $\bar{\nu}_\mu$ flux is about a factor of 8 below the ν_μ flux, only a few of these events are $\bar{\nu}_\mu e$ interactions. To compute the total cross section for $\nu_\mu e$ elastic scattering from the event number observed one must correct for the $\bar{\nu}_\mu e$ contamination and for the 4 GeV energy cut.

One can account for the energy cut in a model independent way by using the phenomenological cross sections based on the coupling

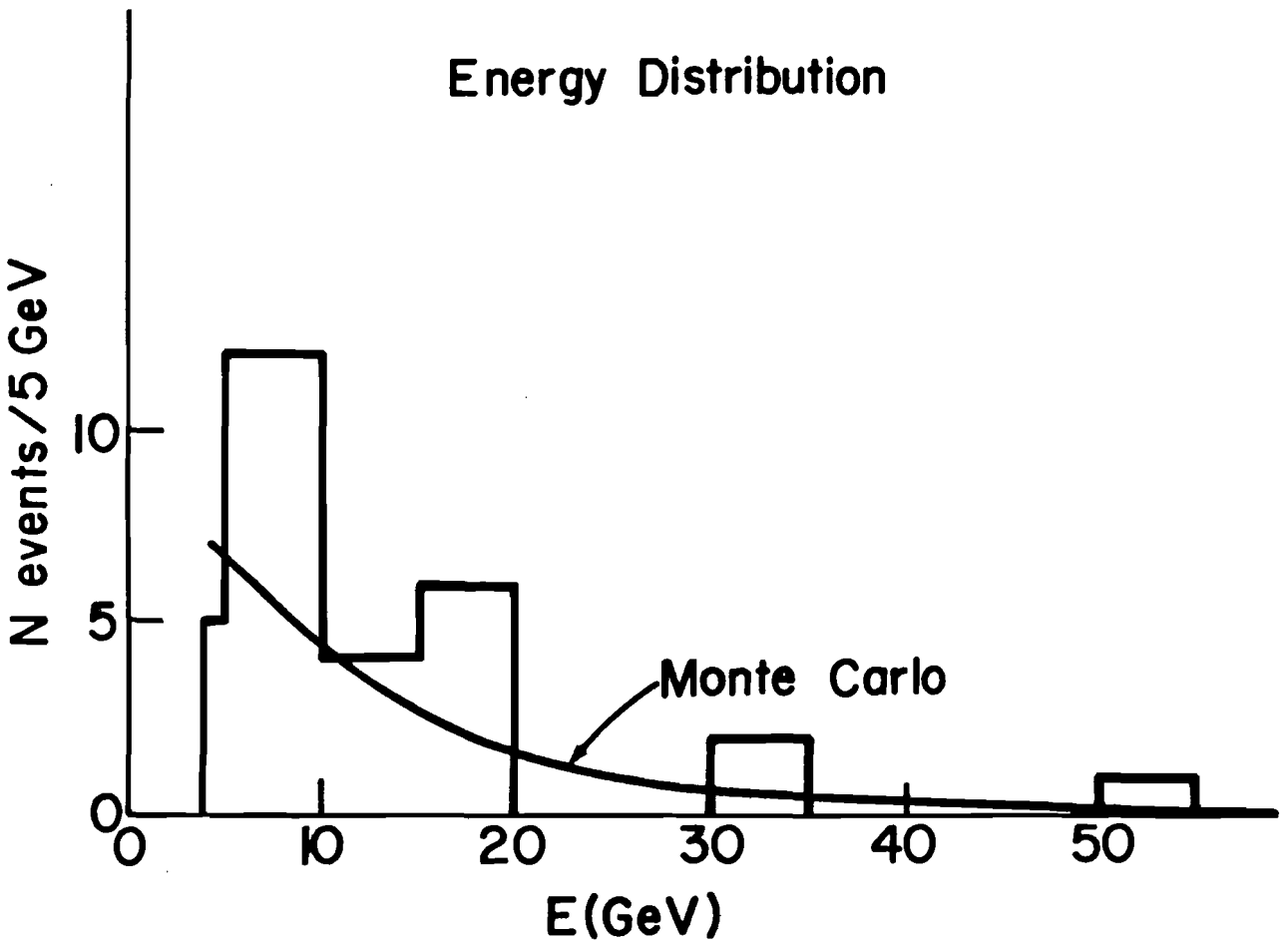

Fig. VIII.2. The energy distribution of the selected events compared to the electroweak model

parameters g_V and g_A. The differential cross sections for $\nu_\mu e$ and $\bar{\nu}_\mu e$ elastic scattering are given by:

$$\frac{d\sigma}{dE_e}\left(\overset{(-)}{\nu}_\mu e \to \overset{(-)}{\nu}_\mu e\right) = \frac{G^2 m_e}{2\pi}\left[(g_V \mp g_A)^2 + (g_V \pm g_A)^2\left(1 - \frac{E_e}{E_\nu}\right)\right] \qquad \text{(VIII-4)}$$

The lower (upper) sign gives the cross section for neutrino (anti-neutrino) scattering. The effective cross section with an energy cut at 4 GeV is:

$$\sigma_{\overset{(-)}{\nu}_\mu e}(E_\nu, E_e > 4) = \int_4^{E_\nu} dE_e \frac{d\sigma}{dE_e}\overset{(-)}{\nu}_\mu e \qquad \text{(VIII-5)}$$

Let $\phi_{\overset{(-)}{\nu}_\mu}(E_\nu)$ be the incident $\overset{(-)}{\nu}_\mu$ flux in units of number of $\overset{(-)}{\nu}_\mu$ per meter squared per GeV per proton incident on the neutrino area target. The number of observed events will be:

$$N = N_e N_p \int_4^\infty dE_\nu \left[\phi_{\nu_\mu}(E_\nu)\sigma_{\nu_\mu e}(E_\nu, E_e > 4) + \phi_{\bar{\nu}_\mu e}(E_\nu)\sigma_{\bar{\nu}_\mu e}(E_\nu, E_e > 4)\right] \qquad \text{(VIII-6)}$$

The constants N_e and N_p are the number of target electrons and the number of protons on target respectively. This equation is an ellipse in the variables g_V and g_A. The region in the g_V-g_A plane allowed by this experiment is shown in Figure VIII.3. The allowed values in the electro-weak model are also shown as a function of $\sin^2\theta_W$. The result of the experiment leaves considerable ambiguity in the allowed values of g_V and g_A.

In order to constrain the allowed values of g_V and g_A in a model independent way, the results of other experiments can be used. Figure VIII.4 shows the allowed regions in the g_V-g_A plane from this experiment, $\bar{\nu}_\mu e$ elastic scattering,[1] and $\bar{\nu}_e e$ elastic scattering.[2] The results of these other two experiments reduce the ambiguity to two allowed regions, a vector dominant solution with $g_V \sim .5$ and $g_A \sim .0$ and an

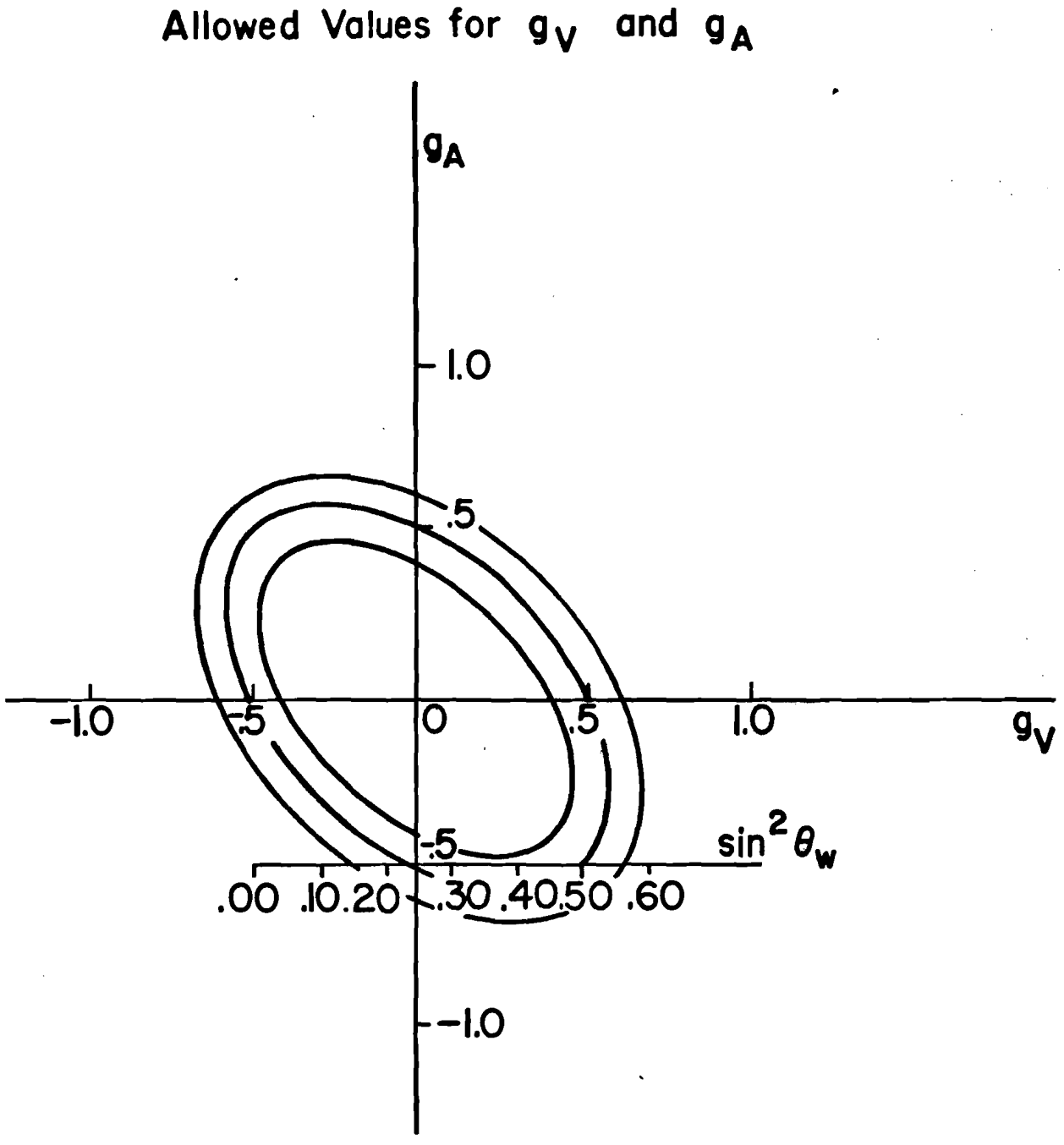

Fig. VIII.3 The experimentally allowed values for g_V and g_A

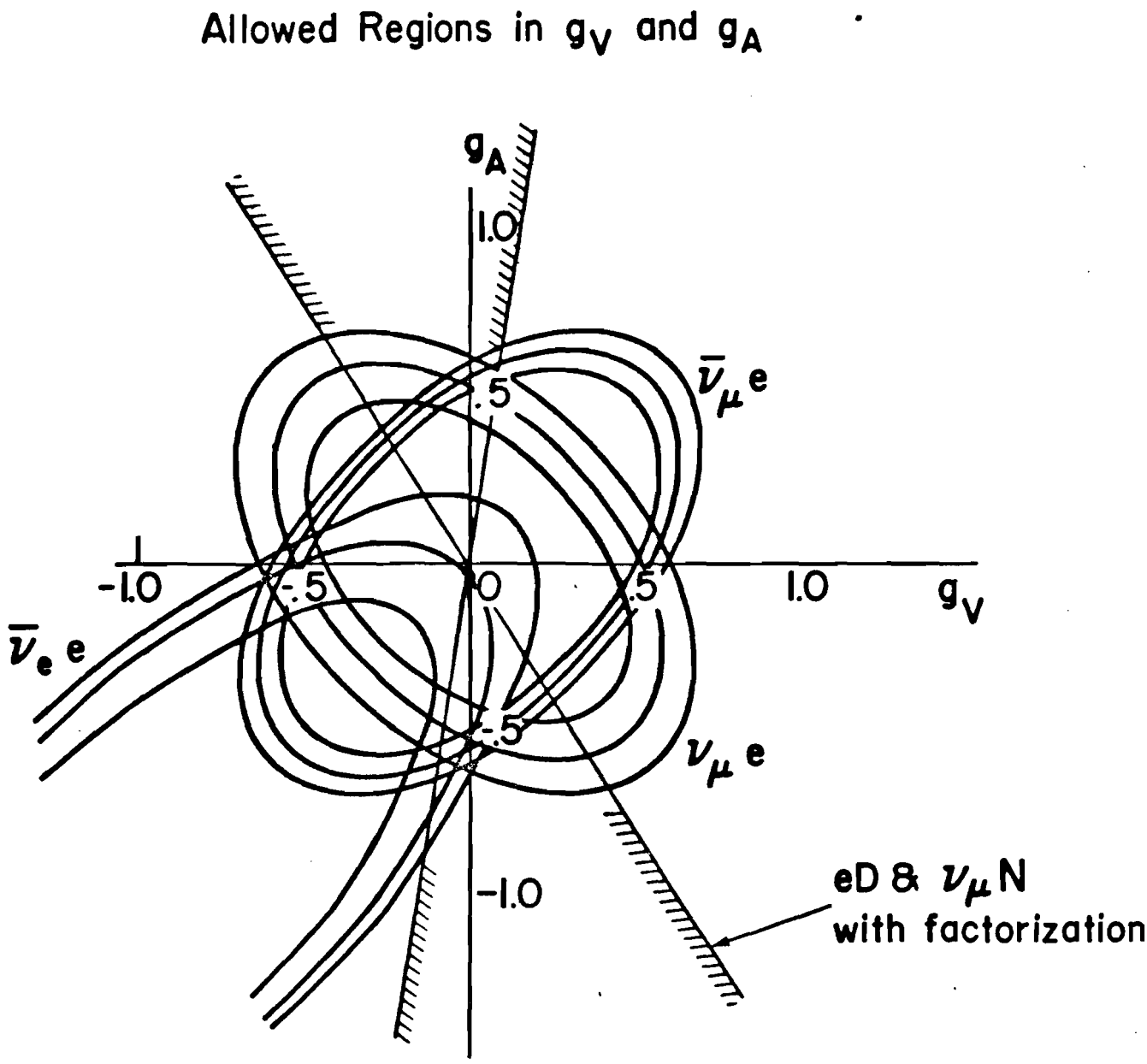

Fig. VIII.4 The allowed regions for g_V and g_A from several experiments

axial dominant solution with $g_A \sim .5$ and $g_V \sim .0$. The axial vector dominant solution is favored by the electroweak model, in order to further resolve the remaining ambiguity, the factorization relation given by equation II-15 can be used to relate the data on $\nu_\mu N$ inclusive scattering and the SLAC interference experiment to the values of g_V and g_A. The addition of this constraint g_A (see Figure VIII.4) accepts the axial vector dominant solution. This solution is $g_V = -0.01 \pm .13$ and $g_A = -.54 \pm .10$. The total cross section corresponding to these coupling parameters is $1.6 \pm .5 \times 10^{-42}\ E_\nu\ cm^2/GeV$.

The electroweak model prediction for the total cross section is shown in Figure VIII.5. A total cross section of $1.6 \pm .5 \times 10^{-42}\ E_\nu\ cm^2/GeV$ only weakly constrains the allowed value of $\sin^2\theta_W$ since the cross section is near the minimum. The allowed values divide into two regions with $\sin^2\theta_W = .23\ ^{+.12}_{-.06}$ and $.53\ ^{+.06}_{-.12}$. The first region is consistent with other experiments.

The parameter $\sin^2\theta_W$ can also be determined from the g_V-g_A plot. In the electroweak model $g_A = 1/2$ and $g_V = 1/2 + 2\sin^2\theta_W$. For $g_V = .01 \pm .13$, $\sin^2\theta_W$ is $.25 \pm .06$.

The errors quoted so far have been statistical errors only. The experiment is also subject to systematic errors from the uncertainty in the incident ν_μ and $\bar{\nu}_\mu$ flux, uncertainty in the correct value for R, the ratio of the neutral current to charged current rates for single π° production used to calculate the hadronic background, and uncertainty in the electron selection efficiency. Table VIII.2 summarizes the effect these uncertainties have on the observed event rate.

The 15% error in the incident $\overset{(-)}{\nu}_\mu$ flux will contribute directly to a 15% error in the expected event rate. Since the kinematic cuts eliminate

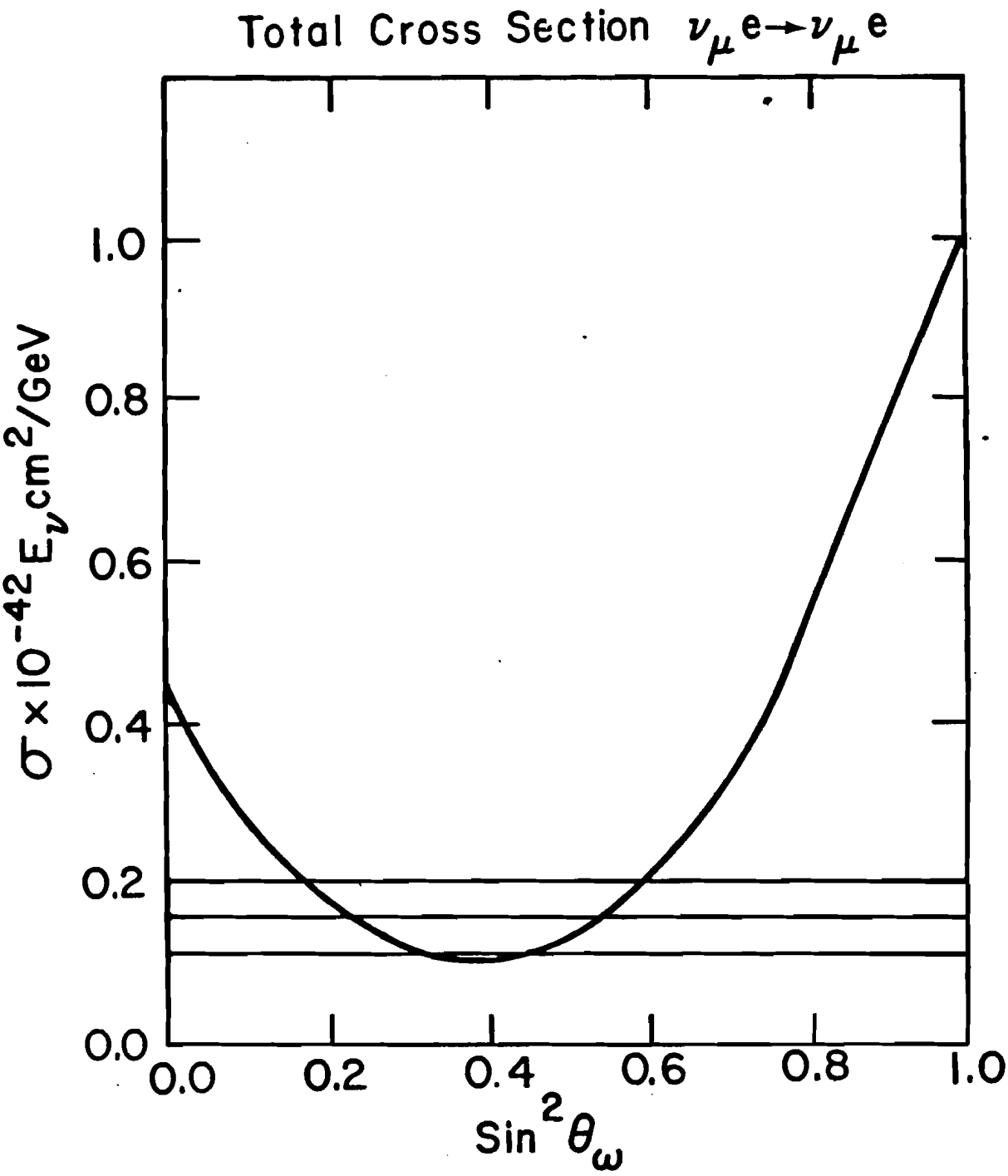

Fig. VIII.5 A comparison of the electroweak cross section with the experimental cross section

much of the quasielastic background, the 100% error in the incident $\overset{(-)}{\nu}_e$ flux contributes an error of only ± 3 events or 10% of the measured signal. As discussed in Chapter V, if the $\overset{(-)}{\nu}_e$ flux is in error it probably is underestimated so that this systematic error will tend to reduce the measured $\nu_\mu e$ signal.

The background due to single π° production was calculated using a value for R of .60 ± .15. This value was determined by fitting the observed charged current events at angles above 20 milliradians to the neutral current distribution. Other experiments have measured this ratio to be .42 ± .14. Using the latter value for R to calculate the background will increase the measured signal by 2 events or by 7%.

As discussed earlier, the error in the total electron selection efficiency is 26% or 8 events.

The overall systematic error can be estimated by adding all of the systematic errors in quadrature. This gives a total error of 10.7 events or 33%. This probably overestimates the systematic error since the error in the $\overset{(-)}{\nu}_e$ flux and the error in R will tend to cancel. The number of observed events is then 33.0 ± 11.3 (statistical) ± 11.0 (systematic). Including systematic effects in the total cross section gives σ = 1.6 ± .5 (statistical) ± .5 (systematic) x 10^{-42} E_ν cm^2/GeV. The calculated value for the parameter $\sin^2\theta_W$ is .25 ± .06 (statistical) ± .06 (systematic).

REFERENCES FOR CHAPTER VIII

1. CERN Charm Collaboration, presented at the Neutrino '81 Conference.

2. F. Reines, et al., Physical Review Letters, 37, 315 (1976).

3. P. Hung and J. Sakurai, Physics Letters, 72B, 208 (1977).

CHAPTER IX

CONCLUSIONS

An experiment to measure the total cross section for $\nu_\mu e$ elastic scattering was performed at Fermi National Accelerator Laboratory from November 1978 to March 1979. This interaction is an important test of the electroweak model developed by Weinberg, Salam and Glashow. In contrast to $\nu_\mu N$ interactions which are complicated theoretically since the quark content of the nucleon is not well known, $\nu_\mu e$ scattering involves the scattering of point-like particles making the theoretical predictions fairly straightforward. However, the experiment is very difficult since the cross section is of the order of 10^{-42} E_ν cm^2/GeV and the backgrounds from other neutrino interactions are difficult to eliminate.

The Fermilab wide-angle neutrino beam was used with an accelerator energy of 350 GeV. This beam offers a high flux and a broad incident energy distribution. A total of $.9 \times 10^{19}$ protons were incident on the neutrino area target to produce the neutrinos with a total of 249,000 triggers written to tape. The analysed data sample consisted of 190,000 triggers corresponding to $.7 \times 10^{19}$ protons on target. The neutrino beam also consists of a small contamination of antineutrinos (8%) and electron type neutrinos (.2%).

The neutrinos are incident on a 12 ton, modular detector. Each of the 49 modules of the detector consists of 1.1 radiation lengths of aluminum, a delay-line proportional chamber, and a plastic scintillator.

The neutrino scatters off an electron in the aluminum and the recoiling electron forms an electromagnetic shower which propagates through the detector. The aluminum acts as both the target and the radiator for the electromagnetic shower. The delay-line proportional chamber measures the x and y position of the shower centroid in each module, thereby determining the shower angle. The energy is determined by the scintillator phototube pulse height. The detector has an angular resolution of 10 milliradians and an energy resolution given by $\sigma_E/E = .29/\sqrt{E}$.

The vast majority of the interactions occurring in the detector are $\nu_\mu N$ interactions. The data reduction procedure must reject the $\nu_\mu N$ events while retaining the $\nu_\mu e$ interactions. A computer program was used to preselect the likely $\nu_\mu e$ candidates. The $\nu_\mu N$ interactions will have a hadronic component consisting of charged hadrons and an electromagnetic component from π° decay. The $\nu_\mu e$ events are single electromagnetic showers kinematically constrained at small angles. The preselection criteria consisted of a loose set of cuts rejecting wide electromagnetic showers with accompanying hadrons and showers at an angle larger than 50 milliradians. A total of 26,000 interactions passed the cuts.

Each of the preselected events was scanned by a physicist implementing a tighter set of cuts on the shower characteristics to isolate only single electromagnetic showers. If the event is a charged current then the presence of the muon was ignored so that the same selection criteria applied to both the charged and neutral current interactions. This reduced the data sample to 149 neutral currents and

104 charged currents. The event reconstruction and shower fit were then checked by hand in an unbiased way to obtain the final shower angle.

The backgrounds remaining in the final sample were the $\overset{(-)}{\nu}_e$ quasielastic interactions $\nu_e n \rightarrow e^- p$ and $\bar{\nu}_e p \rightarrow e^+ n$, and single π° production by the hadronic neutral current and by the charged current with the muon unidentified. The quasielastic background was calculated using a Mone Carlo calculation. The single π° production background in the neutral current sample as calculated using the observed charged current distributions correcting for the muon acceptance.

The overall $\nu_\mu e$ event selection efficiency was $.54 \pm .12$. This efficiency is a product of the computer preselection efficiency, the scanning selection efficiency, and the efficiency of the scanner in consistently implementing the scanning costs. Using the overall selection efficiency and the calculated backgrounds, then the observed signal can be computed. Applying an angle cut at 20 milliradians gives a signal of 35.4 ± 13.0. A tighter kinematic constraint is an angle cut at 20 milliradians and a cut on $E\theta^2$ at 3 MeV. This gives a signal of 33.0 ± 10.8. The systematic error, due mainly to the uncertainty in the incident neutrino flux, is 33%.

It is clear that the statistical error in this experiment could be improved by relaxing the fiducial cut made during scanning, contributing however, to a larger systematic error. Taking into account these errors gives a total cross section of $1.6 \pm .5$ (statistical) $\pm .5$ (systematic). The parameter $\sin^2\theta_W$ is $.25 \pm .06$ (statistical) $\pm .06$ (systematic).